The Pennsylvania State University

The Graduate School

LOW TEMPERATURE PROCESSING OF ELECTRO-CERAMIC MATERIALS AND DEVICES

A Dissertation in

Materials Science and Engineering

by

Dixiong Wang

Submitted in Partial Fulfillment
of the Requirements
for the Degree of

Doctor of Philosophy

May 2020

The dissertation of Dixiong Wang was reviewed and approved by the following:

Susan E. Trolier-McKinstry
Steward S. Flaschen Professor of Ceramic Science and Engineering
Dissertation Advisor
Chair of Committee

Clive A. Randall
Professor of Material Science and Engineering

Thomas N. Jackson
Robert E. Kirby Chair Professor of Electrical Engineering

Qing Wang
Professor of Materials Science and Engineering

John C. Mauro
Professor of Materials Science and Engineering and Electrical Engineering
Chair of Intercollege Graduate Degree Program in Materials Science and Engineering

ABSTRACT

The dissertation investigated two low temperature processing methods: Applying deep ultra-violet (DUV) radiation during the sol-gel deposition of Bi_3NbO_7 (BNO) thin films to facilitate carbon removal, and the cold sintering process (CSP) of Pb(Zr, Ti)O_3 (PZT) powder/tape.

A DUV treatment between the drying and pyrolyzing steps during sol-gel deposition can effectively eliminate the residual carbon in BNO thin films at < 350 °C, which decreases the porosity, and improves the energy storage densities of the BNO capacitors. As a result, the BNO thin film, when annealed between 350-450 °C, presented energy storage densities of 13-39 J/cm^3, which is comparable with many thin films crystallized at 700 °C. Furthermore, by suppressing the maximum heat treatment temperature, high performance thin film capacitors can be directly deposited on the polymer/metal substrates. This will shorten the processing flow of flexible electronics and can be beneficial to the production of wearable devices.

The cold sintering process was also employed in order to densify lead zirconate titanate, one of the most widely used piezoelectric materials. The CSP often utilizes a water-based transient liquid phase to either partially dissolve the ceramic powder, creating a liquid phase sintering (LPS) condition; or lubricate the powder to enhance the compaction. Because it is difficult to dissolve PZT powder, moistened $Pb(NO_3)_2$ was mixed with PZT to help packing the PZT powder to a relative density over 80% during cold sintering at 300 °C, 500 MPa. The $Pb(NO_3)_2$ also decomposes into PbO, which helps to liquid phase sinter the PZT when the cold sintered samples were post-annealed at 700-900 °C. The 900 °C post-annealed PZT showed a relative density ~99% with a room-temperature relative permittivity over 1300 and a d_{33} ~200 pC/N. Further study also suggested the cold sintering of PZT/$Pb(NO_3)_2$ obeys a viscous sintering model, which differs from the cold sintering mechanisms reported for many other materials.

The dissertation also evaluated the processing of PZT/metal/PZT 2-2 composites via cold sintering and post-annealing. It was found that the cold sintering process can suppress micro-cracking in the PZT layer, presumably by strengthening the ceramic compact at low temperatures. Constrained sintering was observed when PZT was cold sintered on Ni or Cu foils; these could be avoided by laminating tape cast PZT and Cu powder instead. However, the Cu_2O interface formed between PZT and Cu is still problematic. The relative permittivity of the 800 °C annealed PZT on Cu is only ~500, with an $-e_{31,f}$ less than 5 C/m^2. If future work is able to achieve a clean interface, this process can be helpful for the fabrication of piezoelectric energy harvesters with high open circuit voltages.

TABLE OF CONTENTS

LIST OF FIGURES

LIST OF TABLES

ACKNOWLEDGEMENTS

Even many years later, as I will probably still keep striving for my ambition somewhere, I shall never forget that distant summer afternoon when I first landed in State College, the willow was gently fiddled by the wind. Now, Nittany Mountain is hibernating amongst the cold rain, and the finale of my student era is near. This is the seventh year of me being a "Penn Stater". Although it is never possible to list every person I have received help from in the past seven years, a few of them must be addressed for their importance in my life.

First and foremost, I would like to present my greatest appreciation to Dr. Susan Trolier-McKinstry. She is not only a knowledgeable advisor with inspiring ideas, excellent teaching skills, and brilliant problem-solving techniques, but also an educator of merits to be admired. After an intensive four-and-half-year PhD program, I have been taught to love my career, stay humble, be suspicious as a scientist, and always shoot for perfection.

I would also acknowledge my thesis committee members: Dr. Clive Randall, Dr. Tom Jackson, and Dr. Qing Wang. They have led me to many helpful discussions to strengthen my weak points during the comprehensive exam, as well as providing suggestions for my project from their expertise.

I would like to thank the staff members in MSC, including Beth Jones, Amanda Baker, Bangzhi Liu, Bill Drawl, Mike Labella, Andy Fitzgerald, Guy Lavallee, Kathy Gehoski, Chad Eichfeld, Ke Wang, Julie Anderson, Nicole Wonderling, Katya Bazilevskaya, Maria Dicola, Manuel Villalpando, Gino Tambourine, Jeff Long, Steve Perini, Tim Klinger, and Damina Richards for their support.

My appreciation should also be shared with the past and current group members of Dr. Susan Trolier-McKinstry and Dr. Clive Randall: Sandie Elder, Elizabeth Michael, Ryan Keech, Hong Goo Yeo, Carl Morandi, Wanlin Zhu, Song Won Ko, Jung In Yang, Smitha Shetty,

Veronika Kovacova, Daisuke Hama, Sanshiro Aman, Lyndsey Dennis, Trent Borman, Betul Akkopru Akgun, Tianning Liu, Kathleen Coleman, Chris Cheng, Leonard Jacques, Nicole Hall, Shruti Gupta, Nathan Bishop, Mike Hahn, Travis Peters, Pannawit Tipsawat, Joanne Aller, Hanzheng Guo, Jing Guo, Lisheng Gao, Seth Berbano, Sinan Dursun, Arnaud Nadayishimiye, Kosuke Tsuji, Joo Hwan Seo, Sun Hwi Bang, and Zane Grady.

This thesis would never be completed without the help from all the collaborators, and I give thanks to Dr. Shad Roundy, Dr. Mehdi Kiani, Binh Duc Truong, Miao Meng, Mike Clark, and Tony Sokolov. I would also like to acknowledge the Dow Chemical Company and Empower Materials, Inc. for their supplies.

A group of friends Yihuang Xiong, Kehao Zhang, Jinwen Zhu, Chengye Dong, Ding Ai, Wenbo Guo, Ying Zhang, Weinan Chen, Zhuqing Wang, Ning Yi, and Xiaotian Zhang, and Siyu Xu should be acknowledged for all the interdisciplinary discussions during our weekly “Hot Pot Seminar.” Some really interesting ideas engendered during these discussions are reflected in the future work of this thesis.

I have to mention two of my previous advisors: Dr. Joshua Robinson and Dr. Yaming Wang (Harbin Institute of Technology, China). The experiences working in their groups have solidified the foundation of my research and have brought me a broad vision.

Financial support for this thesis was provided by Dow Chemical and NSF ASSIST funding.

Last but not the least, I would give a special thanks to my parents Baojin Wang and Li Cai, and my family for their love and care.

Chapter 1

Statement of Goals and Thesis Organization

1.1 Statement of purpose

The rapidly growing market of wearable and implantable electronics has brought convenience to people's lives as well as challenges to material scientists: How to advance the material synthesis and processing techniques that suits the fabrication of those devices. In particular, there is a need to develop flexible, miniaturized, non-toxic, and high-performance material systems. Especially for electro-ceramics, the synthesis and processing of which are generally carried out at temperatures too high for most flexible organic and metallic substrates, technology upgrades are essential.

As an example, the deposition of oxide thin films by either chemical solution deposition or physical/chemical vapor deposition, requires minimum crystallization temperatures typically above 600 °C, where almost all polymers will be immediately pyrolyzed, and base metals are subject to oxidation. Lowering the deposition temperatures, however, induces degraded crystallinity, secondary phases, or chemical residues that diminish the energy storage densities of the products. A low temperature deposition process should be proposed along with novel material systems to maximize the energy storage performance.

Another important trend for future implantable electronics is self-powering, since many devices are expected to provide continuous service. Currently developed self-power solutions based on piezoelectric energy harvesters have limited power density and low energy conversion

efficiencies due to constraints on piezoelectric layer thickness. Thicker piezoelectric layers deposited by sol-gel or sputtering method are not only expensive but also present high micro-crack densities. And ceramic thick films prepared by low temperature co-fired ceramic (LTCC) technologies are typically difficult to densify. Cold sintering has the potential to densify ceramic pellets and thick films at an acceptably low temperature range, and might be useful for manufacturing high figure of merit piezoelectric energy harvester beams.

1.2 Dissertation structure

The thesis was constructed with three main topics focusing on the processing of ceramic thin films, pellets, and thick films at temperatures lower than conventional techniques.

Chapter 2 discusses the development of bismuth-based thin film energy storage capacitors. Facilitated by deep ultra-violet (DUV) treatment, bismuth niobate thin films with improved electrical properties were achieved. The influences of DUV radiation on density, crystallinity, relative permittivity, and electric breakdown strength were compared under different heat treatment temperatures. Future work also suggested some preliminary results for the further increase in the energy densities.

Chapter 3 depicts an exploration on the cold sintering process of bulk lead zirconate titanate (PZT) ceramics. The microstructure, dielectric properties, and piezoelectric constants of PZT powder cold sintered with moistened lead nitrate are presented. The underlying densification mechanisms of PZT as well as the effects of cold sintering temperature, pressure, and holding time were incorporated into a modified viscous sintering model. A one-step sintering technique is introduced at the end of this chapter that can potentially fully densify PZT below 400 °C.

Chapter 4 describes the attempt to cold sinter PZT thick films with metal for high voltage piezoelectric energy harvesters. With the pathways paved by the studies on pellet cold sintering,

this process was successfully integrated with tape cast piezoelectric layers. The behaviors of PZT along with multiple commonly used metals during cold sintering and post-sintering was evaluated.

Chapter 2

Ultra-Violet-Assisted Low Temperature Processing of Bismuth Niobate Thin Film for Dielectric Energy Storage Capacitors

2.1 Introduction

Capacitive energy storage is of interest for high charge-discharge rates in electronic circuits. With the rapid development of wearable electronic devices, flexible electronics, and embedded passive components, integration of capacitors on polymer films [1–3] or metal foils [4,5] has drawn recent interest. Moreover, the miniaturization of microelectronic devices requires materials with high volumetric energy storage densities. Thus, there is interest in developing new materials and processes for high energy storage density capacitors on flexible substrates. Many widely studied oxide thin films, such as $BaTiO_3$ [6] and $Bi_{1.5}ZnNb_{1.5}O_7$ [7], are suitable for dielectric energy storage, but require high crystallization temperatures beyond the glass transition temperatures of polymers, and annealing atmospheres that oxidize base metal foils.

This work explores low temperature processed Bi_3NbO_7 (BNO) thin films as potential candidates for high energy density capacitors. The BNO samples were fabricated by a chemical solution deposition method followed by ultra-violet (UV) exposure and heat treatments. A UV treatment prior to the final pyrolysis step was found to eliminate bound carbon and promote crystallization of BNO at low temperatures. Following a series of heat treatments from 350 °C - 450 °C, the energy storage density of the BNO thin film increased from 13 J/cm^3 to 39 J/cm^3. Furthermore, 350 °C and 375 °C treated BNO samples showed that the efficiencies of the films remained above 97% up to 150 °C at 10 kHz under 1 MV/cm applied field.

* *Part of this chapter is reproduced from D. Wang, M. Clark, and S. Trolier-McKinstry "Bismuth Niobate Thin Films for Dielectric Energy Storage Applications." Journal of the American Ceramic Society 101 (8), 3343-3451 (2018).*

2.2 Literature review

2.2.1 Dielectric energy storage capacitors

A capacitor is a device that stores electrical energy. Compared with batteries and fuel cells, capacitors have low to modest levels of specific energy (or energy densities) but very high specific power (or power densities) due to their fast charge-discharge rates, as shown in Figure 2-1 (a). Some capacitors that utilize space charge as the storage mechanism have high permittivity and specific energy, but only operate at comparatively low frequencies where the space charge does not relax. These are known as electrochemical capacitors [8]. In contrast, dielectric capacitors rely on polarization of the dielectric layer. These capacitors exhibit lower energy densities with very high power per unit volume. Figure 2-1 (b) indicates the typical working frequency ranges of electrochemical capacitors and dielectric capacitors respectively. [9]

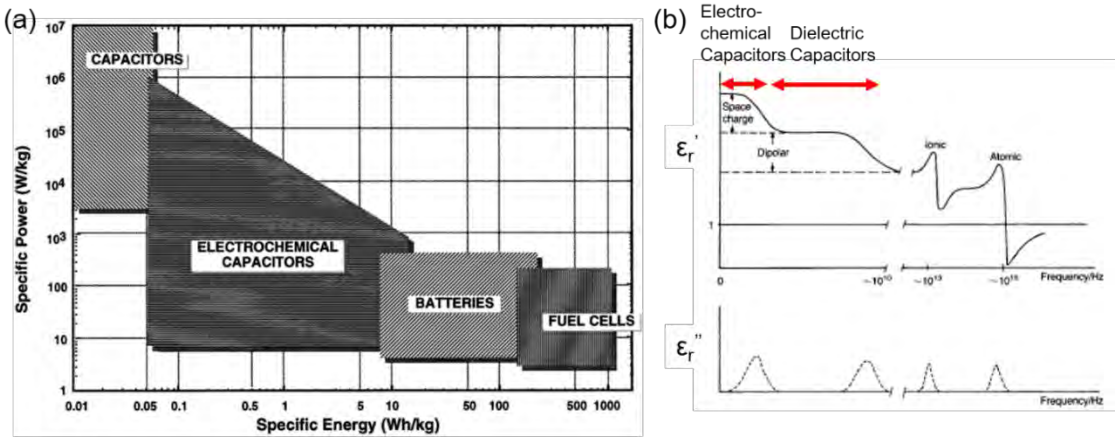

Figure **2-1**: (a) Comparisons between (dielectric) capacitors, electrochemical capacitors, batteries and fuel cells in terms of their power density and energy density. [8] (b) The working frequency ranges of electrochemical and dielectric capacitors where ε_r' and ε_r'' represent relative dielectric permittivity and dielectric loss, respectively. [9]

The energy density of a capacitor, U, can be determined experimentally from the polarization-electric field loop (P-E loop). Figure 2-2 is a schematic plot of the P-E loop of a

linear dielectric material. The energy storage density is given by the area enclosed by the loop and the y-axis in the 1st quadrant.

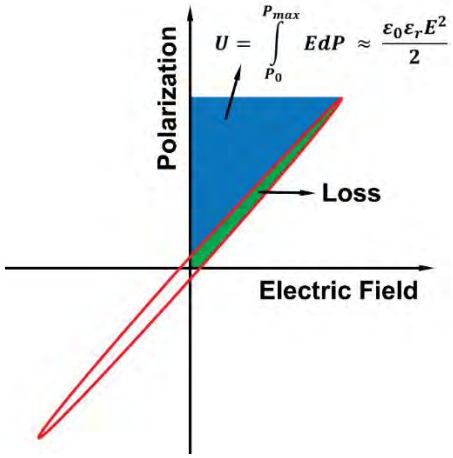

Figure **2-2**: A schematic plot of a P-E loop. The area shown in blue shading represents the amount of energy stored per unit volume in a capacitor, while the green area shows the energy loss due to Joule heating. [10]

The stored energy (W) can also be described by the volumetric integration of the dot product of electric displacement ($\vec{D}$) and electric field ($\vec{E}$):

$$W = \iint \vec{E}\, d\vec{D} dv \qquad \text{(Eq. 2-1)} \ [9]$$

That means that the energy density (U) of a capacitor can be represented as:

$$U = \frac{dW}{dv} = \int_{D_0}^{D_{max}} \vec{E}\, d\vec{D} \qquad \text{(Eq. 2-2)}$$

In most capacitors, the dielectric material is sandwiched between two parallel electrodes, and the total dielectric displacement $\vec{D}$ is given by:

$$\vec{D} = \varepsilon_0 \vec{E} + \vec{P} \qquad \text{(Eq. 2-3)}$$

The polarization ($\vec{P}$) is a function of electric field (E):

$$\vec{P} = \varepsilon_0 \chi_e \vec{E} \qquad \text{(Eq. 2-4)}$$

where $\varepsilon_0 = 8.85*10^{-12}$ F/m is the vacuum dielectric constant, and χ_e is the electric susceptibility which is related to relative dielectric permittivity (ε_r):

$$\chi_e = \varepsilon_r - 1 \qquad \text{(Eq. 2-5)}$$

For many dielectric materials, the relative permittivity is much larger than 1, $\chi_e \approx \varepsilon_r$. Thus:

$$U = \int_{P_0}^{P_{max}} \vec{E}\, d\vec{P} \qquad \text{(Eq. 2-6)}$$

For an ideal linear dielectric material with no loss, all the input energy can be stored and fully extracted upon discharging the capacitor, giving an inclined single line for the P-E loop. However, in practice, materials have a finite electrical conductivity and part of the input energy is dissipated via Joule heating. This loss is represented as the green region in Figure 2-2, which has an area of:

$$w_e = 2\pi \cdot U \cdot tan\delta \qquad \text{(Eq. 2-7)} \ [11]$$

where tanδ is called the loss tangent of a material.

Considering the loss of a capacitor, the energy storage efficiency (η) can be defined as:

$$\eta = \frac{U_{rec}}{U_{total}} = \frac{U_{rec}}{U_{rec}+w_e} \times 100\% \qquad \text{(Eq. 2-8)}$$

U_{rec} is the recoverable (or discharge) energy density, U_{total} is the total energy input during charging. Figure 2-2 shows that the energy storage efficiency is the fraction of the blue area with respect to the sum of blue and green areas. During the design of novel energy storage materials, it is almost as important to consider the energy storage efficiency as the magnitude of recoverable energy density; less efficient capacitors waste energy, and have shorter lifetimes due to degradation caused by accumulated Joule heating.

By plugging Eq. 2-3, Eq. 2-4, and Eq. 2-5 into Eq. 2-2, and assuming the electric displacement is in the same direction as the applied electric field:

$$U = \frac{1}{2}\varepsilon_0 \varepsilon_r E^2 \qquad \text{(Eq. 2-9)}$$

From Eq. 2-9, it is obvious that in the case of an ideal linear dielectric material with negligible loss tangent, the energy density is proportional to ε_r and E^2, which means that high energy storage densities can be achieved in materials with not only large dielectric constants but also high breakdown strengths (BDS, the highest applicable electric field before short circuiting the capacitor). And since energy density is proportional to the square of electric field, materials with modest permittivity but outstanding BDS are more suitable for energy storage in high voltage systems. Therefore, it is of interest to understand the electrical breakdown mechanisms.

2.2.2 Electrical breakdown mechanisms

The electrical breakdown defines the "failure of dielectrics under electrical stress". [9] There are three main mechanisms that contribute to electrical breakdown: intrinsic (avalanche) breakdown, thermal breakdown, and discharge breakdown.

2.2.2.1 Intrinsic (avalanche) breakdown

Intrinsic breakdown describes the process during which, upon steadily increasing electric fields, the leakage currents in a sample first saturate, and then increase sharply within 10^{-8} sec. The intrinsic breakdown process can be depicted as the electric current amplification due to a combination of electron injection from the cathode and the collision ionization with the dielectrics: [12]

$$J(d) = J_0 exp\left[-\frac{4(2m)^{\frac{1}{2}}\Phi^{\frac{3}{2}}}{3\hbar eE} + \frac{eEd}{E_a}\right] \qquad \text{(Eq. 2-10)}$$

where J is the current density, d is the thickness of the sample, m is the effective mass of the electrons, Φ is the work function of the cathode, E_a is the material-dependent activation energy

for collision ionization, ħ=h/2π represents the reduced Planck's constant, e is the electron charge, and E is the applied electric field.

From Eq. 2-10, breakdown should occur when the current density starts to increase and do damage to the dielectric, namely, when

$$-\frac{4(2m)^{\frac{1}{2}}\Phi^{\frac{3}{2}}}{3\hbar eE}+\frac{eEd}{E_a}=0 \qquad \text{(Eq. 2-11)}$$

Solving for E yields:

$$E_{breakdown}=\sqrt{\frac{4(2m)^{\frac{1}{2}}\Phi^{\frac{3}{2}}E_a}{3\hbar e^2 d}}\approx\frac{3\times10^4}{d^{\frac{1}{2}}}\ V/cm \qquad \text{(Eq. 2-12)}$$

Eq. 2-12 suggests for the same homogeneous material with the same electrodes, the intrinsic breakdown strength should be inversely proportional to the square root of the dielectric thickness.

2.2.2.2 Thermal breakdown

Thermal breakdown appears when a device generates heat faster than the heat is dissipated. The accumulated heat increases the temperature of the dielectric, elevates the ionic and electronic conductivities, and eventually leads to breakdown. [9] Thermal breakdown behavior is governed by Eq. (2-13), according to O'Dwyer. [12]

$$C_v\frac{dT}{dt}-grad(\kappa\cdot divT)=\sigma E^2 \qquad \text{(Eq. 2-13)}$$

where C_v is the volumetric specific heat, T is the temperature, t is the time, κ is the thermal conductivity, σ is the electrical conductivity, and E represents the electric field strength. This equation associates the heat accumulation ($C_v\frac{dT}{dt}$) and the heat dissipation ($-grad(\kappa\cdot divT)$) with the heat generation (σE^2).

Practically, however, it is difficult to solve this equation because there are too many variables. For example, the electric field can be a function of both position and time (AC fields), so too the temperature; the electrical conductivity σ is affected by both electric field and temperature; the thermal conductivity κ is related to the temperature of the dielectric. These variables make it nearly impossible to find an analytical solution for a material. Even numerical solutions from experimental data vary as a function of the electrode geometry. Additionally, external conditions such as field frequency, and the heat transfer rate between the dielectric and their environment further influence the results.

2.2.2.3 Discharge breakdown

Discharge breakdown results from defects in the dielectric, such as compositional inhomogeneity, interfaces, and pores. These defects produce field concentrations and can potentially become sites for discharge under electrical stress. [9]

One of the most notorious culprits for discharge breakdown is porosity. For instance, in a disc-shaped pore perpendicular to the applied electric field, the electric field inside the pore is [9]

$$E_{cavity} = \frac{\varepsilon_{r,matrix}}{\varepsilon_{r,pore}} E \qquad \text{(Eq. 2-14)}$$

Note that the relative permittivity of the gas (or vacuum) in the cavity ($\varepsilon_{r,pore}$) is typically ~1, while the relative permittivity of the dielectric matrix ($\varepsilon_{r,matrix}$) is much larger. This leads to high electric field accumulation inside the pore, which is sufficient to initiate failure. Therefore, a homogeneous dense sample is essential to mitigate discharge breakdown. Moulson *et al*. illustrate the relationship between breakdown strengths and the relative density of high purity alumina, as shown in Figure 2-3. [9] The dependence of breakdown strength on the relative density of the alumina is believed to be dominated by discharge phenomenon.

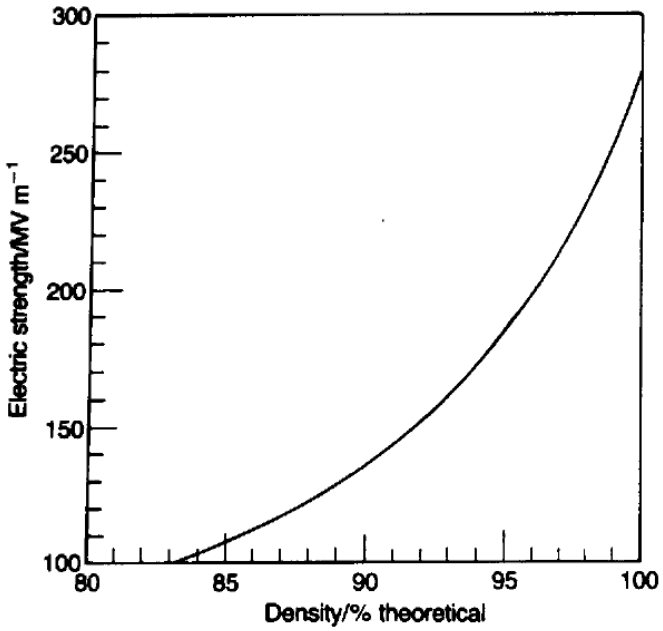

Figure **2-3**: The relationship between breakdown strength and the relative density of high purity alumina. Plot from Moulson *et al*. [9]

The discharge breakdown strength can also be enhanced by miniaturizing the dimensions of the devices. This trend is observed because the smaller the sample thickness/electrode area, the lower the possibility of a critical defect, as shown by many authors, including Moulson *et al*. on high purity alumina [9] and Michael *et al*. in bismuth zinc niobate tantalite (BZNT) [13].

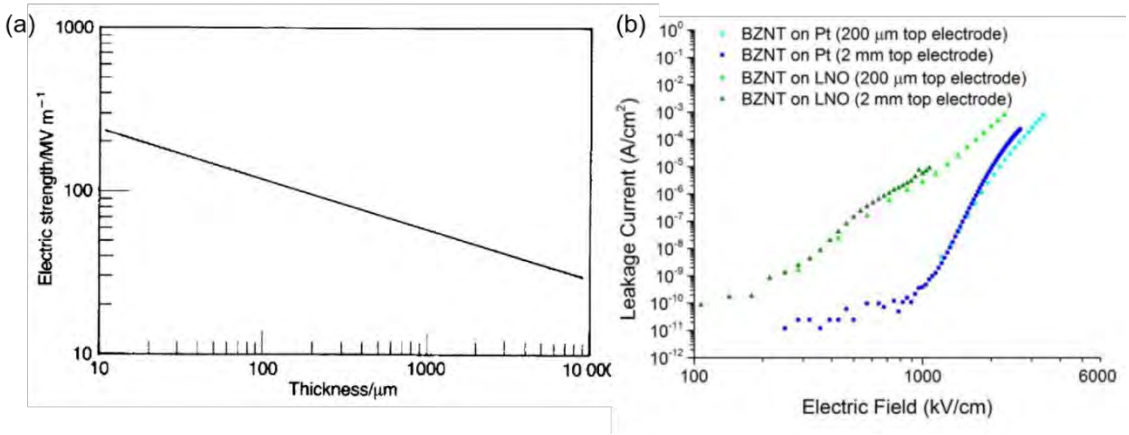

Figure **2-4**: (a) The variation of electric breakdown strengths of high purity alumina with different thicknesses. Figure reproduced from Moulson *et al*. [9]. (b) The leakage current versus electric field

of bismuth zinc niobate tantalate thin film with $LaNiO_3$ (LNO) or Pt top electrodes of two different diameters (200 μm or 2 mm). Complete breakdown happens at the upper right of the plot. Figure adopted from the Ph.D. thesis of E. Michael. [13]

In summary, high permittivity is often associated with high valence cations with appreciable net polarizations, while outstanding breakdown strength should appear in a system with high bandgap, short bonds, and extraordinary homogeneity.

2.2.3 Materials for dielectric energy storage

Linear dielectric materials, ferroelectric materials, relaxors, and anti-ferroelectric materials can all be used as dielectrics.

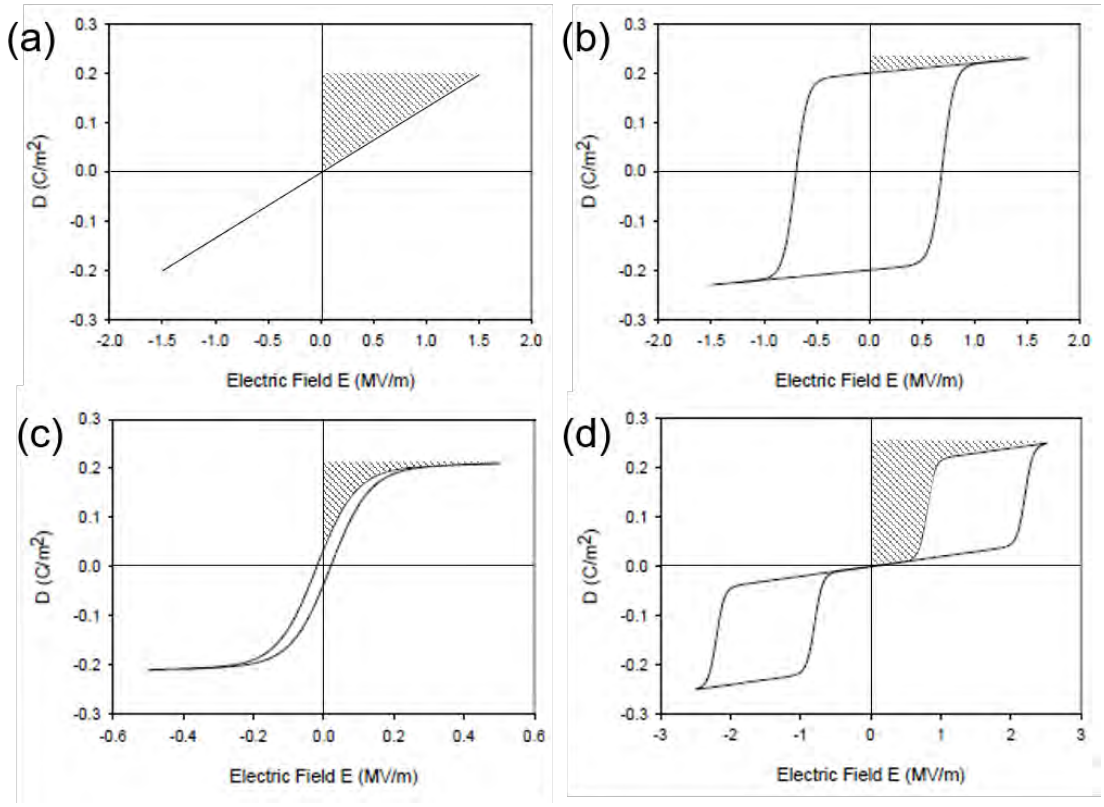

Figure **2-5**: The characteristic polarization-electric field hysteresis loops for (a) linear dielectrics, (b) ferroelectric materials, (c) relaxors, and (d) anti-ferroelectric materials. The shaded area represents the energy storage densities in each case. (Modified figure based on Sherrit *et al*. [14])

Ferroelectric (FE) materials present switchable spontaneous polarizations under electric fields exceeding the coercive field. [9] After most of the spontaneous polarization is re-oriented, the polarization saturates. Upon removal of the external electric field, a remanent polarization remains at zero field. Compared with most linear dielectric materials, ferroelectric materials have relatively large dielectric permittivities due to the existence of the spontaneous polarization. However, the high remanent polarizations are detrimental for energy storage because they limit efficiency.

Relaxors are ferroelectric materials but with disrupted long-range polar order [15]. Relaxors contain polar nanoregions (PNR) with characteristic lengths scales of 2 – 20 nm, distributed in a high polarizability matrix. Characteristically, the P-E loop of a relaxor is slimmer than a normal ferroelectric material, with a lower remanent polarization. This makes relaxors more suitable for energy storage capacitors as both the energy densities and the energy storage efficiencies are improved.

Antiferroelectric (AFE) materials are characterized by "double hysteresis" in the P-E trace as a result of sublattices with opposing polarizations within a unit cell. [16] Near zero electric field, antiferroelectric materials have very small remanent polarizations, yielding large energy densities. However, large hysteresis along with saturation of polarization appears at higher fields; this reduces the potential of AFE materials as energy storage capacitors especially at high duty cycles.

In the following sections, five materials families for dielectric energy storage are discussed.

2.2.3.1 Polymers

Polymer film capacitors are widely used for dielectric energy storage due to a combination of high breakdown strength (BDS) [17,18] and graceful failure. In addition, ease in processing and flexibility in achievable shapes make them useful in wearable electronics. The high breakdown strengths in polymers arise from their relatively low electrical conductivities. [19] Since both free electrons and ion concentrations tend to be low, electric fields up to several MV/cm can be applied to polymeric parts without damaging the devices. Therefore, polymer capacitors are commonly used in some pulsed power systems with high peak voltages, [20] such as wound capacitors made with polyethylene and biaxially oriented polypropylene (BOPP). [21–23]

Unfortunately, most polymeric capacitors have relative dielectric constants < 3, resulting in low energy density; for example, the typical energy density for BOPP is ~ 1-1.2 J/cm^3. [20] In the past decade, attempts to increase the polarizability of polymers led to research on poly(vinylidene fluoride) (PVDF) and its derivatives. PVDF (especially β-PVDF) has a high relative permittivity ~ 12. [20] Although the energy density of PVDF is almost 2 times larger than BOPP, it was not initially utilized due to its low efficiency, large dielectric loss, and low breakdown strength. In addition, as β-PVDF is a ferroelectric material, the polarization saturates above a critical electric fields.

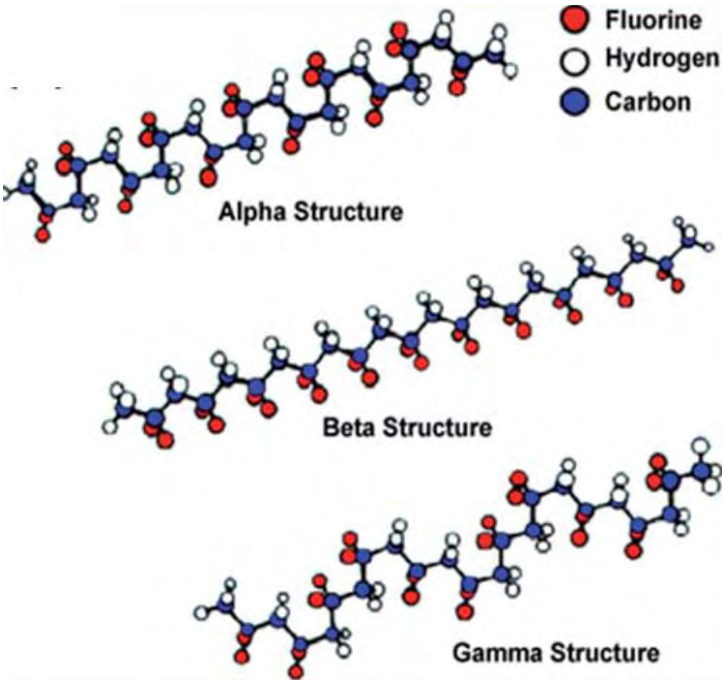

Figure **2-6**: The molecular structures of α, β, and γ-phase PVDF. The red balls represent fluorine atoms, white balls represent hydrogen atoms, and blue balls are carbon atoms. (Figure adopted from Wan *et al*. [24])

The situation had drastically changed in the past 10-15 years, however. Li *et al*. compared the energy storage performance of α, β, and γ-phase PVDF, finding that γ-PVDF is more promising. Because of the reduced crystallinity produced by the β to γ transition, the breakdown strength increases, yielding an energy density as high as 14 J/cm^3. [25] Chu *et al*. developed a 17 J/cm^3 poly(vinylidene fluoride-trifluoroethylene-chlorofluoroethylene) (P(VDF-TrFE-CFE)) capacitor by inducing relaxor behavior to reduce the remanent polarization, as illustrated in Figure 2-7. [26] Later development of a hexafluoropropylene modified PVDF (P(VDF-HFP)) increased the breakdown strength from ~5 MV/cm to over 7 MV/cm, generating higher energy densities (25 J/cm^3 – 30 J/cm^3) in such compounds. [27,28] Poly(arylene ether urea) (PEEU) [29], sulfonylated poly(2,6-dimethyl-1,4-phenylene oxide) (SO2-PPO) [30], and –(SnF_2)-backboned polymers [31] with highly polarized functional groups to boost relative dielectric constants are also being investigated.

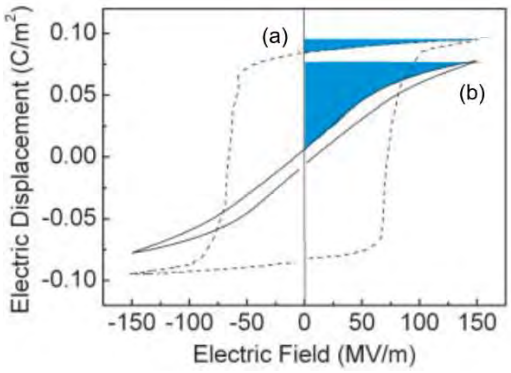

Figure **2-7**: P-E loops for (a) P(VDF-TrFE) which is ferroelectric and (b) P(VDF-TrFE-CFE) as a relaxor. The blue areas indicated the energy densities of the two materials. Figure by B. Chu *et al*. [26]

2.2.3.2 Nanocomposites

To surpass the relative dielectric constants of polymer-based materials, many groups have explored increasing the storage densities through use of filler particles in polymer matrices. Bi *et al*. showed that 30 vol% $BaTiO_3$ inclusion in mixed α and β-phase PVDF increased the energy density from 2.5 J/cm^3 to 4.1 J/cm^3.[32] This increase can be attributed to the $BaTiO_3$ filler that raises the composite permittivity from 8 to 17, at the expense of reducing the BDS of the composite to ~ 2 MV/cm. Similarly, Zhang *et al*. achieved a relative permittivity of 23 with 3 vol% TiO_2@$BaTiO_3$ (TiO_2-coated $BaTiO_3$) nanorods in PVDF, while the BDS remains above 6 MV/cm.[33] These examples illustrate that filled nanocomposites can benefit the overall energy storage densities. As the relative permittivity and BDS are often negatively correlated (as indicated in Figure 2-8 [34]), nanocomposites are advantageous because one can easily engineer the volume fractions of inclusions to seek the best mixture for energy storage performance.

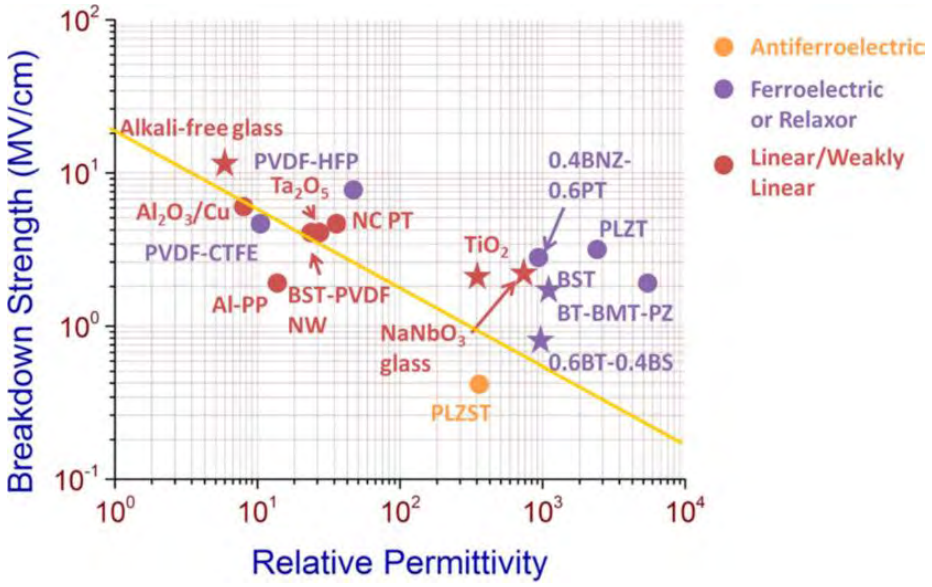

Figure **2-8**: The BDS vs relative permittivity plot for some polymers, composites, and ceramics with antiferroelectric, ferroelectric, relaxor, or linear dielectric character. The figure shows that the BDS and relative permittivity are inversely related in most materials. The abbreviations are: poly(vinylidene fluoride-hexafluoropropylene) (P(VDF-HFP)), poly(vinylidene fluoride-chlorotrifluoroethylene) (P(VDF-CTFE)), polypropylene (PP), barium strontium titanate (BST), nanowire (NW), nanocomposite (NC), lead titanate (PT), lanthanum-doped lead zirconate stannate titanate (PLZST), bismuth nickelate zirconate-lead titanate (BNZ-PT), lanthanum-doped lead zirconate titanate (PLZT), barium titanate-bismuth magnesium titanate-lead zirconate (BT-BMT-PZ), and barium titanate-bismuth scandate (BT-BS). Plot from Michael *et al*. [34]

Nano-fillers can increase the permittivity of the composites by:

I. Utilizing the high intrinsic relative permittivity of nano-fillers to elevate the average dielectric constants of the composites.

II. Creating additional interfaces that add to the space charge polarizations (which is effective at low frequencies).

Proper physical models can guide design of the dielectric properties of composites with different compositions.

Lichtenecker's rule [9] is widely used to describe the first mechanism:

$$\varepsilon_{eff}^{\alpha} = \varphi_f \varepsilon_f^{\alpha} + \varphi_m \varepsilon_m^{\alpha} \qquad \text{(Eq. 2-15)}$$

where ε_{eff} is the effective dielectric constant of the composite. ε_m and φ_m are the relative permittivity and the volume fraction of the matrix, and ε_m and φ_m are the relative permittivity and the volume fraction of the filler. The exponent α varies from -1 (for capacitors in series) to 1 (for parallel-connected capacitors). When $\alpha \rightarrow 0$, the equation can be re-written as:

$$log\varepsilon_{eff} = \varphi_f log\varepsilon_f + \varphi_m log\varepsilon_m \qquad \text{(Eq. 2-16)}$$

This equation, also known as the logarithmic mixing rule, describes the situation where series and parallel-connected capacitors are distributed randomly, typical in nanocomposites. Other models focus on the connectivities of composite structures (parallel/series connection models, i.e., Wiener bounds [35]), the dielectric contrasts between the fillers and the matrix (Maxwell-Garnett equation [36] and Bruggeman's model [35]), or the filler shapes (Yamada's model [37]) and gas-phased fillers (Knott equation [38]). A plot of ε_{eff} vs. φ_f in different models is displayed in Figure 2-9. [39]

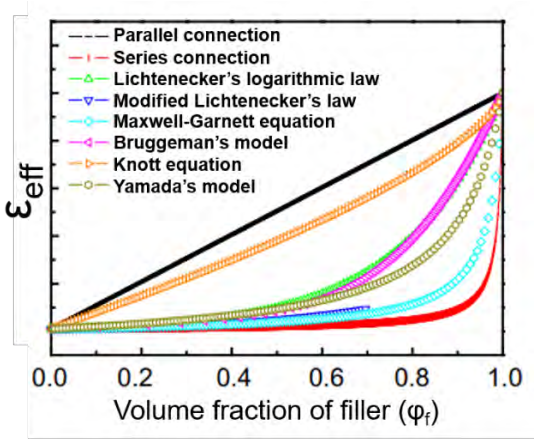

Figure **2-9**: The variation of the effective permittivity of composites with respect to the volume fraction of high permittivity filler, predicted by multiple models including parallel connection [35], series connection [35], Lichtenecker's logarithmic law [9], modified Lichtenecker's law [39], Maxwell-Garnett equation [36], Bruggeman's model [35], Knott equation [38], and Yamanda's model [37]. Figure from Zhang *et al*. [39]

As for mechanism II, Tanaka *et al*. proposed a "multi-core" model to describe the dielectric properties of polymer-based nanocomposites. This model divides the interface between

the matrix and the nano-filler into a bonded layer, a bound layer, and a loose layer (Figure 2-10). [40] The bonded layer (~1 nm thick) represents the region in which the matrix materials are bonded with the nano-fillers through ionic bonds, covalent bonds, hydrogen bonds, or van der Waals forces. The bound layer (2-9 nm thick) is an intermediate layer with altered polymer chain mobility, chain conformation, crystallinity, cross-link stoichiometry and Coulombic potential, affected by both the bonded layer and the nano-filler. The loose layer (several tens of nm) is a layer where the polymer chain properties are slightly different from the matrix due to the influence of the bound layer. The interfacial polarizations can be induced via a Gouy-Chapman diffuse layer that overlaps with all 3 layers.

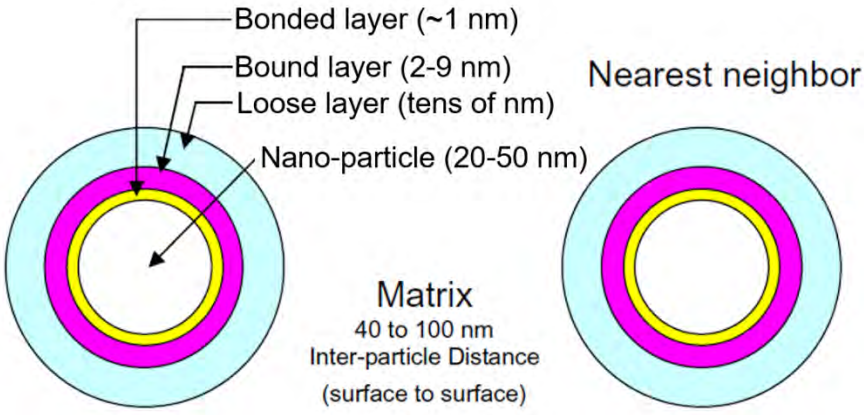

Figure **2-10**: The multi-core model for polymer-based nanocomposites interfaces developed by Tanaka *et al*. [40]

Nano-fillers can affect more than the permittivity of the composites. Tomer *et al*. showed that poly(vinylidene fluoride-hexafluoropropylene) (P(VDF-HFP)) and kaolinite nanocomposites possess both a high breakdown strength (7800 kV/cm) and an energy density of 19 J/cm^3.[18] The small charge density in kaolinite destabilizes β-phase PVDF, lowering the remanent polarization. At the same time, the high aspect ratio kaolinite fillers form conduction barriers in the P(VDF-HFP) matrix, amplifying the BDS. Other low dimensional materials are also of interest. For instance, Li *et al*. crosslinked divinyltetramethyldisiloxane-bis(benzocyclobutene) (c-BCB) with

hexagonal boron nitride nanosheets (BNNS) to form a nanocomposite (cBCB/BNNS) that takes advantage of the high in-plane thermal conductivity of BNNS to dissipate Joule heat, hence avoiding thermal breakdown, while using the high-aspect-ratio nanosheets to elongate the breakdown path, delaying avalanche breakdown. [3] Shen *et al*. shown (See Figure 2-11) [41] that nanosheets that are perpendicular to the electric field direction hinder the propagation of the breakdown tree, making the breakdown event more torturous.

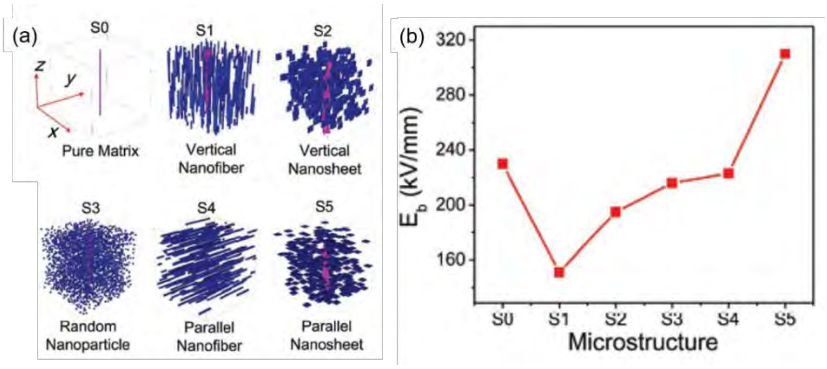

Figure **2-11**: (a) Some possible geometrical arrangements of various-shaped nano-fillers ($BaTiO_3$) in an amorphous matrix (PVDF) and (b) their corresponding BDS estimated by phase field simulations. Figure by Shen *et al*. [41]

These results clearly violate criteria in typical breakdown theories. It is likely that the overall breakdown strength in nanocomposites is an outcome of trade-offs between different breakdown mechanisms.

2.2.3.3 Inorganic glass

Similar to polymers, inorganic glasses have bonds with relatively high covalency like B-O, Si-O, and Al-O, and show small net field-induced polarization. As a consequence, the relative permittivity for most inorganic glasses is below 10. To enhance the relative permittivity of glasses, highly polarizable modifiers are added; these modifiers break up the network, increase

relative permittivity and drop the softening points. [42] However, any modifiers with a high ionic conductivity can induce electrical failure. [43] Larger alkali-earth ions such as Ca^{2+}, Sr^{2+}, and Ba^{2+} have hence been adopted to produce glasses with improved relative permittivity. [44]

Some high energy density inorganic glass materials display outstanding breakdown strengths, typically on the order of several MV/cm. [45] Smith *et al*., for example, tested a barium modified aluminoborosilicate glass (AF-45) with a BDS of 12 MV/cm, which led to an energy density of 35 J/cm^3. [43] Inorganic glasses also show high efficiency and excellent temperature stability. The loss tangent for alkali-free glass capacitors is below 1%, giving an energy storage efficiency over 90%. In Figure 2-12 (a), the P-E loop for the alkali-free aluminoborosilicate glass is as slim as that of polypropylene (PP) whereas the slope is much steeper owing to a higher relative permittivity. [44] Since the glass transition temperatures of inorganic glasses are much higher than those of polymers, glass capacitors maintain their performance up to >180 °C (Figure 2-12 (b)). [43,44] Therefore, glass capacitors show potential for use in harsh environments such as automobile engines and outer space.

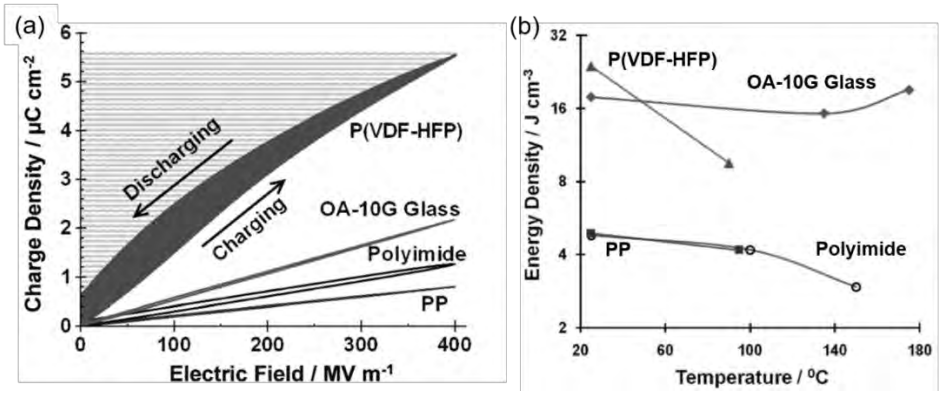

Figure **2-12**: (a) The P-E loops of P(VDF-HFP), OA-10G glass, polyimide, and polypropylene (PP). (b) The dependence of energy storage densities with respect to temperatures for the above 4 materials. Plots are originally from Manoharan *et al*. [44]

2.2.3.4 Bulk ceramics

Appropriately formulated ceramic materials have a high dielectric permittivity, which provides better energy storage performance at lower fields. $BaTiO_3$, a widely used dielectric ceramic has a room temperature permittivity over 1000 [19],[46] There have been reports on TiO_2-based ceramics with III-V cation complexes (In^{3+}-Nb^{5+} or Pr^{3+}-Nb^{5+}) that showed colossal relative permittivity on the order of 10^4. [47–49] However, the losses of those systems are also 1-2 orders of magnitude higher than conventional energy storage materials, making these compounds unsuitable for energy storage applications. In fact, many reported bulk ceramics with high energy densities have relative dielectric constants between several hundreds and low thousands (Figure 2-13). [50–70].

The energy densities in Figure 2-13 are on average lower than the values from PVDF-based polymer and nanocomposite films because bulk ceramic samples are generally 100 μm – 1 cm thick. The thickness dependence described in section 2.2.2.3 significantly diminishes the BDS of bulk ceramics. Typical BDS for bulk ceramics are less than 1 MV/cm.

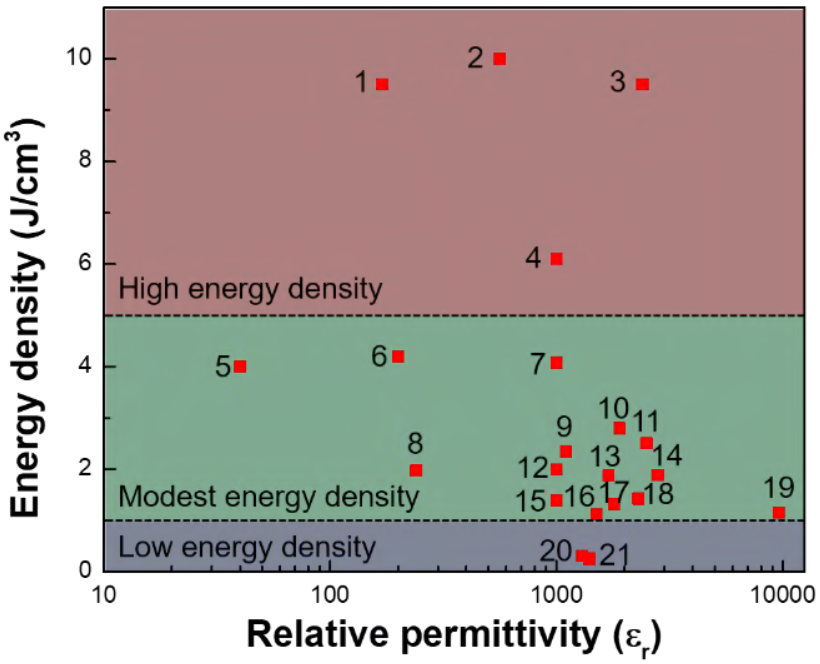

Figure **2-13**: The energy density-relative permittivity relationship of some recently proposed bulk ceramics. Numbers on the figure represent: (1) Mn-doped $0.8CaTiO_3$-$0.2CaHfO_3$ [50] (2) $BaTiO_3/0.65Bi_2O_3$-$0.2B_2O_3$-$0.15SiO_2$ ceramic glass [51] (3) $(Na_{0.5}Bi_{0.5})TiO_3$-$0.4(Sr_{0.7}Bi_{0.2})TiO_3$ [62] (4) $0.7BaTiO_3$-$0.3BiScO_3$ [64] (5) $CaZr_{0.8}Ti_{0.2}O_3$ [65] (6) $AgNb_{0.85}Ta_{0.15}O_3$ [66] (7) $0.9(K_{0.5}Na_{0.5})NbO_3$-$0.1Bi(Mg_{2/3}Nb_{1/3})O_3$ [67] (8) $AgNbO_3$ [68] (9) $(Na_{0.5}Bi_{0.5})_{0.8}Ba_{0.2}Ti_{0.8}Sn_{0.2}O_3$ [69] (10) $BaTiO_3$-$Bi(Zn_{0.5}Ti_{0.5})O_3$ [70] (11) $0.92BaTiO_3$-$0.08K_{0.73}Bi_{0.09}NbO_3$ [52] (12) $0.9Bi_{0.48}La_{0.02}Na_{0.48}Li_{0.02}Ti_{0.98}Zr_{0.02}O_3$-$0.1Na_{0.73}Bi_{0.09}NbO_3$ [53] (13) $0.5(SrTiO_3)$-$0.5(0.94Bi_{0.54}Na_{0.46}TiO_3$-$0.06BaTiO_3)$ [54] (14) $0.5SrTiO_3$-$0.5(0.95Bi_{0.5}Na_{0.5}TiO_3$-$0.05BaAl_{0.5}Nb_{0.5}O_3)$ [55] (15) $Bi_{0.5}K_{0.5}TiO_3$-$0.06La(Mg_{0.5}Ti_{0.5})O_3$ [56] (16) $0.8BaTiO_3$-$0.2Bi(Mg_{2/3}Nb_{1/3})O_3$ [57] (17) $0.695Bi_{0.5}Na_{0.5}TiO_3$-$0.3Sr_{0.7}Bi_{0.2}TiO_3$-$0.005LaTi_{0.5}Mg_{0.5}O_3$ [58] (18) CuO-doped $BaTiO_3$-SiO_2 ceramic-glass [59] (19) $Ba_{0.997}Sm_{0.002}Zr_{0.15}Ti_{0.85}O_3$ [60] (20) $0.8BaTiO_3$-$0.2BiYO_3$ [61] (21) $Sr_{0.92}(Bi,Li)_{0.08}TiO_3$ [63].

Recent energy storage research on bulk ceramics has been mainly focusing on enhancing the BDS of ceramics by setting obstructions in the path of progressing breakdown trees. There are three strategies that will be discussed.

I. Suppression of grain growth: In some materials, the grain boundaries are better insulators than the grain interiors. In this case, ceramics with smaller grain sizes, or equivalently, higher grain boundary densities, should have higher BDS and energy densities. An impedance spectroscopy analysis done by Michael *et al*. is a classic illustration of this situation (See Figure

2-14 (a)). [34] After fitting, the extrapolated conductivities indicated a 100-fold drop from grain interiors to grain boundaries, as shown in Figure 2-14 (b).

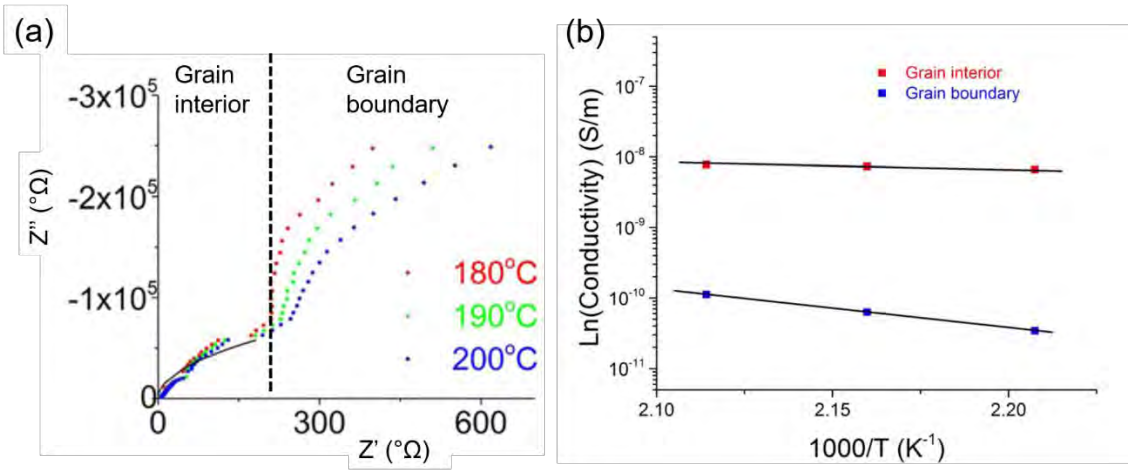

Figure **2-14**: (a) The Cole-Cole plot of $Bi_{1.5}Zn_{0.9}Nb_{1.35}Ta_{0.15}O_{6.9}$ (BZNT) at different temperatures. (b) The extrapolated electrical conductivities of BZNT grain interiors and grain boundaries from (a). Figure by Michael *et al*. [34]

There are numerous approaches to reducing grain growth in ceramics. [63,71] For example, in Bi and Li co-doped $SrTiO_3$, increasing the doping level resulted in finer grains, hence the BDS and energy densities were improved by 5 times. [63]

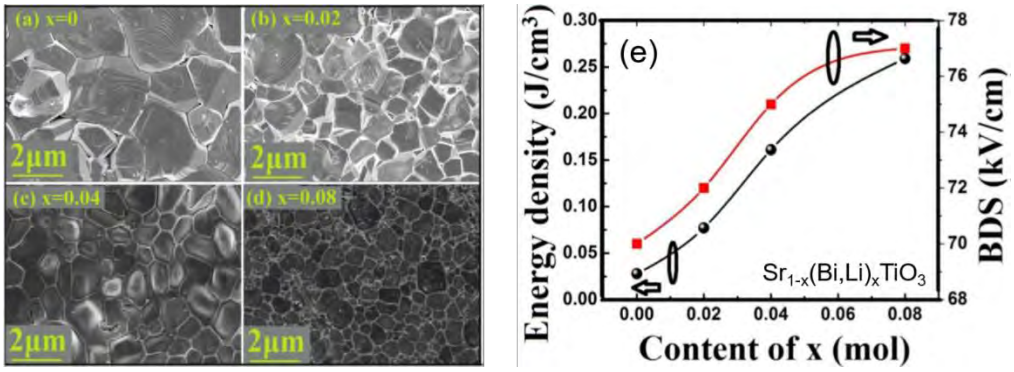

Figure **2-15**: (a)-(d) The cross-sections showing microstructure evolutions of $Sr_{1-x}(Bi,Li)_xTiO_3$ (SBLT) with x=0, 0.02, 0.04, and 0.08 respectively. (e) The corresponding electrical BDS and energy densities of SBLT ceramics. Reproduced from Alkathy *et al*. [63]

II. Introduction of inhomogeneity with resistive grain boundaries: More insulating grain boundary phases, such as alkali-free glasses, can be intentionally introduced for performance improvements. Such ceramic-glass systems, unlike nanocomposites, will preserve a modest permittivity because of the low volume fraction of the glass phase. In a SiO_2-coated $BaTiO_3$ ceramic-glass system (Figure 2-16) proposed by Zhang *et al*., the composite permittivity dropped from 4000 for pure $BaTiO_3$ to 2500 for 2 wt% SiO_2 coated $BaTiO_3$ while the BDS increased from 80 kV/cm to 200 kV/cm, leading to an energy density enhancement from 0.37 J/cm^3 to 1.2 J/cm^3. [72] Adding highly polarizable Pb^{2+} or Bi^{3+} modifiers to the glass should also help in mitigating the reduced relative permittivity. [51]

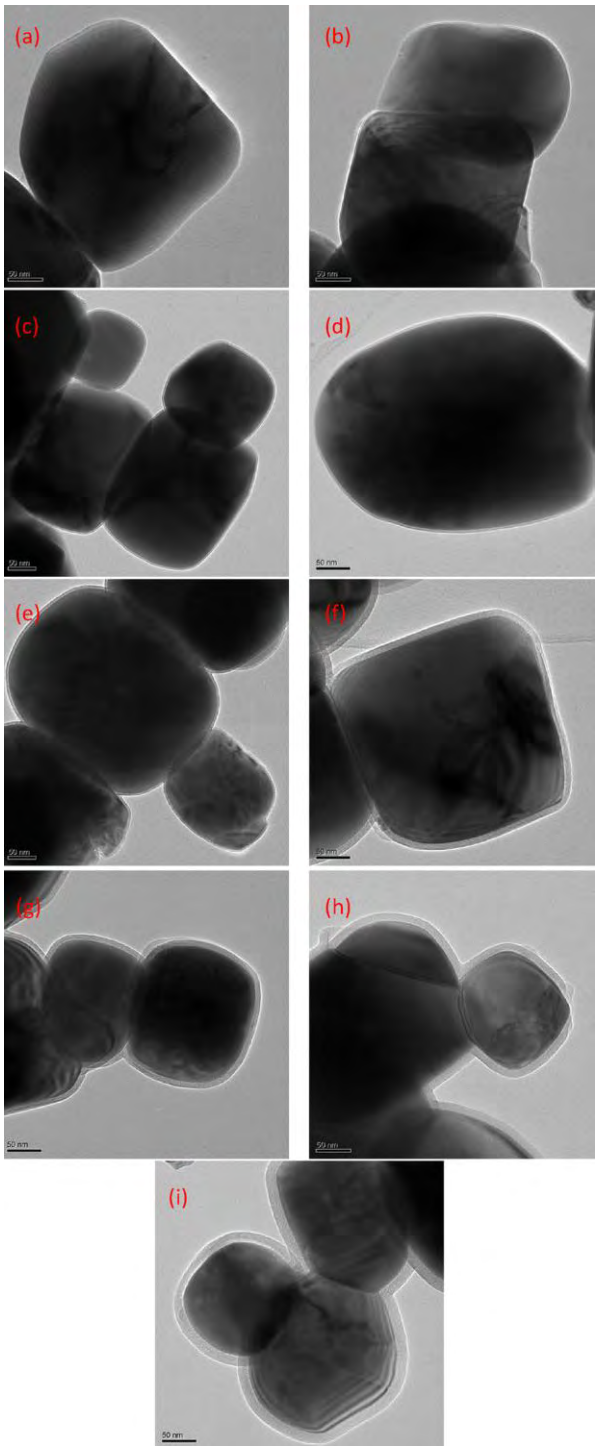

Figure **2-16**: TEM of SiO_2-coated $BaTiO_3$ nanoparticles when the SiO_2 content is (a) 0 wt%, (b) 1.0 wt%, (c) 1.5 wt%, (d) 2.0 wt%, (e) 2.5 wt%, (f) 3.0 wt%, (g) 4.0 wt%, (h) 6.0 wt% and (i) 8.0 wt%. Figure from Zhang *et al*. [72]

III. Phase engineering of complex oxides: By stabilizing certain phase(s), it is possible to tune the energy storage performance of materials. For example, it is well-known that AFE materials are suitable for energy storage up to the electric field that switches the spontaneous polarization. If the re-orientation of polarization can be delayed in an antiferroelectric, the energy density should increase accordingly, as illustrated by Figure 2-17. This idea was successfully demonstrated by Zhao *et al*. in Ta-doped silver niobate. [66]

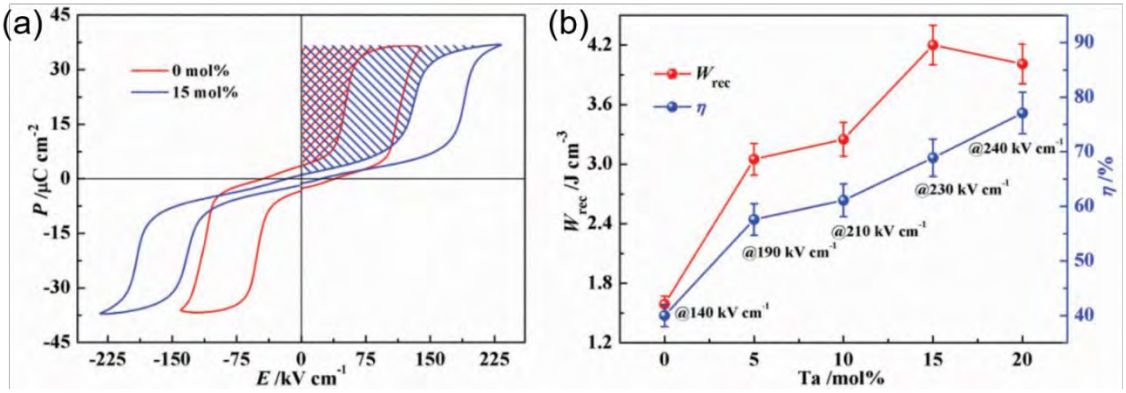

Figure **2-17**: (a) The P-E loops of $AgNbO_3$ and 15 mol% Ta^{5+}-doped $AgNbO_3$. The shaded areas indicate the recoverable energy densities. (b) The recoverable energy storage densities (W_{rec}) and corresponding energy storage efficiencies of $AgNbO_3$ with dependence of Ta doping levels. (Figure from Zhao *et al*. [66])

In addition, facilitating the appearance of polar nanoregions (PNR) in relaxors is also effective in improving energy storage ceramics. This is achieved by substituting aliovalent cations on the same site to destroy the long-range polar order in the ceramics [73], thus often leading to compositions of high complexity. [55,60]

2.2.3.5 Thin film ceramics

Thin film ceramic capacitors have become a popular topic in recent years in part due to intensifying needs for electronics miniaturization. Films can be grown by multiple deposition

methods, including chemical solution deposition [74], sputtering [6], pulsed laser deposition [75], and atomic layer deposition [76]. In addition, as the thicknesses of ceramic thin films can be precisely controlled between 10 nm and several microns, it is possible to integrate some thin film capacitors on flexible substrates such as mica [77], metal foils [5], and polyimide [2], which could enable the commercialization of wearable electronics.

The strategies to elevate energy storage densities in bulk ceramics also apply to films. [75,78] Additionally, with the decrease of sample dimensions, thin film ceramics present significantly higher BDS than bulk specimen since there is less of a chance that critical defects will appear in the thin films. In cases where the breakdown strengths of ceramic thin films can be engineered to be comparable to those of polymer and nanocomposite films, very large energy storage densities can be achieved. For example, Hu et al. demonstrated an antiferroelectric La-doped lead zirconate titanate (PLZT) thin film with an energy storage density of 61 J/cm^3 at 4.3 MV/cm [79]. Ta-doped bismuth zinc niobate (BZNT) films also show a high energy density (67 J/cm^3) and high breakdown strength (6.1 MV/cm) [34].

Specifically for thin films, the interactions between films and substrates, or between films of different compositions can also play an important role. Recently, ultrahigh energy densities were achieved in films deposited on defect engineered substrates. For instance, $SrTiO_3$ on $La_{0.67}Sr_{0.33}MnO_3$ substrate (STO/LSMO) had been proposed to exhibit an energy density as large as 307 J/cm^3 at 6.6 MV/cm due to the increased BDS via interfacial local electric field re-distribution induced within the inter-diffusion layer between STM and LSMO. [80] Another case that is akin to STO/LSMO was demonstrated in aluminum/amorphous alumina (Al/AmAO) films where residual AmAO depressed the leakage current of dense crystalline Al_2O_3. [81] In terms of film-film interactions, sandwich structured multilayer films were claimed to be effective in enhancing energy densities. These systems succeeded by either tuning the permittivity-BDS

relationships (like nanocomposites) [82] or using one layer as a template to control the morphology of the other layer. [83]

Although the energy densities reported in thin film ceramic capacitors are much larger than those of bulk materials, it is often unfair to compare the numbers with those of polymers, nanocomposites, glasses, and bulk ceramics. This is because almost all the reported values for thin films are measured at 1 kHz – 10 kHz, while for other materials frequency ranges from 1-10 Hz are used. High frequency P-E loops tend to significantly inflate the maximum achievable electric fields, but demonstrate the potentials for high power density applications. Secondly, in most thin films, the volume of the substrate is ignored in calculating the energy density. Therefore, it makes more sense to state thin films are more competitive for low voltage devices with outstanding power densities while polymers, nanocomposites, glasses, and bulk ceramics are suitable for storing a large amount of energy in a high-voltage, lower-power system.

One common drawback of bulk and thin film ceramic capacitors is the high processing temperatures. Most bulk ceramics are sintered at >1000 °C [67,84] while many films are crystallized above ~ 500 °C.[13,75,79,85] These temperatures exceed the decomposition temperatures of polymer substrates. Base metal substrates such as Ni, Cu, and Al foil are also susceptible to oxidation at these temperatures. Michael-Sapia et al. reported a BZNT film with a maximum heat treatment temperature of 350 °C [2] in which the presence of nanocrystallites increased the permittivity. These films showed a dielectric constant of ~ 50 and an energy density ~ 40 J/cm^3 under an applied field of 4 MV/cm [2]. It was suggested by Michael-Sapia et al. that the crystalline phase is based on δ-Bi_2O_3 [2]. δ-Bi_2O_3 is a fluorite structured phase that is only thermodynamically stable at high temperature but can be stabilized at room temperature with Nb doping [86]. One possible chemical formula of Nb-doped δ-Bi_2O_3 is Bi_3NbO_7 [86]. Inspired by Michael-Sapia's work, Bi_3NbO_7 thin films were made to study the energy storage behavior of this material.

2.3 Experimental procedures

0.1 mol/L BNO (Bi_3NbO_7) sol-gel solutions were made using Pechini's method, based on the research of Michael-Sapia et al. [2]. First, bismuth nitrate pentahydrate (Sigma-Aldrich Corp., St. Louis, MO) and niobium ethoxide (Sigma-Aldrich) were dissolved separately into two flasks of anhydrous ethylene glycol (Sigma-Aldrich) in a N_2 filled glove box. For tungsten or tantalum-doped solutions, tungsten (VI) ethoxide (Sigma-Aldrich) or tantalum (V) ethoxide (Sigma-Aldrich) was added to the niobium ethoxide flask. Then citric acid (Sigma-Aldrich) was added to both of the flasks so as to stabilize the precursors. The molar ratio of organometallic precursors and citric acid is 2:1. Finally, the solution in the Nb flask was added to the Bi flask. While the solutions were stable (without precipitation) for periods of up to a year, it was found that the viscosity changed over time, resulting in thicker films from aged solutions.

Chemical solution deposition processes were used for the fabrication of the BNO thin films, as shown in Figure 2-18. A 5 μm filter was used during the deposition. The BNO solution was spin cast on platinized silicon wafers (Pt (150 nm)/Ti (20 nm)/SiO_2 (500 nm)/Si, NOVA Electronic Materials, Flower Mound, TX) at a speed of 4000 rpm for 40 sec, followed by a drying procedure on the hotplate at 250 °C for 3 min. The samples were then heated on the hotplate at temperatures varied from 350 °C to 450 °C for 10 min. The hot plate temperatures were calibrated using a thermometer embedded in the hot plate for temperatures below 250 °C. At higher temperatures, a thermocouple was placed on the hot plate surface to provide a more accurate measurement. The heat treatments occurred after the deposition of each layer of BNO solution and 5 cycles of deposition/heat treatment cycles were used to build up a film thickness of ~ 120-140 nm. Some films were exposed to UV radiation to improve organic removal. For this purpose, a 260 nm, 385 mW ultra-violet (Fusion DUV system, Heraeus Noblelight America LLC, Gaithersburg, MD) exposure, with the substrate held at 60°C for 3 min in air was added between

drying and annealing. Due to the effect of UV radiation, the temperature of the sample rose to ~ 150°C at the end of the UV exposure.

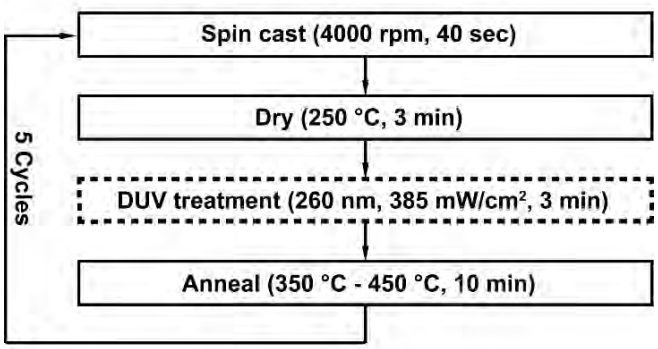

Figure **2-18**: Chemical solution deposition process of BNO thin films. DUV denotes deep UV exposure.

The crystallinity of the film was studied using an X-ray diffractometer (XRD, Empyrean, PANalytical Corp., Almelo, Netherlands) with Cu Kα radiation. The XRD data were collected from 2θ = 10° to 72° with a step size of 0.026° 2θ and a scan rate of 0.067°/sec.

The surface morphology and the thickness of the film were observed using a field emission scanning electron microscope (FESEM, Merlin, Carl Zeiss, Inc., Jena, Germany). For the thickness measurements, the samples were cleaved and the cross sections were observed via FESEM. The thicknesses of the samples were then measured from the captured SEM images.

The compositions of the BNO thin films were characterized by X-ray photoelectron spectroscopy (XPS) and secondary ion mass spectrometry (SIMS) depth profiling. The XPS data were collected using a Thermo K-alpha X-ray photoelectron spectrometer (Thermo Fisher Scientific Inc., Waltham, MA) with monochromatic Al Kα (72 Watts, 12 kV) X-rays. The X-ray spot size was 200 μm. Profiles were obtained using a 1 kV Ar^+ ion beam, on a low current setting that was rastered over a 2.0 mm x 1.5 mm area. Azimuthal rotation was employed during the sputter cycle. Spectra were acquired in snapshot mode with a 150 eV pass energy and a 15 sec/element integration time. All data were collected with a 90° take-off angle. The electron flood

gun with standard settings (0.4 V beam voltage, 100 μA emission) was used for charge compensation. The data were processed with the Thermo Advantage software.

The SIMS data were collected using an IonTof IV secondary ion mass spectrometer (Ion-Tof GmbH, Münster, Germany). Negative ion profiles were collected with 25kV Bi^+ primary ions (1.2 pA) and a 1 kV Cs^+ sputter beam (100 nA). The primary ions were rastered over a 150 μm x 150 μm area with a pixel density of 128 pixels x 128 pixels and the Cs^+ beam was rastered over a 400 μm x 400 μm area. The analysis area was centered in the sputter area and profiles were collected in interlace mode. A cycle time of 60 μsec was employed which resulted in a mass range of 0-323 Da. The data were processed using the IonTof-SurfaceLab 6.6 software.

A spectroscopic ellipsometer (M-2000, J. A. Woollam Co., Lincoln, NE) was used to characterize the optical properties of the BNO thin films as well as quantifying the porosity of the non-UV treated BNO thin film. Data within wavelengths from 400 nm to 1690 nm and 3 incident angles (55°, 65° and 75°) were collected and fitted with CompleteEASE software (J. A. Woollam Co.). A stack of BNO/intermix/Pt model was utilized to fit the ellipsometry data. A Sellmeier model was initially applied to fit the BNO layer over the wavelength range where the film was transparent; these data were used to help parameterize the optical properties to a general oscillator model by Tauc-Lorentz function. Assuming 100% density for 450 °C-annealed UV treated BNO, the porosity of the 450 °C-annealed non-UV treated BNO thin film was calculated by replacing the BNO layer with an effective medium layer of BNO and void.

For electrical measurements, 50 nm thick sputtered Pt top electrodes (CMS-18 Sputter System, Kurt J. Lesker Company, Pittsburgh, PA) were patterned using a double layer lithography process. The diameter of the circular electrodes was 200 μm. After the lift-off process, the film was annealed in a rapid thermal annealing (RTA) furnace (RTP-600S, Modular Process Technology Corp., San Jose, CA) at 300 °C for 10 min.

An LCR meter (Hewlett-Packard 4284A, Agilent Technologies, Inc., Palo Alto, CA) and a pA meter (Hewlett-Packard 4140B, Agilent Technologies, Inc., Palo Alto, CA) were used to measure the permittivity/loss and the leakage current densities of the patterned films, respectively. The polarization-electric field loops (P-E loops) were measured using the Precision Multiferroic Analyzer from Radiant Technologies, Inc., Albuquerque, NM. The samples are connected with the equipment by microprobes. The capacitor yield exceeded 90%.

2.4 Results and discussion

2.4.1 The BNO thin films without UV treatment

The BNO thin film phase formation was characterized by XRD, as is shown in Figure 2-19. The XRD spectra indicate that the BNO thin film annealed at 350°C is XRD amorphous. There is a slight increase of background at $2\theta = 28°$ for the BNO sample annealed at 375°C, suggesting a small volume fraction of BNO crystals starts to form. When annealed at 400°C and higher, the intensity of BNO (111) peak increased, and additional peaks could be detected. [86]

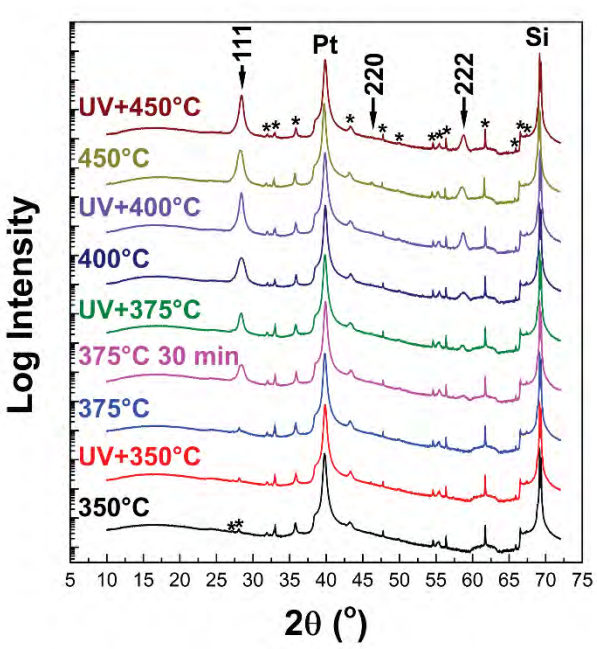

Figure **2-19**: XRD of BNO thin films with and without UV treatment, and annealed at different temperatures after spin casting. Unless specifically mentioned in the figure, the 2nd step heat treatment time was 10 min. Substrate peaks are marked by "*". Curves are offset vertically for clarity.

The dielectric constants of BNO thin films increase as the annealing temperatures rise. As seen in Figure 2-20 (a), the 350 °C-annealed BNO thin film has a dielectric permittivity of 24, and the permittivity increases to 55 when the processing temperature was raised to 400 °C. Notice that the loss tangent of the BNO film treated at 400 °C also goes up to ~ 4 %, presumably due to a finite space charge contribution to the response [9].

The BNO thin films without UV treatment have a breakdown strength < 3 MV/cm at 10 kHz. As can be seen from Figure 2-20 (b), the highest field a BNO thin film heat treated at 400 °C survived was ~ 2 MV/cm when measured at 10 kHz, leading to a relatively low energy density ~ 9 J/cm^3. The energy density is lower for films heated at 350 °C (~ 6 J/cm^3) or 375 °C (~ 7 J/cm^3).

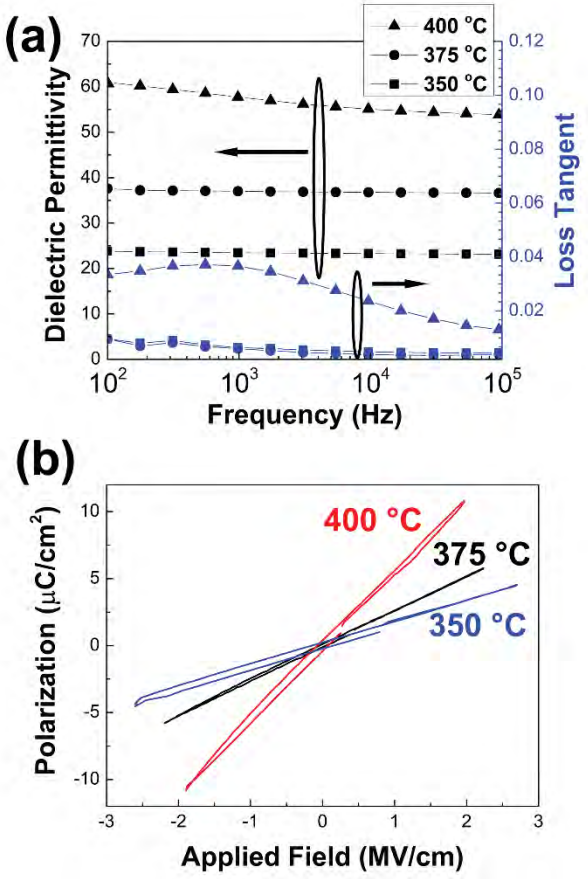

Figure **2-20**: (a) The dielectric permittivity and loss tangent as a function of frequency for BNO films annealed at 350 °C, 375 °C and 400 °C without UV treatment. The thicknesses of the films are 140 nm, 140 nm and 120 nm respectively. (b) The 10 kHz P-E loops of BNO thin films annealed at 350 °C, 375 °C and 400 °C without UV treatment.

It was hypothesized that the comparatively lower breakdown strengths were associated with carbon residue. Carbon residues in the film after annealing could not only give rise to dielectric loss but also slow down the collapse of internal pores. The presence of residual carbon was verified by both XPS and SIMS depth profiles, as shown in Figure 2-21.

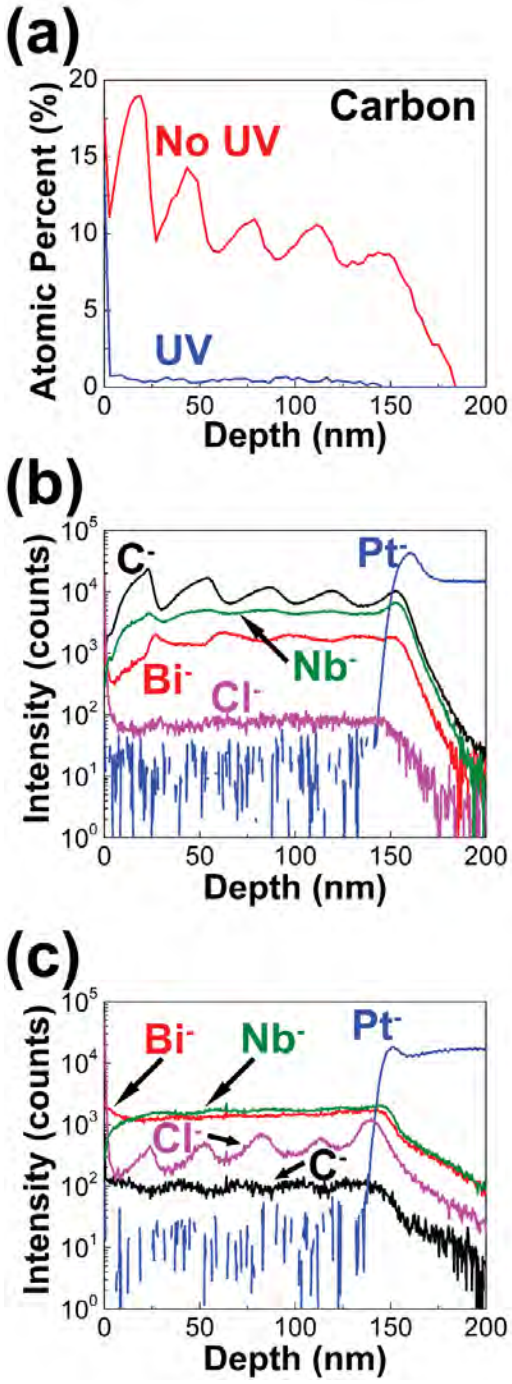

Figure **2-21**: (a) Overlay of the carbon XPS depth profiles of BNO thin films annealed at 350 °C with and without UV treatment. (b) The SIMS depth profiles of the BNO thin films treated without UV exposure and annealed at 350 °C. (c) The SIMS depth profiles of the BNO thin films treated with UV exposure and annealed at 350 °C.

2.4.2 UV treated BNO thin films

In an attempt to reduce residual carbon, a UV treatment was applied to the amorphous film prior to the final heat treatment in each layer. It was found that this treatment substantially reduced the carbon detected in the final film, as shown in Figure 2-21. Less than 1 atomic percent carbon was detected in the UV treated films. The SIMS profile shows a decrease of carbon intensity by 2 orders of magnitude in the films after DUV exposure. The modulations in the carbon traces in XPS and SIMS profiles of the non-UV treated film correspond to the 5-layer stack of the BNO thin films since the carbon on the surface of each layer can more easily be removed during UV treatment. Notice that chlorine was also detected by SIMS. SIMS is very sensitive to chlorine with low ppm detections limits. The source of the chlorine is believed to be either a trace amount of impurity in the bismuth nitrate pentahydrate precursor used to make the BNO solution or contamination from the UV system. Although the exact mechanism of UV assisted carbon removal process in BNO thin film is not well understand, it might result from the photolysis of organic and organometallic compounds under continuous UV radiation. [87]

In addition, the densification of the BNO thin film annealed at 450 °C was improved after exposing the amorphous film to UV. As indicated in Figure 2-22, the pores in the 450 °C-annealed BNO film that caused the shorting of the capacitors were effectively removed with the addition of the UV exposure procedure. Ellipsometry data verified the porosity of the BNO film with no DUV treatment. As shown in Figure A-1, the refractive index of the 450 °C-annealed non-UV treated film is lower than the 450 °C-annealed UV treated film. The porosity of the non-UV treated film was then calculated to be ~ 13.2%.

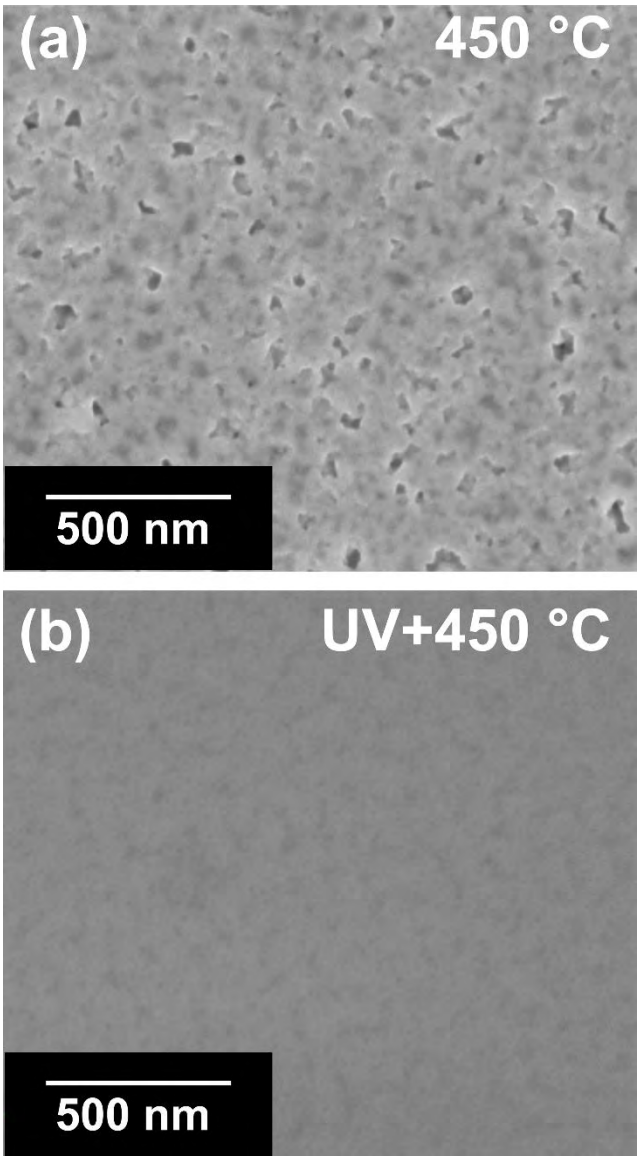

Figure **2-22**: The top-down FESEM images of BNO thin films (a) annealed at 450 °C without UV treatment and (b) annealed at 450 °C with the UV treatment procedure.

Possibly due to the removal of residual carbon in the films, the crystallinity of the UV treated BNO thin films increased when treated films were annealed ≥ 375 °C. As can be seen from Figure 2-19, the UV treated BNO thin film annealed at 375 °C has higher XRD peak intensities than those without the UV treatment. Also, as apparent in Table 2-1, the UV treated BNO thin films show smaller full width at half maximum (FWHM) values than the samples without UV exposure. This suggests the crystallite sizes are larger for the BNO thin films treated

with the UV exposure procedure. Furthermore, similar peak intensities were achieved in shorter anneal times at 375 °C (10 min for the UV exposed samples) compared to the 30 min required without UV treatment. This indicates that the UV exposure may have increased the growth rate of the BNO nanocrystals by eliminating the residual carbon.

Table **2-1**: The FWHM values for the BNO thin films.

Annealing Temperatures (°C)	**FWHM of BNO (111) Peak (°)**	
	No UV Treatment	**UV Treated**
350	---	---
375	---	0.52
400	0.82	0.39
450	0.65	0.42

The DUV treatment also influenced the dielectric properties of BNO thin films. As illustrated in Figure 2-23 (a), the dielectric constants of the BNO thin films increased in films processed using the UV treatment. For example, the dielectric permittivity increased from 24 to 44 in films annealed at 350 °C, and from 55 to 67 in films annealed at 450 °C. The loss tangents were suppressed below 1% in the UV treated BNO thin films. This probably resulted from the combination of larger crystallite sizes, lower carbon concentrations, and possibly a change in porosity.

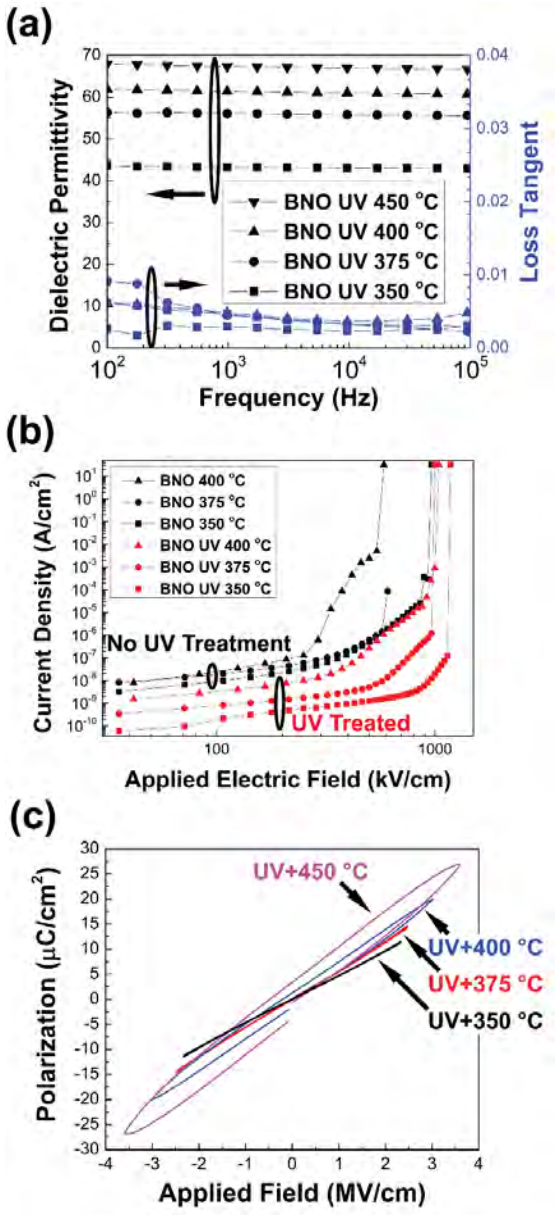

Figure **2-23**: (a) The dielectric constants and loss tangent of UV treated BNO thin films as a function of frequency. (b) The DC leakage currents of BNO thin films with and without DUV exposure. (c) The P-E loops of UV treated BNO thin films at 10 kHz.

Through the elimination of the residual carbon, the DC breakdown strengths of the UV treated BNO thin films were enhanced, and the leakage current density dropped, as seen in Figure 2-23 (b). The average DC breakdown strengths (with 95% confidence interval (CI)) of the BNO

thin films are given in Table 2-2. The calculated result confirms the improved breakdown strengths of BNO films with UV exposure.

Table **2-2**: The average DC breakdown strengths of the BNO thin films with 95% CI. Five electrodes were tested to allow an average value to be calculated.

Annealing Temperatures (°C)	Breakdown Strengths (MV/cm)	
	No UV Treatment	UV Treated
350	0.93 ± 0.16	0.98 ± 0.20
375	0.57 ± 0.03	0.96 ± 0.03
400	0.52 ± 0.06	0.94 ± 0.15
450	---	1.05 ± 0.06

As a consequence, with the improved dielectric constants and breakdown strengths, higher energy storage densities were achieved. From the P-E loops in Figure 2-23 (c), the maximum energy densities and the efficiencies of DUV treated BNO thin films at 10 kHz right before breakdown are listed in Table 2-3. The data indicate the energy storage densities increase as the annealing temperatures increase; an energy density of 39 J/cm^3 was achieved in UV treated BNO thin film annealed at 450 °C. However, the loss of the BNO thin film increased with the applied field. The energy storage efficiency of 450 °C-annealed BNO thin film at the maximum applied field is 72%.

Table **2-3**: The maximum energy storage densities and the efficiencies of BNO thin films prepared using the UV treatment.

Annealing Temperatures (°C)	Energy Storage Densities at 10 kHz (J/cm^3)	Applied Field (MV/cm)	Efficiency
350	13	2.4	87%
375	18	2.5	95%
400	28	3.0	85%
450	39	3.6	72%

Table 2-4 shows the energy densities for the BNO films calculated for a minimum of 90% efficiency. The efficiencies are higher at lower electric fields, while the energy densities are lower. For example, the 450 °C-annealed BNO thin film has an energy density of 25 J/cm^3 with an efficiency of 91%. Notice that for 375 °C-annealed BNO, the efficiencies are larger than 95%.

Table **2-4**: The maximum energy storage densities and the efficiencies of the DUV treated BNO thin films with efficiencies ≥ 90%.

Annealing Temperatures (°C)	**Energy Storage Densities at 10 kHz (J/cm^3)**	**Applied Field (MV/cm)**	**Efficiency**
350	12	2.3	92%
375	18	2.5	95%
400	24	2.8	90%
450	25	2.8	91%

The temperature stability of the UV treated BNO thin films was tested by measuring P-E loops at 10 kHz and 1 MV/cm applied field at elevated temperatures as plotted in Figure 2-24. The energy storage densities and efficiencies of the BNO films annealed at 400°C and 450°C decreased sharply with rising temperatures. However, the films annealed at lower temperatures (350°C and 375°C) preserved efficiencies above 90% under 150°C at 10 kHz. This is likely to be a consequence of the fact that the BNO thin films annealed at lower temperatures have lower dielectric loss and leakage current densities (Figure 2-23 (a) and (b)). Because BNO is not ferroelectric, its energy storage density should be a weak function of temperature, until the point at which dielectric losses degrade the performance. Figure A-2 shows the evolution of energy densities and efficiencies of UV treated BNO thin films at their maximum applied electric fields from 25 °C to 200 °C. The UV exposed BNO thin films showed similar trends as Figure 2-24, except that the energy densities are higher at low temperatures (< 100 °C) because of larger maximum applicable electric fields.

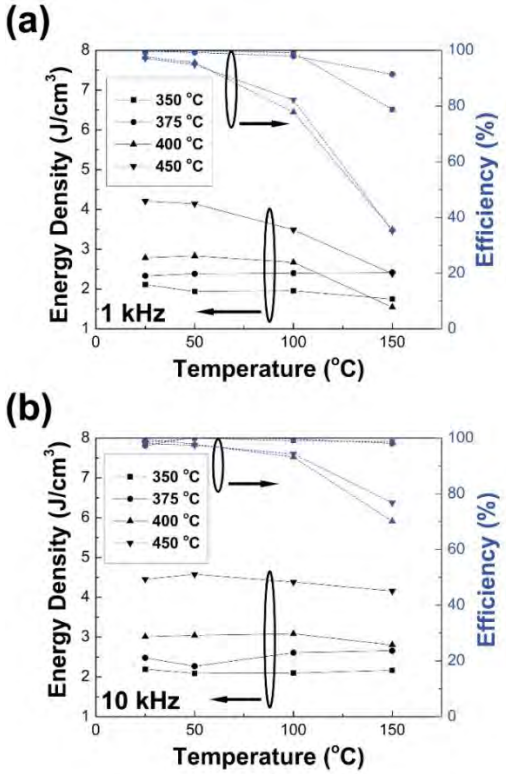

Figure **2-24**: (a) The 10 kHz energy densities and efficiencies of the UV treated BNO thin films measured under different temperatures at 1 MV/cm. (b) The 1 kHz energy densities and efficiencies of the UV treated BNO thin films measured at different temperatures at 1 MV/cm.

The energy densities of the BNO thin films were then compared in Figure 2-25 with a number of recent reports. [2,17,18,25,27,28,32–34,43,50,51,55,57,60,61,64,66,67,70,75,76,80,84,85,88–97] Since the energy densities of the plotted materials were measured and calculated under different conditions, additional information including frequencies, sample thicknesses, electrode materials and electrode diameters are listed in Table S1. It is apparent that the BNO thin films have comparatively high energy storage densities relative to bulk ceramics, polymers and polymer-based nanocomposites. While some thin film ceramics have higher energy storage densities, the lower processing temperatures of the BNO films are of interest. Besides, polymers and polymer-based nanocomposites have also shown potential for application on flexible substrates as most of them can be processed at temperatures ≤ 200 °C and have fairly high energy storage densities. However, the thicknesses of the polymers and polymer-based nanocomposites are still large

compared with thin film ceramics (Table A-1), which may limit their usage in microelectronic devices.

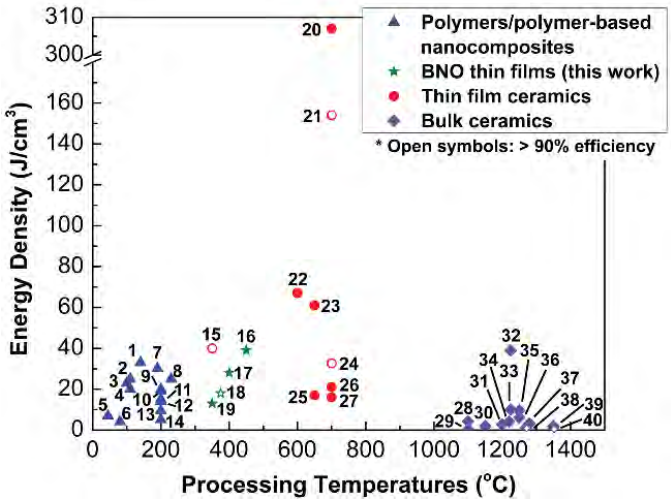

Figure **2-25**: Comparison of reported dielectric energy densities for materials processed at different temperatures. [2,17,18,25,27,28,32–34,43,50,51,55,57,60,61,64,66,67,70,75,76,80,84,85,88–97] The open symbols are materials with efficiency > 90%. Notice that the frequencies under which the energy densities and efficiencies were measured are not uniform. The numbers correspond to materials listed in Table A-1.

2.5 Conclusions

BNO thin films are a potential candidate for energy storage devices on flexible substrates. It was found that exposure of the amorphous films to a UV light source facilitated the removal of organics. Crystallization was initiated at 375°C on being annealed for 10 min. Due to the elimination of carbon in the film through the UV treatment, the film annealed at 450°C achieved an energy density of 39 J/cm^3 at room temperature at 10 kHz with an applied electric field of 3.6 MV/cm. The BNO thin films annealed at 350°C and 375°C, have shown lower energy storage densities but better temperature stability. When compared to other recently developed materials, the BNO thin films are competitive due to their high energy densities and relatively low processing temperatures.

References

[1] Zhao, L.; Zhou, Z. L.; Guo, Z.; Gibson, G.; Brug, J. A.; Lam, S.; Pei, J.; Mao, S. S. Development of Semi-Interpenetrating Polymer Networks and Quantum Dots–Polymer Nanocomposites for Low-Cost, Flexible OLED Display Application. J. Mater. Res. 2012, 27 (4), 639–652.

[2] Michael-Sapia, E. K.; Li, H. U.; Jackson, T. N.; Trolier-McKinstry, S. Nanocomposite Bismuth Zinc Niobate Tantalate for Flexible Energy Storage Applications. J. Appl. Phys. 2015, 118 (23), 234102.

[3] Li, Q.; Chen, L.; Gadinski, M. R.; Zhang, S.; Zhang, G.; Li, H.; Haque, A.; Chen, L. Q.; Jackson, T.; Wang, Q. Flexible High-Temperature Dielectric Materials from Polymer Nanocomposites. Nature 2015, 523 (7562), 576–579.

[4] Wu, A.; Vilarinho, P. M.; Kingon, A. I. Ceramic Processing Strategies for Thick Films on Copper Foils. Acta Mater. 2010, 58 (6), 2282–2290.

[5] Maria, J.; Cheek, K.; Streiffer, S.; Kim, S.; Dunn, G.; Kingon, A. Lead Zirconate Titanate Thin Films on Base-Metal Foils: An Approach for Embedded High-Permittivity Passive Components. J. Am. Ceram. Soc. 2001, 84 (10), 2436–2438.

[6] Nderson, W. A. $BaTiO_3$ Thin Film Capacitors Deposited by r.f. Magnetron Sputtering. Thin Solid Films. 1992, 209 (2), 230–239.

[7] Ren, W.; Trolier-McKinstry, S.; Randall, C. A.; Shrout, T. R. Bismuth Zinc Niobate Pyrochlore Dielectric Thin Films for Capacitive Applications. J. Appl. Phys. 2001, 89 (1), 767–774.

[8] Ko, R.; Carlen, M. Principles and Applications of Electrochemical Capacitors. Electrochim. Acta. 2000, 24, 83–98.

[9] Moulson, A. J.; Herbert, J. M. Electroceramics: Materials, Properties, Applications, 2nd ed.; John Wiley & Sons, Ltd., 2003.

[10] Wang, D.; Clark, M. B.; Trolier-McKinstry, S. Bismuth Niobate Thin Films for Dielectric Energy Storage Applications. J. Am. Ceram. Soc. 2018, 101 (8), 3443–3451.

[11] Uchino, K.; Hirose, S. Loss Mechanisms in Piezoelectrics: How to Measure Different Losses Separately. IEEE Trans. Ultrason. Ferroelectr. Freq. Control 2001, 48 (1), 307–321.

[12] O'Dwyer, J. J. Theory of Dielectric Breakdown in Solids. Solid State Sci. 1969, 116 (2), 239–242.

[13] Michael, E. K. Bismuth Pyrochlore-Based Thin Films for Dielectric Energy Storage, Ph.D. thesis in Materials Science and Engineering, Pennsylvania State University, 2015.

[14] Sherrit, S. Analytical Model for the Strain-Field and Polarization-Field Hysteresis Curves for Ferroic Materials. Proc. SPIE 2009, 6526 (8), 1–11.

[15] Bokov, A. A.; Ye, Z. Recent Progress in Relaxor Ferroelectrics with Perovskite Structure. J. Mater. Sci. 2006, 41, 31–52.

[16] Kittel, C. Theory of Antiferroelectric Crystals. Phys. Rev. 1950, 82 (5), 729–732.

[17] Zhou, X.; Chu, B.; Neese, B.; Lin, M.; Zhang, Q. M. Electrical Energy Density and Discharge Characteristics of a Poly(Vinylidene Fluoride-Chlorotrifluoroethylene) Copolymer. IEEE Trans. Dielectr. Electr. Insul. 2007, 14 (5), 1133–1138.

[18] Tomer, V.; Manias, E.; Randall, C. A. High Field Properties and Energy Storage in Nanocomposite Dielectrics of Poly(Vinylidene Fluoride-Hexafluoropropylene). J. Appl. Phys. 2011, 110 (4), 044107.

[19] Newnham, R. E.; Trolier-McKinstry, S. Materials Engineering: Bonding, Structure, and Structure-Property Relationships; Cambridge University Press, 2017.

[20] Rabuffi, M.; Picci, G. Status Quo and Future Prospects for Metallized Polypropylene Energy Storage Capacitors. IEEE Trans. Plasma Sci. 2002, 30 (5), 1939–1942.

[21] Huan, T. D.; Boggs, S.; Teyssedre, G.; Laurent, C.; Cakmak, M.; Kumar, S.; Ramprasad, R. Advanced Polymeric Dielectrics for High Energy Density Applications. Prog. Mater. Sci. 2016, 83, 236–269.

[22] Shigeyoshi, N.; Takashi, M.; Hirokazu, S.; Morihiko, H.; Katsuji, K.; Kazuo, I. Impregnated Capacitor. U. S. Patent 4131931 A, 1978.

[23] Yoshinori, M.; Tadakazu, I.; Fumio, J. Biaxially Oriented Polyproplyene Film. U. S. Patent 7872085 B2, 2011.

[24] Wan, C.; Bowen, C. R. Multiscale-Structuring of Polyvinylidene Fluoride for Energy Harvesting: The Impact of Molecular-, Micro- and Macro-Structure. J. Mater. Chem. A 2017, 5, 3091–3128.

[25] Li, W.; Meng, Q.; Zheng, Y.; Zhang, Z.; Xia, W.; Xu, Z. Electric Energy Storage Properties of Poly(Vinylidene Fluoride). Appl. Phys. Lett. 2010, 96 (19), 192905.

[26] Chu, B. A Dielectric Polymer with High Electric Energy Density and Fast Discharge Speed. Science 2006, 313 (5785), 334–336.

[27] Zhou, X.; Zhao, X.; Suo, Z.; Zou, C.; Runt, J.; Liu, S.; Zhang, S.; Zhang, Q. M. Electrical Breakdown and Ultrahigh Electrical Energy Density in Poly(Vinylidene Fluoride-Hexafluoropropylene) Copolymer. Appl. Phys. Lett. 2009, 94 (16), 162901.

[28] Rahimabady, M.; Yao, K.; Arabnejad, S.; Lu, L.; Shim, V. P. W. Intermolecular Interactions and High Dielectric Energy Storage Density in Poly (Vinylidene Fluoride-Hexafluoropropylene)/Poly(Vinylidene Fluoride) Blend Thin Films. Appl. Phys. Lett. 2012, 100 (25), 252907.

[29] Cheng, Z.; Lin, M.; Wu, S.; Thakur, Y.; Zhou, Y.; Jeong, D.; Shen, Q.; Zhang, Q. M. Aromatic Poly(Arylene Ether Urea) with High Dipole Moment for High Thermal Stability and High Energy Density Capacitors. Appl. Phys. Lett. 2015, 106 (20), 202902.

[30] Zhang, Z.; Wang, D. H.; Litt, M. H.; Tan, L. S.; Zhu, L. High Temperature and High Energy Density Dipolar Glass Polymers Based on Sulfonylated Poly(2,6-Dimethyl-1,4-Phenylene Oxide). Angew. Chemie - Int. Ed. 2017, 57 (6), 1528–1531.

[31] Wang, C. C.; Pilania, G.; Boggs, S. A.; Kumar, S.; Breneman, C.; Ramprasad, R. Computational Strategies for Polymer Dielectrics Design. Polymer (Guildf). 2014, 55 (4), 979–988.

[32] Bi, M.; Hao, Y.; Zhang, J.; Lei, M.; Bi, K. Particle Size Effect of $BaTiO_3$ Nanofillers on the Energy Storage Performance of Polymer Nanocomposites. Nanoscale 2017, 9 (42), 16386–16395.

[33] Zhang, X.; Shen, Y.; Zhang, Q.; Gu, L.; Hu, Y.; Du, J.; Lin, Y.; Nan, C. W. Ultrahigh Energy Density of Polymer Nanocomposites Containing $BaTiO_3$@TiO_2 Nanofibers by Atomic-Scale Interface Engineering. Adv. Mater. 2015, 27 (5), 819–824.

[34] Michael, E. K.; Trolier-McKinstry, S. Bismuth Pyrochlore Thin Films for Dielectric Energy Storage. J. Appl. Phys. 2015, 118 (5), 054101.

[35] Dang, Z. M.; Yuan, J. K.; Zha, J. W.; Zhou, T.; Li, S. T.; Hu, G. H. Fundamentals, Processes and Applications of High-Permittivity Polymer−Matrix Composites. Prog. Mater. Sci. 2012, 57, 660–723.

[36] Maxwell-Garnett, J. C.; Larmor, J. Colours in Metal Glasses and in Metallic Films. Phil. Trans. A 1904, 203, 385–420.

[37] Yamada, T.; Ueda, T.; Kitayama, T. Piezoelectricity of a High-Content Lead Zirconate Titanate Polymer Composite. J. Appl. Phys. 1982, 53 (6), 4328–4332.

[38] Knott, E. F. Dielectric Constant of Plastic Foams. IEEE Trans. Antennas Propag. 1993, 41 (8), 1167–1171.

[39] Zhang, L.; Bass, P.; Cheng, Z. Y. Physical Aspects of 0-3 Dielectric Composites. J. Adv. Dielectr. 2015, 5 (2), 1550012.

[40] Tanaka, T.; Kozako, M. Proposal of a Multi-Core Model for Polymer Nanocomposite Dielectrics. IEEE Trans. Dielectr. Electr. Insul. 2005, 12 (4), 669–681.

[41] Shen, Z. H.; Wang, J. J.; Lin, Y.; Nan, C. W.; Chen, L. Q.; Shen, Y. High-Throughput Phase-Field Design of High-Energy-Density Polymer Nanocomposites. Adv. Mater. 2018, 30 (2), 1–6.

[42] Varshneya, A.; Mauro, J. Fundamentals of Inorganic Glasses, 3rd ed.; Academic Press: London, UK, 2019.

[43] Smith, N. J.; Rangarajan, B.; Lanagan, M. T.; Pantano, C. G. Alkali-Free Glass as a High Energy Density Dielectric Material. Mater. Lett. 2009, 63 (15), 1245–1248.

[44] Manoharan, M. P.; Zou, C.; Furman, E.; Zhang, N.; Kushner, D. I. Flexible Glass for High Temperature Energy Storage Capacitors. Energy Technol. Commun. 2013, 1, 313–318.

[45] Solomon, P. Breakdown in Silicon Oxide-A Review. J. Vac. Sci. Technol. 1977, 14, 1122–1130.

[46] Tsurumi, T.; Adachi, H.; Kakemoto, H.; Wada, S.; Mizuno, Y.; Chazono, H.; Kishi, H. Related Content Dielectric Properties of $BaTiO_3$-Based Ceramics under High Electric Field. Jpn. J. Appl. Phys. 2002, 41 (1), 6929–6933.

[47] Gai, Z.; Cheng, Z.; Wang, X.; Zhao, L.; Yin, N.; Abah, R.; Zhao, M.; Hong, F.; Yu, Z.; Dou, S. A Colossal Dielectric Constant of an Amorphous TiO_2:(Nb, In) Film with Low Loss Fabrication at Room Temperature. J. Mater. Chem. C 2014, 2, 6790–6795.

[48] Hu, W.; Liu, Y.; Withers, R. L.; Frankcombe, T. J.; Norén, L.; Snashall, A.; Kitchin, M.; Smith, P.; Gong, B.; Chen, H.; Schiemer, J.; Brink, F.; Wong-Leung, J. Electron-Pinned Defect-Dipoles for High-Performance Colossal Permittivity Materials. Nat. Mater. 2013, 12 (9), 821–826.

[49] Liu, Z.; Zhao, C.; Wu, J. Reduced Dielectric Loss in New Colossal Permittivity (Pr, Nb)TiO_2 Ceramics by Suppressing Adverse Effects of Secondary Phases. Phys. Chem. Chem. Phys. Commun. 2018, 20 (34), 21814–21821.

[50] Shay, D. P.; Podraza, N. J.; Donnelly, N. J.; Randall, C. A. High Energy Density, High Temperature Capacitors Utilizing Mn-Doped $0.8CaTiO_3$-$0.2CaHfO_3$ Ceramics. J. Am. Ceram. Soc. 2012, 95 (4), 1348–1355.

[51] Su, X.; Riggs, B. C.; Tomozawa, M.; Nelson, J. K.; Chrisey, D. B. Preparation of $BaTiO_3$/Low Melting Glass Core–Shell Nanoparticles for Energy Storage Capacitor Applications. J. Mater. Chem. A 2014, 2 (42), 18087–18096.

[52] Lin, Y.; Li, D.; Zhang, M.; Zhan, S.; Yang, Y.; Yang, H.; Yuan, Q. Excellent Energy-Storage Properties Achieved in $BaTiO_3$-Based Lead-Free Relaxor Ferroelectric Ceramics via Domain Engineering on the Nanoscale. ACS Appl. Mater. Interfaces 2019.

[53] Yang, H.; Yan, F.; Lin, Y.; Wang, T.; Wang, F. High Energy Storage Density over a Broad Temperature Range in Sodium Bismuth Titanate-Based Lead-Free Ceramics. Sci. Rep. 2017, 7 (1), 8726.

[54] Wang, C.; Yan, F.; Yang, H.; Lin, Y.; Wang, T. Dielectric and Ferroelectric Properties of $SrTiO_3$-$Bi_{0.54}Na_{0.46}TiO_3$-$BaTiO_3$ Lead-Free Ceramics for High Energy Storage Applications. J. Alloys Compd. 2018, 749, 605–611.

[55] Yan, F.; Yang, H.; Lin, Y.; Wang, T. Dielectric and Ferroelectric Properties of $SrTiO_3$–$Bi_{0.5}Na_{0.5}TiO_3$–$BaAl_{0.5}Nb_{0.5}O_3$ Lead-Free Ceramics for High-Energy-Storage Applications. Inorg. Chem. 2017, 56 (21), 13510–13516.

[56] Li, F.; Jiang, T.; Zhai, J.; Shen, B.; Zeng, H. Exploring Novel Bismuth-Based Materials for Energy Storage Applications. J. Mater. Chem. C 2018, 6 (30), 7975–7981.

[57] Wang, T.; Jin, L.; Li, C.; Hu, Q.; Wei, X. Relaxor Ferroelectric $BaTiO_3$-$Bi(Mg_{2/3}Nb_{1/3})O_3$ Ceramics for Energy Storage Application. J. Am. Ceram. Soc. 2015, 98 (2), 559–566.

[58] Zhao, N.; Fan, H.; Ning, L.; Ma, J.; Zhou, Y. Temperature-Stable Dielectric and Energy Storage Properties of La($Ti_{0.5}Mg_{0.5}$)O_3-Doped ($Bi_{0.5}Na_{0.5}$)TiO_3-($Sr_{0.7}Bi_{0.2}$)TiO_3 Lead-Free Ceramics. J. Am. Ceram. Soc. 2018, 101 (12), 5578–5585.

[59] Lu, X.; Zhang, L.; Talebinezhad, H.; Tong, Y.; Cheng, Z. Y. Effects of CuO Additive on the Dielectric Property and Energy-Storage Performance of $BaTiO_3$-SiO_2 Ceramic-Glass Composite. Ceram. Int. 2018, 44 (14), 16977–16983.

[60] Sun, Z.; Li, L.; Yu, S.; Kang, X.; Chen, S. Energy Storage Properties and Relaxor Behavior of Lead-Free $Ba_{1-x}Sm_{2x/3}Zr_{0.15}Ti_{0.85}O_3$ Ceramics. Dalt. Trans. 2017, 46 (41), 14341–14347.

[61] Wei, M.; Zhang, J.; Zhang, M.; Yao, Z.; Chen, H.; Yang, C. Relaxor Behavior of $BaTiO_3$-$BiYO_3$ Perovskite Materials for High Energy Density Capacitors. Ceram. Int. 2017, 43 (6), 4768–4774.

[62] Li, J.; Li, F.; Xu, Z.; Zhang, S. Multilayer Lead-Free Ceramic Capacitors with Ultrahigh Energy Density and Efficiency. Adv. Mater. 2018, 1802155, 1–7.

[63] Alkathy, M. S.; James Raju, K. C. Enhancement of Dielectric Properties and Energy Storage Density of Bismuth and Lithium Co-Substituted Strontium Titanate Ceramics. Ceram. Int. 2018, 44 (9), 10367–10375.

[64] Ogihara, H.; Randall, C. A.; Trolier-McKinstry, S. High-Energy Density Capacitors Utilizing $0.7BaTiO_3$-$0.3BiScO_3$ Ceramics. J. Am. Ceram. Soc. 2009, 92 (8), 1719–1724.

[65] Lee, H.; Kim, J. R.; Lanagan, M. J.; Trolier-McKinstry, S.; Randall, C. A. High-Energy Density Dielectrics and Capacitors for Elevated Temperatures: Ca(Zr, Ti)O_3. J. Am. Ceram. Soc. 2013, 96 (4), 1209–1213.

[66] Zhao, L.; Liu, Q.; Gao, J.; Zhang, S.; Li, J. F. Lead-Free Antiferroelectric Silver Niobate Tantalate with High Energy Storage Performance. Adv. Mater. 2017, 29 (31), 1701824.

[67] Shao, T.; Du, H.; Ma, H.; Qu, S.; Wang, J.; Wang, J.; Wei, X.; Xu, Z. Potassium-Sodium Niobate Based Lead-Free Ceramics: Novel Electrical Energy Storage Materials. J. Mater. Chem. A 2017, 5 (2), 554–563.

[68] Gao, J.; Zhao, L.; Liu, Q.; Wang, X.; Zhang, S.; Li, J. F. Antiferroelectric-Ferroelectric Phase Transition in Lead-Free $AgNbO_3$ Ceramics for Energy Storage Applications. J. Am. Ceram. Soc. 2018, 101, 5443–5450.

[69] Pu, Y.; Zhang, L.; Cui, Y.; Chen, M. High Energy Storage Density and Optical Transparency of Microwave Sintered Homogeneous $(Na_{0.5}Bi_{0.5})_{(1-x)}Ba_xTi_{(1-y)}Sn_yO_3$ Ceramics. ACS Sustain. Chem. Eng. 2018, 6 (5), 6102–6109.

[70] Kumar, N.; Ionin, A.; Ansell, T.; Kwon, S.; Hackenberger, W.; Cann, D. Multilayer Ceramic Capacitors Based on Relaxor $BaTiO_3$-$Bi(Zn_{1/2}Ti_{1/2})O_3$ for Temperature Stable and High Energy Density Capacitor Applications. Appl. Phys. Lett. 2015, 106 (25), 252901.

[71] Funahashi, S.; Guo, J.; Guo, H.; Wang, K.; Baker, A. L.; Shiratsuyu, K.; Randall, C. A. Demonstration of the Cold Sintering Process Study for the Densification and Grain Growth of ZnO Ceramics. J. Am. Ceram. Soc. 2017, 100 (2), 546–553.

[72] Zhang, Y.; Cao, M.; Yao, Z.; Wang, Z.; Song, Z.; Ullah, A.; Hao, H.; Liu, H. Effects of Silica Coating on the Microstructures and Energy Storage Properties of $BaTiO_3$ Ceramics. Mater. Res. Bull. 2015, 67, 70–76.

[73] Huang, X.; Hao, H.; Zhang, S.; Liu, H.; Zhang, W.; Xu, Q.; Cao, M. Structure and Dielectric Properties of $BaTiO_3$-$BiYO_3$ Perovskite Solid Solutions. J. Am. Ceram. Soc. 2014, 97 (6), 1797–1801.

[74] Yang, C. H.; Yao, Q.; Qian, J.; Han, Y. J.; Chen, J. Growth , Microstructure , Energy–Storage and Dielectric Performances of Chemical–Solution NBT–Based Thin Films : Effect of Sodium Nonstoichiometry. Ceram. Int. 2018, 44 (8), 9152–9158.

[75] Peng, B.; Zhang, Q.; Li, X.; Sun, T.; Fan, H.; Ke, S.; Ye, M.; Wang, Y.; Lu, W.; Niu, H.; et al. Giant Electric Energy Density in Epitaxial Lead-Free Thin Films with Coexistence of Ferroelectrics and Antiferroelectrics. Adv. Electron. Mater. 2015, 1 (5), 1500052.

[76] Zhang, L.; Liu, M.; Ren, W.; Zhou, Z.; Dong, G.; Zhang, Y.; Peng, B.; Hao, X.; Wang, C.; Jiang, Z. D.; et al. ALD Preparation of High-k HfO_2 Thin Films with Enhanced Energy Density and Efficient Electrostatic Energy Storage. RSC Adv. 2017, 7 (14), 8388–8393.

[77] Liang, Z.; Liu, M.; Shen, L.; Lu, L.; Ma, C.; Lu, X.; Lou, X.; Jia, C. All-Inorganic Flexible Embedded Thin-Film Capacitors for Dielectric Energy Storage with High Performance. ACS Appl. Mater. Interfaces 2019, 11 (5), 5247–5255.

[78] Pan, H.; Li, F.; Liu, Y.; Zhang, Q.; Wang, M.; Lan, S.; Zheng, Y.; Ma, J.; Gu, L.; Shen, Y.; et al. Ultrahigh–Energy Density Lead-Free Dielectric Films via Polymorphic Nanodomain Design. Science. 2019, 365 (6453), 578–582.

[79] Hu, Z.; Ma, B.; Koritala, R. E.; Balachandran, U. Temperature-Dependent Energy Storage Properties of Antiferroelectric $Pb_{0.96}La_{0.04}Zr_{0.98}Ti_{0.02}O_3$ Thin Films. Appl. Phys. Lett. 2014, 104 (26), 263902.

[80] Hou, C.; Huang, W.; Zhao, W.; Zhang, D.; Yin, Y.; Li, X. Ultrahigh Energy Density in $SrTiO_3$ Film Capacitors. ACS Appl. Mater. Interfaces 2017, 9 (24), 20484–20490.

[81] Su, Z.; Yao, M.; Li, M.; Gao, W.; Li, Q.; Feng, Q.; Yao, X. A Novel and Simple Aluminium/Sol–Gel-Derived Amorphous Aluminium Oxide Multilayer Film with High Energy Density. J. Mater. Chem. C 2018, 6 (21), 5616–5623.

[82] Hou, Y.; Han, R.; Li, W.; Luo, L.; Fei, W. Significantly Enhanced Energy Storage Performance in $BiFeO_3/BaTiO_3/BiFeO_3$ Sandwich-Structured Films through Crystallinity Regulation. Phys. Chem. Chem. Phys. 2018, 20 (34), 21917–21924.

[83] Zhang, T.; Li, W.; Hou, Y.; Yu, Y.; Song, R.; Cao, W.; Fei, W. High-Energy Storage Density and Excellent Temperature Stability in Antiferroelectric/Ferroelectric Bilayer Thin Films. J. Am. Ceram. Soc. 2017, 100 (7), 3080–3087.

[84] Zhang, G.; Zhu, D.; Zhang, X.; Zhang, L.; Yi, J.; Xie, B.; Zeng, Y.; Li, Q.; Wang, Q.; Jiang, S. High-Energy Storage Performance of $(Pb_{0.87}Ba_{0.1}La_{0.02})(Zr_{0.68}Sn_{0.24}Ti_{0.08})O_3$ Antiferroelectric Ceramics Fabricated by the Hot-Press Sintering Method. J. Am. Ceram. Soc. 2015, 98 (4), 1175–1181.

[85] Ahn, C. W.; Amarsanaa, G.; Won, S. S.; Chae, S. A.; Lee, D. S.; Kim, I. W. Antiferroelectric Thin-Film Capacitors with High Energy-Storage Densities, Low Energy Losses, and Fast Discharge Times. ACS Appl. Mater. Interfaces 2015, 7 (48), 26381–26386.

[86] Castro, A.; Aguado, E.; Rojo, J. M.; Herrero, P.; Enjalbert, R.; Galy, J. The New Oxygen-Deficient Fluorite Bi_3NbO_7: Synthesis, Electrical Behavior and Structural Approach. Mater. Res. Bull. 1998, 33 (1), 31–41.

[87] Bretos, I.; Jiménez, R.; Ricote, J.; Calzada, M. L. Low-Temperature Crystallization of Solution-Derived Metal Oxide Thin Films Assisted by Chemical Processes. Chem. Soc. Rev. 2018, 47 (2), 291–308.

[88] Tang, H.; Sodano, H. A. Ultra High Energy Density Nanocomposite Capacitors with Fast Discharge Using $Ba_{0.2}Sr_{0.8}TiO_3$ Nanowires. Nano Lett. 2013, 13 (4), 1373–1379.

[89] Li, Q.; Zhang, G.; Liu, F.; Han, K.; Gadinski, M. R.; Xiong, C.; Wang, Q. Solution-Processed Ferroelectric Terpolymer Nanocomposites with High Breakdown Strength and Energy Density Utilizing Boron Nitride Nanosheets. Energy Environ. Sci. 2015, 8 (3), 922–931.

[90] Puli, V. S.; Ejaz, M.; Elupula, R.; Kothakonda, M.; Adireddy, S.; Katiyar, R. S.; Grayson, S. M.; Chrisey, D. B. Core-Shell like Structured Barium Zirconium Titanate-Barium Calcium Titanate-Poly(Methyl Methacrylate) Nanocomposites for Dielectric Energy Storage Capacitors. Polymer. 2016, 105, 35–42.

[91] Wang, G.; Huang, Y.; Wang, Y.; Jiang, P.; Huang, X. Substantial Enhancement of Energy Storage Capability in Polymer Nanocomposites by Encapsulation of $BaTiO_3$ NWs with Variable Shell Thickness. Phys. Chem. Chem. Phys. 2017, 19 (31), 21058–21068.

[92] Pan, Z. B.; Yao, L. M.; Zhai, J. W.; Liu, S. H.; Yang, K.; Wang, H. T.; Liu, J. H. Fast Discharge and High Energy Density of Nanocomposite Capacitors Using $Ba_{0.6}Sr_{0.4}TiO_3$ Nanofibers. Ceram. Int. 2016, 42 (13), 14667–14674.

[93] Wang, J.; Liu, S.; Wang, J.; Hao, H.; Zhao, L.; Zhai, J. Improving Dielectric Properties and Energy Storage Performance of Poly(Vinylidene Fluoride) Nanocomposite by Surface-Modified $SrTiO_3$ Nanoparticles. J. Alloys Compd. 2017, 726, 587–592.

[94] Wang, X.; Hao, X.; Zhang, Q.; An, S.; Chou, X. Energy-Storage Performance and Pyroelectric Energy Harvesting Effect of PNZST Antiferroelectric Thin Films. J. Mater. Sci. Mater. Electron. 2017, 28 (2), 1438–1448.

[95] Zhang, Y. L.; Li, W. L.; Cao, W. P.; Zhang, T. D.; Bai, T. R. G. L.; Yu, Y.; Hou, Y. F.; Feng, Y.; Fei, W. D. Enhanced Energy-Storage Performance of 0.94NBT-0.06BT Thin Films Induced by a $Pb_{0.8}La_{0.1}Ca_{0.1}Ti_{0.975}O_3$ Seed Layer. Ceram. Int. 2016, 42, 14788–14792.

[96] Dong, W. D.; Carlos Valadez, J.; Gallagher, J. A.; Jo, H. R.; Sahul, R.; Hackenberger, W.; Lynch, C. S. Pressure, Temperature, and Electric Field Dependence of Phase Transformations in Niobium Modified 95/5 Lead Zirconate Titanate. J. Appl. Phys. 2015, 117 (24), 244104.

[97] Rahimabady, M.; Qun Xu, L.; Arabnejad, S.; Yao, K.; Lu, L.; Shim, V. P. W.; Gee Neoh, K.; Kang, E. T. Poly(Vinylidene Fluoride-Co-Hexafluoropropylene)-Graft-Poly(Dopamine Methacrylamide) Copolymers: A Nonlinear Dielectric Material for High Energy Density Storage. Appl. Phys. Lett. 2013, 103 (26), 262904.

Chapter 3

The Cold Sintering Process and Electrical Characterizations of Lead Zirconate Titanate Ceramics

3.1 Introduction

Electro-ceramic materials are widely utilized in commercial electronics. For example, multilayer ceramic capacitors [1] and semiconducting varistors [2] are used in computers, cellphones and surge protection circuits. Thermoelectric [3] and piezoelectric sensors/actuators [4] incorporated in health monitors help save lives. Perovskite solar cells [5] and lithium-based battery electrodes [6] generate and store local power as well as renewable energy for next-generation vehicles and accommodations.

In every circumstance, the density of an electro-ceramic material is critical to its performance. For example, pores in a capacitor cause lower dielectric breakdown strength, reduced effective relative permittivities, and decreased device lifetimes; cracks in piezoelectric sensors cause a significant drop in sensitivity, etc. Consequently, a relative density >95% is desired for most electroceramics; this is typically difficult to realize at low temperatures.

Lead zirconate titanate (PZT) is a piezoelectric material widely employed in ultrasound transducers [7], precise positioning actuators, [8] sensors, and energy harvesters [9]. Typically, PZT requires a sintering temperature > 1200 °C [10]. Therefore, a number of methods have been explored to reduce the maximum processing temperature of PZT to 700˚C-1000˚C, including hot pressing [11,12], liquid phase sintering [13–15], microwave sintering [16] and field assisted sintering (spark plasma sintering) [17].

* *Part of this chapter is reproduced from D. Wang, H. Guo, C. S. Morandi, C. A. Randall, and S. Trolier-McKinstry "Cold Sintering and Electrical Characterization of Lead Zirconate Titanate Piezoelectric Ceramics." APL Materials 6, 016101 (2018).*

The cold sintering process (CSP) significantly reduces PZT's processing temperature by enabling substantive densification of ceramics at < 300 °C under uniaxial pressure in the presence of a transient liquid phase. In principle, low sintering temperatures can reduce lead loss, decrease the concentration of point defects, and potentially increase the range of metals utilized for inner electrodes. This research described optimization of cold sintering for $Pb(Zr,Ti)O_3$.

This chapter starts with a brief literature review of sintering techniques. The cold sintering process for PZT ceramics is then demonstrated, followed by the structural characterization as a function of post-annealing procedures and electrical characterizations of sintered samples. A viscous sintering model is introduced and compared with experimental data to describe the CSP of PZT.

3.2 Literature review

3.2.1 Sintering of ceramics

Sintering is both a kinetic and thermodynamic process. For example, grain growth is controlled by kinetics, and is concurrent with late stage sintering. The thermodynamic driving force for sintering comes from the reduction of surface free energy of a powder compact. [18] Powder compacts typically have a relative density of only 50%-70%. To achieve a higher density, one must rely on the mass transport between particles; diffusion is therefore crucial. [19] Figure 3-1 shows possible diffusion pathways between two ceramic particles [20]. Among the listed mechanisms, boundary diffusion (4), lattice diffusion (5), and plastic flow (6) contribute to the densification of ceramics as they effectively extend the area of necking and shorten the center to center distance between particles.

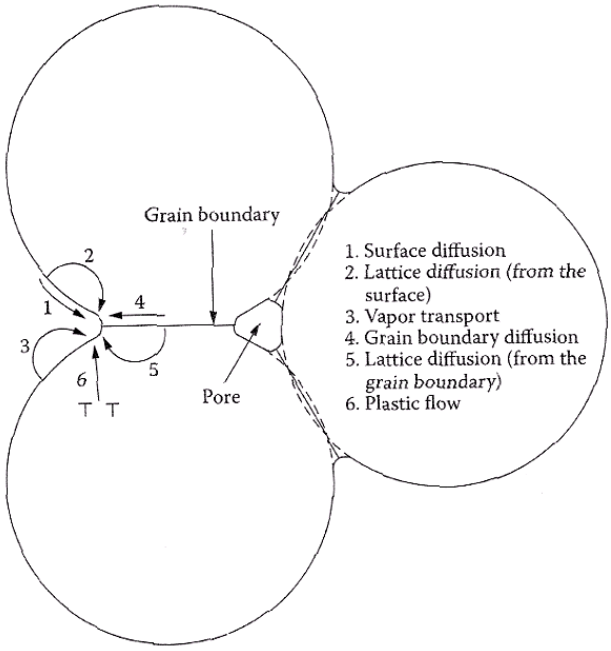

Figure **3-1**: The 6 pathways for diffusion between ceramic particles: 1. Surface diffusion. 2. Lattice diffusion from the surface. 3. Vapor transport. 4. Grain boundary diffusion. 5. Lattice diffusion from the grain boundary. 6. Plastic flow. (Picture from Rahaman *et al*. (2003). [20])

It is well known that the diffusion rate is proportional to the diffusion coefficient. Diffusion coefficients vary with materials, but are generally small for solids at low temperatures, making the densification of solid materials extremely slow under ambient conditions. Therefore, conventional sintering techniques use heat to accelerate mass transport in packed powder compacts.

Most electro-ceramics are sintered at temperatures over 1000 °C: ZnO (1200 °C) [21], Y_2O_3-ZrO_2 (1500 °C), [22] $BaTiO_3$ (1250 °C) [23], and Pb(Zr, Ti)O_3 (1300 °C) [10]. That is, sintering temperatures generally correspond to 50-75% of the materials melting temperature in order to achieve >95% relative densities. However, such high temperatures not only consume more energy and exacerbate greenhouse gas emissions, they also wear out the furnaces. Lower sintering techniques are therefore desirable. As the integration of electro-ceramics and metals/polymers continues, lower sintering temperatures will reduce the propensity towards

stress- or reaction- induced delaminate, and reduce the thermal expansion coefficient mismatch-induced strains.

Several methods to reduce sintering temperature (or at least reduce the thermal energy input during sintering) have been studied, including hot pressing (HP), liquid phase sintering (LPS), microwave/millimeter wave sintering (MWS), flash sintering (FS), and a combinations of these techniques, such as field assisted sintering technique (FAST, or spark plasma sintering (SPS)), liquid-phase-assisted HP, liquid-phase-assisted FAST, and the cold sintering process (CSP). All these techniques have utilized at least one of these three physical approaches:

I: Altering the form of energy delivered to the system (Ex. HP).

II: Manipulating the efficiency of energy delivered to the system (Ex. MWS and FS).

III: Adding a highly diffusive transport agent into the system (Ex. LPS).

General sintering techniques, including the low temperature sintering techniques mentioned above, will be introduced in the following sections.

3.2.2 Solid state sintering (SSS)

Solid state sintering uses only heat to increase both grain boundary and lattice diffusion, so as to achieve a high density. SSS can be divided into 3 stages: initial stage, intermediate stage and final stage. Figure 3-2 shows the microstructural evolution of ceramic particles in these different stages [24].

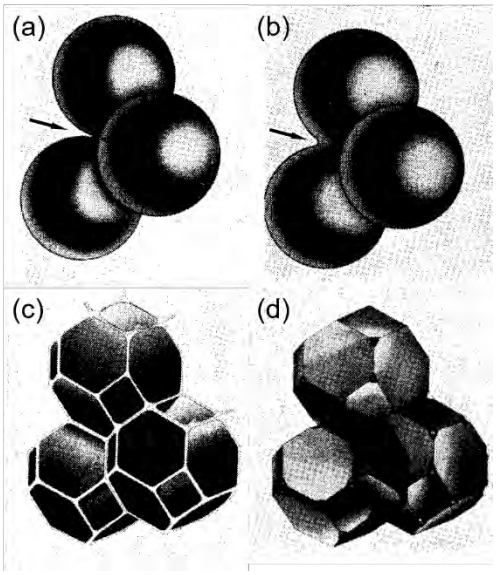

Figure 3-2: Illustration of morphology change in ceramic grains (a) before sintering, (b) at the initial stage of sintering when necks begin to form, (c) during the intermediate stage of sintering when grains turn into tetrakaidecahedrons with inter-connected pores, and (d) at final stage during which the channels along the grain edge close up and pores are isolated. (Figure adopted from Coble *et al*. (1961). [24])

The initial stage of sintering is characterized by the formation of "necks" between particles as the ceramic compacts start to coalesce. At this state, the relative density of a ceramic compact is normally < 65%. Then, during the intermediate stage, as diffusion expands the necking area, ceramic particles develop a tetrakaidecahedron morphology. Meanwhile, the pores shrink into inter-connected narrow channels on the edge of the grains. These channels begin to disappear at a relative density above 92%, known as the final stage, resulting in isolated pores and closed triple points.

For the intermediate and the final stages of sintering, there are mathematical models describing the density evolution. These were developed by Coble *et al.*[24] by solving self-diffusion equations under the assumption that the grains are uniform in size, with the exact shapes depicted in Figure (c) and (d) respectively for the intermediate and the final stage of sintering.

For the intermediate stage:

$$\frac{1}{\rho}\frac{d\rho}{dt} = \frac{4}{3}\frac{D_{GB}\delta_{GB}\gamma_{SV}\Omega}{\rho(1-\rho)^{1/2}G^4k_BT} \qquad \text{(Eq. 3-1)}$$

And for the final stage:

$$(1-\rho) = \frac{6\pi}{\sqrt{2}}\frac{D_{GB}\gamma_{SV}\Omega}{l^3k_BT}(t_f - t) \qquad \text{(Eq. 3-2)}$$

where ρ is the relative density, t is the sintering time, D_{GB} is the grain boundary diffusivity, δ_{GB} is the grain boundary thickness, γ_{SV} is the solid-vapor surface free energy, Ω is the molecular volume of the diffusing species, G is the grain size, k_B is Boltzmann's constant, T is the sintering temperature, l is the edge length of the polyhedron, and t_f is the time when pores are completely eliminated.

SSS is one of the most widely applied sintering techniques because it is an inexpensive batch process and has almost no limitations on the shape and size of the samples. However, there are a couple of drawbacks when applying SSS. First, SSS requires a high temperature that sometimes causes decomposition of ceramics (Ex. $BiFeO_3$ [25]). Also, continuous high temperature operation may shorten furnace lifetime. In addition, it is difficult to get ultra-high density (>99.9%) with SSS because pores surrounded by many grains tend to grow at high temperatures, as shown in Fig. 3-3 [20]. This is because the pore stability is related to the dihedral angle, and the ratio of the pore size compared with the grain size. Larger pores with concave dihedral angles are more stable and will enlarge while the smaller pores will diminish as the grains grow in the ceramics. Although pre-sintering treatments such as uniaxial pressing and cold isostatic pressing (CIP) are applied to enhance the packing, the green density is still lower than ideal.

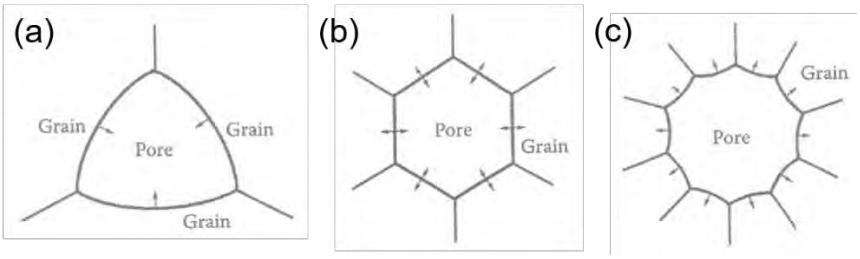

Figure 3-3: Schematics of pores in 2 dimensions in connections with (a) 3 grains, (b) 6 grains and (c) 9 grains. The pore tends to shrink in (a), exists metastably in (b) but grows larger in (c). (Schematics from Rahaman *et al*. (2003). [20])

3.2.3 Pressure-assisted sintering: hot pressing (HP) and hot isostatic pressing (HIP)

Pressure-assisted sintering involves applying uniaxial (HP) or isostatic pressure (HIP) during the sintering of ceramics. The effect of pressure can be simply understood as providing additional driving force for mass transport. And due to this extra driving force, when a ceramic sample is pressed at high temperatures, part of the activation energy for densification is supported by pressure rather than heat. Therefore, compared with SSS, HP and HIP techniques facilitate development of ultra-high ceramic densities. Thus, HP and HIP can be utilized for sintering carbide cutting tools (WC [26]) and highly transparent ceramics (β-sialon ceramics [27]) in which even a low level of porosity can be critical to the performance. Figure 3-4 shows a microstructure of a HIP β-sialon ceramics sintered to >99% density.

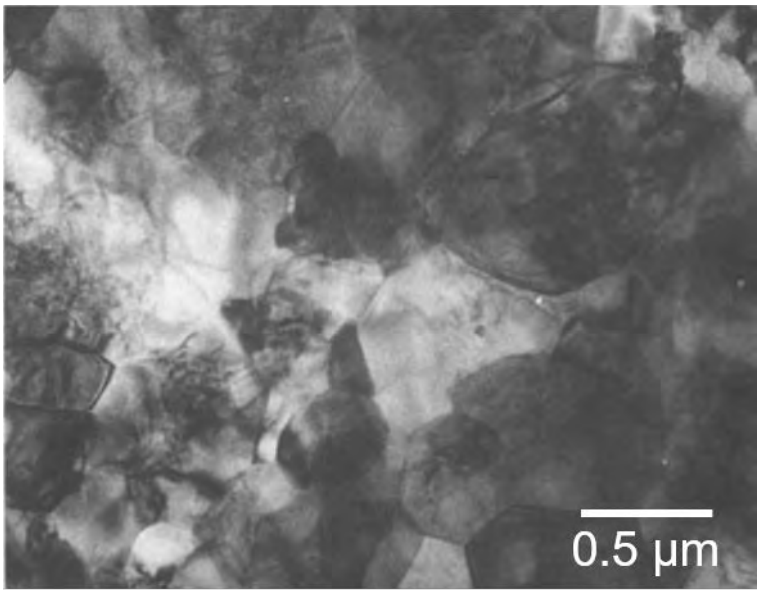

Figure 3-4: The SEM of a polished surface showing dense microstructure of β-sialon sintered by HIP. (Image from T. Ekström et al. (1989). [27])

Drawbacks of pressure-assisted sintering includes process cost and difficulties in removal of interior grain porosity in HIP. In terms of cost, pressure-assisted sintering requires additional equipment, and tends to increase the total expense during mass production of ceramics. Secondly, for HIP, pressurized gas may get trapped in the grains during grain growth, forming grain interior pores, which will become larger on pressure release. This issue is more serious on the surface than in the center of the sample.

3.2.4 Liquid phase sintering (LPS)

Liquid phase sintering takes advantages of melted sintering aids to help increase the system diffusivity. The sintering aids forming transient liquid phases will first lubricate and rearrange ceramic particles and then trigger a "dissolution-precipitation process." This process involves the partial dissolution of ceramic particles and the re-precipitation of the dissolved ions in the pores, as illustrated in Figure 3-5.

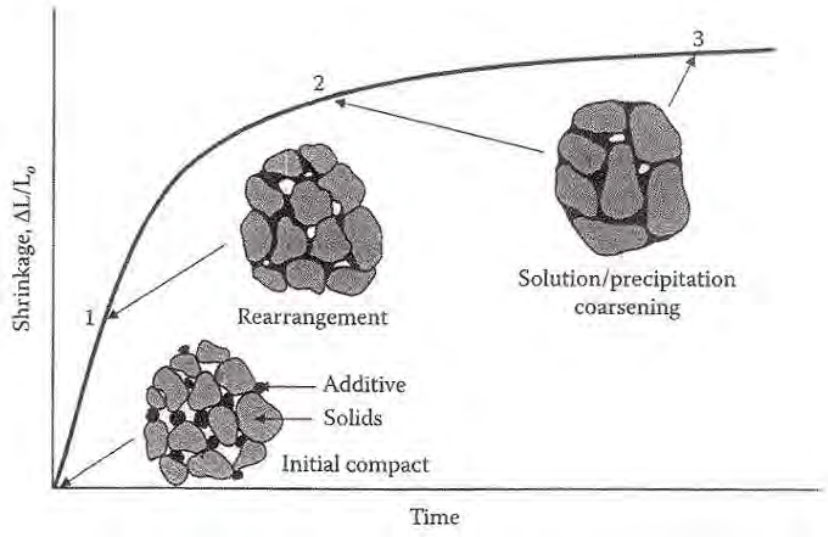

Figure 3-5: A schematic of the LPS at different stages. The initial compact consists of solid ceramic powder and additive sintering aid. The sintering aid melts at elevated temperature and lubricates the ceramic powder, resulting in particle rearrangement. Later on, as the dissolution-precipitation process proceeds, densification and grain growth take place and the sample is sintered. (Figure adopted from O. H. Kwon *et al*.) [28]

Kwon *et al*. [28] studied the governing kinetics of LPS. The sintering rate is a function of surface diffusion and interface reactions and can be described by the following equations:

For surface diffusion:

$$\frac{d(\frac{\Delta\rho}{\rho})}{dt} = \frac{A\delta D_l C_0 \gamma_{lv} \Omega}{k_B T} r_s^{-4} \qquad \text{(Eq. 3-3)}$$

$$\frac{d(\frac{\Delta\rho}{\rho})}{dt} = \frac{BKD_l C_0 \gamma_{lv} \Omega}{k_B T} r_s^{-2} \qquad \text{(Eq. 3-4)}$$

in which ρ and t are relative density and sintering time respectively, A and B are geometrical factors, δ is the thickness of the liquid film, D_l is the liquid phase diffusivity, C_0 is the concentration of the solute at equilibrium, γ_{lv} is the liquid-vapor surface tension, Ω is the molecular volume of the dissolved species, k_B is Boltzmann's constant, T is the sintering temperature, r_s is the particle radius, and K is the reaction constant at the liquid-solid interface.

The application of LPS can be dated to 25,000 years ago when Upper Paleolithic humans started to use firewood to sinter clay for containers and tools. [29] This example demonstrates that the sintering temperature can be lowered via the utilization of a sintering aid. As a result, even with fuels of low heating values such as firewood, some ceramics can be sintered.

Typical liquid phase sintering aids are compounds:

I: With low melting temperatures;

II: That can wet and dissolve the ceramics to be sintered;

III: Ideally, have little influence on the performances of sintered ceramics, or serve as a useful dopant.

Criteria I suggests the sintering aid should have weak bonds, low valences, or compositions with low-temperature eutectic points. Criteria II indicates the sintering aid should be (mostly) ionically bonded to act as a sintering aid for a material such as PZT. Criteria I and II suggest the use of fluorites, oxides and chlorides of low-valence cations. Thus, widely used sintering aids include LiF (although LiF fulfills criteria I and II, the origin of its low melting temperature is the strong repulsive force between fluorine atoms due to the small lithium radius) [30], Na_2O [31], CaF_2 [32], PbO [13], CuO [33], and B_2O_3 [34] both satisfy criteria I and II. In addition, ternary or quaternary compositions such as PbO-CuO/Cu_2O [35,36], PbO-GeO_2 [15], and Li_2CO_3-B_2O_3-CuO (LBCu) [37] are also widely used in LPS.

Criteria III depends on the materials and its applications. For example, in the LPS of lead zirconate titanate (PZT), PbO is generally used as the sintering aid. With PbO, closed pores and grain growth were observed as low as 1000 °C, 250-300 °C lower than conventional SSS. [38] Because PbO is volatile at >700 °C and a small amount of excess PbO has a modest influence on the dielectric and piezoelectric properties of PZT are generally not too strongly degraded by the PbO. [13] Sometimes, when PZT needs to be acceptor-doped for high quality factor applications, PbO-CuO or occasionally, LBCu systems may serve as the sintering aid in which Cu^{2+} is a useful

dopant [35,37]. Other sintering aids, such as $PbO\text{-}GeO_2$ and $LiBiO_2$ result in mediocre piezoelectric properties due to Ge/Li-contained grain boundaries; hence these are not as useful as other sintering aids, even though sintering temperatures < 800 °C were claimed. [14,15]

The presence of a transient liquid phase is a "double-edged sword". On one hand, the liquid phase increases the diffusivity significantly, resulting in densification at a lower temperature; on the other hand, it facilitates grain interior pores formation caused by rapid grain growth and, most of the time, unwanted secondary phases formed by residual sintering aids.

3.2.5 Viscous sintering

Viscous sintering is widely employed in the sintering of glass materials; in this process, plastic flow fills the pores. During sintering, glasses gradually become less viscous as the temperature increases. Commercially, glass materials are sintered and processed between their softening points (viscosity = $10^{7.65}$ Poise, where the glass materials start to "deform under its own weight" [39]) and working points (viscosity = 10^4 Poise, below which the glass can be worked on a machine [39]). This interval is called the "working range". [39] For alkali-lead glasses and soda-lime glasses, the working range is between 600-1000 °C while for borosilicate glasses and aluminosilicate glasses the working range increases to 800-1200 °C. [39] Notice that these temperatures are slightly lower than typical sintering temperatures for ceramics.

Viscous sintering can also be treated as a special case of LPS when the liquid phase is the main component to be sintered. For a system containing viscous phase and hard inclusions, if the liquid phase volume fraction is below 40%, it is considered to be LPS. Otherwise the process is treated as viscous sintering. [20]

3.2.6 Electromagnetic field-assisted sintering

The motivation for electromagnetic field-assisted sintering is to enhance the efficiency of the energy input during sintering. It is achieved by applying high currents or electromagnetic waves that directly heats the samples instead of heating the rest of the chamber. Due to the smaller heating volume than conventional sintering, electromagnetic field-assisted sintering techniques are characterized by ultra-fast heating and cooling rates, leading to fine grain sizes [40]. This enables the production of cutting tools and abrasives with high hardness, such as tungsten carbide [41] and alumina [42].

Electromagnetic field-assisted sintering encompasses two techniques: microwave/ millimeter-wave sintering (MWS) and electric current-assisted sintering (ECAS). MWS operates similar to a microwave oven in that the ceramic samples are heated by the electromagnetic radiation. ECAS is sometimes considered as a combination of two similar sintering techniques: field-assisted sintering technique (FAST) and flash sintering (FS), both of which uses large currents to generate significant Joule heating that densifies the ceramics. The only difference is in FS, a ceramic green body is heated to an "onset temperature" at which the electrical conductivity is significantly increased, resulting in complete sintering in a "flash" [43].

Depending on their mechanisms, one of the drawbacks of electromagnetic field-assisted sintering techniques is the need for absorption of electromagnetic fields by the samples. This has been accommodated by either utilizing a susceptor that resonates/conducts well with the applied fields or by adding a small amount of dopants or phases that increase the absorption. [44,45]

3.2.7 Cold sintering process (CSP)

Of all the energy-efficient sintering techniques, the cold sintering process (CSP) holds the most potential for ultra-low temperature sintering. In many studies, ceramic pellets can be sintered to >95% relative density at <300 °C.[46–48] The densifications under such low temperatures are realized by introducing uniaxial pressures in conjunction with transient liquid phases that (often) partially dissolve the ceramics, re-arrange the particle compact, and re-precipitate the dissolved ions at the pores when the liquid phase is vaporized. Figure 3-6 schematically shows the CSP at a microstructural level. [49] It is obvious that CSP should be cataloged into LPS as their mechanisms and general steps are identical.

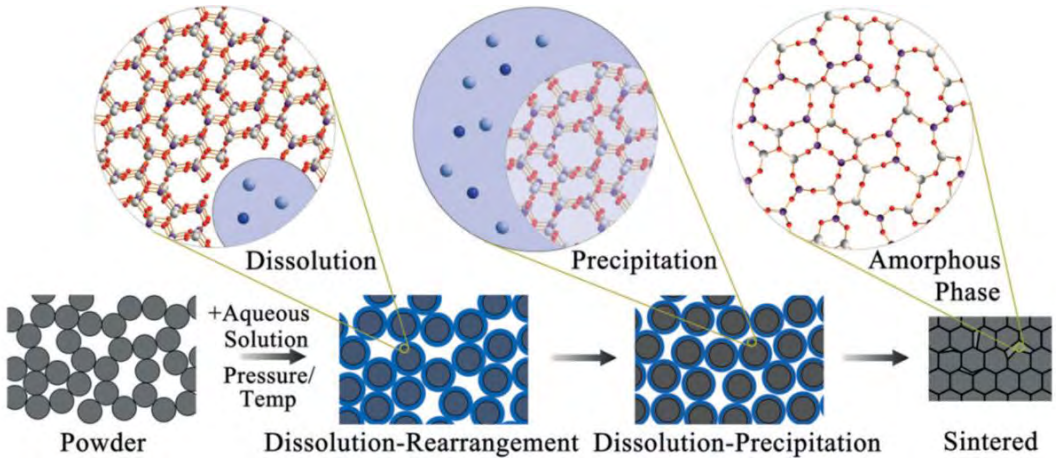

Figure 3-6: A schematic of the general cold sintering process, including dissolution, rearrangement, and precipitation procedures. Magnified regions represent typical microstructures of ceramics within the different stages. (Figure adopted from Guo *et al*. (2016) [49])

Though most of the CSP papers have been published within the past 5 years, the origin of this technique may be traced back to the 1960s when researchers started to realize the presence of moisture increased the green density in MgO and reduced the sintering temperatures. [50] In the 1970-1980s, the word “cold sintering” was first used to refer to a process utilizing “plastic deformation of powder particles in a high pressure gradient at ambient temperature result(ing) in

green densities close to theoretical" for metals, glass, and ionic crystals. [51] At the same time, the hydrothermal hot-pressing (HHP) method, another important branch of CSP, was proposed for the densification of cement materials at low temperatures. [52,53] In 2014-2015 Kähäri *et al*. and Guo *et al*. initiated a renaissance of CSP; their research showed that more complex compounds such as Li_2MoO_4 (LMO) and KH_2PO_4 (KDP) can be cold sintered near room temperature by adding water and higher uniaxial pressures. [46,47] Research of CSP bloomed thereafter with hundreds of publications and patents on the CSP of oxides [48,54–58], inorganic salts [59–62], and composites [63–66] covering applications in high frequency antennas [67,68], energy storage capacitors [69,70], battery components [59,61,62], varistors [48,63], and piezoelectric sensors/actuators [55,71].

Critical process parameters during CSP include liquid phase content and composition, temperature, pressure and time. Table 3-1 describes the cold sintering conditions of some typical material systems.

Table 3-1: Some typical materials that have been cold sintered. The cold sintering conditions and their potential applications are also listed.

Materials System	Liquid Phase	CSP Conditions	2nd Heat Treatment	Relative Density	Applications
NaCl [72]	Water	120 °C, 300 MPa, 10 min	80 °C 24 hrs	93%-98%	High frequency dielectrics
ZnO [48]	Water/Acetic acid	300 °C, 387 MPa, 2 hrs	--	>90%	Varistors, transistors
SiO_2 [73]	Water	300 °C, 190 MPa, 90 min	--	74%	Industrial waste immobilization
$CaCO_3$ [74]	Water	25 °C, 500 MPa, 30 min	--	84%	Construction materials
Li_2MoO_4 [46]	Water	25 °C, 130 MPa	120 °C, 4 hrs	87%-93%	High frequency dielectrics
$LiFePO_4$ [61]	LiOH water solution	240 °C, 750 MPa, 30 min	--	85%	Battery cathodes
$Na_{3.4}Sc_{0.4}Zr_{1.6}Si_2PO_{12}$ [62]	KOH	250 °C, 300 MPa, 10 min	1000 °C, 1 hr	87% (as cold sintered) 98% (after post-anneal)	Battery electrolytes
$BaTiO_3$ [47]	$Ba(OH)_2$ and TiO_2 water suspension	180 °C, 430 MPa, 3 hrs	900 °C, 3 hrs	94% (as cold sintered) 95% (after post-anneal)	Energy storage capacitors
$Pb(Zr,Ti)O_3$ [55]	$Pb(NO_3)_2$ water solution	300 °C, 500 MPa, 3 hrs	900 °C, 3 hrs	89% (as cold sintered) 99% (after post-anneal)	Piezoelectric sensors and actuators
$Pb(Zr,Ti)O_3/Li_2MoO_4$ [71]	Water	25 °C, 250 MPa	120 °C, 18 hrs	90%	Piezoelectric sensors and actuators
Al_2SiO_5/NaCl [75]	Water	120 °C, 200 MPa, 50 min	120 °C, 24 hrs	92%	High frequency dielectrics
PTFE/ZnO [63]	Acetic acid	285 °C, 300 MPa, 1 hr	--	92%-96%	High field varistors
ZnO/MXene [65]	Acetic acid	300 °C, 250 MPa, 1 hr	--	92%-98%	Thermal electric energy conversion

A few general trends can be concluded from the table:

Transient liquid phase: The liquid phases used in CSP are often water-based solutions. These solutions may cause either congruent dissolution (Li_2MoO_4 [46], KH_2PO_4 [47], $NaNO_2$ [47], ZnO [48], ZrO_2 [76], etc.) or incongruent dissolution ($BaTiO_3$ [47,77,78]) of the materials. Congruent dissolution favors rapid densification via cold sintering, but is not always available in solids with complex chemistries. For example, in the case of $BaTiO_3$, the use of water as a liquid phase promotes leaching of Ba^{2+} with subsequent formation of $BaCO_3$ and passivation of the powder surfaces with an unreactive hydrated titanium-rich surface layer that prevents densification [79]. Thus, to avoid incongruent dissolution of $BaTiO_3$, a water based suspension of $Ba(OH)_2$ and TiO_2 can be utilized during cold sintering [77,78].

Temperature: The operation temperatures of CSP are below 300 °C. Generally, oxides and complex compounds that are more difficult to dissolve are cold sintered at higher temperatures. CSP is advantageous because of its operating temperatures; it is environmentally friendly due to low energy consumption. New composites with ceramic inclusions beyond percolation points can be fabricated by CSP without decomposition of polymer phases. [63,65] Moreover, as sintering temperatures decrease, the energy for grain growth drops significantly, enabling controllable microstructure engineering.

Pressure: Compared with uniaxial pressure by itself, the pressures applied during CSP are much higher. This is likely to be part of what enables the ultra-low working temperatures; even though dissolution of the ceramics can increase the diffusivities by 4-5 orders of magnitudes, the grain growth during CSP is still not comparable with the conventional processes carried out at higher temperatures. A study by Funahashi *et al*. [48] confirmed that CSP produces similarly dense samples at lower temperature but with more limited grain growth than conventional methods. [80]

Density and secondary heat treatment: The relative densities of cold sintered materials are mostly over 80% due to plastic deformation of powders during pressing. Sometimes the as-cold-sintered samples need to be post-annealed at a higher temperature to eliminate secondary phases and complete the sintering process. This procedure can be important for perovskites that are difficult to dissolve congruently. In $BaTiO_3$-based systems cold sintered in air using water as the transient liquid phase, for example, CO_2 stabilizes an amorphous phase that fills the pores between the crystalline particles. This kinetically limits the sintering process until the carbonate is decomposed at a temperature of ~ 830 °C. Therefore a post-annealing stage is required to further densify and equilibrate the grain structures. A post-annealing at 900 °C produced high quality $BaTiO_3$ at a net reduction in temperature of 300-500 °C, relative to conventional methods [47]. The result is well-densified ceramics with high dielectric performance.

Overall, CSP is still a technique under development. It remains promising despite potential disadvantages such as secondary phase residue, incongruent dissolution of cations, and restricted sample sizes/shapes due to pressure limits.

3.3 Experimental procedures

In this work, a $Pb(NO_3)_2$ solution was used as a transient liquid sintering aid to densify PZT powder. This solution was selected for 4 reasons: its high solubility in water, its low reactivity with CO_2 (limiting carbonate secondary phases), its compensation for lead loss during post annealing, and its ability to act as a liquid phase sintering aid during post annealing. A 0.5 mol/L $Pb(NO_3)_2$ solution was made by dissolving 5.02 g $Pb(NO_3)_2$ (Sigma-Aldrich Corp., St. Louis, USA) into 30 mL deionized water.

A bimodal PZT powder was utilized for cold sintering PZT, as this leads to a higher driving force for sintering and also can aid in the packing density. The coarse PZT powder is a

commercial PZT-5A powder (PKI-509, Piezo Kinetics, Inc., Bellefonte, PA). To reduce the average particle size of ~ 3 μm, the powder was attrition milled (Szegvari Attritor System Type B Model 01-HD, Union Process, Inc., Akron, OH) to an average diameter to ~ 400 nm. For the attrition milling, 25 vol% PZT powder was suspended in deionized water with 3 vol% Darvan A-21 dispersant (Vanderbilt Minerals, LLC, Norwalk, CT). The pH of the suspension was adjusted to ~ 10 with NH_4OH. The mixture was milled for 12 hours, dried at 200 °C, and heat treated at 500°C for 5 hours to remove any residual carbon.

The finer powder (undoped PZT 52/48) was made through a 2-methoxyethanol (2-MOE) based sol-gel method as described elsewhere [81,82]. Lead acetate trihydrate (Sigma-Aldrich) was added to 2-MOE in a rotary evaporator flask under Ar flow, dissolved at 120 °C and distilled until a semi-dry powder precipitated. Zirconium n-propoxide (Sigma-Aldrich) and titanium iso-propoxide (Sigma-Aldrich) were mixed in 2-MOE at room temperature, and then were added to the lead acetate. The mixture was refluxed for 3 hours and distilled. Acetylacetone (22.5 vol%, Sigma-Aldrich) and 2-MOE (Sigma-Aldrich) were added to make a 0.4 M solution. The solution was dried by stirring in air on a hot plate at 120 °C until a gel formed. The gel was crushed in an agate mortar and pestle and calcined at 600 °C for 42 hours to remove the residual carbon from the precursors. The average diameter of the finer powder is ~ 100 nm.

To cold sinter PZT, 0.7 g of PZT bimodal powder (1:1 mixture of 400 nm and 100 nm powders in terms of weight) was mixed with 0.5 ml lead nitrate solution and ground in a mortar and pestle. The mixture was then loaded into a cylindrical die (Wartburg Tool & Die, Inc., Wartburg, TN) and pressed at 500 MPa uniaxial pressure (MP40 pellet press, Across International, LLC, Livingston, NJ). The die was held at room temperature for 30 min, heated to 300 °C for 150 min and cooled down to < 80 °C in 30 min. The PZT pellets after cold sintering had a diameter of 0.5 inch (12.77 mm) and thicknesses ~ 0.8-1.0 mm. Some of the cold sintered

PZT pellets underwent a post-annealing step at 700 °C for 3 h, 700 °C for 24 h, or 900 °C for 3 h. The heating rate was 5 °C/min for all samples during the post-annealing process.

To compare with the cold sintering process, in a conventional method, 0.7 g bimodal PZT powder was uniaxially pressed to a pellet under the same condition as CSP samples but without the addition of $Pb(NO_3)_2$ solution. The conventionally pressed pellet was also annealed 900 °C for 3 h, which is the same as the CSP sample.

For grain size measurement, the PZT samples were polished using 15 μm, 9 μm, 6 μm, 3 μm and 1 μm diamond polish, successively. Each step lasted for 2 min at a rotation speed of 240 rpm. The average grain size of the PZT samples was calculated by the line intercept method using the equation shown below [83]:

$$Average\ grain\ size = 1.5 \times \frac{total\ line\ length}{number\ of\ grain\ boundaries} \quad \text{(Eq. 3-5)}$$

The crystal structure and phase purity of the PZT samples were identified by X-ray diffraction (XRD, Empyrean, PANalytical Corp., Almelo, Netherlands) with Cu Kα radiation. Scans were taken from 2θ = 10° to 72° with a step size of 0.026° 2θ and a scan rate of 0.067°/sec. A scanning electron microscope (SEM, Merlin, Carl Zeiss, Inc., Jena, Germany) and a transmission electron microscope (TEM, FEI Talos, Eindhoven, Netherlands) with an Energy dispersive spectroscopy (EDS) detector were utilized to observe the microstructural development of the ceramics. After cutting, polishing, and focused ion beam milling the samples to electron transparency, they were mounted on copper grids.

The piezoelectric coefficients were measured by a direct method with a d_{33} PiezoMeter system (PM 300, Piezotest Pte. Ltd., Singapore) after a poling process at 25 °C for an hour under 3 times the coercive field. The polarization-electric field hysteresis loops (P-E loops) were characterized using a custom system with a Trek Model 30/20 high voltage amplifier system (Trek, Inc., Lockport, NY) and LabVIEW software (National Instruments Corporation, Austin,

TX). The dielectric permittivity and loss tangent were measured using a Hewlett-Packard 4284A LCR meter (Agilent Technologies, Inc., Palo Alto, CA) over a temperature range from 500 °C to 30 °C.

PZT powders with a bimodal size distribution (medium particle sizes of 50 nm and 600 nm) were used for the study of $Pb(NO_3)_2$ content, temperature, pressure and holding time. The powder was produced by attrition milling (Szegvari Attritor System Type B Model 01-HD, Union Process, Inc., Akron, OH) commercial PZT-5A powder (PKI-509, PiezoKinetics Inc., Bellefonte, PA) for 12 hrs. The particle size analysis was double checked under a laser diffractometer (Mastersize 3000, Malvern Analytical Ltd., Malvern, UK) and a scanning electron microscope (Verios G4, FEI, Eindhoven, Netherlands).

The study on cold sintering temperature and pressure strained the capabilities of conventional hydraulic presses as the heat from the die transferred to the hydraulic cylinder, raised the oil temperature, and caused pressure fluctuations. An advanced hydraulic press with a pressure stabilizing regulator, designed by Richard Floyd *et al.* [84], increased the repeatability of CSP. This pressure regulator uses a spring-loaded nozzle to constrain oil flow and stabilize pressure, allowing independent control of temperature and pressure. Following the designs of Floyd, a new press was constructed. This press was utilized for research on cold sintering temperature, pressure and time.

To make PZT pellets, 0.7 g (per pellet) raw powder was mixed and ground with different volume fractions of $Pb(NO_3)_2$ powder (Sigma-Aldrich Corp., St. Louis, MO). 0.5 mL deionized water was added to the mixture to dissolve the lead nitrate. The mixture was then ground in a mortar and pestle until the water was mostly vaporized, removing the soft agglomerates in PZT. After grinding, the mixture was loaded into a cylindrical die (Wartburg Tool & Die, Wartburg, TN) and pressed at 25-300 °C, under 50-1000 MPa for 15-180 min. The pellets cold sintered at

<100 °C were dried in open air for over 24 hrs to remove residual water that might affect the measured sintered density. The densities of the pellets were measured by the geometrical method.

3.4 Results and discussion

3.4.1 Cold sintering and electrical characterization of lead zirconate titanate piezoelectric ceramics

Table 3-2 shows the geometric densities of PZT pellets with 15 vol% $Pb(NO_3)_2$ cold sintered at 300 °C, 500 MPa for 3 hrs, and heat treated at different temperatures. Using a theoretical density of 7.8 g/cm^3, the green compact sample (pressed without the $Pb(NO_3)_2$ sintering aid) yields a relative density of 59%. Cold sintering at 300 °C increases the relative density to 89%; after post-annealing at 900 °C the relative density increases to 99%.

Table 3-2: The densities and d_{33} of cold sintered (300 °C, 500 MPa, 3 hrs) PZT with different post-annealing temperatures. The d_{33} values are the average of 3 measurements of the same sample for each condition.

PZT samples	Geometric density (g/cm^3)	Relative density (%)	Dielectric constant (100 kHz, 25 °C)	Loss (%)	d_{33} (pC/N)
Green compact 300 °C pressed	4.6	59	--	--	--
CSP 300 °C as sintered	6.9	89	207	2.0	4
CSP 700 °C 3 h post-annealed	7.1	91	917	2.7	80
CSP 900 °C 3 h post-annealed	7.7	99	1324	4.0	197

Figure 3-7 shows the XRD patterns after cold sintering and post-annealing according to the conditions mentioned in the above table. Crystalline $Pb(NO_3)_2$ and PbO are present after the cold-sintering step because $Pb(NO_3)_2$ decomposes slowly from 250 °C. In contrast, after the post-annealing step at higher temperatures the samples are XRD phase pure, as $Pb(NO_3)_2$ fully

decomposes and PbO begins to volatilize. It is probable that the relative densities of ceramics immediately following the cold sintering step and after a 700 °C post-annealing are similar due to the loss of this mass. After the 700 °C post-anneal, although the sample surfaces are phase pure by XRD, there are clues that residual lead oxides may remain. This is inferred because, orange stains (presumably due to lead oxide) were still seen on the sectioned surface of the pellet.

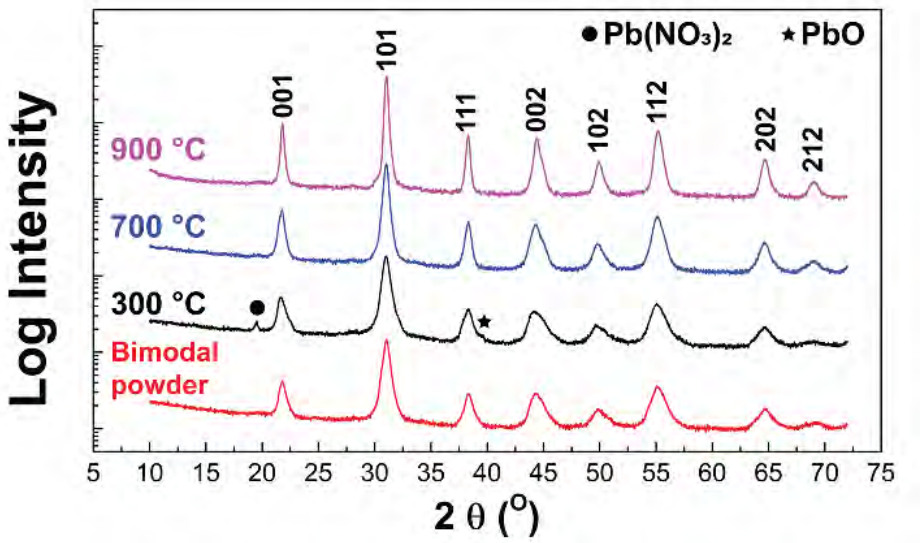

Figure 3-7: XRD of the bimodal PZT powder, as-cold-sintered at 300 °C, and the samples after a 3 hour long post-annealing step. The patterns are offset vertically for clarity.

The microstructural evolution was investigated further using TEM with diffraction contrast imaging techniques. Upon cold-sintering at 300 °C, a dense structure forms due to consolidation of particles, and the grain boundaries have thick layers of amorphous phases. This lead-rich matrix fills the spaces between the crystalline PZT particles. Nanocrystalline PbO or $Pb(NO_3)_2$, and amorphous phases form at the surface of the large PZT particles, presumably due to heterogeneous nucleation. Therefore, a primary benefit of cold-sintering is a major densification to a relative density of ~ 90%; there is a reduction in distance between PZT particles and hence diffusion lengths. Upon post annealing at 700 °C, well-defined grain boundaries and

equilibrated triple points started to form, with dihedral angles ~ 120°. When the temperature increases to 900 °C, melting of PbO increases mass transport, bringing the densification to completion. Within the grains, complex high-density domain configurations are formed as shown in Figure 3-8 (f), (j) and (k). As for compositions, the EDS results presented in Figure B-1, B-2, and B-3 indicate low carbon concentrations in cold sintered PZT although some zirconia impurities, possibly from the commercial powder, were observed. This is shown in Figure B-1 (c).

Piezoelectric coefficients (d_{33}) of the cold sintered PZT are listed in Table 3-2 as well. The 900 °C annealed PZT has the highest d_{33} ~ 200 pC/N. This value is lower than commercial PZT-5A (350-550 pC/N) probably because the addition of 50 wt% undoped PZT and the nanograin size [12]. It nonetheless demonstrates that it is possible to cold sinter PZT while retaining the functional properties, although at this point a post-annealing step is required to remove the grain boundary phases, and obtain a better density. The 700 °C annealed sample has a modest d_{33} most likely due to the presence of porosity, defects and residual lead oxides. For the 300 °C cold sintered sample, almost no piezoelectric behavior can be detected.

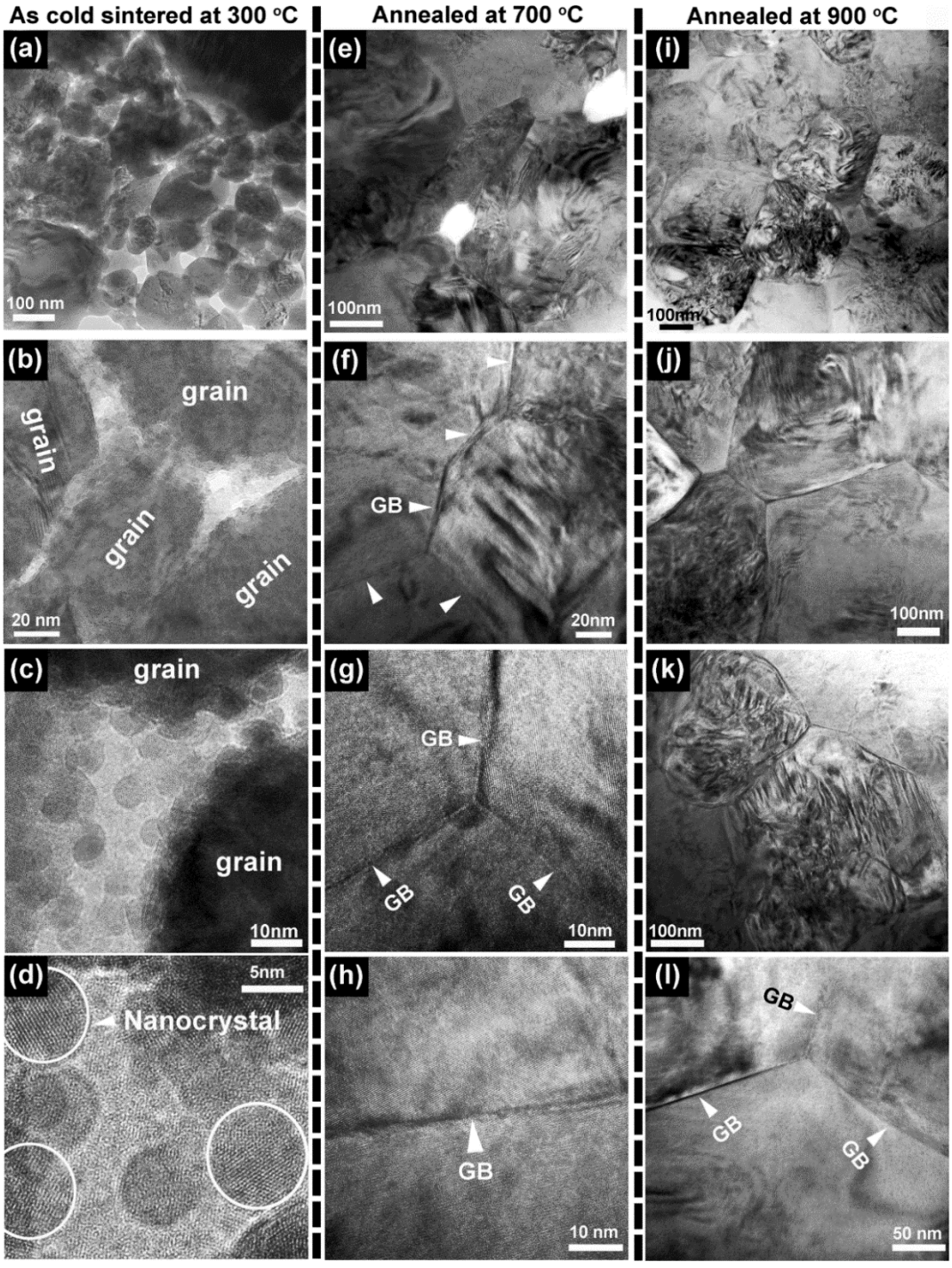

Figure 3-8: Representative TEM bright-field micrographs of the microstructural evolution of PZT ceramics after (a)-(d) cold sintering at 300 °C, (e)-(h) annealing at 700 °C, and (i)-(l) annealing at 900 °C. Images with different magnifications are shown for each case to demonstrate the overall configuration and the local characteristics around grain boundaries. Grain boundaries (GB) have been marked by the bright triangles.

In Figure 3-9, the P-E loops and the permittivity-loss vs temperature curves of the PZT samples processed at different conditions are compared. It is clear that the CSP PZT post-annealed at 900 °C for 3 hrs has well saturated P-E loops with a higher remanent polarization and lower coercive field than the PZT pressed without cold sintering with $Pb(NO_3)_2$ (Figure 3-9 (a)). Moreover, (Figure 3-9 (c)), the dielectric permittivity of the 900 °C annealed CSP PZT is significantly higher than that of 900 °C annealed PZT without the cold sintering step (~ 1380 vs. ~ 650 at room temperature). This is most likely due to the pores in the conventionally processed PZT (Figure B-4) as it only has a geometric density ~ 75% after 900 °C annealing. The slightly higher dielectric loss in the CSP PZT annealed at 900 °C is likely to be a consequence of domain wall motion (the lower loss tangent at elevated temperatures suggests that the space charge contribution to the loss tangent is reduced in the cold sintered specimens).[79]

The TEM data also suggests the possibility for reducing the maximum process temperature of bulk PZT based on the closed triple point junctions. It was hypothesized that post-annealing at 700°C for longer times may further improve the densification and yield better properties. Attempting to verify this hypothesis, a 24 hour post-annealing procedure was utilized. The sample had a similar P-E hysteresis loop as the 3-hour annealed sample when measured to maximum fields of 40 kV/cm (Figure 3-9 (a)). On increasing the maximum field to 60 kV/cm, the polarization hysteresis loop began to saturate, and showed a remanent polarization of 10 $\mu C/cm^2$ (Figure 3-9 (b)). Furthermore, the longer anneal at 700°C produced a higher relative density (~ 93%) and dielectric permittivity, as indicated by Figure 3-9 (c). In addition, the long-time annealed PZT had a lower dielectric loss when the sample was heated to > 350 °C, suggesting the reduction of excess PbO on increased annealing time.

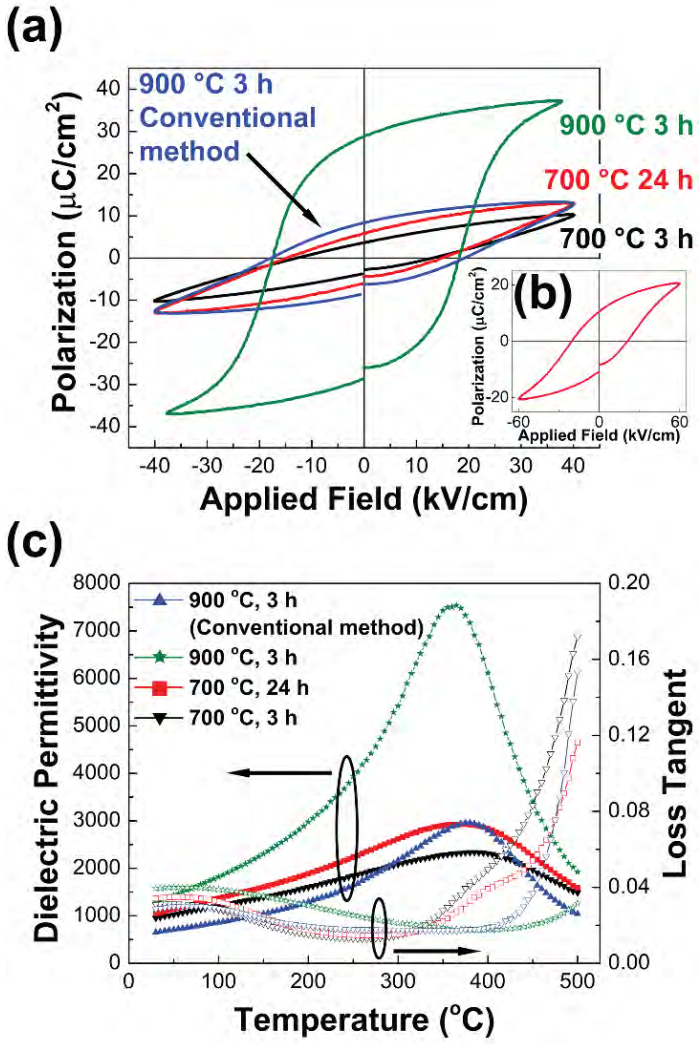

Figure 3-9: (a) The P-E hysteresis loops of PZT post-annealed at 700 °C for 3 h and 24 h, and at 900 °C for 3 h. The samples were measured under 10 Hz. (b) The P-E loop of 700 °C 24 h annealed PZT with higher maximum applied field (60 kV/cm) at 10 Hz. (c) The permittivity and loss of the post-annealed PZT at different temperatures under 100 kHz.

Figure 3-10 compares the microstructure of the cold sintered ceramics with different second step annealing times. The 700 °C 3 h annealed PZT has an average grain size of ~ 180 nm while the 700 °C 24 h annealed PZT has an average grain size of ~ 340 nm. In addition, the crystals in the 24-hour annealed sample have polyhedral shapes, which indicates the final sintering stage.

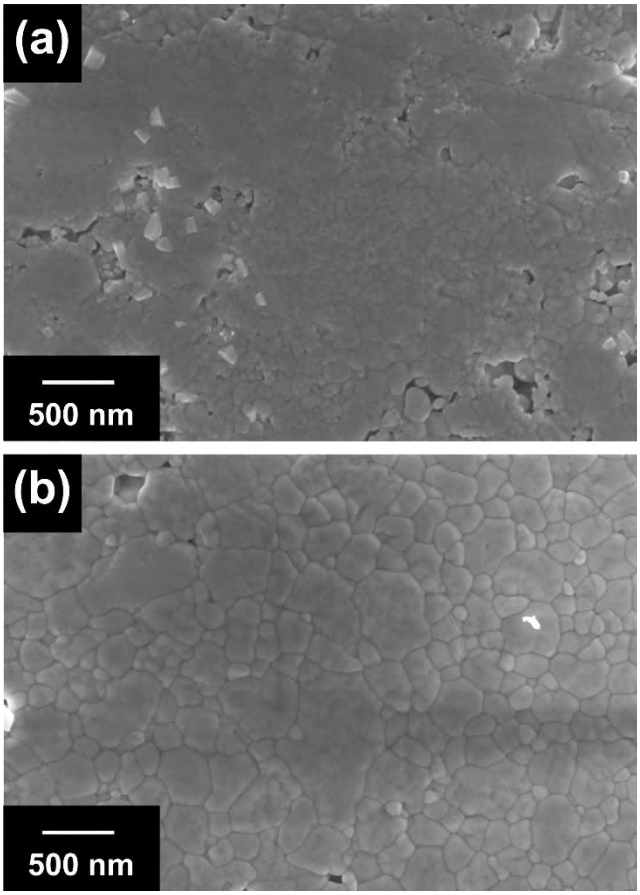

Figure 3-10: Cross-section FESEM images of (a) cold sintered PZT ceramic annealed at 700 °C for 3 hours. (b) Cold sintered PZT ceramic annealed at 700 °C for 24 hours, with nanograin structures.

The experiments on long-time annealing indicate that nanograined powders have a high surface energy that facilitates diffusion at lower temperatures. This helps further reduce the sintering temperature for PZT. Using the cold sintering procedure as a pre-treatment of the PZT powder, bulk PZT can possibly be sintered at temperatures as low as 700 °C. In the ceramic phase, since grain boundaries act as pinning points, the piezoelectric properties will be somewhat degraded by the fine grain size. Further work is needed to reduce the thickness of the cold sintered grain boundary layers to minimize the reduction in functional properties.

3.4.2 Unveiling the underlying physics during the CSP of PZT

With the early success on cold sintering PZT, understanding the effects of experimental parameters including lead nitrate volume fraction, temperature, pressure, holding time, and particle size distributions is of interest.

This study used the attrition-milled PZT-5A powder for which the size distributions are plotted in Figure 3-11 (a). The peaks above 3 μm probably reflected the soft agglomerates in the powder, which was further corroborated by the SEM in Figure 3-11 (b). Those soft agglomerates were believed to be eliminated by the high shear grinding procedure in a mortar and pestle prior to the cold sintering process.

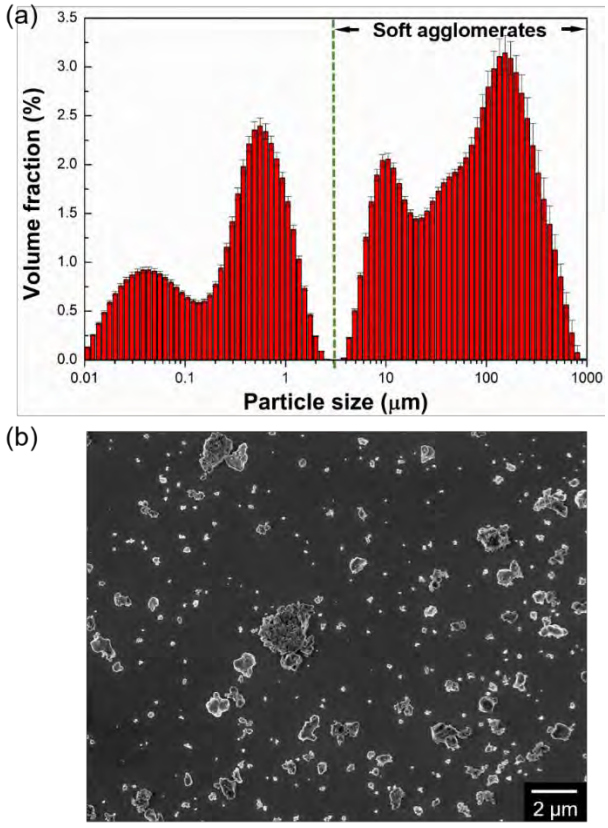

Figure 3-11: Figure 3-11 (a) The size distribution and (b) the SEM image of the attrition-milled PZT-5A powder.

Should the densification of PZT powder during the CSP be attributed to the lubrication of lead nitrate solution under pressure and temperature, the effect of the lead nitrate volume fraction in the system would be obvious. Because there is no dissolution of PZT in the transient liquid phase during the CSP, the as-cold sintered pellet can be considered to be a composite of PZT, $Pb(NO_3)_2$ and air (pores). For the purposes of the model, the possibility of partial decomposition of lead nitrate was ignored for simplicity; this should be a reasonable approximation because the weight loss from nitrogen oxide is much less than the remaining lead oxide. Therefore, one can easily estimate that the lead nitrate serves to: densify the PZT at low volume fraction while "diluting" the PZT at high volume fraction. Experimentally, this trend can be described in Figure 3-12.

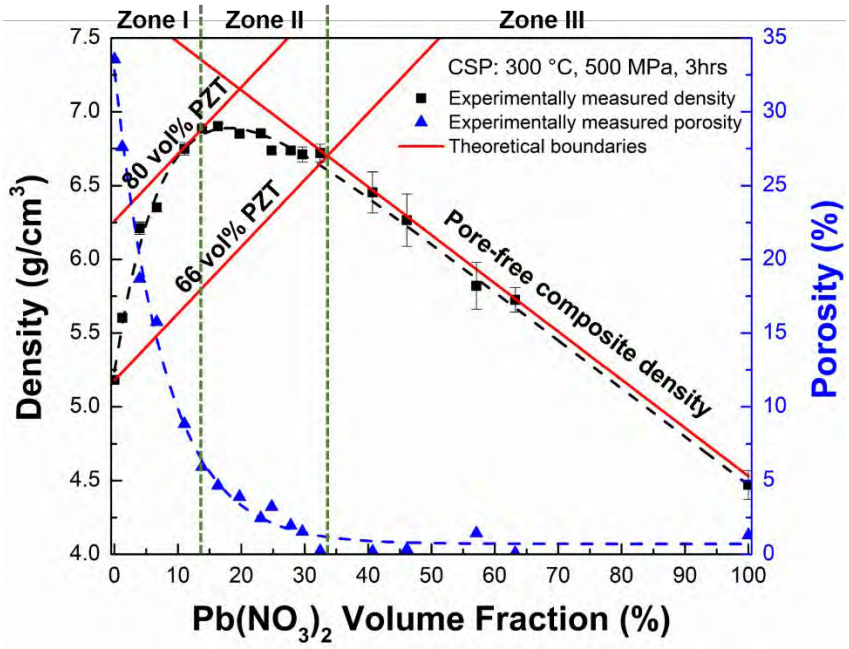

Figure 3-12: The density (black) and porosity (blue) evolutions of PZT/$Pb(NO_3)_2$ with respect to $Pb(NO_3)_2$ volume fraction. The chart was divided into 3 zones based on the densification of PZT and the reduction of porosity. The red lines represent the theoretical density boundaries.

Figure 3-12 were constructed using ρ_{PZT} = 7.80 g/cm^3, $\rho_{Pb(NO3)2}$ = 4.53 g/cm^3, ρ_{total} from the geometrical measurements, and the calculated $\rho_{theoretical}$ based on the composite composition. The porosity curve is a function of the lead nitrate volume fractions as described by Eq. 3-6.

$$Porosity = V_{pore}^{relative} = 1 - \frac{\rho_{total}}{\rho_{theoretical}} = 1 - \frac{\rho_{total}}{\rho_{PZT}\cdot\frac{V_{PZT}^{relative}}{V_{PZT}^{relative}+V_{Pb(NO_3)_2}^{relative}} + \rho_{Pb(NO_3)_2}\cdot\frac{V_{Pb(NO_3)_2}^{relative}}{V_{PZT}^{relative}+V_{Pb(NO_3)_2}^{relative}}}$$

(Eq. 3-6)

where ρ_{total} is the real density of the pellet, and $V^{relative}$ is the volume fractions in the composite. From the same equation, a relationship between the PZT volume fraction and lead nitrate volume fraction can be acquired, assuming "$\frac{V_{PZT}^{relative}}{V_{Pb(NO_3)_2}^{relative}}$" are constant before and after the CSP.

A second relationship between PZT volume fraction ($V_{PZT}^{relative}$) and lead nitrate volume fraction ($V_{Pb(NO_3)_2}^{relative}$) was then given by the experimentally measured densities (Eq. 3-7), in which m is the mass.

$$\rho_{total} = \frac{m_{total}}{V_{total}} = \frac{m_{PZT}+m_{Pb(NO_3)_2}}{V_{PZT}+V_{Pb(NO_3)_2}+V_{pore}} = \frac{\rho_{PZT}V_{PZT}+\rho_{Pb(NO_3)_2}V_{Pb(NO_3)_2}}{V_{PZT}+V_{Pb(NO_3)_2}+V_{pore}} =$$

$$\frac{\rho_{PZT}V_{PZT}^{relative}+\rho_{Pb(NO_3)_2}V_{Pb(NO_3)_2}^{relative}}{V_{PZT}^{relative}+V_{Pb(NO_3)_2}^{relative}+V_{pore}^{relative}} \qquad \text{(Eq. 3-7)}$$

When all the known values as well as the calculated porosities were plugged into Eq. 3-7, the PZT volume fraction and the lead nitrate volume fraction could be calculated via solving a binary equation.

As can be seen from Figure 3-12, the densities of the pellets increase with $Pb(NO_3)_2$ content until the volume fraction of the lead nitrate reaches 16 vol%; this is accompanied by a rapid decrease of porosity. Then, pellet densities drop because the PZT particles are diluted by the lead nitrate. It should be noted that the PZT packing densities are slightly offset from the pellet densities. Because the pellet densities represent the composite densities of PZT and $Pb(NO_3)_2$, while the PZT packing densities only focus on the PZT volume fractions in the pellet. Although

the PZT powder shows improved relative packing densities from 66% to 80% when there is 0-14 vol% lead nitrate, more lead nitrate starts to reduce the PZT volume fraction in the composite while continuing filling the pores. As a result, when the lead nitrate volume fractions increases from 14 vol% to 34 vol%, the relative packing density of PZT drops from 80 vol% to 66 vol%. In summary, the contributions of lead nitrate to the cold sintered pellet can be briefly divided into 3 zones:

Zone I: $Pb(NO_3)_2$ lubricates and densifies PZT while helping fill the pores.

Zone II: $Pb(NO_3)_2$ keeps filling the pore but also starts to dilute PZT.

Zone III: $Pb(NO_3)_2$ finished filling most of the pores and only dilutes PZT.

Experimental data has shown the pellet densities rise with elevated cold sintering temperatures and/or cold sintering pressures. This is shown in Figure 3-13 (a) and (b). Here, a theoretical density of 7.32 g/cm^3 was used as a reference, corresponding to a composite of 85 vol% PZT and 15 vol% $Pb(NO_3)_2$.

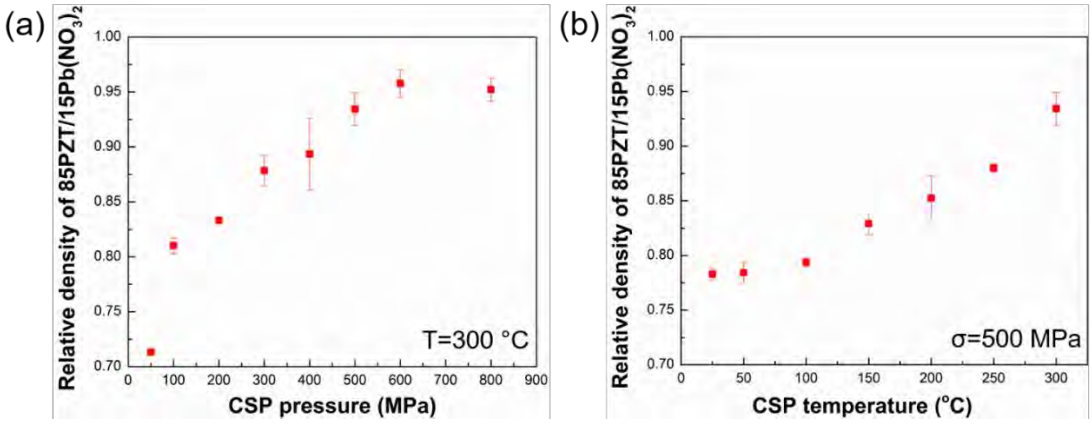

Figure 3-13: Relative densities of 85 vol% PZT and 15 vol% $Pb(NO_3)_2$ composite after cold sintering at (a) different uniaxial pressures (at 300 °C) and (b) different temperatures (pressed using 500 MPa). A theoretical density of 7.32 g/cm^3 was used as a reference.

The liquid phase sintering models used to describe cold sintering of ZnO are not applicable here due to the lack of a PZT dissolution-precipitation process. Therefore, a different

model that illustrates the contributions of temperature and pressure during the CSP of PZT is necessary. This was attempted by assuming that the lead nitrate experiences plastic deformation under uniaxial pressure. The resulting "pseudo viscous flow" is temperature dependent due to the thermal activation of the viscosity. Under this assumption, the widely used equation from Murray *et al*. [50] for viscous sintering can be adopted as a starting point.

The original equation developed by Murray *et al.* has the form:

$$\rho = 1 - e^{-\left(\frac{3\sigma}{4\eta}\right)t+c} \qquad \text{(Eq. 3-8)}$$

where ρ is relative density, σ is the applied uniaxial pressure in MPa, η is the viscosity of the material, t is the sintering time in minute, and c is a constant. This equation describes the relationship between relative density and pressure, but an explicit temperature term is missing. This can be rectified using Vogel-Fulcher-Tammann (VFT) [85] equation for the temperature dependence of the viscosity:

$$\eta = \eta_0 e^{\frac{b}{T-T_0}} \qquad \text{(Eq. 3-9)}$$

Here η is the viscosity, T is temperature in °C, b and T_0 are constants.

By plugging Eq. 3-9 into Eq. 3-8, Eq. 3-10 can be derived. This equation directly relates the relative density, temperature, pressure and time:

$$\rho = 1 - e^{-\left(\frac{3t}{4\eta_0}\right)\sigma e^{-b/(T-T_0)}+c} \qquad \text{(Eq. 3-10)}$$

With some re-arrangement, the following two forms occur:

$$ln(1-\rho) = -\left(\frac{3t}{4\eta_0}\right)e^{-b/(T-T_0)}\sigma + c \qquad \text{(Eq. 3-11)}$$

$$ln(-ln(1-\rho)+c) = ln\left(\frac{3t\sigma}{4\eta_0}\right) - \frac{b}{T-T_0} \qquad \text{(Eq. 3-12)}$$

Eq. 3-9 and Eq. 3-10 imply that there is a linear relationship between ln(1-ρ) and pressure, and a hyperbolic relationship between ln(-ln(1-ρ)+c) and temperature.

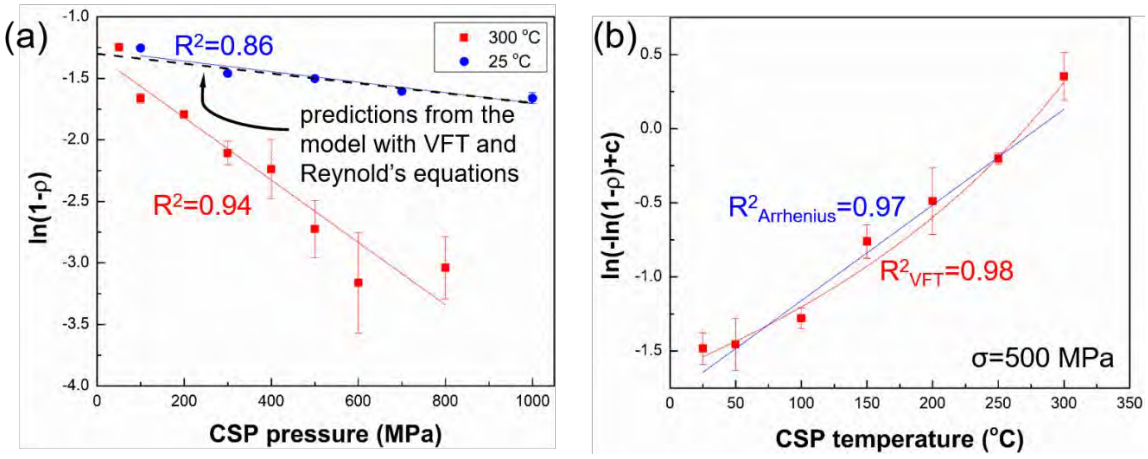

Figure **3-14**: The experimental data in Figure 3-13 is replotted in the forms of (a) Eq. 3-11 and (b) Eq. 3-12/Eq. 3-17, respectively. Relative densities vs. uniaxial pressures acquired at room temperature are shown by a blue curve in (a). The dashed lines in (a) represent the predictions from the model with VFT and Reynold's equations. (The slopes and intercepts of the predictions from VFT and Reynold-based models are too close to differentiate the two dashed lines in the figure.)

Fig. 3-14 (a) shows the experimental data plotted as for Equation 3-8. Fitting the 300 °C data in Figure 3-14 (a) gives Eq. 3-13:

$$ln(1-\rho)_{T=300\,^{\circ}C} = -0.00254 \pm 0.000313\sigma - 1.30 \pm 0.138 \qquad \text{(Eq. 3-13)}$$

Using c = -1.30 in Eq. 3-12, Figure 3-14 (b) can be plotted and Eq. 3-12 can be parameterized as Eq. 3-14:

$$ln(-ln(1-\rho)+c) = -4.21 \pm 1.79 - \frac{1790\pm1890}{T-696\pm274} \qquad \text{(Eq. 3-14)}$$

These fits give R^2 of 0.94 for the density-pressure relationship and 0.98 for the density-temperature relationship, suggesting the cold sintering of PZT can possibly be reasonably described as a viscous-sintering-related process.

Meanwhile, the fitting in Eq. 3-14 indicates large standard deviations for b and T_0. This is mostly likely because the curve shape from the VFT model is insensitive to b and T_0 changes in this temperature range. Thus, an alternative fitting strategy is to apply the Arrhenius relationship (Eq. 3-15), resulting in two linear relationships (Eq. 3-16 and Eq. 3-17):

$$\eta = \eta_0 e^{-b'T} \qquad \text{(Eq. 3-15)}$$

$$ln(1-\rho) = -\left(\frac{3t}{4\eta_0}\right) e^{b'T}\sigma + c \qquad \text{(Eq. 3-16)}$$

$$ln(-ln(1-\rho)+c) = ln\left(\frac{3t\sigma}{4\eta_0}\right) + b'T \qquad \text{(Eq. 3-17)}$$

Where b' is another constant.

Obviously, the fit for ln(1-ρ) - pressure plot is not affected by the Arrhenius/VFT model. The ln(-ln(1-ρ)+c) – temperature fit also resulted in a good R^2 (97%) with Eq. 3-18:

$$ln(-ln(1-\rho)+c) = -1.79 \pm 0.0936 + 0.00670 \pm 0.000440T \qquad \text{(Eq. 3-18)}$$

Moreover, this model may also be applied to predict and optimize cold sintering conditions. For example, from Eq. 3-13, by assuming constant t – η_o, b (b'), T_0 and c, the ln(1-ρ) – pressure relation can be predicted for 25 °C, giving the following equations by VFT model (Eq. 3-19) and Arrhenius model (Eq. 3-20):

$$ln(1-\rho)_{VFT,T=25\,^\circ C} = -0.000398\sigma - 1.30 \qquad \text{(Eq. 3-19)}$$

$$ln(1-\rho)_{Arrhenius,T=25\,^\circ C} = -0.000402\sigma - 1.30 \qquad \text{(Eq. 3-20)}$$

Likewise, from experimental data at 25 °C, Eq. 3-21 can be extrapolated from Figure 3-14 (a):

$$ln(1-\rho)_{T=25\,^\circ C} = -0.000415 \pm 0.0000834\sigma - 1.27 \pm 0.0506 \qquad \text{(Eq. 3-21)}$$

The similarity in slopes and intercepts of Eq. 3-19, Eq. 3-20, and Eq. 3-21 suggests that the model is capturing essential physics of the behavior.

In addition, according to Eq. 3-11, the sintering time should present a linear relationship with ln(1-ρ). This portion of the hypothesis, however, could not be proven experimentally at 300 °C. Figure 3-15 (a) depicts the pellet relative densities with respect to CSP time at 300 °C. The schematic temperature profile indicates the heating system requires ~17 min to reach 300 °C and ~20 min to cool to below 60 °C (a temperature low enough to unload the sample safely) while the porosity dropped to <10% during the heating and cooling procedures.

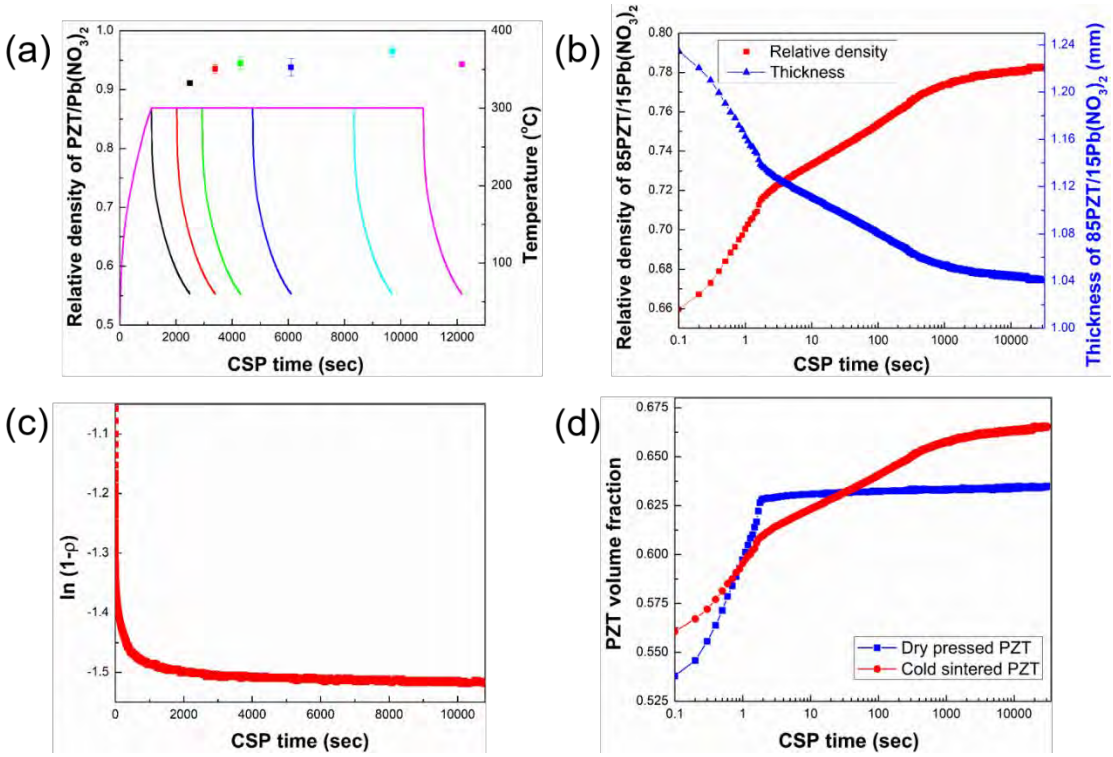

Figure **3-15**: (a) The relative densities of 85PZT/15Pb$(NO_3)_2$ after being cold sintered for different durations under 500 MPa at 300 °C with the temperature profiles shown as the colored lines. (b) The thickness shrinkage and the corresponding density evolution of a 25 °C cold sintered 85PZT/15Pb$(NO_3)_2$ part measured by dilatometry on the uniaxial press. (c) A replot of the density curve in (b) in the form of Eq. 3-11. (d) A comparison of the PZT volume fraction evolution in a cold sintered pellet and a dry pressed pellet.

To better characterize the effect of sintering time on the density of the pellet, cold sintering experiments were carried out at 25 °C. Using the dilatometer on the press, the thickness shrinkage of the sample, and the calculated relative density curve are shown in Figure 3-15 (b). The figure indicates that the densification behavior of the PZT/Pb$(NO_3)_2$ alters in the first 1000 sec (~16 min). The curve suggests that there are most likely 3 stages to the densification of the composite: The first stage happens in the initial two seconds, and is characterized by the rapid increase in relative density. This is probably caused by the rearrangement of PZT powder in the pressing die. This stage should happen regardless of the presence of lead nitrate but can only

achieve limited densification. The second stage occurs from ~3 – ~1000 sec, during which the densification of the composite slows down. It is speculated that this is related to a combination of viscous sintering and water evaporation. Specifically, the lead nitrate starts to deform under pressure and moisture, enabling the further optimization of PZT compaction; as the water escapes from the die, the re-precipitation of lead nitrate causes a shrinkage in volume. After 16 min of cold sintering at room temperature, the rearrangement of PZT becomes significantly retarded as the packing is close to its geometrical limit.

The $\ln(1-\rho)$ vs time curve was obtained by replotting Figure 3-15 (b) in the form of Eq. 3-11, and is shown in Figure 3-15 (c). It is obvious that the modified viscous sintering equation failed to describe, at least for the first 16 min, that $\ln(1-\rho)$ is linearly related to the cold sintering time at room temperature, presumably because the cold sintering process is complicated by the initial particle rearrangements and the water volatilization process. In stage 3 of the CSP (after 16 min), the curve presents a more linear shape and the fitting R^2 returns to 78%.

To test the hypothesis regarding stage 2, the dilatometry curves of a cold sintered sample and a dry pressed sample are shown in Figure 3-15 (d). Notice that the y axis has been replaced by PZT volume fraction to facilitate comparison between the two samples. It is clear that both systems experience the rapid loose packing in the first 2 sec. However, while the dry pressed sample displays almost no densification over the next couple of hours, the density of the cold sintered sample continues to increase, which corroborates the previous hypothesis that the moisturized lead nitrate can further optimize the packing of the particles. Interestingly, at the end of the first stage, the PZT volume fraction of the dry pressed sample is a little higher than the cold sintered sample. This is possibly because the addition of moisturized lead nitrate will hinder the rapid particle rearrangement by thickening the spacing between PZT particles, but this effect can be mitigated as the lead nitrate deforms in the following 16 min and eventually leads to a higher density.

3.5 Conclusions

PZT ceramics were cold sintered to >80% relative densities at 300 °C using bimodal PZT powder with moisturized $Pb(NO_3)_2$ as a sintering aid. The underlying mechanism of PZT densification during cold sintering is improved PZT particle packing induced by the plastic deformation of either moisturized lead nitrate or lead oxide. Therefore, a viscous sintering model can be utilized to explain the effects of temperature, pressure and time on the final pellet densities; the model showed good agreement with experimental results in terms of pressure and temperature, while the particle rearrangement at the initial stage of CSP deviates the behavior of densification with respect to time. Because there is no noticeable necking between PZT particles during cold sintering with lead nitrate, a post-annealing procedure at 900 °C for 3 hours, which is 300-400 °C lower than conventional methods, is needed to develop good ferroelectric properties. In addition, 700 °C annealing indicated promising densification for longer annealing times. The post-annealing step promotes densification improvement and equilibration of a nanosized grain structure; it produces ceramics with high relative permittivity, well-developed polarization switching with high remanent polarizations, and strong piezoelectric coefficients.

References

[1] Kishi, H.; Mizuno, Y.; Chazono, H. Base-Metal Electrode-Multilayer Ceramic Capacitors: Past, Present and Future Perspectives. Japanese J. Appl. Physics, Part 1 Reg. Pap. Short Notes Rev. Pap. 2003, 42 (1), 1–5.

[2] Levinson, L. M.; Philipp, H. R. Zinc Oxide Varistors — A Review. Am. Ceram. Soc. Bull. 1986, 65 (4), 639–647.

[3] Ohtaki, M. Recent Aspects of Oxide Thermoelectric Materials for Power Generation from Mid-to-High Temperature Heat Source. J. Ceram. Soc. Japan 2011, 119 (1395), 770–775.

[4] Kok, S. L.; White, N. M.; Harris, N. R. Free-Standing Thick-Film Piezoelectric Multimorph Cantilevers for Energy Harvesting. IEEE International Ultrasonics Symposium; IEEE, 2009, 1977–1980.

[5] Snaith, H. J. Present Status and Future Prospects of Perovskite Photovoltaics. Nat. Mater. 2018, 17 (5), 372–376.

[6] Padhi, A. K.; Nanjundaswamy, K. S.; Goodenough, J. B. Phospho-Olivines as Positive-Electrode Materials for Rechargeable Lithium Batteries. J. Electrochem. Soc. 1997, 144 (4), 1188.

[7] Wang, Z.; Xue, Q.-T.; Chen, Y.-Q.; Shu, Y.; Tian, H.; Yang, Y.; Xie, D.; Luo, J.-W.; Ren, T.-L. A Flexible Ultrasound Transducer Array with Micro-Machined Bulk PZT. Sensors 2015, 15 (2), 2538–2547.

[8] Miyahara, Y.; Deschler, M.; Fujii, T.; Watanabe, S.; Bleuler, H. Non-Contact Atomic Force Microscope with a PZT Cantilever Used for Deflection Sensing, Direct Oscillation and Feedback Actuation. Appl. Surf. Sci. 2002, 188 (3–4), 450–455.

[9] Yeo, H. G.; Ma, X.; Rahn, C.; Trolier-McKinstry, S. Efficient Piezoelectric Energy Harvesters Utilizing (001) Textured Bimorph PZT Films on Flexible Metal Foils. Adv. Funct. Mater. 2016, 26 (32), 5940–5946.

[10] Cho, S. H.; Biggers, J. V. Characterization and Sintering of Lead Zirconate-Titanate Powders. J. Am. Ceram. Soc. 1983, 66 (10), 743–746.

[11] Haertling, G. H. Grain Growth and Densification of Hot-Pressed Lead Zirconate-Lead Titanate Ceramics Containing Bismuth. J. Am. Ceram. Soc. 1966, 49 (3), 113–118.

[12] Randall, C. A.; Kim, N.; Kucera, J.-P.; Cao, W.; Shrout, T. R. Intrinsic and Extrinsic Size Effects in Fine-Grained Morphotropic-Phase-Boundary Lead Zirconate Titanate Ceramics. J. Am. Ceram. Soc. 2005, 81 (3), 677–688.

[13] Atkin, R. B.; Fulrath, R. M. Point Defects and Sintering of Lead Zirconate-Titanate. J. Am. Ceram. Soc. 1971, 54 (5), 265–270.

[14] Hayashi, T.; Inoue, T.; Nagashima, Y.; Tomizawa, J.; Akiyama, Y. Low-Temperature Sintering of PZT with $LiBiO_2$ as a Sintering Aid. Ferroelectrics 2001, 258 (1), 53–60.

[15] Hayashi, T.; Inoue, T.; Akiyama, Y. Low Temperature Sintering of PZT Powders Coated with $Pb_5Ge_3O_{11}$ by Sol–Gel Method. J. Eur. Ceram. Soc. 1999, 19 (6–7), 999–1002.

[16] Sharma, P. K.; Ounaies, Z.; Varadan, V. V; Varadan, V. K. Dielectric and Piezoelectric Properties of Microwave Sintered PZT. Smart Mater. Struct. 2001, 10 (5), 878–883.

[17] Wu, Y. J.; Li, J.; Kimura, R.; Uekawa, N.; Kakegawa, K. Effects of Preparation Conditions on the Structural and Optical Properties of Spark Plasma-Sintered PLZT (8/65/35) Ceramics. J. Am. Ceram. Soc. 2005, 88 (12), 3327–3331.

[18] Bansal, N. P.; Boccaccini, A. R. Eds. Ceramics and Composites Processing Methods; John Wiley & Sons, Inc.: Hoboken, NJ, USA, 2012.

[19] Bordia, R. K.; Kang, S. J. L.; Olevsky, E. A. Current Understanding and Future Research Directions at the Onset of the next Century of Sintering Science and Technology. J. Am. Ceram. Soc. 2017, 100 (6), 2314–2352.

[20] Rahaman, M. N. Ceramic Processing and Sintering, 2nd ed.; CRC Press: New York, NY, 2003.

[21] Houabes, M.; Bernik, S.; Talhi, C.; Bui, A. The Effect of Aluminium Oxide on the Residual Voltage of ZnO Varistors. Ceram. Int. 2005, 31 (6), 783–789.

[22] Gibson, I. R.; Dransfield, G. P.; Irvine, J. T. S. Sinterability of Commercial 8 Mol% Yttria-Stabilized Zirconia Powders and the Effect of Sintered Density on the Ionic Conductivity. J. Mater. Sci. 1998, 33 (17), 4297–4305.

[23] Lu, W.; Quilitz, M.; Schmidt, H. Nanoscaled $BaTiO_3$ Powders with a Large Surface Area Synthesized by Precipitation from Aqueous Solutions: Preparation, Characterization and Sintering. J. Eur. Ceram. Soc. 2007, 27 (10), 3149–3159.

[24] Coble, R. L. Sintering Crystalline Solids. I. Intermediate and Final State Diffusion Models. J. Appl. Phys. 1961, 32 (5), 787–792.

[25] Rojac, T.; Bencan, A.; Malic, B.; Tutuncu, G.; Jones, J. L.; Daniels, J. E.; Damjanovic, D. $BiFeO_3$ Ceramics: Processing, Electrical, and Electromechanical Properties. J. Am. Ceram. Soc. 2014, 97 (7), 1993–2011.

[26] Gubernat, A.; Rutkowski, P.; Grabowski, G.; Zientara, D. Hot Pressing of Tungsten Carbide with and without Sintering Additives. Int. J. Refract. Met. Hard Mater. 2014, 43, 193–199.

[27] Ekström, T.; Käll, P. O.; Nygren, M.; Olsson, P. O. Dense Single-Phase β-Sialon Ceramics by Glass-Encapsulated Hot Isostatic Pressing. Journal of Materials Science. 1989, pp 1853–1861.

[28] Kwon, O. H.; Messing, G. L. A Theoretical Analysis of Solution-Precipitation Controlled Densification during Liquid Phase Sintering. Acta Metall. Mater. 1991, 39 (9), 2059–2068.

[29] Carter, C. B.; Norton, M. G. Ceramic Materials: Science and Engineering, 2nd ed.; Springer New York: New York, NY, 2013.

[30] Sutorik, A. C.; Gilde, G.; Cooper, C.; Wright, J.; Hilton, C. The Effect of Varied Amounts of LiF Sintering Aid on the Transparency of Alumina Rich Spinel Ceramic with the Composition $MgO{\cdot}1.5\ Al_2O_3$. J. Am. Ceram. Soc. 2012, 95 (6), 1807–1810.

[31] Suprapedi; Sardjono, P.; Muljadi; Rusnaeni, N.; Humaidi, S. Effect of Additive Na_2O on Sintering Temperature, Crystal Structure and Magnetic Properties of $BaFe_{12}O_{19}$ Magnet. J. Phys. Conf. Ser. 2017, 817 (1), 012056.

[32] Xia, W. S.; Li, L. X.; Zhang, P.; Ning, P. F. Effects of CaF_2 Addition on Sintering Behavior and Microwave Dielectric Properties of $ZnTa_2O_6$ Ceramics. Mater. Lett. 2011, 65 (21–22), 3317–3319.

[33] Hagiwara, M.; Fujihara, S. Effects of CuO Addition on Electrical Properties of $0.6BiFeO_3$-$0.4(Bi_{0.5}K_{0.5})TiO_3$ Lead-Free Piezoelectric Ceramics. J. Am. Ceram. Soc. 2015, 98 (2), 469–475.

[34] Yuksel, B.; Ozkan, T. O. Grain Growth Kinetics for B_2O_3-Doped ZnO Ceramics. Mater. Sci. 2015, 33 (2), 220–229.

[35] Corker, D. L.; Whatmore, R. W.; Ringgaard, E.; Wolny, W. W. Liquid-Phase Sintering of PZT Ceramics. J. Eur. Ceram. Soc. 2000, 20 (12), 2039–2045.

[36] Wu, J.; Chang, Y.; Yang, B.; Wang, X.; Zhang, S.; Sun, Y.; Qi, X.; Wang, J.; Cao, W. Densification Behavior and Electrical Properties of CuO-Doped $Pb(In_{1/2}Nb_{1/2})O_3$-$Pb(Mg_{1/3}Nb_{2/3})O_3$-$PbTiO_3$ Ternary Ceramics. Ceram. Int. 2016, 42 (6), 7223–7229.

[37] Medesi, A.; Greiner, T.; Benkler, M.; Megnin, C.; Hanemann, T. Low Temperature Sintering of PZT. J. Phys. Conf. Ser. 2014, 557, 012132.

[38] Kingon, A. I.; Clark, J. B. Sintering of PZT Ceramics: II, Effect of PbO Content on Densification Kinetics. J. Am. Ceram. Soc. 1982, 66 (4), 256–260.

[39] Varshneya, A.; Mauro, J. Fundamentals of Inorganic Glasses, 3rd ed.; Academic Press: London, UK, 2019.

[40] Agrawal, D. Microwave Sintering of Ceramics, Composites and Metallic Materials, and Melting of Glasses. Trans. Indian Ceram. Soc. 2006, 65 (3), 129–144.

[41] Grasso, S.; Poetschke, J.; Richter, V.; Maizza, G.; Sakka, Y.; Reece, M. J. Low-Temperature Spark Plasma Sintering of Pure Nano WC Powder. J. Am. Ceram. Soc. 2013, 96 (6), 1702–1705.

[42] Cheng, J.; Agrawal, D.; Roy, R.; Jayan, P. S. Continuous Microwave Sintering of Alumina Abrasive Grits. J. Mater. Process. Technol. 2000, 108 (1), 26–29.

[43] Biesuz, M.; Sglavo, V. M. Flash Sintering of Ceramics. J. Eur. Ceram. Soc. 2019, 39 (2–3), 115–143.

[44] Vaidhyanathan, B.; Singh, A. P.; Agrawal, D. K.; Shrout, T. R.; Roy, R.; Ganguly, S. Microwave Effects in Lead Zirconium Titanate Synthesis: Enhanced Kinetics and Changed Mechanisms. J. Am. Ceram. Soc. 2004, 84 (6), 1197–1202.

[45] Dargatz, B.; Gonzalez-Julian, J.; Guillon, O. Effect of Electric Field and Atmosphere on the Processing of Nanocrystalline ZnO. Proc. of SPIE. 2014, 89871H, 1-8.

[46] Kahari, H.; Teirikangas, M.; Juuti, J.; Jantunen, H. Dielectric Properties of Lithium Molybdate Ceramic Fabricated at Room Temperature. J. Am. Ceram. Soc. 2014, 97 (11), 3378–3379.

[47] Guo, H.; Baker, A.; Guo, J.; Randall, C. A. Cold Sintering Process: A Novel Technique for Low-Temperature Ceramic Processing of Ferroelectrics. J. Am. Ceram. Soc. 2016, 99 (11), 3489–3507.

[48] Funahashi, S.; Guo, J.; Guo, H.; Wang, K.; Baker, A. L.; Shiratsuyu, K.; Randall, C. A. Demonstration of the Cold Sintering Process Study for the Densification and Grain Growth of ZnO Ceramics. J. Am. Ceram. Soc. 2017, 100 (2), 546–553.

[49] Guo, J.; Guo, H.; Baker, A. L.; Lanagan, M. T.; Kupp, E. R.; Messing, G. L.; Randall, C. A. Cold Sintering: A Paradigm Shift for Processing and Integration of Ceramics. Angew. Chemie - Int. Ed. 2016, 55 (38), 11457–11461.

[50] Murray, P.; Rodgers, E. P.; Williams, A. E. Practical and Theoretical Aspects of Hot Pressing of Refractory Oxides. Trans. Br. Ceram. Soc. 1954, 53 (8), 474–510.

[51] Gutmanas, E. Y.; Lawley, A. Cold Sinteirng - A New Powder Consolidation Process. Prog. Powder Metall. 1983, 39, 1–15.

[52] Roy, D. M.; Gouda, G. R.; Bobrowsky, A. Very High Strength Cement Pastes Prepared by Hot Pressing and Other High Pressure Techniques. Cem. Concr. Res. 1972, 2 (3), 349–366.

[53] Yamasaki, N.; Yanagisawa, K.; Nishioka, M.; Kanahara, S. A Hydrothermal Hot-Pressing Method: Apparatus and Application. J. Mater. Sci. Lett. 1986, 5, 355–356.

[54] Guo, H.; Bayer, T. J. M.; Guo, J.; Baker, A.; Randall, C. A. Cold Sintering Process for 8 Mol%Y_2O_3-Stabilized ZrO_2 Ceramics. J. Eur. Ceram. Soc. 2017, 37 (5), 2303–2308.

[55] Wang, D.; Guo, H.; Morandi, C. S.; Randall, C. A.; Trolier-McKinstry, S. Cold Sintering and Electrical Characterization of Lead Zirconate Titanate Piezoelectric Ceramics. APL Mater. 2018, 6 (1), 016101.

[56] Liu, J. A.; Li, C. H.; Shan, J. J.; Wu, J. M.; Gui, R. F.; Shi, Y. S. Preparation of High-Density $InGaZnO_4$ Target by the Assistance of Cold Sintering. Mater. Sci. Semicond. Process. 2018, 84, 17–23.

[57] Huang, H. Q.; Tang, J.; Liu, J. Preparation of $Na_{0.5}Bi_{0.5}TiO_3$ Ceramics by Hydrothermal-Assisted Cold Sintering. Ceram. Int. 2019, 45 (6), 6753–6758.

[58] Ma, J.; Li, H.; Wang, H.; Lin, C.; Wu, X.; Lin, T.; Zheng, X.; Yu, X. Composition, Microstructure and Electrical Properties of $K_{0.5}Na_{0.5}NbO_3$ Ceramics Fabricated by Cold Sintering Assisted Sintering. J. Eur. Ceram. Soc. 2019, 39 (4), 986–993.

[59] Lee, W.; Lyon, C. K.; Seo, J. H.; Lopez-Hallman, R.; Leng, Y.; Wang, C. Y.; Hickner, M. A.; Randall, C. A.; Gomez, E. D. Ceramic–Salt Composite Electrolytes from Cold Sintering. Adv. Funct. Mater. 2019, 29 (20), 1–8.

[60] Hong, W. Bin; Li, L.; Cao, M.; Chen, X. M. Plastic Deformation and Effects of Water in Room-Temperature Cold Sintering of NaCl Microwave Dielectric Ceramics. J. Am. Ceram. Soc. 2018, 101 (9), 4038–4043.

[61] Seo, J. H.; Guo, J.; Guo, H.; Verlinde, K.; Heidary, D. S. B.; Rajagopalan, R.; Randall, C. A. Cold Sintering of a Li-Ion Cathode: $LiFePO_4$-Composite with High Volumetric Capacity. Ceram. Int. 2017, 43 (17), 15370–15374.

[62] Pereira da Silva, J. G.; Bram, M.; Laptev, A. M.; Gonzalez-Julian, J.; Ma, Q.; Tietz, F.; Guillon, O. Sintering of a Sodium-Based NASICON Electrolyte: A Comparative Study between Cold, Field Assisted and Conventional Sintering Methods. J. Eur. Ceram. Soc. 2019, 39 (8), 2697–2702.

[63] Zhao, X.; Guo, J.; Wang, K.; Herisson De Beauvoir, T.; Li, B.; Randall, C. A. Introducing a ZnO–PTFE (Polymer) Nanocomposite Varistor via the Cold Sintering Process. Adv. Eng. Mater. 2018, 20 (7), 1–8.

[64] Zhao, Y.; Berbano, S. S.; Gao, L.; Wang, K.; Guo, J.; Tsuji, K.; Wang, J.; Randall, C. A. Cold-Sintered V_2O_5-PEDOT:PSS Nanocomposites for Negative Temperature Coefficient Materials. J. Eur. Ceram. Soc. 2019, 39 (4), 1257–1262.

[65] Guo, J.; Legum, B.; Anasori, B.; Wang, K.; Lelyukh, P.; Gogotsi, Y.; Randall, C. A. Cold Sintered Ceramic Nanocomposites of 2D MXene and Zinc Oxide. Adv. Mater. 2018, 30 (32), 1–6.

[66] Wang, D.; Zhou, D.; Zhang, S.; Vardaxoglou, Y.; Whittow, W. G.; Cadman, D.; Reaney, I. M. Cold-Sintered Temperature Stable $Na_{0.5}Bi_{0.5}MoO_4$ –Li_2MoO_4 Microwave Composite Ceramics. ACS Sustain. Chem. Eng. 2018, 6, 2438-2444.

[67] Faouri, S. S.; Mostaed, A.; Dean, J. S.; Wang, D.; Sinclair, D. C.; Zhang, S.; Whittow, W. G.; Vardaxoglou, Y.; Reaney, I. M. High Quality Factor Cold Sintered Li_2MoO_4 –$BaFe_{12}O_{19}$ Composites for Microwave Applications. Acta Mater. 2019, 166, 202–207.

[68] Kähäri, H.; Ramachandran, P.; Juuti, J.; Jantunen, H. Room-Temperature Densified Li_2MoO_4 Ceramic Patch Antenna and the Effect of Humidity. Int. J. Appl. Ceram. Technol. 2017, 14, 50–55.

[69] Wang, D.; Zhou, D.; Song, K.; Feteira, A.; Randall, C. A.; Reaney, I. M. Cold-Sintered C0G Multilayer Ceramic Capacitors. Adv. Elecron. Mat. 2019, 1900025, 1-5.

[70] Ma, J. P.; Chen, X. M.; Ouyang, W. Q.; Wang, J.; Li, H.; Fang, J. L. Microstructure, Dielectric, and Energy Storage Properties of $BaTiO_3$ Ceramics Prepared via Cold Sintering. Ceram. Int. 2018, 44 (4), 4436–4441.

[71] Nelo, M.; Siponkoski, T.; Kähäri, H.; Kordas, K.; Juuti, J.; Jantunen, H. Upside - down Composites: Fabricating Piezoceramics at Room Temperature. J. Eur. Ceram. Soc. 2019, 39 (11), 3301–3306.

[72] Li, L.; Hong, W. Bin; Yang, S.; Yan, H.; Chen, X. M. Effects of Water Content during Cold Sintering Process of NaCl Ceramics. J. Alloys Compd. 2019, 787, 352–357.

[73] Ndayishimiye, A.; Largeteau, A.; Mornet, S.; Duttine, M.; Dourges, M. A.; Denux, D.; Verdier, M.; Gouné, M.; Hérisson de Beauvoir, T.; Elissalde, C.; Goglio, G. Hydrothermal Sintering for Densification of Silica. Evidence for the Role of Water. J. Eur. Ceram. Soc. 2018, 38 (4), 1860–1870.

[74] Bouville, F.; Studart, A. R. Geologically-Inspired Strong Bulk Ceramics Made with Water at Room Temperature. Nat. Commun. 2017, 8, 14655.

[75] Induja, I. J.; Sebastian, M. T. Microwave Dielectric Properties of Mineral Sillimanite Obtained by Conventional and Cold Sintering Process. J. Eur. Ceram. Soc. 2017, 37 (5), 2143–2147.

[76] Guo, H.; Bayer, T. J. M.; Guo, J.; Baker, A.; Randall, C. A. Current Progress and Perspectives of Applying Cold Sintering Process to ZrO_2-Based Ceramics. Scr. Mater. 2017, 136, 141–148.

[77] Guo, H.; Guo, J.; Baker, A.; Randall, C. A. Hydrothermal-Assisted Cold Sintering Process: A New Guidance for Low-Temperature Ceramic Sintering. ACS Appl. Mater. Interfaces 2016, 8 (32), 20909–20915.

[78] Guo, H.; Baker, A.; Guo, J.; Randall, C. A. Protocol for Ultralow-Temperature Ceramic Sintering: An Integration of Nanotechnology and the Cold Sintering Process. ACS Nano 2016, 10 (11), 10606–10614.

[79] Damjanovic, D. Ferroelectric, Dielectric and Piezoelectric Properties of Ferroelectric Thin Films and Ceramics. Reports Prog. Phys. 1998, 61 (9), 1267–1324.

[80] Dutta, S. K.; Spriggs, R. M. Densification and Grain Growth in Hot-Pressed Zinc Oxide. Mater. Res. Bull. 1969, 4 (11), 797–806.

[81] Wolf, R. A.; Trolier-McKinstry, S. Temperature Dependence of the Piezoelectric Response in Lead Zirconate Titanate Films. J. Appl. Phys. 2004, 95 (3), 1397–1406.

[82] Budd, K. D.; Dey, S. Y.; Payne, D. A. Sol-Gel Processing of $PbTiO_3$, $PbZrO_3$, PZT, and PLZT Thin Films. Br. Ceram. Soc. Proc. 1985, 36, 107–121.

[83] ASTM E112-13. ASTM E112-13: Standard Test Methods for Determining Average Grain Size. ASTM Int. 2013, 1–28.

[84] Floyd, R.; Lowum, S.; Maria, J. P. Instrumentation for Automated and Quantitative Low Temperature Compaction and Sintering. Rev. Sci. Instrum. 2019, 90 (5).MISSING PAGE OR ARTICLE #

[85] Mauro, J. C.; Yue, Y.; Ellison, A. J.; Gupta, P. K.; Allan, D. C. Viscosity of Glass-Forming Liquids. Proc. Natl. Acad. Sci. 2009, 106 (47), 19780–19784.

Chapter 4

Cold Sintered Lead Zirconate Titanate Thick Films on Metal Foils for Piezoelectric Energy Harvesters

4.1 Introduction

The internet of things (IoT) is driving an evolution in which individual devices that seldom communicate with each other are being replaced by those driven by inter-device collaboration and information sharing. [1] Therefore, demands for sensors and actuators that collect and share data are growing. Powering these devices remains challenging due to the sheer number of devices; utilizing these devices in all-weather conditions or as body implants compounds these challenges. However, self-powered devices utilizing energy harvesters show promise and are gaining attention.

There are a number of ways to scavenge energy from the environment. Sunlight [2], wind [3], tide [4], and geothermal heat [5] energies have been employed for decades. These sources are suitable for infrastructure power supplies but have limited potential in implantable devices. However, piezoelectric electromechanical energy harvesters (PEH) have been utilized successfully in wearable and implanted devices that are small, low power, and isolated from the external environments [6,7].

In PEHs, cantilever structures have been widely adopted for low power wearable and implantable electronics;[8] in these devices, when the beams are strained, power can be generated using the piezoelectric as the transducer. As will be shown below, the output power depends on the materials figure of merit, the strain on the piezoelectric, and the volume of the piezoelectric. Most high $e_{31,f}$ piezoelectric thin films cannot be made thicker than 4 μm due to cracking [9] while

thinning bulk ceramics below about 50 microns requires sophisticated polishing processes. [10,11] Consequently, there is interest in developing new processing methods for preparing thick, high-quality piezoelectric films.

This chapter discusses use of the cold sintering process (CSP) and tape cast PZT layers for the fabrication of crack-free piezoelectric energy harvesters. Processing improvements that increase the yield and densification of the PZT tape are studied. In particular, the impact of different metals, as well as the use of dense foils vs. co-sintered powders, is discussed.

4.2 Literature review

In general, three mechanisms for electromechanical energy harvesting have been adopted: electrostatic (capacitive) mechanism, electromagnetic (inductive) mechanism, and piezoelectric mechanisms.

4.2.1 Electromagnetic (inductive) energy harvesters

Electromagnetic harvesters operate based on Faraday's law; that is, inductive currents appear when conducive wires experience a changing magnetic flux. The generated voltage can be calculated from equation 4-1.

$$V = -N\frac{d\Phi}{dt} = -N\frac{d(B\cdot A)}{dt} \qquad \text{(Eq. 4-1)}$$

where V is the open circuit voltage, N is the number of coils, Φ is the magnetic flux, B is the magnitude of magnetic field strength, A is the cross-sectional area of the wires exposed in the magnetic field, and t is time.

One advantage of electromagnetic harvesters is that they operate without an external voltage source. However, the need for magnets typically prevent miniaturization and complicates

compatibility with wafer scale MEMS processing. Several approaches to shrink coil dimensions via lithography or low-temperature co-fired ceramics (LTCC) technologies have been attempted, as shown in Figure 4-1 [12,13], however the resultant voltage and power output is limited: The harvester described in Figure 4-1 (a) by Williams *et al*. [12] operated under a magnetic field as large as 0.9 T but only presented a maximum open circuit voltage of 26 μV at 3.73 kHz. The LTCC coils [13] in Figure 4-1 (b) produced a power level of 0.26 mW/cm^3 at 35 Hz (with no reported acceleration). From Eq. 4-1, at constant acceleration, higher voltages result from an increased number of coils or a higher magnetic field. In practice, harvester dimensions limit the number of available coils and strong magnetic fields (>1 mT) pose potential threats to electronics like pacemakers [14].

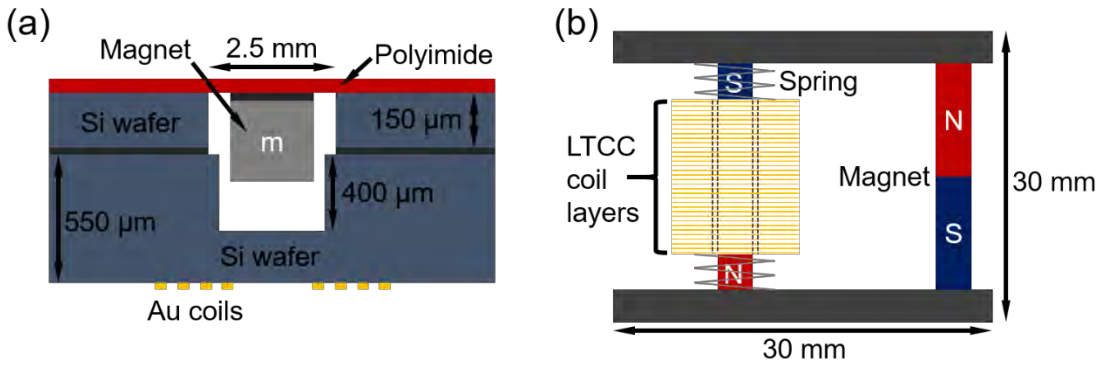

Figure **4-1**: (a) The electromagnetic energy harvester fabricated by wafer scale methods, proposed by Williams *et al*. [12] (b) A electromagnetic energy harvester designed by Scherrer *et al*. using LTCC techniques. [13]

4.2.2 Electrostatic (capacitive) energy harvesters

Capacitive energy harvesters scavenge mechanical energy through a change in capacitance. When a parallel plate capacitor is exposed to stress, such that the distance between

the top and bottom electrodes drops [15,16], a change is induced in either voltage or charge, as described in equation 4-2:

$$C = \frac{Q}{V} = \frac{\varepsilon_0 \varepsilon_r A}{t} \qquad \text{(Eq. 4-2)}$$

Here C is the capacitance, Q is charge, V is the voltage between the electrodes, ε_0 is the vacuum permittivity (=8.85*10^{-12}), ε_r is the relative permittivity, A is the electrode area, and t is the distance between the electrodes.

It can be seen from Equation 4-2 that varying either the thickness or area changes the capacitance. Therefore, 3 designs of electrostatic energy harvesters can be derived from these variables[15], as shown in Figure 4-2 (a)-(c). The in-plane overlap-varying type changes the capacitance by varying the electrode overlap area; the in-plane gap-closing type alters the distance between two electrodes; and the out-of-plane gap-closing type converts out-of-plane motion into capacitance differences. Notice that to maximize the area to volume ratio of a harvester, the electrodes in the in-plane types are normally made into a comb-like shape, which is equivalent to multiple capacitors in parallel connection. Out-of-plane gap-closing type harvesters avoid the comb structure.

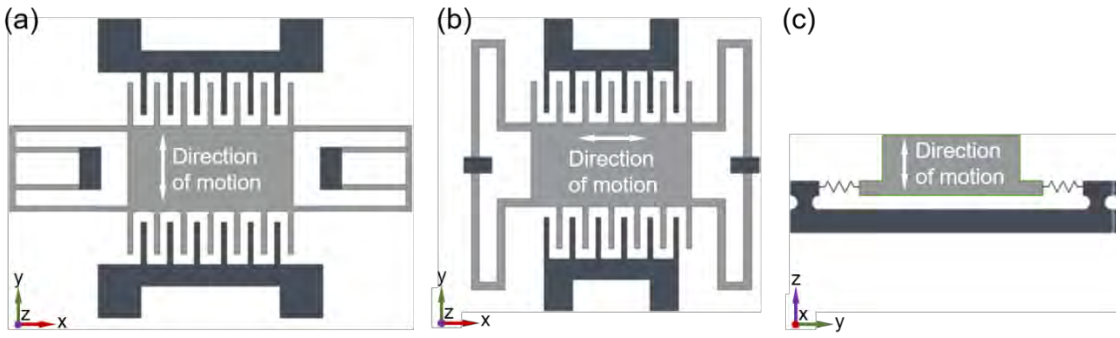

Figure **4-2**: Three different types of electrostatic energy harvesters including (a) in-plane overlap varying type, (b) in-plane gap-closing type, and (c) out-of-plane gap-closing type. (Figure from Beeby *et al*. [15])

Electrostatic harvesters are compatible with wafer scale processing; in-plane types can be easily integrated into the micro-electronics in cellphones, smart watches, implantable defibrillators, *etc*. In-plane harvesters are reliable as their mechanics are relatively simple, with no free-moving parts. However, an external voltage is required to initialize these devices, and as the capacitors can be lossy, this voltage source is frequently needed.

4.2.3 Piezoelectric energy harvesters (PEH)

Piezoelectric materials convert stress or strain directly to electricity. As shown in equation 4-3, the change in stress ($\Delta\sigma_{jk}$) is linearly related to a change in polarization (ΔP_i) through a piezoelectric coefficient (d_{ijk}):

$$\Delta P_i = d_{ijk} \cdot \Delta\sigma_{jk} = d_{in} \cdot \Delta\sigma_n \qquad \text{(Eq. 4-3)}$$

where i, j, and k ϵ {1, 2, 3}. Voigt notation reduces the order of this equation so that i ϵ {1, 2, 3} and n ϵ {1, 2, 3, 4, 5, 6}.

Like capacitive harvesters, the structures of PEH can be categorized by in-plane (31 mode) and out-of-plane modes (33 mode), corresponding to piezoelectric coefficients d_{31} and d_{33} respectively. The shear d_{15} mode can also be applied for energy harvesting. Schematics of the three different modes are shown in Figure 4-3, where 31 mode presents polarization in the z direction with compressive or tensile stress/strain in the x-y plane, while in 33 mode the z direction polarization is associated with compressive or tensile stress/strain in the z direction. Since most piezoelectric materials have larger d_{33} than d_{31}, [17] 33 mode PEHs normally show higher power densities, as indicated by Kim *et al*. [18] However, 31 mode PEHs have simpler structures that are readily integrated with wafer scale systems. Because $|d_{15}| > |d_{33}| > |d_{31}|$ in many materials, shear mode harvesters are in principle interesting; in practice mechanical design of the

harvesters is more challenging, and less amenable to fabrication with thin films. [19,20,21] As a result, shear mode harvesters will not be discussed further in this thesis.

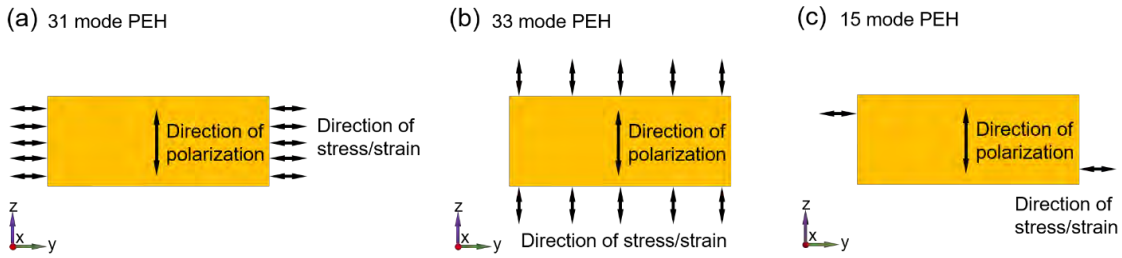

Figure **4-3**: The polarization and stress/strain directions in (a) a 31 mode PEH, (b) a 33 mode PEH, and (c) a 15 (shear) mode PEH.

In contrast with inductive and capacitive energy harvesters, piezoelectric energy harvesters don't require an external energy source or a built-in magnet. In principle, the space saved can be used to fit in more piezoelectric material in order to increase the power output. In some cases, PEHs designed for micro-electronic systems have shown outstanding potential. [6,18]

4.2.4 Device configurations for PEH performance enhancement

As a structure that obeys a mass-spring damper model, [15] there exists a range of resonance frequency (bandwidth) within which the PEH displacement and power output are maximized. Unfortunately, in reality the vibration sources typically adopt a wide distribution of frequencies, such that the PEH cannot always operate efficiently. One way to increase the bandwidth of the PEH is to employ nonlinear responses, as indicated in Figure 4-4 (a). [22] For example, by applying Duffing mode resonance, Hajati *et al*. invented a PEH with ultra-wide bandwidth that exceeds 20% of the center resonance frequency. [23] Their PEH utilizes PZT thin films that simultaneously stretch and bend during operation, as illustrated in Figure 4-4 (b). Because of the complexity in oscillation modes, it is difficult to calculate the acceleration.

Nevertheless, the PEH presented a power density of 2 W/cm^3, more than 2 orders of magnitude higher than the PEH reviewed in the work by Beeby *et al*., if we assume the Duffing harvester always operates on the most efficient branch of the curve in Figure 4-4 (a). [15] Additionally, bistable and tristable PEH have also demonstrated outstanding capabilities to scavenge ambient vibrations distributed over a wide frequency range. [24,25]

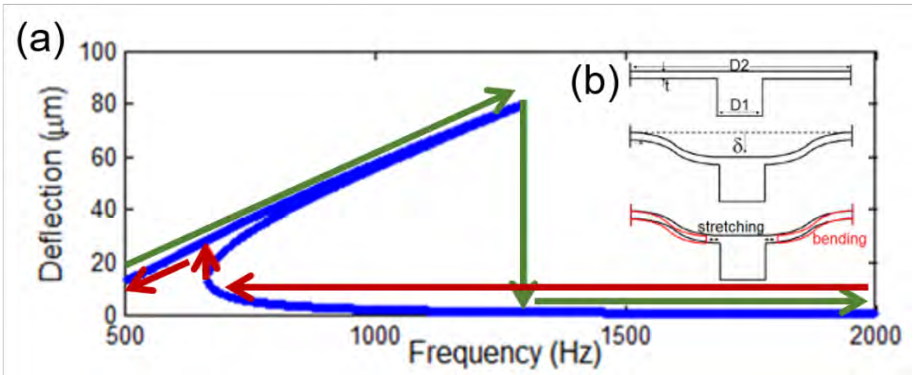

Figure **4-4**: (a) The theoretical deflection vs increasing (green arrows) and decreasing (red arrows) frequency of the Duffing PEH structure described in (b). (b) Schematic of a Duffing PEH experiencing stretching and bending motions. (c) Experimental setup for the bistable pendulum PEH. (Figure from Hajati *et al*. [23])

Increasing the magnitude of the strain also yields higher levels of harvested energy. However, it is important that this be done without inducing excessive strain concentrations. For example, Roundy *et al*. found that conventional rectangular-shaped cantilever harvesters experience stress accumulation near the clamping site. At high accelerations, this can cause crack initiation; [26] trapezoidal beams at least partially alleviate this issue. [26] Shown in Figure 4-5, Ma *et al*. designed a piezoelectric compliance mechanism (PCM) that improved strain uniformity in cantilevers, allowing PEHs to work under larger average stresses without exceeding cracking stresses near the cantilever root. [27] (001) textured bimorph PZT thin films on Ni foils using PCM designs demonstrated an outstanding power density ~3.9 mWcm^{-3}G^{-2}. [28]

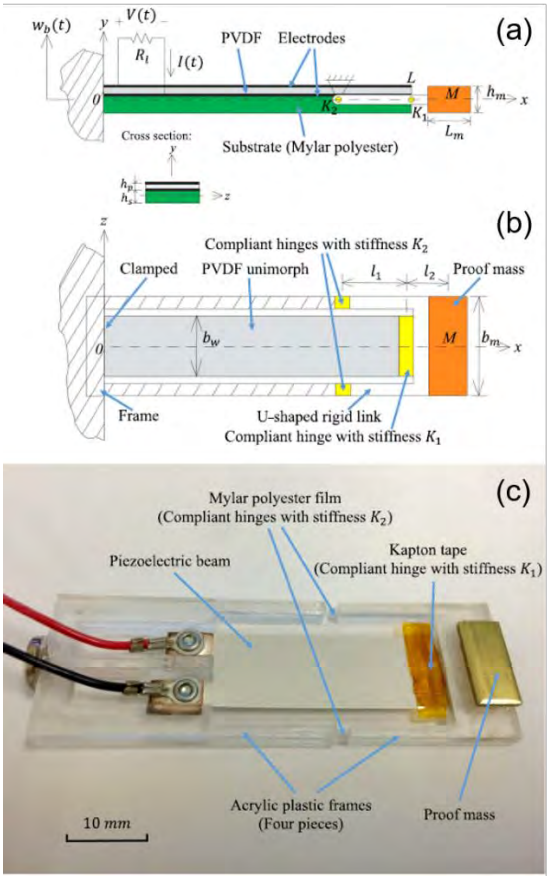

Figure **4-5**: (a) Side view, (b) top view and (c) a photograph of the PCM design proposed by Ma *et al*. [27]

4.2.5 Materials selection and processing for piezoelectric energy harvesters

Specifically for a 31 mode cantilever PEH, the two mostly used structures are shown in Figure 4-6. The power of the PEH can be calculated by the following equation: [29]

$$P_{rms} = \frac{\omega}{4}\left(\frac{e_{31,f}^2}{\varepsilon_0 \varepsilon_r}\right)(At)S^2 \qquad \text{(Eq. 4-4)}$$

where P_{rms} is the root mean square (RMS) power, ω is the angular velocity of the vibration, $e_{31,f}$ is the transverse piezoelectric constant, ε_0 is the vacuum permittivity, ε_r is the relative dielectric

constant of the piezoelectric layer, A and t are the active area/thickness of the piezoelectric materials, and S is the zero to peak strain level.

Because area and thickness are directly proportional to the power, bimorph construction is more commonly used so as to maximize the volume of the piezoelectrics. Also, within this equation, $(e_{31,f})^2/\varepsilon_r$ is material-related and independent of the device dimensions and vibration status. This parameter is the intrinsic figure of merit (FoM) for the piezoelectric layers.

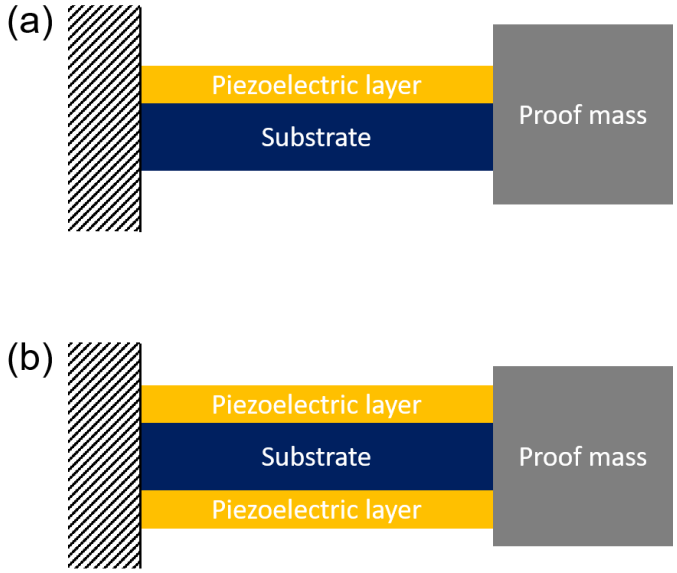

Figure **4-6**: The structures of (a) unimorph and (b) bimorph 31 mode PEH cantilevers.

A second important equation for PEH is the open circuit voltage [9]:

$$V_{OC} = \sigma_x g_{31,f} t \qquad \text{(Eq. 4-5)}$$

V_{OC} is the open-circuit voltage, σ_x is the in-plane stress, $g_{31,f}$ is the effective piezoelectric voltage constant, and t is the thickness of the piezoelectric layer.

The magnitude of open-circuit voltage is important because the output from a PEH needs to be rectified, and most rectifying circuitries require a threshold voltage to operate. [30] The voltages from thin film harvesters is often too low for rectification due to the small thickness, while the bulk piezoelectrics are often too large for easy recharging of batteries.

In summary, a good PEH should at least have two characteristics:

I. The piezoelectric materials should have a large FoM.

II. The thickness of the piezoelectrics is neither too large nor too small.

Guided by the above two rules of thumb, a review of material systems for PEH applications is presented.

4.2.5.1 Polymers

Piezoelectric polymers, such as polyvinylidene difluoride (PVDF) [31], polyurethane [32], and cellulose [33], have the potentials to harvest vibration energy. Among them, PVDF and its derivatives including polyvinylidene fluoride-trifluoro ethylene (PVDF-TrFE) [34] and polyvinylidene dluoride-co-hexafluoropropylene (PVDF-HFP) [35] are more extensively studied due to their superior piezoelectric charge coefficients (d_{33} and d_{31}). This type of materials is characterized by the low relative permittivity, normally below 20, [36] resulting in a large FoM. The same reason also produces high piezoelectric voltage coefficients (g_{33} and g_{31}). As a consequence, the open circuit voltages of the polymeric PEH are generally very high. [37] In addition, the outstanding flexibility has made piezoelectric polymers off the hook from mechanical failure and suitable for high strain rate harvesters.

However, a major drawback of polymer piezoelectrics is the low power density. Cao *et al*. reported a PVDF generator of power density ~1.94 $mWG^{-2}cm^{-3}$ under 100 Hz resonance frequency. [38] Through optimization of device configuration of PVDF PEH, Song *et al*. achieved a slightly higher power density of 3.44 $mWcm^{-3}G^{-2}$ at ~ 34 Hz. [37] This is because the resistivity of the polymer is large enough that the current generated in the PEH is quite limited.

4.2.5.2 Single crystals

According to Neumann's law [39], 21 of 32 point group symmetries have non-zero piezoelectric constants. According to Neumann's law. [39] One of the earliest known piezoelectric single crystals is quartz. For α-quartz, the two non-zero piezoelectric constants are d_{11}=2.29 pC/N and d_{14}=-0.680 pC/N, [40] both of which are too small for high power PEHs. Wurtzite ZnO single crystals have an e_{33} of ~0.96 C/m^2, an e_{31} of ~-0.62 C/m^2, and an e_{15} of ~-0.37 C/m^2. [41] Numerous ZnO nano-wires have been used in miniature PEHs; these often produce small average power levels due to the small volume of piezoelectric material. [42]

In recent years, the discovery of ferroelectric relaxor single crystals with high piezoelectric coefficients, such as (1-x)Pb($Mg_{1/3}Nb_{2/3}O_3$)-x$PbTiO_3$ (PMN-PT) [43], (1-x)Pb($Zn_{1/3}Nb_{2/3}O_3$)-x$PbTiO_3$ (PZN-PT) [44], and (1-x-y)Pb($In_{1/2}Nb_{1/2}$)O_3–xPb($Mg_{1/3}Nb_{2/3}$)O_3–y$PbTiO_3$ (PIN-PMN-PT) [45], has enabled the fabrication of high-power-density PEHs. For instance, Yang *et al*. reported a cantilever PEH using PZN-PT single crystals that produced a power density over 24 mWcm^{-3}G^{-2}, while a power density over 14 mWcm^{-3}G^{-2} was reported for device using PMN-PT single crystals. [46] Despite their outstanding piezoelectric coefficients, relaxor single crystals have large relative permittivities; as a result the materials FoM is not very high. Moreover, miniaturization of these materials without degrading the properties is difficult.

4.2.5.3 Ceramics

As piezoelectric ceramics are readily fabricated, they are widely utilized in PEHs. Most ceramic powders are sintered at 50%-75% of their melting temperatures, production costs are significantly smaller than single crystals of the same compositions. Not all piezoelectric ceramics can be made into energy harvesters. For example, polycrystalline quartz does not show

piezoelectricity, because the polarizations generated within the grains are randomized and will cancel each other. In contrast, ferroelectric materials present switchable spontaneous polarizations. After being poled, the spontaneous polarization can be re-aligned so that a net polarization develops, as illustrated in Figure 4-7. This net polarization grants the ceramics non-zero piezoelectric coefficients.

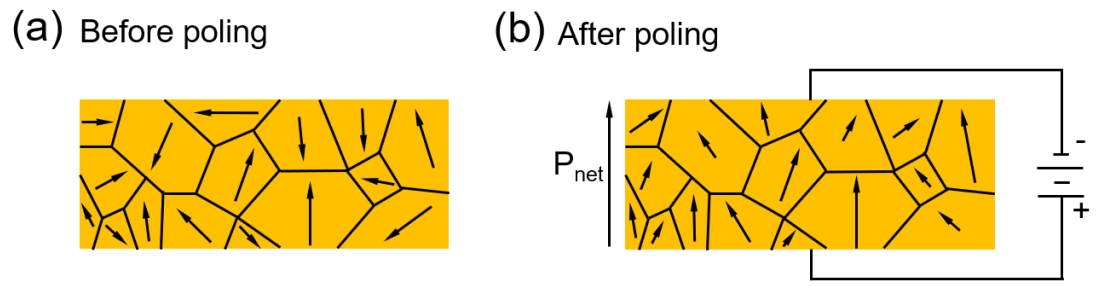

Figure **4-7**: The schematics of local polarization in ferroelectric ceramics (a) before poling and (b) after poling. The schematic is simplified such that only the net polarization direction of each grain is shown, rather than the polarization vectors of individual domains.

Table 4-1 compares d_{33} values between single crystals and ceramics of the same composition. Notice that ceramic piezoelectric coefficients depend on many factors; d_{33} values vary in the literature. [47] Ceramics generally show reduced piezoelectric coefficients relative to single crystals due to less efficient poling and a high concentration of pinning points for domain wall motion, including grain boundaries. Shkuratov *et al*. compared PEHs made with PIN-PMN-PT single crystal and PZT 52/48 ceramic, revealing a 4-fold difference in power density. [48]

Table **4-1**: Comparisons of piezoelectric coefficients (d_{33}) between single crystals and ceramics.

Materials	Single crystal d_{33} (pC/N)	Ceramic d_{33} (pC/N)
$Pb(Zr_{1-x}Ti_x)O_3$	1223 (along $[001]_c$) [49]	295 [48]
$(1-x-y)Pb(In_{1/2}Nb_{1/2})O_3–xPb(Mg_{1/3}Nb_{2/3})O_3–yPbTiO_3$	1800 (along $[111]_c$) [48]	416 [50]
$BaTiO_3$	500 (along $[001]_c$) [51]	416 [52]

Optimized PEH requires ceramics with high piezoelectric constants (d_{33} or $e_{31,f}$) and low relative permittivity, so that both the current and voltage can be high. While many ferroelectric ceramics have higher piezoelectric responses, their FoM may be much smaller than those with medium piezoelectric coefficients. For example, despite the modest piezoelectric coefficients (~3 C/m^2), Sc-doped AlN thin films have a high FoM ($(e_{31,f})^2/\varepsilon_r$) over 0.5 C^2/m^4 due to the low permittivity ~18. [53] One of the primary challenge on improving materials for energy harvesting applications is how to maximize the piezoelectric coefficients while suppressing the relative permittivity. Figure 4-8 demonstrates that in random ceramics, the d_{33} and relative permittivity are correlated. For in-plane piezoelectric coefficients-related FoM this trend still holds: The $(e_{31,f})^2/\varepsilon_r$ values for PZT-5A and PZT-5H are 0.064 and 0.081 C^2/m^4 respectively, although the $e_{31,f}$ of PZT-5H is ~2.5 times higher that of PZT-5A. Because the relative permittivity of PZT-5H is doubled. [54] Therefore, doping piezoelectric layers to alter the FoM does not always work.

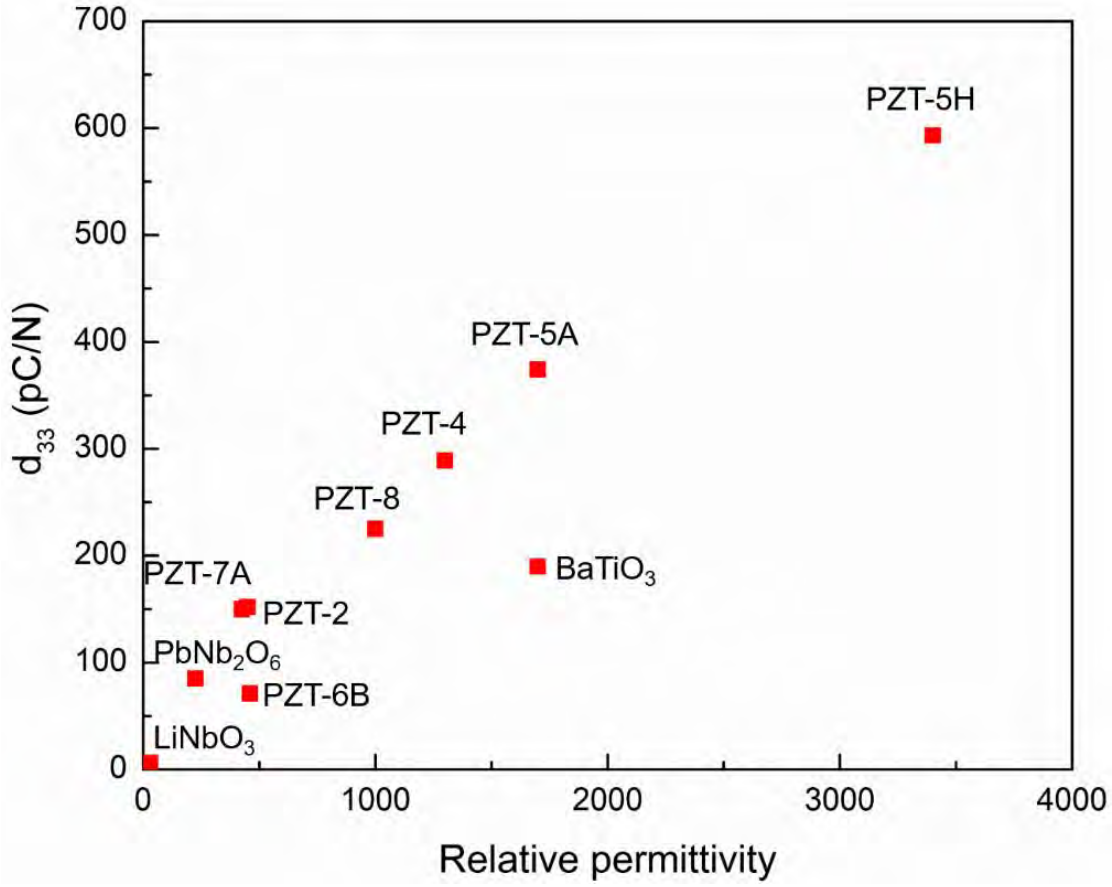

Figure **4-8**: A plot of d_{33} and relative permittivity of different piezoelectric ceramics, including different compositions of PZT ceramics, $BaTiO_3$, $PbNb_2O_6$, and $LiNbO_3$. Data from Zhang *et al*. [55]

Instead of composition, the preferred orientation of ceramics can be tuned for higher FoM. Sintering highly oriented ceramics by templated grain growth raises piezoelectric properties. [56] Chang *et al*. found when the orientations PIN-PMN-PT ceramics change from random to 90% (001)-oriented, the d_{33} almost doubled (from 416 pC/N to 824 pC/N) while the relative permittivity only increased a little (from 2356 to 2531). In the same way, oriented thin films boost the FoM for PEHs. For example, the $e_{31,f}$ of PZT 43/57 on $SrRuO_3$ increased from -4 C/m^2 to -15 C/m^2 as the volume fractions of {001} grains increased from 20 vol% to 100 vol%, while the relative permittivities dropped from 800 to 250. [57] By sputtering highly {100} oriented

Mn-doped PZT 52/48 on $LaNiO_3/HfO_2$/Ni substrate, Yeo *et al*. demonstrated c-domain PZT films stabilized by compressive stress; a cantilever structured PEH achieved a FoM ~0.36 C^2/m^4. [58]

Another prospect that ceramic scientists have to be confronted with is fabricating ceramic films between 5-50 μm thick. Bulk piezoelectric materials provide high voltage with low power densities due to low strain levels experienced as a consequence of the stiffness of the piezoelectric layers. A multilayer PZT stack harvester exhibited an 18.8 mW output power at 613 Hz at extremely high accelerations (over 340 G, 1 G = 9.8 m/s^2. This yielded a power density of only 0.1 $mWcm^{-3}G^{-2}$. [59] Polishing bulk PZT to mitigate the stiffness is simple yet wasteful. Yang *et al*. thinned PZT plates from 300 μm to 50 μm to gain more flexibility and found that the plates curved after polishing (shown in Figure 4-9 (a)). [60] The warped plates were made into a "gullwing"-structured PEH with an power density of 6.54 mW/cm^3 at 7.8 Hz. Notice that the power density does not involve an acceleration because the piezoelectric layers were excited via a rotating gear (Figure 4-9 (b)) and the applied force was unknown.

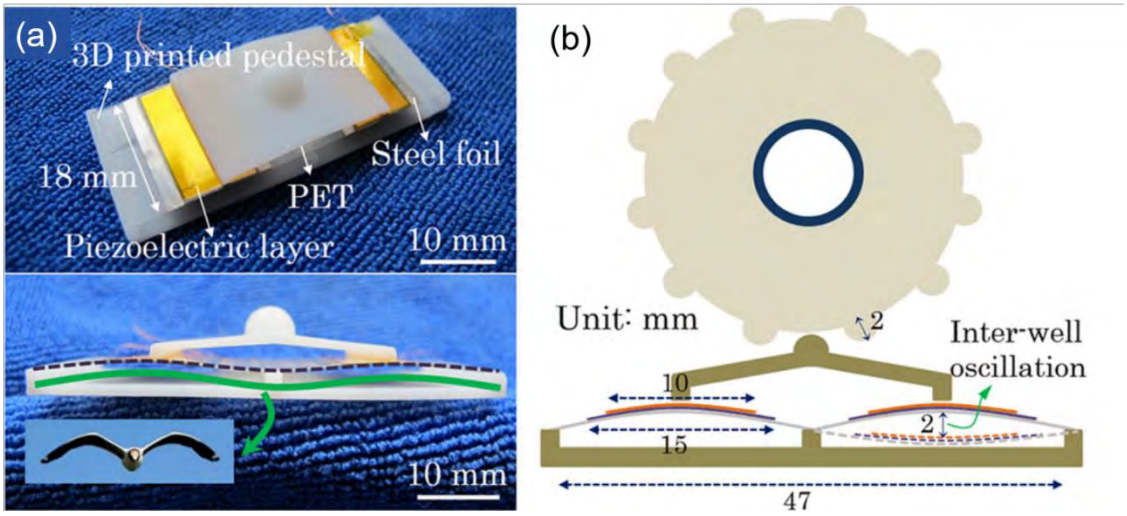

Figure **4-9**: (a) Photos of curved PZT plates attached to 3D printed PET frames. (b) The device configuration of "gullwing"-structured PEH excited by a rotating gear. Figure by Yang *et al*. [60]

Low temperature ceramic co-fire (LTCC) technologies enabled screen printing of PZT thick films on metal foils [61,62] but their electrical properties are typically not comparable with

bulk ceramics and sol-gel thin films, likely due to poor densification [63]. Fully sintered PZT and PMN-PT thick films from 10-100 μm were reported by Xu *et al*. [64] and Gentil *et al*. [65] via screen printing tapes on sapphire and sintering over 1100 °C. The films showed comparable performances as bulk samples, but have to be transferred to a different substrate for energy harvester applications. A sol infiltration process for the fabrication of PZT thick films has presented a relative permittivity exceeding 900 with d_{33} values above 300 pC/N when crystallized around 700 °C. [66–68] While relative densities exceeding 90% have been reported by this method, the residual porosity tends to yield low in-plane piezoelectric responses.

Thin film technologies, such as physical vapor deposition [69,70] and chemical solution deposition [71] have also been investigated to fabricate miniaturized PEHs. Benefitting from the reduced thickness, thin film harvesters can be excited under large strains without damaging the piezoelectric layers. However, if the thickness is too small, it becomes difficult to produce high enough voltages for easy rectification. Increasing the thicknesses of the piezoelectric thin films is not only time consuming, but also subject to mechanical failure. Yeo *et al*. observed micro-cracks emerging in sputtered thin film PZT above 5 μm in thickness (see Figure 4-10). [9] Bimorph [28] and multilayered [69] thin film PEHs have also been reported as means of achieving increased effective thicknesses, however their processing remains difficult. [72]

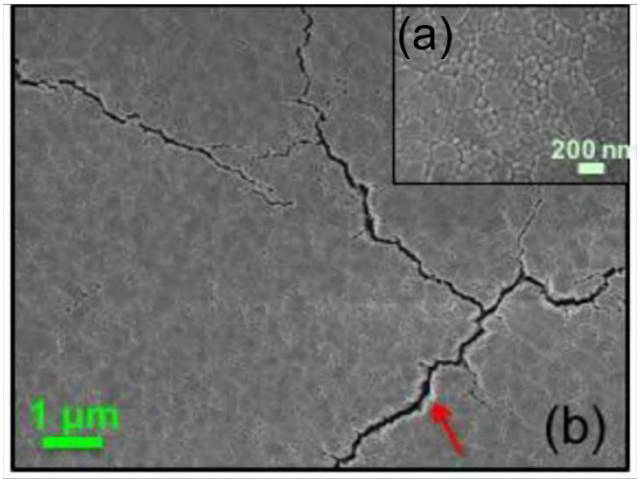

Figure **4-10**: SEM showing (a) the microstructure and (b) micro-cracks on 5.4 µm thick PZT thin films. Images from Yeo *et al*. [9]

One of the principle goals of this work is to improve the mechanical and electrical properties of the tape cast PZT thick films on metal substrates such that PEH can be further optimized. This was attempted by adoption of cold sintering approaches to break the typical thickness limitation imposed by standard film deposition methods, without sacrificing the film density. In particular, the hope was that by densifying the films at low temperatures, films would be less prone to mechanical failure due to thermal strains.

4.3 Experimental procedure

The fabrication of PZT/metal/PZT 2-2 composites, a common configuration for cantilever PEH, can be divided into 3 phases: the preparation of PZT and substrates, the sintering of PZT/metal/PZT composites, and the characterizations of sintered composites.

4.3.1 Preparation of PZT tape, metal foils and Cu tapes

The PZT powder used for this experiment is PZT-5A (PKI-509, Piezo Kinetics, Inc., Bellefonte, PA) with a medium particle size of ~500 nm. The size distribution and the milling procedures were described in the previous chapter. Before tape casting, 2 g PZT powder was mixed with 0.2 g $Pb(NO_3)_2$ (Sigma-Aldrich Corp., St. Louis, MO) and 1.5 mL deionized water in a mortar and pestle. The mixture was then dried in a box oven at 120 °C for 12 hours to remove humidity. The tape cast recipe included two vehicles: vehicle A was composed of 95 wt% methyl ethyl ketone (MEK, Alfa Aesar, Tewksbury, MA) and 5 wt% poly(propylene carbonate) (QPAC®-40, Empower Materials, Inc., New Castle, DE); vehicle B consisted of 65 wt% MEK, 28 wt% QPAC®-40, and 7 wt% butyl benzyl phthalate (Santicizer-160, Tape Casting Warehouse, Inc., Morrisville, PA). The dried PZT/$Pb(NO_3)_2$ powder was mixed with 1.38 g vehicle A, 1 g MEK, and 0.68 g vehicle B with 1 min mixing between each step (Thinky Mixer AR-250, Laguna Hills, CA). After de-foaming for 30 min, the slurry was tape cast on a Mylar sheet with a blade height of ~8 mil (~203 μm). The as-cast tape was then air dried at room temperature for 10 min to remove MEK; and the final thickness of the dried tape was ~20 μm.

This work also explored the use of Ni foils, Ag foils and Cu foils as substrates for the PZT films. Ni foils (25 μm, 99.99+%, Goodfellow Corporation, Coraopolis, PA) oxidize easily; if the oxygen partial pressure during firing is low enough to retain metallic Ni, Pb is reduced. $LaNiO_3/HfO_2$/Ni substrates were used to suppress the formation of NiO and reduce contact between Ni and PZT. Here HfO_2 was the passivation layer while $LaNiO_3$ (LNO) served as the bottom electrode. The processing details were similar to those described by Yeo *et al*. [71] except that 100 nm HfO_2 was deposited by atomic layer deposition at a rate of 0.93 Å/cycle. The silver foils (25 μm, 99.9%, Sigma-Aldrich Corp., St. Louis, MO) were cut and laminated with PZT

tape. 5 layers of PbO thin film were spun cast on the surface of the Cu foils (25 μm, 99.8%, Alfa Aesar, Tewksbury, MA), following procedures described by Coleman *et al*. [73]

In awareness of the constrained sintering issue of densifying PZT on metal foils, as an alternative to the use of dense metal foils, tape cast Cu powder layers were also explored. The tape casting procedures for Cu resembles that of the PZT tape: 6.70 g Cu (Shoei Chemical, Inc., Tokyo, Japan) were mixed with 5.5 g binder containing 20 vol% QPAC®-40 and 80 vol% propylene carbonate. 0.4 mL MEK was added to the slurries in order to adjust the viscosity before the slurries were homogenized in a mixer for 3 min. The mixtures were then tape cast on Mylar sheets followed by baking in an oven at 80 °C for 5 hours to remove the solvent. The thickness of the Cu tapes after drying was ~90 μm when the tapes were cast with a 13 mil doctor blade height.

4.3.2 Cold sintering and co-firing of PZT/metal/PZT 2-2 composites

The PZT tape was cut into circular pieces one half-inch in diameter (~12.7 mm) and were stacked in a PZT/metal/PZT sandwich structure, in which one layer of PZT tape was attached on each side of the metal substrate. Lamination was done in a half-inch-diameter circular pressing die at 50 MPa, 80 °C for 20 min [74]. The organics were then burnt out. For PZT on Ni or Ag foils, the burn out took place in a box furnace under ambient conditions with a ramping rate of 0.4 °C/min to 275 °C, a hold time of 180 min, and a cooling rate of 5 °C/min. For PZT on Cu tapes, a low pO_2 furnace with dry nitrogen, wet nitrogen and forming gas (0.1 vol% H_2 + 99.9 vol% N_2) flow ($pO_2 = 10^{-12}$ atm) was used. The temperature profile was the same as described above.

Following burn out, the samples were hung in a beaker half-filled with deionized water heated to 80 °C for 60 min. Water vapor condenses on the sample and re-moistens the lead nitrate; this is referred to as the “steaming” procedure. The stack was immediately cold sintered at

300 °C under 500 MPa uniaxial pressure for 180 min. Two pieces of 100 µm thick Kapton sheets were placed between the sample and die plunges to reduce the surface roughness of the PZT.

The cold sintered PZT on Ni or Ag foils were then post-sintered at 700-900 °C with a ramp rate of 5 °C/min and a holding time of 180 min in a box furnace, while the PZT on Cu was heat treated in a tube furnace with a $pO_2 = 10^{-12}$ atm to fully sinter the PZT and Cu while preventing oxidation of Cu.

A schematic of the process flow is given in Figure 4-11.

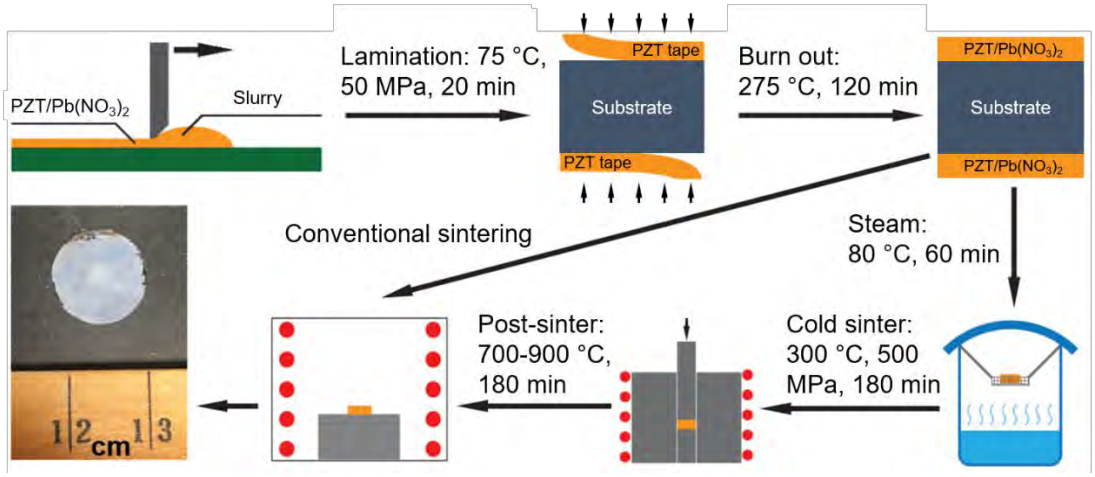

Figure **4-11**: Schematic flow chart for the fabrication of PZT/metal/PZT 2-2 composites. The photograph on the bottom left shows a PZT thick film on Ni foil after post-sintering.

4.3.3 Characterization of PZT/metal/PZT 2-2 composites

The sintered sample surfaces and cross-sections were examined in a field emission scanning electron microscope (FESEM, Merlin, Carl Zeiss, Inc., Jena, Germany). Energy dispersive spectroscopy (EDS) was conducted using Aztec detector (Oxford Instruments, High Wycombe, UK) on a NanoSEM 630 (FEI, Hillsboro, OR). The phase purity of the PZT and the substrate were assessed by X-ray diffraction (XRD, Empyrean, PANalytical Corp., Almelo,

Netherlands), using Cu Kα radiation from 2θ = 10° to 72° with a step size of 0.026° 2θ and a scan rate of 0.067°/sec.

After processing, 2 mm diameter circular silver electrodes (Leitsiber 200, Ted Pella, Inc., Redding, CA) were painted on the sintered PZT, the permittivity-loss and polarization-electric field (P-E) hysteresis loops were measured by an LCR meter (Hewlett-Packard 4284A, Agilent Technologies, Inc., Palo Alto, CA) and a precision multiferroic analyzer (Radiant Technologies, Inc., Albuquerque, NM), respectively. The P-E loops helped determine the coercive fields (E_c) of the PZT films, which were then used to calculate the poling voltage. Samples were DC poled at room temperature under 3-4 times E_c using a pA meter (Hewlett-Packard 4140B, Agilent Technologies, Inc., Palo Alto, CA) for 20 min before piezoelectric coefficient ($e_{31,f}$) measurements. For all of the measurements, the high voltages were driven from the substrates (bottom electrodes).

The $e_{31,f}$ measurements were carried out on a custom wafer flexure station [75]. The specimens were glued on 4-inch silicon wafers, with strain gauges (gauge factor ~1.95, Omega Engineering, Inc., Norwalk, CT) attached on top. Every measurement utilized two strain gauges that were perpendicular to each other. The wafers were flexed at 4 Hz via a speaker controlled by a lock-in amplifier (SR830, Stanford Research Systems, Sunnyvale, CA). A quarter Wheatstone bridge was used to process the signals from the strain gauges while a charge integration circuit collected the charges generated from the electrodes. The $e_{31,f}$ coefficient was calculated from [76]:

$$e_{31,f} = \frac{Q}{A(x_1+x_2)} \qquad \text{(Eq. 4-6)}$$

where Q represents the charge generated from the electrode, A is the area of the electrode, and x_1, x_2 are strains in two directions.

4.4 Results and discussion

4.4.1 PZT thick films on metal foils

In initial experiments, it was found that the burnt out PZT tapes collapsed either during steaming or when loaded into the pressing die if the samples were hand-stacked without lamination; this is likely related to the low green density and small thickness of the PZT tape. This problem could be largely ameliorated by adding a lamination step before cold sintering. Figure 4-12 (a)-(d) compares the 700 °C post-sintered PZT tapes on Ni foils with and without the lamination process. Lamination did not change the film microstructure significantly but it greatly suppressed the macro-flaws in the PZT layer.

A control sample was sintered at 700 °C without steaming and cold sintering to study the effects of CSP on the PZT quality. As seen in Figure 4-12 (d)-(g), after post-sintering the cold sintered sample presented mostly closed pores, suggesting a relative density over 92% [77], while the conventionally sintered PZT tape was still in the initial stage of sintering. The cold sintered tape was only a little over 10 μm thick. In contrast, for conventionally sintered PZT tape was 16 μm thick, consistent with its low density.

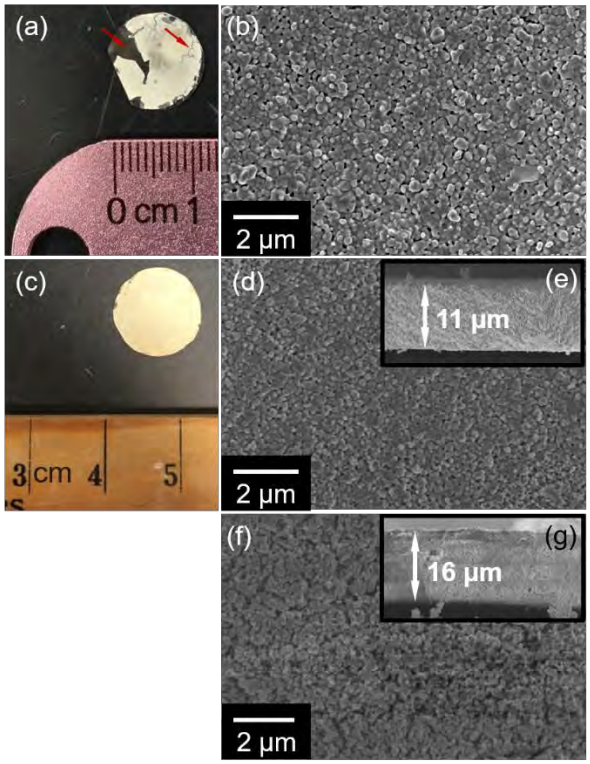

Figure **4-12**: (a) 700 °C post-sintered bimorph PZT thick films on LNO/HfO_2/Ni foil without use of a lamination step. The red arrows indicate regions of delamination and macro-cracks. (b) SEM image of the top PZT surface for a 700 °C post-sintered sample prepared with lamination. (c) (d) The 700 °C post-sintered sample with lamination procedure, and its top surface microstructure under FESEM. (f) The top surface morphology of the 700 °C post-sintered PZT tape without steaming and cold sintering steps. (e) (g) The cross-sectional SEM images showing the thicknesses of 700 °C post-sintered PZT tape with and without steaming and cold sintering steps.

The dielectric permittivity and loss tangent of the PZT thick films annealed at 700 °C annealed with and without a cold sintering step are displayed in Figure 4-13 (a). The cold sintered sample experienced a possible Maxwell-Wagner relaxation at 2 kHz. As shown in Figure 4-13 (b) the sample with steaming and cold sintering steps had a relative permittivity >3 times larger at 100 Hz than a conventionally sintered film and a remanent polarization improvement of nearly 10 times, due to improved densification. P_r of the cold sintered PZT thick film was comparable with 1 μm randomly-oriented Nb-PZT thin film obtained from the sol-gel method [78].

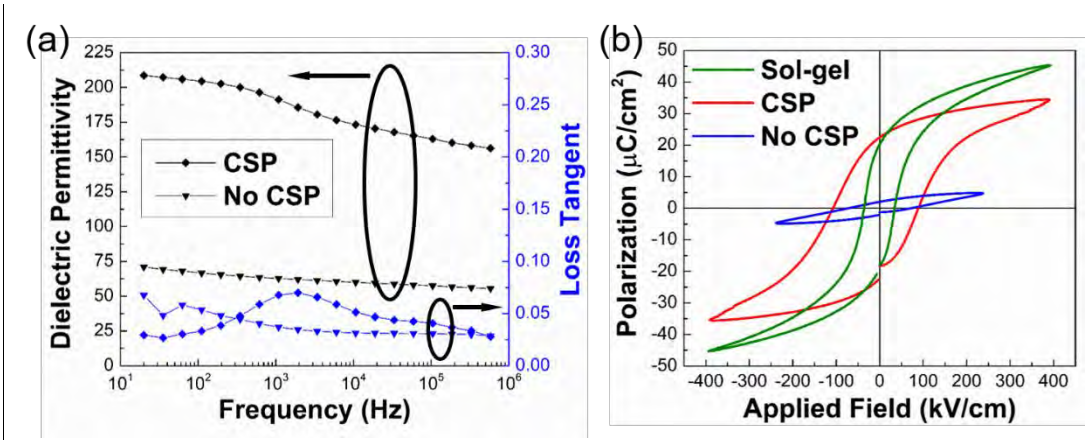

Figure **4-13**: (a) The relative permittivity and loss tangent of 700 °C sintered PZT thick films with and without CSP. (b) The P-E hysteresis loops of sol-gel Nb-PZT thin film (data provided by Akkopru Akgun *et al*. [78]), cold sintered PZT thick film, and not cold-sintered PZT.

Notice that the relative permittivity of the cold sintered film is still much lower than the typical permittivity of PZT-5A [79]. The coercive field is ~2 times as high as Nb-doped PZT thin film. These results indicate the existence of residual porosity and possibly lead oxide-rich grain boundaries. In Figure 4-12 (d): closed pores can be seen in the sintered PZT and the grain boundaries are not clear. Consequently, after the cold sintered PZT film was poled at $3E_c$ (300 kV/cm), the measured $e_{31,f}$ was only -2.6 C/m^2, a significantly lower value than is typical of dense PZT-5A (-16.04 C/m^2) [79,80]. The sintered sample without CSP, however, returned zero $e_{31,f}$.

Attempts were then made to improve the density of PZT films via increasing the annealing temperature. When cold sintered PZT tapes were annealed at 900 °C, the PbO remaining from the $Pb(NO_3)_2$ melted and served as a sintering aid [81]. Previous work proved the cold sintered PZT pellet reached 99% relative density after 900 °C post-annealing for 3 hours. [82] The microstructure of PZT tape annealed at 900 °C were shown in Fig. 4-14 (a). At 900 °C, cleaner grain boundaries can be observed from PZT compared with 700 °C anneal, but the density of the film was still not satisfactory.

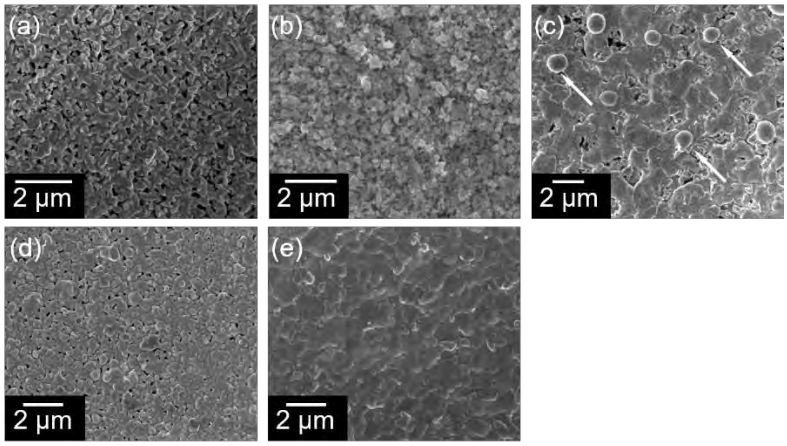

Figure **4-14**: SEM images of cold sintered and 900 °C-annealed PZT thick films on (a) LNO/HfO_2/Ni foil, (b) Cu foil, (c) Ag foil (Ag particles marked by arrows), and (d) (e) different regions of a PbO coated Cu foil.

The porosity at 900 °C may be attributed to the degradation and oxidation of the substrate. The XRD spectra in Figure 4-15 indicates that the $LaNiO_3$ layer was mostly eliminated above 850 °C [83] while the Ni was heavily oxidized, degrading the quality of the PZT film. Thickening the HfO_2 did not eliminate oxidation, suggesting Ni foil may not be the best solution for such devices.

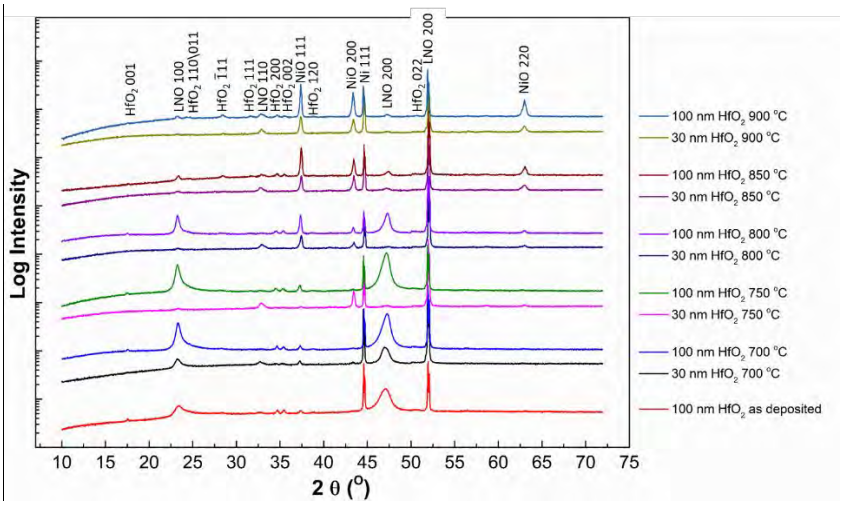

Figure **4-15**: XRD spectra of the Ni foil coated by 30 nm/100 nm HfO_2 and 100 nm $LaNiO_3$ after being annealed from 700 °C to 900 °C for 180 min.

Other commonly used metal foils that are more oxygen resistive while remaining an excellent electrical conductor were consequently considered as replacements, including Cu foil and Ag foil. Specifically, the annealing of cold sintered PZT/Cu/PZT specimen were carried out in a low pO_2 furnace. Unlike Ni, there is a processing window where the Cu can remain metallic while the Pb is oxidized. [84] These experiments exposed more issues on sintering PZT on metal foils. Judging from the microstructures in Figure 4-14 (b) and (c), porosities still existed in the PZT films. However, on Ag foil, clean grain boundaries, closed triple points, and significant grain growth were observed.

There are at least two reasons why incomplete densification was observed. First, the post-annealing temperature may be too low to allow complete densification. Secondly, the use of dense metal foils could have induced constrained sintering [85]. The second hypothesis helps explain why denser PZT films were obtained on Ag rather than on Cu: Because 900 °C is close to the melting temperature of Ag, (which could be further lowered due to the formation of Ag-PbO solid solution [86]), a thin layer of liquid phase may be formed at the interface of PZT and Ag. Therefore, the constrained sintering problem may be mitigated by the relaxation of stress at the Ag/PZT interface. However this also degraded the potential of utilizing Ag as a substrate. Silver droplets were seen on the PZT surface, as confirmed in the EDS in Figure 4-16. These shorted the PZT film. (Notice that there are some zirconium-rich sites on the film, probably originating from the zirconia media used during the milling of the PZT powder. The Al and C EDS peaks are likely from the sample holder and environmental contamination, respectively.)

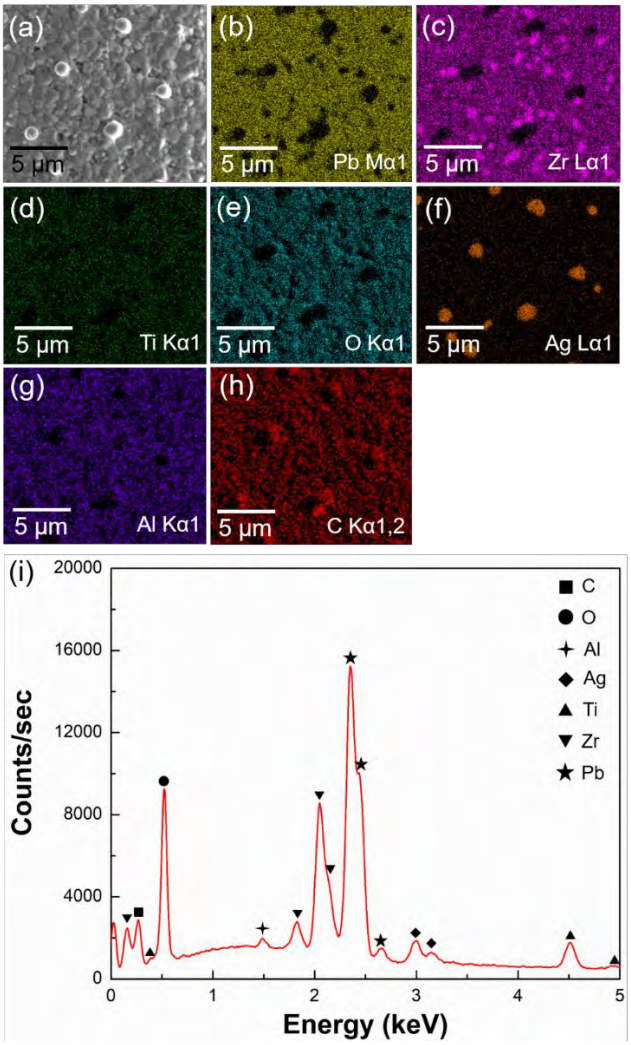

Figure **4-16**: (a) The top surface of 10 μm PZT thick film on Ag foil after a 900 °C, 180 min anneal. (b)-(h) The EDS mapping showing the distribution of Pb, Zr, Ti, O, Ag, Al, and C respectively. (i) The EDS spectrum of PZT surface.

Attention were then drawn back to Cu. It was hypothesized that if a thin layer PbO was spin cast on the surface of Cu foil, the constrained sintering issue may be relieved with the melting of PbO at 900 °C. It turned out the sintering of PZT thick film was significantly improved, except that the densification was not uniform, as shown by Figure 4-14 (d) and (e).

4.4.2 PZT thick films on tape cast Cu films

Based on the preliminary success of PZT sintering on PbO coated Cu foil, a second approach to the avoidance of constrained sintering issue is the simultaneous densification of PZT and the Cu substrate. Tape cast Cu thick films were laminated with PZT tapes and the rest of the procedures remained unchanged. In practice, it was found that the burnt out PZT/Cu tape/PZT structure is very fragile. PZT and Cu densification occurred during cold sintering, which enhanced the strength of the composites. Figure 4-17 (a), (c), and (e) show a high compact density of Cu and PZT after CSP, with a clean PZT-Cu interface.

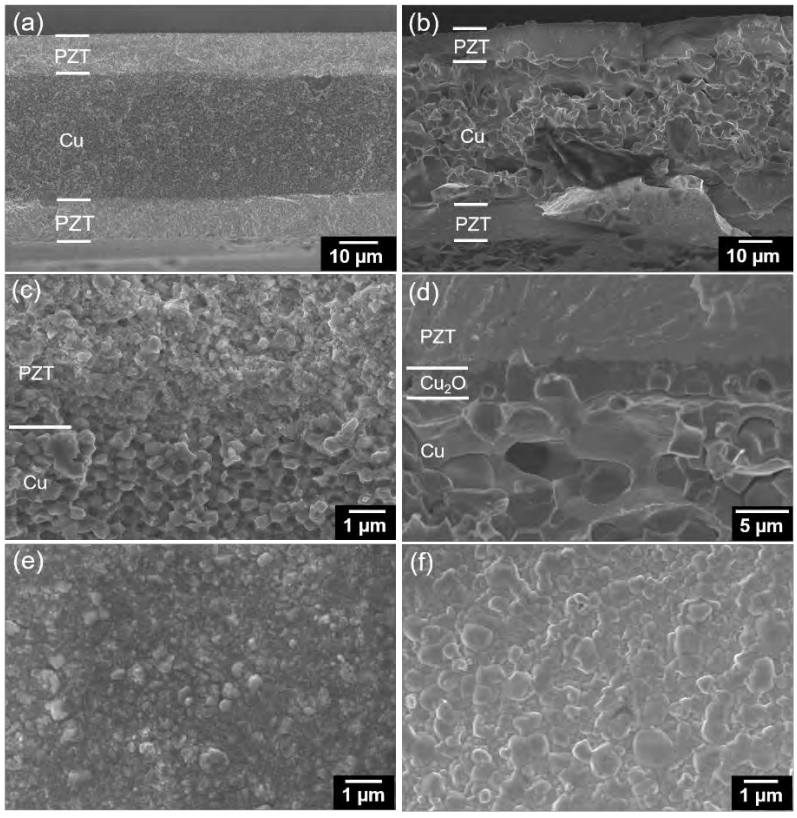

Figure **4-17**: (a) (b) Cross-sections of the PZT on Cu tape after CSP (left) and after 900 °C post-sintering (right) showing PZT/Cu/PZT structures. (c) (d) Zoomed in cross sections of as-cold sintered (left) and 800 °C post-sintered (right) samples emphasizing the PZT-Cu interface. (e) (f) The top surfaces of the as-cold sintered (left) and 800 °C post-sintered (right) PZT films.

Dense PZT was acquired (Figure 4-17 (f)) after annealing at only 800 °C for 180 min in a low pO_2 furnace. This is presumably a result of good PZT and Cu compaction during CSP, and the formation of a PbO-Cu_2O eutectic melt [87]. It is noted that a PZT thick film without lead nitrate failed to sinter under the same conditions (Figure C-1). The sintered Cu layer was 40 μm thick, sandwiched between 10 μm bimorph PZT thick films, as seen in Figure 4-17 (b). Large crystals appeared on the top surface of PZT. These are suggested by Figure C-2 and Figure C-3 to be Cu_2O, which is probably from the contaminated sample holder and can be eliminated by cleaning the sample holder before post-annealing. However, even after cleaning the sample holder, there is still an interface between post-annealed PZT and Cu like the one shown in Figure 4-17 (d). According to Figure C-4, the interface consists of Cu and O. Figure 4-18 further corroborated the existence of a Cu_2O interface. The Cu_2O interface might originate from the oxidation of Cu following the decomposition of lead nitrate during burn out and cold sintering:

$$2Pb(NO_3)_2 \rightleftharpoons 2PbO + 4NO_2 + O_2 \qquad \text{(Eq. 4-7)}$$

$$4Cu + O_2 \rightleftharpoons Cu_2O \qquad \text{(Eq. 4-8)}$$

The above reactions are likely to be more complex in practice as Figure 4-18 indicated some unknown peaks at low angles in the as cold sintered samples. Although difficult to index, these peaks must be from crystal structures with large lattice parameters, for example, lead hydroxyl carbonates and lead hydroxyl nitrates. The oxidation of Cu occurs at the interface between PZT and Cu, which is isolated from the external gas flow. This may explain why the Cu_2O layer cannot be removed even while processing in low pO_2 conditions. The Cu_2O intensity drop above 600 °C anneal is possibly caused by the X-ray absorption in denser PZT, since Figure C-5 showed that necking and grain growth appear at 600 °C. At this same temperature, PbO starts to volatilize and most of it is eventually removed from the system.

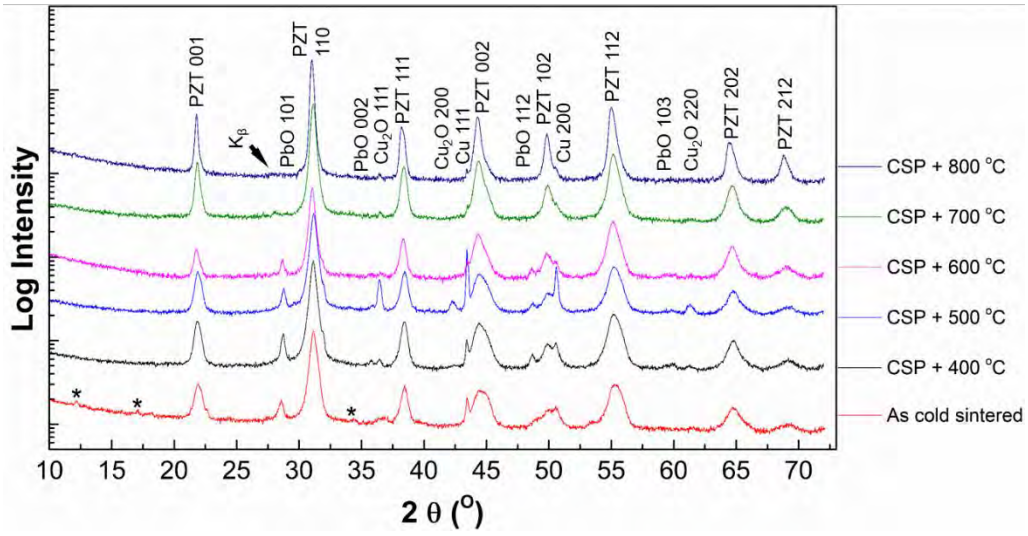

Figure **4-18**: The XRD spectra of as cold sintered and 400-800 °C post-annealed PZT on Cu. The unknown peaks were marked by "*".

Figure 4-19 (a) demonstrates that the relative permittivity of post-sintered PZT on Cu is 550 at 100 Hz, with a loss of 12%; these value are a convolution of the response of the PZT and the Cu_2O-rich inter-layer. The film P-E hysteresis loops were imprinted. Influenced by the inter-layer and the small grain size [47], the $e_{31,f}$ of the thick film was -4.72 C/m^2 after poling at 160 V ($4E_c$) at room temperature for 20 min. The electrical properties of PZT on Cu are much better than that on Ni foils, though the capacitor in series was problematic.

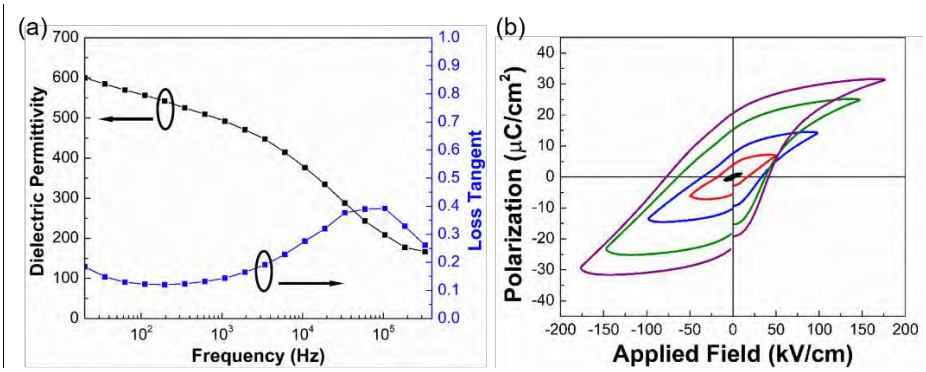

Figure **4-19**: (a) The relative permittivity/loss tangent under different frequencies and (b) the P-E hysteresis loops at different applied electric fields of the 800 °C post-sintered PZT on Cu tape.

4.5 Conclusions

This work studied 10 μm thick film PZT/metal (Ni, Ag, and Cu) composites prepared using cold sinter-assisted processing. It was found that cracking and delamination of PZT on metal can be avoided through cold sintering. LNO/HfO_2/Ni foil has oxidation problem and is not suitable as the substrate for PZT films; Cu foils impede the sintering of PZT tape due to constrained sintering; Ag foil substrates produced electrically shorted PZT because of high diffusivity; PbO coated Cu foil cannot result a uniform densification of PZT. The film densities, relative permittivity and $e_{31,f}$ found in co-fired PZT/Cu tape make it an acceptable candidate for PZT/metal composites and potential piezoelectric energy harvesting applications.

References

[1] Clark, J. What is the Internet of Things? https://www.ibm.com/blogs/internet-of-things/what-is-the-iot/.

[2] Lee, T. D.; Ebong, A. U. A Review of Thin Film Solar Cell Technologies and Challenges. Renew. Sustain. Energy Rev. 2017, 70, 1286–1297.

[3] Joselin Herbert, G. M.; Iniyan, S.; Sreevalsan, E.; Rajapandian, S. A Review of Wind Energy Technologies. Renew. Sustain. Energy Rev. 2007, 11 (6), 1117–1145.

[4] Uihlein, A.; Magagna, D. Wave and Tidal Current Energy - A Review of the Current State of Research beyond Technology. Renew. Sustain. Energy Rev. 2016, 58, 1070–1081.

[5] Barbier, E. Nature and Technology of Geothermal Energy: A Review. Renew. Sustain. Energy Rev. 1997, 1 (1–2), 1–69.

[6] Andosca, R.; McDonald, T. G.; Genova, V.; Rosenberg, S.; Keating, J.; Benedixen, C.; Wu, J. Experimental and Theoretical Studies on MEMS Piezoelectric Vibrational Energy Harvesters with Mass Loading. Sensors Actuators A Phys. 2012, 178, 76–87.

[7] Dagdeviren, C.; Yang, B. D.; Su, Y.; Tran, P. L.; Joe, P.; Anderson, E.; Xia, J.; Doraiswamy, V.; Dehdashti, B.; Feng, X.; et al. Conformal Piezoelectric Energy Harvesting and Storage from Motions of the Heart, Lung, and Diaphragm. Proc. Natl. Acad. Sci. U. S. A. 2014, 111 (5), 1927–1932.

[8] Liu, H.; Zhong, J.; Lee, C.; Lee, S.-W.; Lin, L. A Comprehensive Review on Piezoelectric Energy Harvesting Technology: Materials, Mechanisms, and Applications. Appl. Phys. Rev. 2018, 5 (4), 041306.

[9] Yeo, H. G. Mechanical Energy Harvesters Utilizing {001} Textured PZT Films on Flexible Metal Foils, PhD thesis, the Pennsylvania State University, 2017.

[10] Lee, B. S.; Lin, S. C.; Wu, W. J.; Wang, X. Y.; Chang, P. Z.; Lee, C. K. Piezoelectric MEMS Generators Fabricated with an Aerosol Deposition PZT Thin Film. J. Micromechanics Microengineering 2009, 19 (6), 065014.

[11] Oishi, A.; Okumura, H.; Katsumura, H.; Kagata, H. The Power Generation Characteristics and Durability of a Vibration Power Generation Device Using Piezoelectric Thick Film Formed Directly by Screen Printing on a Stainless Steel Substrate. J. Phys. Conf. Ser. 2014, 557 (1), 012131.

[12] Williams, C. B.; Shearwood, C.; Harradine, M. A.; Mellor, P. H.; Birch, T. S.; Yates, R. B. Development of an Electromagnetic Micro-Generator. IEEE Proc. - Circuits, Devices Syst.; IEEE 2001, 148 (6), 337.

[13] Scherrer, S.; Plumlee, D. G.; Moll, A. J. Energy Scavenging Device in LTCC Materials. Proc. IEEE Workshop on Microelectronics and Electron Devices; IEEE 2005, 1, 77–78.

[14] Beinart, R.; Nazarian, S. Effects of External Electrical and Magnetic Fields on Pacemakers and Defibrillators. Circulation 2013, 128 (25), 2799–2809.

[15] Beeby, S. P.; Tudor, M. J.; White, N. M. Energy Harvesting Vibration Sources for Microsystems Applications. Meas. Sci. Technol. 2006, 17 (12), R175–R195.

[16] Thomson, G.; Yurchenko, D.; Val, D. V. Dielectric Elastomers for Energy Harvesting. In Energy Harvesting; IntechOpen, 2018, 41–61.

[17] Yang, Z.; Zhou, S.; Zu, J.; Inman, D. High-Performance Piezoelectric Energy Harvesters and Their Applications. Joule 2018, 2 (4), 642–697.

[18] Kim, S.-B.; Park, H.; Kim, S.-H.; Wikle, H. C.; Park, J.-H.; Kim, D.-J. Comparison of MEMS PZT Cantilevers Based on d_{31} and d_{33} Modes for Vibration Energy Harvesting. J. Microelectromechanical Syst. 2013, 22 (1), 26–33.

[19] Wang, D.-A.; Liu, N.-Z. A Shear Mode Piezoelectric Energy Harvester Based on a Pressurized Water Flow. Sensors Actuators A Phys. 2011, 167 (2), 449–458.

[20] Zhao, J.; Zheng, X.; Zhou, L.; Zhang, Y.; Sun, J.; Dong, W.; Deng, S.; Peng, S. Investigation of a d_{15} Mode PZT-51 Piezoelectric Energy Harvester with a Series Connection Structure. Smart Mater. Struct. 2012, 21 (10), 105006.

[21] Kulkarni, V.; Ben-Mrad, R.; Prasad, S. E.; Nemana, S. A Shear-Mode Energy Harvesting Device Based on Torsional Stresses. IEEE/ASME Trans. Mechatronics; IEEE 2014, 19 (3), 801–807.

[22] Daqaq, M. F.; Masana, R.; Erturk, A.; Dane Quinn, D. On the Role of Nonlinearities in Vibratory Energy Harvesting: A Critical Review and Discussion. Appl. Mech. Rev. 2014, 66 (4).

[23] Hajati, A.; Kim, S.-G. Ultra-Wide Bandwidth Piezoelectric Energy Harvesting. Appl. Phys. Lett. 2011, 99 (8), 083105.

[24] Cottone, F.; Vocca, H.; Gammaitoni, L. Nonlinear Energy Harvesting. Phys. Rev. Lett. 2009, 102 (8), 080601.

[25] Zhou, S.; Cao, J.; Inman, D. J.; Lin, J.; Liu, S.; Wang, Z. Broadband Tristable Energy Harvester: Modeling and Experiment Verification. Appl. Energy 2014, 133, 33–39.

[26] Roundy, S.; Leland, E. S.; Baker, J.; Carleton, E.; Reilly, E.; Lai, E.; Otis, B.; Rabaey, J. M.; Sundararajan, V.; Wright, P. K. Improving Power Output for Vibration-Based Energy Scavengers. IEEE Pervasive Comput. 2005, 4 (1), 28–36.

[27] Ma, X.; Yeo, H. G.; Rahn, C. D.; Trolier-McKinstry, S. Efficient and Sensitive Energy Harvesting Using Piezoelectric MEMS Compliant Mechanisms. In Volume 8: 27th Conference on Mechanical Vibration and Noise; American Society of Mechanical Engineers, 2015; pp 1–12.

[28] Yeo, H. G.; Ma, X.; Rahn, C.; Trolier-McKinstry, S. Efficient Piezoelectric Energy Harvesters Utilizing (001) Textured Bimorph PZT Films on Flexible Metal Foils. Adv. Funct. Mater. 2016, 26 (32), 5940–5946.

[29] Xue, T. Energy Harvesting from Human Motion Using Eccentric Rotor-Based Generators with Piezoelectric Transducers, PhD Thesis, University of Utah, 2018.

[30] Meng, M.; Ibrahim, A.; Xue, T.; Yeo, H. G.; Wang, D.; Roundy, S.; Trolier-McKinstry, S.; Kiani, M. Multi-Beam Shared-Inductor Reconfigurable Voltage/SECE-Mode Piezoelectric Energy Harvesting of Multi-Axial Human Motion. Proc. 2019 IEEE International Solid- State Circuits Conference - (ISSCC) ; IEEE 2019, 3, 426–428.

[31] Gomes, J.; Serrado Nunes, J.; Sencadas, V.; Lanceros-Mendez, S. Influence of the β-Phase Content and Degree of Crystallinity on the Piezo- and Ferroelectric Properties of Poly(Vinylidene Fluoride). Smart Mater. Struct. 2010, 19 (6), 065010.

[32] Lebrun, L.; Guyomar, D.; Guiffard, B.; Cottinet, P.-J.; Putson, C. The Characterization of the Harvesting Capabilities of an Electrostrictive Polymer Composite. Sensors Actuators A Phys. 2009, 153 (2), 251–257.

[33] Csoka, L.; Hoeger, I. C.; Rojas, O. J.; Peszlen, I.; Pawlak, J. J.; Peralta, P. N. Piezoelectric Effect of Cellulose Nanocrystals Thin Films. ACS Macro Lett. 2012, 1 (7), 867–870.

[34] Omote, K.; Ohigashi, H.; Koga, K. Temperature Dependence of Elastic, Dielectric, and Piezoelectric Properties of "single Crystalline'' Films of Vinylidene Fluoride Trifluoroethylene Copolymer. J. Appl. Phys. 1997, 81 (6), 2760–2769.

[35] Huan, Y.; Liu, Y.; Yang, Y. Simultaneous Stretching and Static Electric Field Poling of Poly(Vinylidene Fluoride-Hexafluoropropylene) Copolymer Films. Polym. Eng. Sci. 2007, 47 (10), 1630–1633.

[36] Mishra, S.; Unnikrishnan, L.; Nayak, S. K.; Mohanty, S. Advances in Piezoelectric Polymer Composites for Energy Harvesting Applications: A Systematic Review. Macromol. Mater. Eng. 2019, 304 (1), 1800463.

[37] Song, J.; Zhao, G.; Li, B.; Wang, J. Design Optimization of PVDF-Based Piezoelectric Energy Harvesters. Heliyon 2017, 3 (9), e00377.

[38] Cao, Z.; Zhang, J.; Kuwano, H. Vibration Energy Harvesting Characterization of 1 cm^2 Poly(Vinylidene Fluoride) Generators in Vacuum. Jpn. J. Appl. Phys. 2011, 50 (9), 09ND15.

[39] Newnham, R. E.; Trolier-McKinstry, S. Materials Engineering: Bonding, Structure, and Structure-Property Relationships; Cambridge University Press, 2017.

[40] Cook, R. K.; Weissler, P. G. Piezoelectric Constants of Alpha- and Beta-Quartz at Various Temperatures. Phys. Rev. 1950, 80 (4), 712–716.

[41] Kobiakov, I. B. Elastic, Piezoelectric and Dielectric Properties of ZnO and CdS Single Crystals in a Wide Range of Temperatures. Solid State Commun. 1980, 35 (3), 305–310.

[42] Song, J.; Zhou, J.; Wang, Z. L. Piezoelectric and Semiconducting Coupled Power Generating Process of a Single ZnO Belt/Wire. A Technology for Harvesting Electricity from the Environment. Nano Lett. 2006, 6 (8), 1656–1662.

[43] Shrout, T. R.; Chang, Z. P.; Kim, N.; Markgraf, S. Dielectric Behavior of Single Crystals near the $(1-x)Pb(Mg_{1/3}Nb_{2/3})O_3$-$xPbTiO_3$ Morphotropic Phase Boundary. Ferroelectr. Lett. Sect. 1990, 12 (3), 63–69.

[44] Kuwata, J.; Uchino, K.; Nomura, S. Phase Transitions in the $Pb(Zn_{1/3}Nb_{2/3})O_3$-$PbTiO_3$ System. Ferroelectrics 1981, 37 (1), 579–582.

[45] Li, F.; Zhang, S.; Xu, Z.; Wei, X.; Luo, J.; Shrout, T. R. Piezoelectric Activity of Relaxor-$PbTiO_3$ Based Single Crystals and Polycrystalline Ceramics at Cryogenic Temperatures: Intrinsic and Extrinsic Contributions. Appl. Phys. Lett. 2010, 96 (19), 192903.

[46] Yang, Z.; Zu, J. Comparison of PZN-PT, PMN-PT Single Crystals and PZT Ceramic for Vibration Energy Harvesting. Energy Convers. Manag. 2016, 122, 321–329.

[47] Randall, C. A.; Kim, N.; Kucera, J.-P.; Cao, W.; Shrout, T. R. Intrinsic and Extrinsic Size Effects in Fine-Grained Morphotropic-Phase-Boundary Lead Zirconate Titanate Ceramics. J. Am. Ceram. Soc. 2005, 81 (3), 677–688.

[48] Shkuratov, S. I.; Baird, J.; Antipov, V. G.; Talantsev, E. F.; Chase, J. B.; Hackenberger, W.; Luo, J.; Jo, H. R.; Lynch, C. S. Ultrahigh Energy Density Harvested from Domain-Engineered Relaxor Ferroelectric Single Crystals under High Strain Rate Loading. Sci. Rep. 2017, 7 (1), 46758.

[49] Xie, Y. Synthesis and Characterization of Piezo- / Ferroelectric Lead Zirconate-Titanate (PZT) Single Crystals and Related Ternary Ceramics, PhD Thesis, Simon Fraser University, 2013.

[50] Chang, Y.; Wu, J.; Sun, Y.; Zhang, S.; Wang, X.; Yang, B.; Messing, G. L.; Cao, W. Enhanced Electromechanical Properties and Phase Transition Temperatures in [001] Textured $Pb(In_{1/2}Nb_{1/2})O_3$-$Pb(Mg_{1/3}Nb_{2/3})O_3$-$PbTiO_3$ Ternary Ceramics. Appl. Phys. Lett. 2015, 107 (8), 082902.

[51] Park, S.-E.; Wada, S.; Cross, L. E.; Shrout, T. R. Crystallographically Engineered $BaTiO_3$ Single Crystals for High-Performance Piezoelectrics. J. Appl. Phys. 1999, 86 (5), 2746–2750.

[52] Shen, Z.-Y.; Li, J.-F. Enhancement of Piezoelectric Constant d_{33} in $BaTiO_3$ Ceramics Due to Nano-Domain Structure. J. Ceram. Soc. Japan 2010, 118 (1382), 940–943.

[53] Akiyama, M.; Umeda, K.; Honda, A.; Nagase, T. Influence of Scandium Concentration on Power Generation Figure of Merit of Scandium Aluminum Nitride Thin Films. Appl. Phys. Lett. 2013, 102 (2), 021915.

[54] Priya, S.; Inman, D. J. Energy Harvesting Technologies; Springer US, 2009.

[55] Zhang, S.; Li, F.; Jiang, X.; Kim, J.; Luo, J.; Geng, X. Advantages and Challenges of Relaxor-$PbTiO_3$ Ferroelectric Crystals for Electroacoustic Transducers – A Review. Prog. Mater. Sci. 2015, 68, 1–66.

[56] Chang, Y.; Watson, B.; Fanton, M.; Meyer, R. J.; Messing, G. L. Enhanced Texture Evolution and Piezoelectric Properties in CuO-Doped $Pb(In_{1/2}Nb_{1/2})O_3$-$Pb(Mg_{1/3}Nb_{2/3})O_3$-$PbTiO_3$ Grain-Oriented Ceramics. Appl. Phys. Lett. 2017, 111 (23), 232901.

[57] Yeager, C. B.; Ehara, Y.; Oshima, N.; Funakubo, H.; Trolier-McKinstry, S. Dependence of $e_{31,\,f}$ on Polar Axis Texture for Tetragonal $Pb(Zr_xTi_{1-x})O_3$ Thin Films. J. Appl. Phys. 2014, 116 (10), 104907.

[58] Yeo, H. G.; Xue, T.; Roundy, S.; Ma, X.; Rahn, C.; Trolier-McKinstry, S. Strongly (001) Oriented Bimorph PZT Film on Metal Foils Grown by RF-Sputtering for Wrist-Worn Piezoelectric Energy Harvesters. Adv. Funct. Mater. 2018, 28 (36), 1801327.

[59] Xu, T.-B.; Siochi, E. J.; Kang, J. H.; Zuo, L.; Zhou, W.; Tang, X.; Jiang, X. Energy Harvesting Using a PZT Ceramic Multilayer Stack. Smart Mater. Struct. 2013, 22 (6), 1–15.

[60] Yang, B.; Yi, Z.; Tang, G.; Liu, J. A Gullwing-Structured Piezoelectric Rotational Energy Harvester for Low Frequency Energy Scavenging. Appl. Phys. Lett. 2019, 115 (6), 063901.

[61] Lozinski, A.; Wang, F.; Uusimäki, A.; Leppävuori, S. PLZT Thick Films for Pyroelectric Sensors. Meas. Sci. Technol. 1997, 8 (1), 33–37.

[62] Le Dren, S.; Simon, L.; Gonnard, P.; Troccaz, M.; Nicolas, A. Investigation of Factors Affecting the Preparation of PZT Thick Films. Mater. Res. Bull. 2000, 35 (12), 2037–2045.

[63] Dorey, R. A.; Whatmore, R. W.; Beeby, S. P.; Torah, R. N.; White, N. M. Screen Printed PZT Thick Films Using Composite Film Technology. Integr. Ferroelectr. 2003, 54 (1), 651–658.

[64] Baomin Xu; Buhler, S.; White, D.; Zesch, J.; Wong, W. Fabrication of Piezoelectric Thick Films for High Frequency Transducers. In Transactions of the IEEE Symposium on Ultrasonics, 2003; IEEE, 2003; Vol. 2, pp 1999–2002.

[65] Gentil, S.; Damjanovic, D.; Setter, N. $Pb(Mg_{1/3}Nb_{2/3})O_3$ and (1 - X)$Pb(Mg_{1/3}Nb_{2/3})O_3$ - $XPbTiO_3$ Relaxor Ferroelectric Thick Films: Processing and Electrical Characterization. Journal of Electroceramics. 2004, pp 151–161.

[66] Kwon, T. Y.; Park, J. H.; Kim, Y. B.; Yoon, D. S.; Cheon, C. Il; Lee, H. L.; Kim, T. S. Preparation of Piezoelectric $0.1Pb(Zn_{0.5}W_{0.5})O_3$–$0.9Pb(Zr_{0.5}Ti_{0.5})O_3$ Solid Solution and Thick Films for Low Temperature Firing on a Si-Substrate. J. Cryst. Growth 2006, 295 (2), 172–178.

[67] Wu, D.; Zhou, Q.; Shung, K. K.; Bharadwaja, S. N.; Zhang, D.; Zheng, H. Dielectric and Piezoelectric Properties of PZT Composite Thick Films with Variable Solution to Powder Ratios. J. Am. Ceram. Soc. 2009, 92 (6), 1276–1279.

[68] Barrow, D. A.; Petroff, T. E.; Tandon, R. P.; Sayer, M. Characterization of Thick Lead Zirconate Titanate Films Fabricated Using a New Sol Gel Based Process. J. Appl. Phys. 1997, 81 (2), 876–881.

[69] Kanda, K.; Hirai, S.; Fujita, T.; Maenaka, K. Piezoelectric MEMS with Multilayered $Pb(Zr,Ti)O_3$ Thin Films for Energy Harvesting. Sensors Actuators A Phys. 2018, 281, 229–235.

[70] Reilly, E. K.; Wright, P. K. Modeling, Fabrication and Stress Compensation of an Epitaxial Thin Film Piezoelectric Microscale Energy Scavenging Device. J. Micromechanics Microengineering 2009, 19 (9), 095014.

[71] Yeo, H. G.; Trolier-McKinstry, S. {001} Oriented Piezoelectric Films Prepared by Chemical Solution Deposition on Ni Foils. J. Appl. Phys. 2014, 116 (1), 014105.

[72] Kim, S.-G.; Priya, S.; Kanno, I. Piezoelectric MEMS for Energy Harvesting. MRS Bull. 2012, 37 (11), 1039–1050.

[73] Coleman, K.; Walker, J.; Beechem, T.; Trolier-McKinstry, S. Effect of Stresses on the Dielectric and Piezoelectric Properties of $Pb(Zr_{0.52}Ti_{0.48})O_3$ Thin Films. J. Appl. Phys. 2019, 126 (3), 034101.

[74] Gao, L.; Ko, S. W.; Guo, H.; Hennig, E.; Randall, C. A.; Jones, J. L. Demonstration of Copper Co-Fired $(Na,K)NbO_3$ Multilayer Structures for Piezoelectric Applications. J. Am. Ceram. Soc. 2016, 99 (6), 2017–2023.

[75] Shepard, J. F.; Moses, P. J.; Trolier-McKinstry, S. The Wafer Flexure Technique for the Determination of the Transverse Piezoelectric Coefficient (d_{31}) of PZT Thin Films. Sensors Actuators A Phys. 1998, 71 (1–2), 133–138.

[76] Garten, L. M.; Trolier-McKinstry, S. The Field Induced $e_{31,f}$ Piezoelectric and Rayleigh Response in Barium Strontium Titanate Thin Films. Appl. Phys. Lett. 2014, 105 (13), 132905.

[77] Rahaman, M. N. Ceramic Processing and Sintering, 2nd ed.; Marcel Dekker: New York, NY, 2003.

[78] Akkopru-Akgun, B.; Zhu, W.; Lanagan, M. T.; Trolier-McKinstry, S. The Effect of Imprint on Remanent Piezoelectric Properties and Ferroelectric Aging of $PbZr_{0.52}Ti_{0.48}O_3$ Thin Films. J. Am. Ceram. Soc. 2019, 102 (9), 5328–5341.

[79] Erturk, A.; Inman, D. J. Piezoelectric Energy Harvesting; Lopes Junior, V., Steffen, V., Savi, M. A., Eds.; John Wiley & Sons, Ltd: Chichester, UK, 2011.

[80] Dubois, M.-A.; Muralt, P. Measurement of the Effective Transverse Piezoelectric Coefficient $e_{31,f}$ of AlN and $Pb(Zr_x,Ti_{1-x})O_3$ Thin Films. Sensors Actuators A Phys. 1999, 77 (2), 106–112.

[81] Atkin, R. B.; Fulrath, R. M. Point Defects and Sintering of Lead Zirconate-Titanate. J. Am. Ceram. Soc. 1971, 54 (5), 265–270.

[82] Wang, D.; Guo, H.; Morandi, C. S.; Randall, C. A.; Trolier-McKinstry, S. Cold Sintering and Electrical Characterization of Lead Zirconate Titanate Piezoelectric Ceramics. APL Mater. 2018, 6 (1), 016101.

[83] Li, A.; Ge, C.; Lü, P.; Ming, N. Preparation of Perovskite Conductive $LaNiO_3$ Films by Metalorganic Decomposition. Appl. Phys. Lett. 1996, 68 (10), 1347–1349.

[84] Gao, L.; Guo, H.; Zhang, S.; Randall, C. Base Metal Co-Fired Multilayer Piezoelectrics. Actuators 2016, 5 (1), 8. PAGE RANGE?

[85] Holmes, P. J.; Loasby, R. G. Handbook of Thick Film Technology; Holmes, P. J., Loasby, R. G., Eds.; Electrochemical Publications, 1976.

[86] Shao, Z. B.; Liu, K. R.; Liu, L. Q.; Liu, H. K.; Dou, S. Equilibrium Phase Diagrams in the Systems PbO-Ag and CuO-Ag. J. Am. Ceram. Soc. 1993, 76 (10), 2663–2664.

[87] Corker, D. L.; Whatmore, R. W.; Ringgaard, E.; Wolny, W. W. Liquid-Phase Sintering of PZT Ceramics. J. Eur. Ceram. Soc. 2000, 20 (12), 2039–2045.

Chapter 5

Conclusions and Future Work

5.1 Conclusions

BNO thin films are a potential candidate for energy storage devices on flexible substrates. It was found that exposure of the amorphous films to a UV light source facilitated the removal of organics. Benefiting from this, the BNO crystallization was initiated at a lower temperature (from 400 °C, 10 min to 375 °C, 10 min) and within shorter heat treatment duration (from 375 °C, 30 min to 375 °C, 10 min). Larger crystallite sizes were also indicated by the XRD peaks of UV-treated BNO compared with not UV-treated samples under the same temperature profile. Due to the elimination of carbon in the film through the UV treatment at an early stage, the film annealed at 450 °C became less porous and achieved an energy density of 39 J/cm^3 at room temperature at 10 kHz with an applied electric field of 3.6 MV/cm. The BNO thin films annealed at 350°C and 375°C, have shown lower energy storage densities but better temperature stability presumably because of the extensive volume fraction of amorphous phase. When compared to other recently developed materials, the BNO thin films are competitive due to their high energy densities and relatively low processing temperatures.

PZT ceramics were cold sintered to >80% relative densities at 300 °C using bimodal PZT powder with moisturized $Pb(NO_3)_2$ as a sintering aid. The underlying mechanism of PZT densification during cold sintering is improved PZT particle packing induced by the plastic deformation of the moist lead nitrate. Therefore, a viscous sintering model can be utilized to explain the effects of temperature, pressure and time on the final pellet densities; the model

showed good agreement with experimental results in terms of pressure and temperature, while the particle rearrangement at the initial stage of CSP deviates the behavior of densification with respect to time. Because there is no noticeable necking between PZT particles during cold sintering with lead nitrate, a post-annealing procedure at 900 °C for 3 hours, which is 300-400 °C lower than conventional methods, is needed to develop good ferroelectric properties. In addition, 700 °C annealing indicated promising densification for longer annealing times. The post-annealing step promotes improved densification and equilibration of a nanosized grain structure; it produces ceramics with high relative permittivity, well-developed polarization switching with high remanent polarizations, and strong piezoelectric coefficients.

This thesis also studied 10 μm thick film PZT/metal (Ni, Ag, and Cu) composites under a cold sinter-assisted processes. It was found that cracking and delamination of PZT on metal can be avoided through cold sintering. LNO/HfO_2/Ni foil has an oxidation problem during the post-sintering anneal, and is not suitable as the substrate for PZT films; both coated Ni foil and Cu foil impede the sintering of PZT tape due to constrained sintering; Ag foil substrates produced electrically shorted PZT because of high Ag diffusivity, but are presumed to form a Ag-PbO liquid interface, which mitigated the constrained sintering problem; PbO coated Cu foil did result a denser PZT although the densification is not uniform across the sample. It was ultimately found that the film densities, relative permittivity and $e_{31,f}$ in co-fired PZT/Cu tape make it an acceptable candidate for PZT/metal composites and potential piezoelectric energy harvesting applications.

5.2 Future work

5.2.1 Understanding the mechanisms of carbon elimination via deep ultra-violet treatment

The success of carbon removal via DUV exposure improved the energy storage performance of BNO thin films. The underlying mechanism for this behavior was not discussed extensively in the section 2.2; this portion of the future work provides a preliminary explanation while indicating a few "loose ends" to further optimize the process.

First, the mechanisms of carbon elimination under DUV is believed to be related to the decomposition of large organic molecules into smaller ones facilitated by the UV radiation. Although, immediately after solution preparation, large organic molecules were not present, the should be generated over time as a result of the esterification of ethylene glycol and citric acid from the moment a bottle of solution was made. [1] As smaller molecules volatilize faster than large ones for the same conditions, more carbon can be removed from the film either during DUV exposure or the following secondary heat treatment. This is supported by the Fourier Transformed Infrared (FTIR) spectra of bismuth zinc niobate tantalate (BZNT) thin films, as shown in Fig. 5-1. Notice that the composition of the BZNT solution is almost the same as BNO solution, except that there are zinc acetate and tantalum ethoxide precursors in BZNT. Before FTIR, two layers of solution were spin cast on the wafer.

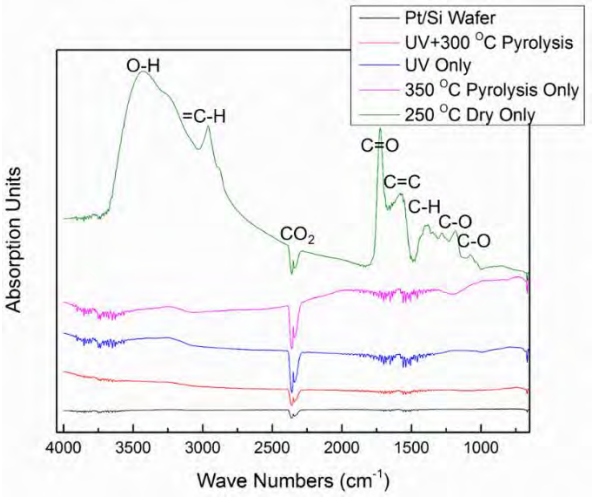

Figure 5-1: FTIR spectra of (lines from the top to bottom) BZNT film after spin casting and drying at 250 °C for 3 min; after being dried and undergoing a 350 °C, 10 min pyrolysis without DUV treatment; after being dried and UV exposed; and after being dried, exposed to the DUV treatment, and subsequently pyrolyzed at 300 °C for 10 min. Shown for comparison is a platinized silicon wafer with no BZNT film.

From the spectra, it is clear that considerable quantities of residual organics remain after the 250 °C drying procedure. The peaks corresponding to residual organics can be effectively suppressed by either pyrolyzing films on a hot plate at 350 °C for 10 min, or exposing the films under UV for 3 min without hot plate heating (the film will still be heated up to ~150 °C by the UV during the exposure). If a secondary heat treatment is applied after DUV exposure, when the temperature is only 300 °C, the organics can almost be eliminated within the films, resulting an FTIR spectrum similar to the wafer background. It is presumed that BNO films will behave in a manner comparable to that of the BNZT, though a direct confirmation should be obtained in the future.

It is also of interest to understand whether the carbon removal is dominated by UV frequency, UV intensity, or the atmospheric environment. This topic has several technical challenges including measuring the absorption spectrum of the solution, tuning the wavelengths/intensities of the UV irradiation, etc. Therefore, the following discussion will only offer a preliminary insight.

The absorption spectrum of the BNO solution may be estimated from the absorption spectrum of ethylene glycol, which is the main component in the solution. According to the work by Xu *et al*., [2] the absorption peak of ethylene glycol is ~195 nm, which is far away from the wavelength of Fusion UV system (260 nm DUV, with a CaF_2 bandpass filter to reduce the intensity of other wavelengths) used in Chapter 2. If similar absorption peak applies for the BNO solution, a UV system with a matching wavelength should be more effective on photolyze the organics. Another UV system with a wavelength of 182 nm – 254 nm (UV 300, Samco Inc., East Brunswick, NJ) was used to compare with the results from the Fusion UV system. Here a compromise had to be made on the intensity of the UV source, as the Fusion UV has a power density of 385 mW/cm^2, while the Samco UV only presents a power density of 10-15 mW/cm^2. Two layers of BNO samples were spin cast and dried at 250 °C for 3 min before UV exposure. After the UV treatments, the samples were annealed at 300 °C for 10 min, and the dielectric permittivity and loss tangent were measured at 1 kHz. The experimental conditions were listed in Table 5-1 and the results were described in Table 5-1 and Figure 5-2.

Table **5-1**: UV treatment conditions and electrical properties of BNO thin films.

Sample	UV system	Substrate Temp. during UV (°C)	UV time (min)	Gas	Anneal temp (°C)	Anneal time (min)	Permittivity (1 kHz)	Loss (1 kHz)
(a)	Fusion	50-150	3	Air	300	10	36	0.01
(b)	Samco	50	3	Oxygen	300	10	32	0.27
(c)	Samco	50	3	Nitrogen	300	10	32	0.28
(d)	Samco	300	10	Air	---	---	36	0.30

The BNO film treated using the Fusion UV system (sample (a)) and 300 °C anneal displayed a slightly higher permittivity and a much lower loss tangent than those exposed in the Samco UV system. Moreover, the dielectric properties of the Samco UV treated samples (sample (b), sample (c), and sample (d)) showed similar electrical properties regardless of the substrate temperatures and atmospheric conditions during UV exposure. This suggests that the UV

intensity plays a dominant role compared to UV wavelength, atmospheric composition, and temperatures during UV treatment for films of this thickness. Figure 5-2 also indicates the densification of BNO is more significant using Fusion UV, as the BNO films was thinner in sample (a).

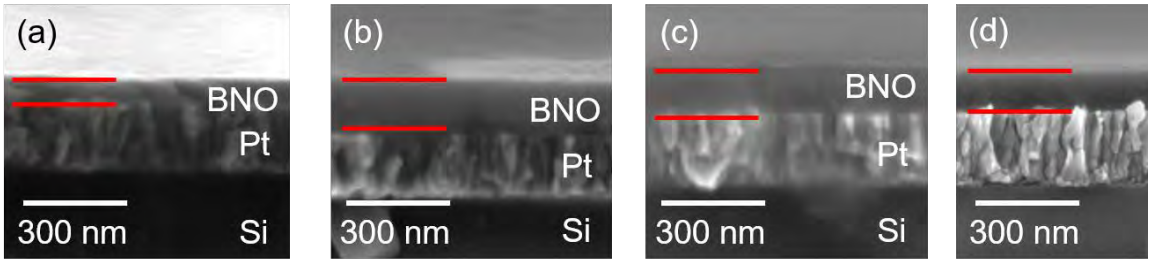

Figure 5-2: Cross-sectional SEM of BNO thin films with different UV treatment procedures. Sample (a) was treated using the Fusion UV system for 3 min in air and annealed on a hot plate in air at 300 °C for 10 min; Sample (b) and (c) were exposed to the Samco UV source at 50 °C for 3 min in oxygen and nitrogen environments, respectively, and then annealed on a hot plate in air at 300 °C for 10 min; Specimen (d) was also treated using the Samco UV system, but at 300 °C for 10 min in air, with no secondary heat treatment applied. The intervals between the two parallel red lines emphasize the thickness of BNO thin films.

In the future, should another UV system with the same wavelength range as Samco UV and a same power density as Fusion UV can be employed, the processing temperature of the BNO films may be suppressed to a lower level.

5.2.2 Constructing heterostructures in BNO thin films with enhanced electrical breakdown strengths

Although the results on UV-treated BNO thin films filled a gap in processing temperatures between polymer-based systems and ceramics, it failed to explain the hypothesis proposed at the end of section 2.2: If δ-Bi_2O_3 nano crystallites are the key to high permittivity and large energy density in BZNT nanocomposites, then removing ZnO from the film should increase

the high-permittivity nano-crystallite, resulting in even higher relative permittivity and energy density even without DUV treatment.

However, it was found that the 350 °C annealed BNO films only showed a relative permittivity of 24 and an energy storage density of 6 J/cm^3. Even with DUV treatment, the BNO showed a relative permittivity of 44 and an energy density of 13 J/cm^3 after 350 °C heat treatment, which is still much lower than the numbers reported in the BZNT nanocomposite [3].

To understand what is happening in the BZNT nanocomposite, TEM analysis was adopted. The microstructures of the BZNT nanocomposites (DUV exposed, 350 °C annealed) are shown in Fig. 5-3.

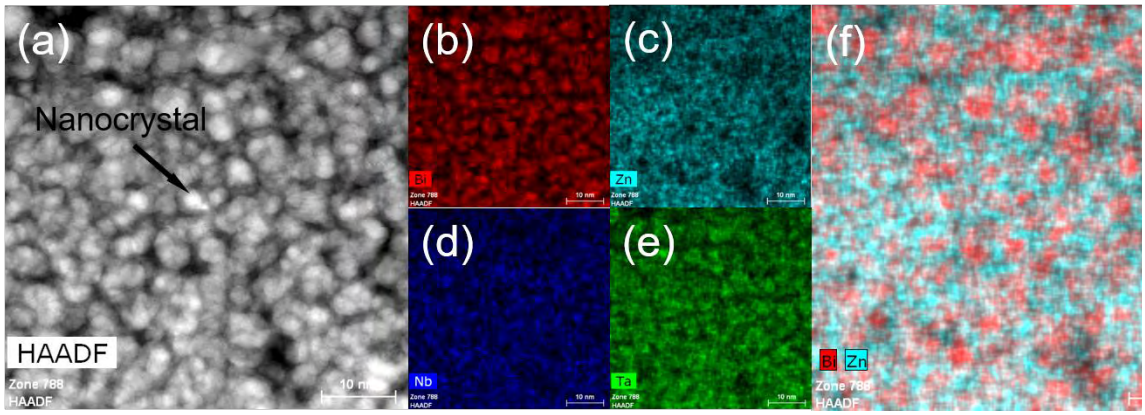

Figure 5-3: (a) A dark-field TEM image of the cross section of a BZNT nanocomposite film. Brighter regions represent heavier elements (Bi/Nb) accumulation. (b)-(e) EDS analysis of BZNT nanocomposite with mappings of Bi (b), Zn (c), Nb (d), and Ta (e). (f) An overlay EDS map of Bi and Zn showing segregation of the two elements.

From Figure 5-3, it is clear that Zn and Bi are segregated (Figure 5-3 (f)). This BZNT sample has an energy storage density ~14 J/cm^3, comparable to that of the BNO film (energy density ~13 J/cm^3) with the same deposition procedure. The BZNT also showed a lightly lower relative permittivity (~38) but a higher BDS at 10 kHz (~2.9 MV/cm), which is reasonable due to the presence of low k ZnO phase (ε_r for ZnO is ~10 [4] while the ε_r for Bi_3NbO_7 is ~60 [5]).

Compared to the high-resolution TEM images acquired by Michael-Sapia *et al*., the crystalline regions are slightly different, as shown in Figure 5-4. [3]

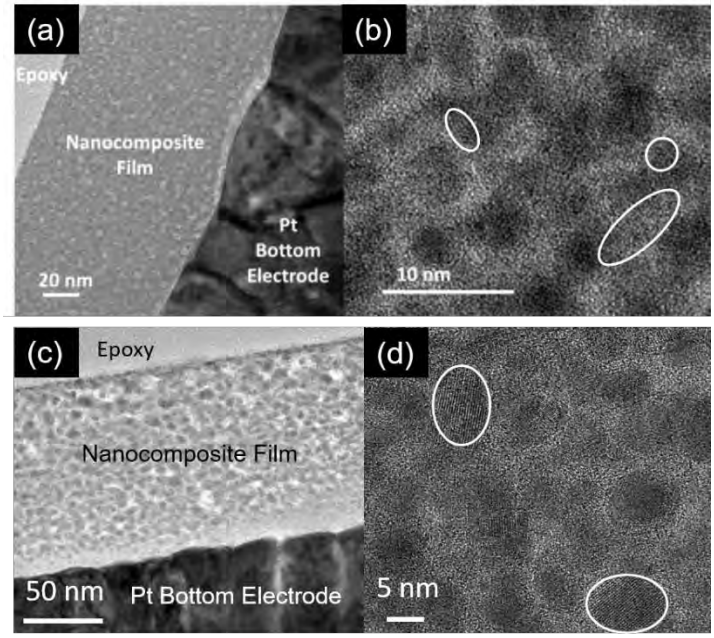

Figure 5-4: (a) (c) TEM image showing cross sections of BZNT nanocomposites reported by Michael-Sapia *et al*. and this work, respectively. (b) (d) High-resolution TEM images of BZNT nanocomposites reported by Michael-Sapia *et al*. and this work respectively; the white circles indicate crystalline regions. (Portions of the figure adopted from Michael-Sapia *et al*. [3])

The above pictures were taken in bright-field mode, meaning darker regions are Bi rich. Note that in Figure 5-4 (b), the crystalline clusters are in both the lighter and darker regions, while in Figure 5-4 (d), the nano-crystallites appear only within darker clusters. In addition, in Figure 5-4 (a), there are isolated brighter particles in the BZNT nanocomposite. This suggests that a different mechanism is governing the outstanding performance of the BZNT nanocomposite fabricated by Michael-Sapia *et al*. Given that the BDS of the reported BZNT nanocomposite is ~3.8 MV/cm at 10 kHz [3], it is most likely that this unknown phase is composed of lighter element(s) with a modest relative permittivity and a high breakdown strength. Hence, niobium or tantalum oxides should be considered.

It was found that using aged niobium ethoxide precursor (a bottle opened for at least 3 months with observed crystallization of unknown compound), the breakdown strength of the BNO thin film increased. From the P-E loop of Figure 5-5, the BNO thin film prepared from an aged niobium precursor exhibited a BDS ~3.6 MV/cm at 10 kHz after being annealed at 350 °C. And correspondingly, the energy density of the aged BNO film rose to 30 J/cm^3.

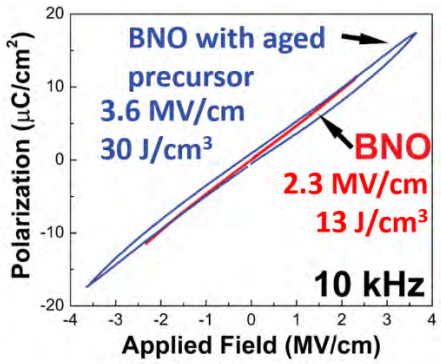

Figure 5-5: The P-E loops of 350 °C-annealed BNO and BNO with aged precursors thin films under 10 kHz electric fields.

XRD data also supported the BNO with aged precursors shared some structural similarity with the reported BZNT nanocomposite as the characteristic peak at $2\theta = 46.5°$ can be observed in both samples, indicated as Figure 5-6. This peak, previously reported to be Bi_2O_3 (220) [3], could also come from hexagonal Nb_2O_5 (002) (PDF#: 04-002-2664), which is consistent with the fact that it had not been seen in normal BNO thin films.

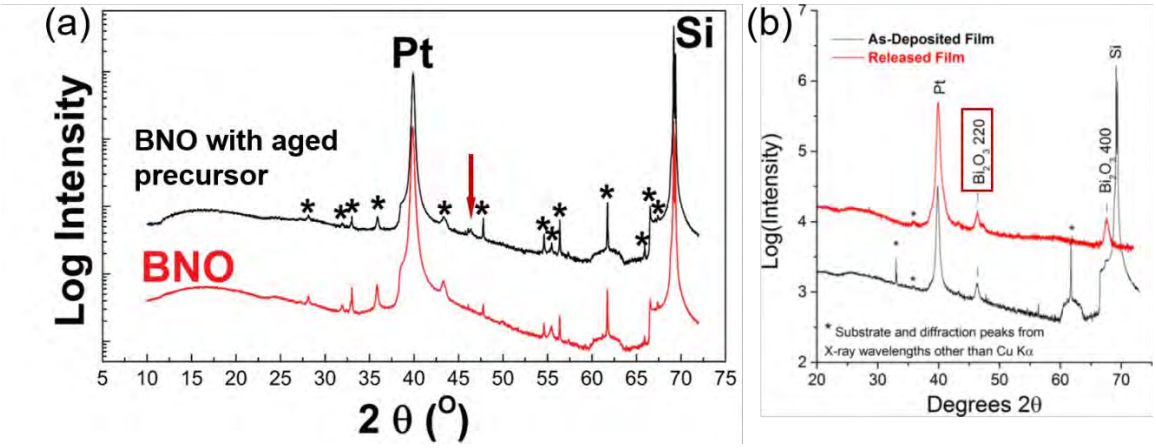

Figure 5-6: (a) The XRD of BNO and aged BNO thin films. (b) The XRD of BZNT nanocomposite reported by Michael-Sapia *et al*. Substrate and diffraction peaks related to the X-ray source were marked by "*". (Figure from Michael-Sapia *et al*. [3])

TEM analysis also suggested microstructural heterogeneities in BNO prepared with aged precursors. From Figure 5-7, dark regions can be seen in BNO with aged precursors at the interfaces between two spin cast layers. In contrast, the cross section is more homogeneous in BNO films made from fresh precursors.

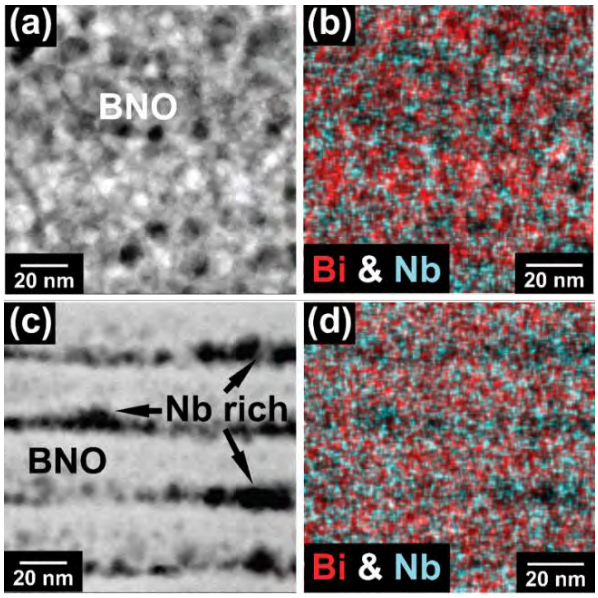

Figure 5-7: (a) (c) The dark field TEM cross sections of (a) normal BNO and (c) BNO with aged precursors. The EDS mapping showing overlays of Bi and Nb in (b) normal BNO and (d) BNO with aged precursors respectively.

In the future, optimization can be focused on the concentration, spatial distribution, and sizes of the niobium oxide phases. As this system more resembles the nanocomposites with high permittivity inclusions and insulated matrix, it is possible that the heterogeneities in the films caused divergence in the breakdown tree propagation. Ultimately, a mixing rule could be developed that describes the behavior of these samples. In addition, the aged niobium precursor may have altered the Bi:Nb ratio which influences the electric properties of the films. This assumption should also be considered in future work.

5.2.3 Isovalent and aliovalent doping of BNO thin films

It was shown in Chapter 2 that BNO thin films have the potential to be applied in high energy density capacitors. It is suggested for future work that the energy density could be improved further by modifying the composition of the thin films. According to Figure 2-2, the energy density is proportional to the dielectric constant and the square of the maximum applied field (controlled by the BDS of the samples). Thus, the influence of BDS on the energy density is more important. One possible research direction for higher BDS is to reduce the conductivity of the thin films. This can be done by doping the BNO system with other cations.

There are currently two types of cation doping that may help increase the BDS of the thin films. First, based on Michael-Sapia's research, an increase doping level of Ta on Nb site leads to higher BDS because Ta_2O_5 has a higher bandgap than Nb_2O_5. [6] Early experiments shown in Figure 5-8 supported the above hypotheses. The average energy densities and BDS of the 350 °C-annealed BNO thin films increase as Ta level rises. 10 mol% Ta doped BNO (BNT10) has an energy density ~ 35 J/cm^3 under 10 kHz while the efficiency remains above 95%.

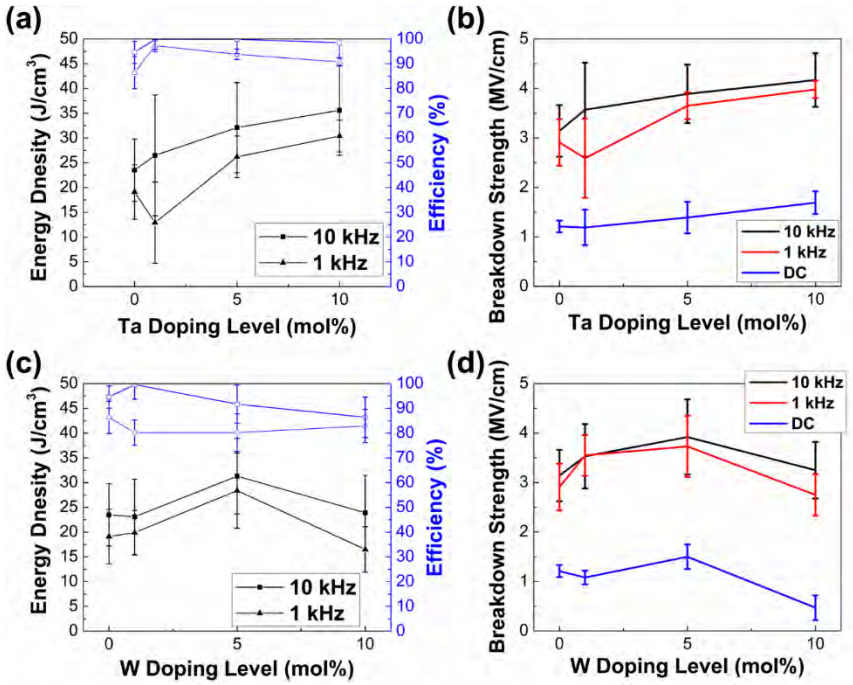

Figure 5-8: (a) The energy densities and efficiencies of different levels Ta doped BNO. (b) The 10 kHz, 1 kHz and DC BDS of different levels Ta doped BNO. (c) The energy densities and efficiencies of different levels W doped BNO. (d) The 10 kHz, 1 kHz and DC BDS of different levels W doped BNO.

On the other hand, it is possible that the BNO thin films can be partially reduced by the residual carbon. This assumption is supported by the XPS spectra presented in Figure 5-9 (a) that low valence Bi can be detected even though the films are exposed under DUV. The wavelength dispersion spectrum (WDS) of UV treated BNO also indicates the Nb:O ratio is ~7.4, and the Bi:Nb ratio is only ~2.5, while the solution composition is Bi_3NbO_7, meaning there might be a Bi deficiency in the BNO thin films.

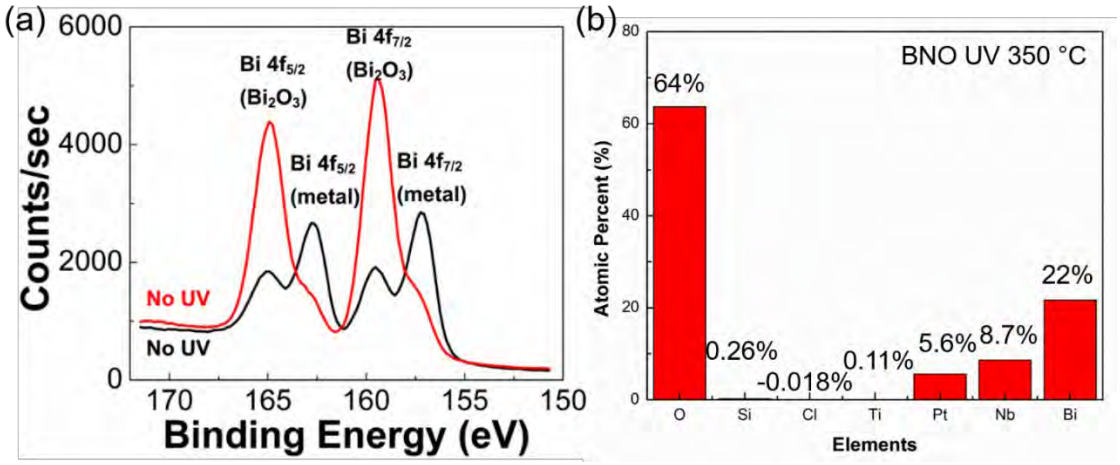

Figure 5-9: (a) The XPS spectra of the Bi in non-UV treated and UV treated BNO thin films annealed at 350 °C. (b) The WDS showing the composition of UV treated and 350 °C annealed BNO. Si, Ti, and Pt signals come from the substrate of the specimen. The negative atomic percent from Cl is probably caused by the trace amount of impurities that are below the detection limit of WDS.

A second possibility is that Bi may volatilize from the film, causing the specimen to be p-type. As a consequence, adding donor cations, for example, tungsten, to the BNO system might help reduce the conductivity of the films and result in higher energy density. In initial experiment on W doped BNO (BNW), the energy densities and BDS increase with increasing W concentrations in the 1% to 5% region, as indicated in Figure 5-8. Then, at still higher W concentrations, both the energy densities and the BDS start to drop. This is possibly because the W is over compensating the oxygen vacancies in the film, leading to a higher carrier concentration.

A Weibull analysis applied to those films indicate wide distribution of electric breakdown strengths. In some samples, especially the BNT thin films, not all the breakdown strengths obeyed the Weibull distribution. These data points (BNT1 at 10 kHz and BNW5 at 1 kHz) were not utilized in the Weibull analysis and are indicated by yellow circles. Future optimization is necessary to produce high-breakdown strength specimens.

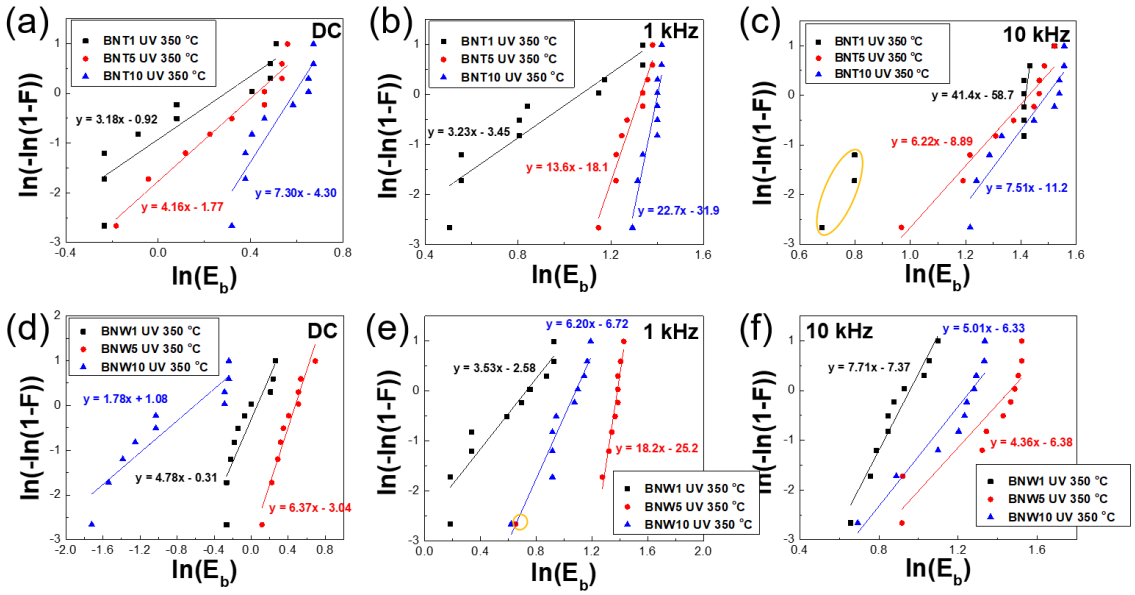

Figure 5-10: (a)-(c) The Weibull analysis of BDS in 1 mol% (BNT1), 5 mol% (BNT5) and 10 mol% (BNT10) Ta-doped BNO thin films under DC, 1 kHz and 10 kHz frequencies respectively. (d)-(f) The Weibull analysis of BDS in 1 mol% (BNW1), 5 mol% (BNW5) and 10 mol% (BNW10) W-doped BNO thin films under DC, 1 kHz and 10 kHz frequencies. Some data points not used in the Weibull analysis are marked by yellow circles.

In addition, to prove the underlying mechanism responsible for the changes in the electrical properties on tungsten doping, thermally stimulated depolarization current (TSDC) measurements can be applied to characterize the migration of oxygen vacancies, along with the evolution of defect dipoles, etc.

5.2.4 Incorporation of small volume fraction high aspect ratio nanosheets with ultra-high k ceramics

Stemming from the study of c-BCB/hBN [7] and PVDF/$BaTiO_3$ [8], in which the breakdown path might have been greatly complicated by the high aspect ratio inclusions, a common disadvantage of these composites is the reduced relative permittivity. As a consequence, the low electric field energy density is not ideal. One can imagine a new composite system with 3-dimensional connected high k ceramics and isolated high aspect ratio PVDF-HFP or hBN that

are parallel, dispersed, and normal to the electric field direction. Because of the small volume fraction of low permittivity inclusions, this nanocomposite should preserve a high relative permittivity from the ceramic matrix while presenting improved BDS due to the existence of insulating phases. Such system may help improving the energy storage performances of ceramics such as $PbMg_{1/3}Nb_{2/3}O_3$-based [9], $BaTiO_3$-based [10], and $NaNbO_3$-based [11] ceramics. These ceramics all displays high relative permittivities, but the breakdown strength is low.

One challenge of fabricating high ceramic volume fraction composites is the sintering of ceramic powders. Because conventionally, ceramic powders need to be densified at ~50-75% of their melting temperatures that the fabrication temperatures of bulk ceramic capacitors are generally over 1000 °C, nanosheet inclusions are subject to decomposition or melting during sintering. The cold sintering process may offer a solution to densify these ceramics below 300 °C. A similar system was successfully demonstrated by cold sintering ZnO/PTFE. [12]

5.2.5 CSP of functional PZT without post-annealing using NaOH/KOH eutectic flux

The cold sintering process, whether via transient liquid phases or viscous flow, is a technique used to sinter ceramic materials at temperatures significantly lower than those processed in furnaces. However, there are a number of materials that need to be post-annealed after CSP to achieve the full range of functional properties. These include perovskites (PZT, BTO), fluorites (YSZ), and spinels (Fe_3O_4). These ceramics are difficult to dissolve in a water-based system and are hard enough to resist plastic deformation during CSP.

One alternative approach to densify cold sintered ceramics is to utilize molten salts. Molten salts are commonly seen in the synthesis of oxides with limited solubility in water, such as Al_2O_3 [13] and $BaTiO_3$ [14]. Recently, carbides and nitrates sintering processes [15] have also been proved compatible with molten salts. Regarding the selection of salt systems, Liu *et al*.

recommended a qualitative "hard-soft acid-base (HSAB)" theory [16] in which the cations and anions are categorized into hard/soft acid/base. "Hard" represents cations (acids) or anions (bases) with small ionic radii, high charges, low (for acids) or high (for bases) electronegativities, and weak polarizabilities; "Soft" refers to cations (acids) or anions (bases) that are large-sized, low-charged, with intermediate values of electronegativity, and strongly polarized.[17,18] "Hard" acids tend to react or form solvents with "hard" bases, and vice versa. This theory might alternatively be explained through the "valence-matching principle" where the Lewis basicity of anions and the Lewis acidity of cations must be matched to form a stable structure. [19] For PZT, the "hard" nature of Zr^{4+} and Ti^{4+} suggest good solubilities with alkali metal fluorides and chlorides, while Pb^{2+} is an intermediate cation between "hard" and "soft". However, the melting points of most fluorides and chlorides are still too high to be incorporated in the CSP. For example, LiF only drops the sintering temperature of PZT to ~ 900-950 °C. Similarly, the eutectic composition, NaCl/KCl still has a melting point of 658 °C [16]

Consequently, oxosalts such as NaOH and KOH are of interest. At the eutectic composition (NaOH/KOH = 51 mol%/49 mol%), NaOH/KOH has a melting point of 170 °C, as indicated by the phase diagram (Figure 5-11).

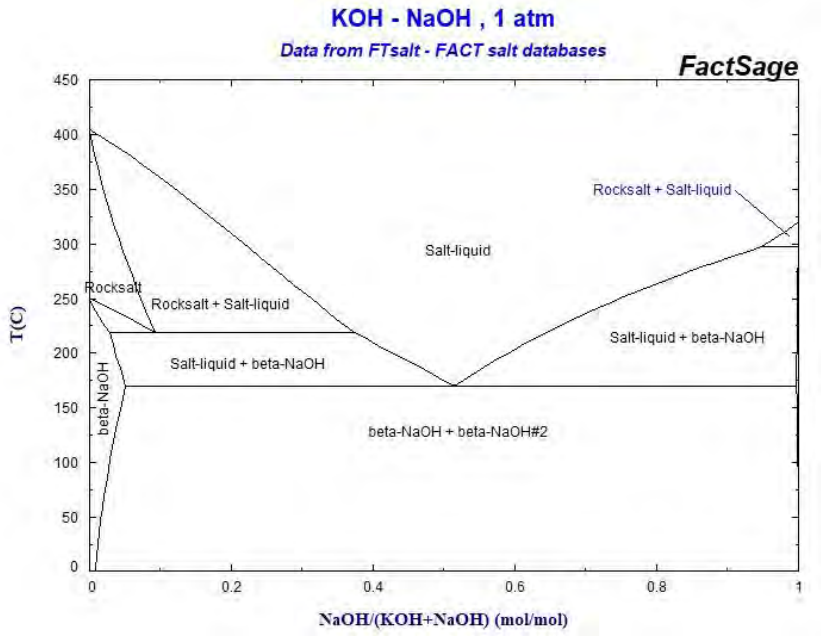

Figure **5-11**: The phase diagram of NaOH-KOH. The eutectic point is at 170 °C with a composition NaOH/KOH = 51 mol%/49 mol%. [20]

Use of NaOH/KOH fluxes during CSP has proven successful on several ceramics including MnO (unpublished work by J.-P. Maria *et al.*), ZnO (unpublished work by J.-P. Maria *et al.*), $BaTiO_3$ (unpublished work by K. Tsuji *et al.*), and $Na_{0.5}K_{0.5}NbO_3$ (unpublished work by J.-P. Maria *et al.*). In PZT however, lead leaches from the ceramic when the pH is either too low or too high. The leached Pb^{2+} leaves a Zr/Ti-rich shell around the PZT particles, making the sintering of PZT extremely difficult. (This did not become an issue in BTO system possibly because the dissolution rates of Ti^{4+} are high enough that the molten hydroxides can effectively remove the shell layer during cold sintering.) Dried NaOH/KOH does not have a pH value, but once the mixture starts to absorb water from the air, the pH level becomes too high and a color change (from light yellow to orange) is immediately apparent during the grinding procedure used prior to cold sintering PZT. This problem can be avoided if the whole process is carried out in a glove box or a glove bag filled with inert gases, such as dry nitrogen.

The particle size of PZT is also problematic. In molten hydroxide CSP of BTO, sintering is more complete using smaller particle sizes. However, very few vendors provide ultra-fine (<100 nm) PZT powder. And even among those who do, most of the PZT powders have a large content of zirconia contamination. To mitigate the issue, commercially available micron-sized PZT powder was attrition milled for 72 hours to fine nano-powder, as shown in Figure 5-12. In addition, a partially crystallized (a mixture of amorphous, pyrochlore, and perovskite phase PZT) powder was made by calcining sol-gel PZT solution at 400 °C.

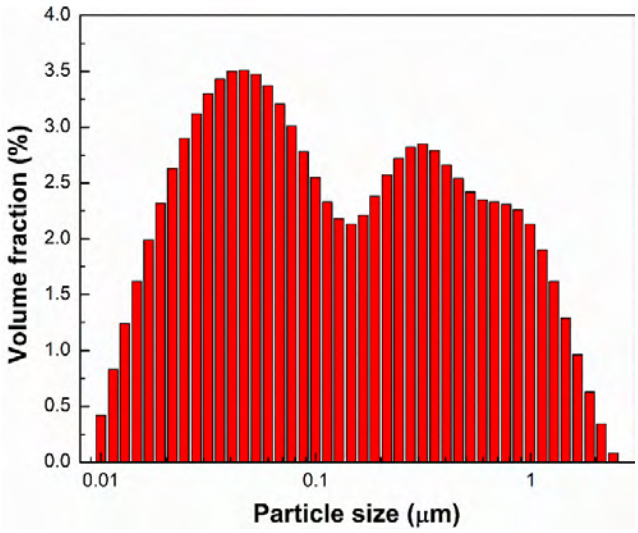

Figure **5-12**: Particle size distribution of commercial PZT powder after 3-day attrition milling.

Bottles of PZT powder, NaOH, and KOH must be loaded and weighted in a glove bag filled with dry nitrogen, along with the balance, a mortar/pestle, and the pressing die. After grinding 15 vol% NaOH/KOH (49/51) and mixing them with 0.7 g attrition milled PZT powder in a mortar and pestle, the mixture was loaded into a half-inch-diameter cylindrical die and cold sintered at 300 °C, 500 MPa for 16 hrs. Notice that the molten hydroxides are corrosive to normal stainless steel dies, thus a tungsten carbide die designed by R. Floyd *et al*. was utilized. The relative densities of the pellets varied between 80%-89%, when 7.8 g/cm^3 was used as a

reference. FESEM images confirmed the existence of necking (Figure 5-13 (a)) and even some fully sintered regions (Figure 5-13 (b)).

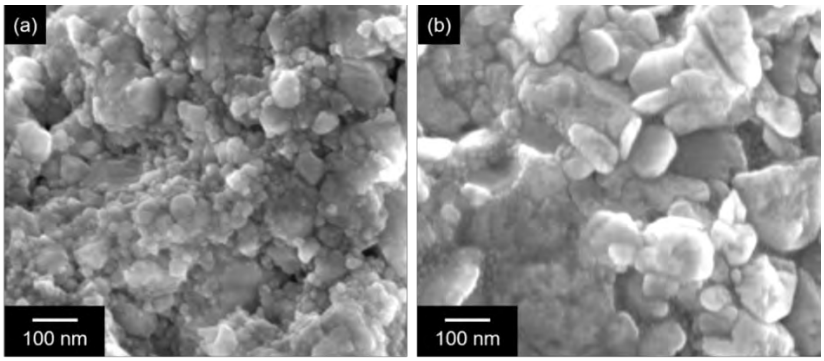

Figure **5-13**: FESEM image on the cross-section of a PZT pellet cold sintered with NaOH/KOH showing (a) necked regions and (b) an almost fully sintered region.

Conducting another cold sintering experiment under exactly the same conditions with calcined sol-gel PZT powder also led to promising results. XRD spectra (Figure 5-14) suggested the NaOH/KOH flux may help the formation of perovskite phase at as low as 300 °C, which is 150-250 °C lower than the typical crystallization temperatures of amorphous PZT.

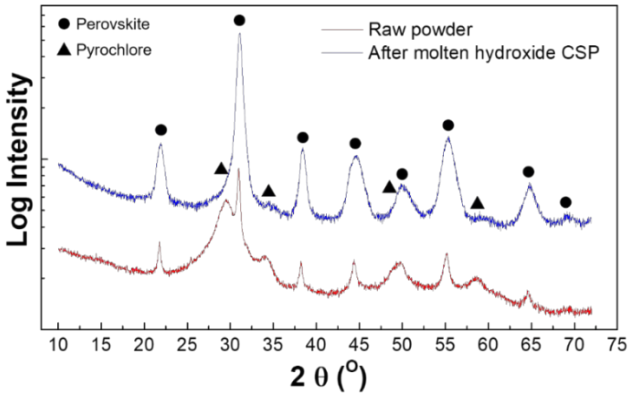

Figure **5-14**: The XRD spectra of sol-gel PZT powder after calcination (red) and after CSP with NaOH/KOH flux (blue). The circle labels the perovskite phase while the triangles represent the positions of pyrochlore peaks.

However, the relative densities of cold sintered pellets with sol-gel powder are below 80%. This might due to the strong repulsive force between particles originated from the ultra-fine

powder sizes and some grain interior porosities caused by incomplete collapsing of PZT gel, as the soft agglomerates are probably crushed during the high shear mixing in a mortar and pestle (see Figure 5-15).

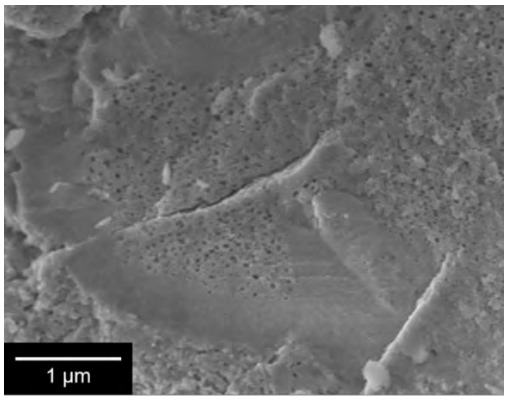

Figure **5-15**: The cross-sectional SEM of PZT sol-gel powder after molten hydroxides CSP showing grain interior porosity.

A high energy planetary mill (Thinky NP-100) should be able to remove some pores by crushing larger PZT particles, as indicated by the size distribution analysis provided by Thinky Company (Figure 5-16).

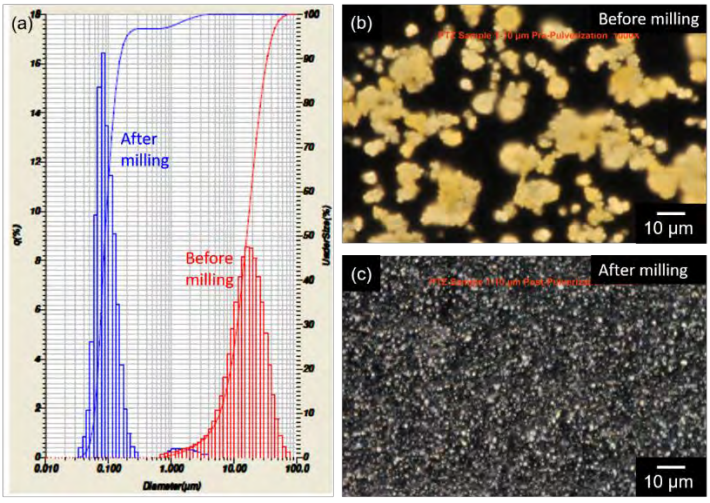

Figure **5-16**: (a) The size distributions of sol-gel PZT powder before (red) and after (blue) pulverization. The optical microscope images of particle sizes (b) before and (c) after pulverization are also presented.

So far, neither the attrition milled powder nor the sol-gel powder is able to produce a ceramic density high enough for the as cold-sintered pellet to show a ferroelectric response. Future research should focus on the optimization of cold sintering conditions as well as the dispersion uniformity of NaOH/KOH in PZT to achieve a higher pellet density.

5.2.6 Innovative sintering techniques

The sintering of ceramics is based on diffusion. The faster the diffusion rate, the more readily the ceramics can be sintered. Increasing the temperature is the most direct way to improve the diffusion rate. This approach is adopted in conventional solid-state sintering. In order to lower the sintering temperature, other forms of energy input are required to compensate the reduction of diffusion rate. Hence, many low-temperature sintering techniques aim at using mechanical energies, electrical energies, and chemical energies. Table 5-2 categorizes some sintering techniques in terms of the forms of energies input. Note that electromagnetic wave and electric current will eventually turn into thermal energy, but both alter the path by which heat is delivered.

Table 5-2: Sintering techniques categorized by forms of energy input.

Forms of energy	Force	Heat	Sound	Electro-magnetic wave	Electric current	Chemical reaction
SSS		X				
HP	X	X				
LPS		X				X
MWS		X		X		
FS		X			X	
FAST	X	X			X	
CSP	X	X				X
LP assisted HP	X	X				X
LP assisted FS		X			X	X
LP assisted FAST	X	X			X	X

That also implies that to significantly reduce sintering temperatures, very high levels of another energy form have to be introduced. For example, when high local pressures are achieved (e.g. through aerosol deposition methods, plastic deformations will be present, and PZT samples can be densified at low temperature (albeit with significantly reduced crystallinity [21,22]). A conceptual equipment to realize this forge-like densification process is shown as Figure 5-17. The top plunge can be accelerated to very high speed via the Lorentz force generated within the die wall and hammer on the powder bed. The shock waves created in this process may result the plastic deformation of PZT and so densify the sample rapidly. Similar samples have been realized by Suzuki *et al*. via idealized packing of bimodal PZT at a high pressure (1 GPa). [23] But interconnected pores still exist.

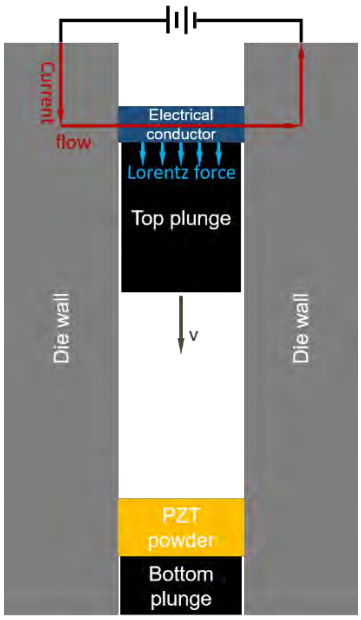

Figure **5-17**: The schematic of a press creating shock waves to cold sinter PZT.

On the other hand, to improve the CSP and decrease the uniaxial pressure to produce larger samples, other forms of energy could be employed to mitigate the need for pressure. For example, high intensity ultrasound has been reported to increase surface diffusion [24]. But

surface diffusion does not help the densification of ceramics. Ultrasound is expected to idealize particle packing [25,26], boost the migration of transient liquid phases, and trigger some sono-chemistry effects [27–29] during sintering. This requires a high-power ultrasound transducer to be attached to the current uniaxial press. A possible design was proposed by O. Khasanov *et al*. [30]

5.2.7 Piezoelectric energy harvesting measurements of PZT/Cu/PZT beams

It is of interest to test the performance of bimorph PZT beams in mechanical energy harvesting applications to demonstrate the harvesting efficiency. However, the fabrication of high power PEH beams requires larger electrodes. For sintered PZT on pure Cu, local micro-cracks were observed near the sample edges, reducing yield and limiting the maximum electrode size of each beam. Inspired by co-fired $BaTiO_3$/Ni MLCCs [31,32], where ceramic additives were incorporated into Ni electrodes to relieve thermal mismatch and prevent cracking, 0 vol%, 2.5 vol% (0.150 g), 5 vol% (0.335 g), 10 vol% (0.670 g) or 15 vol% (1.00 g) PZT powder were added into Cu tapes. Micro-cracks were prevented in sintering PZT on Cu/PZT composite tape when more than 5 vol% PZT powder was incorporated in the Cu powder (Figure 5-18). Substrate stiffness increased as PZT was added to the Cu tape; a 15 vol% PZT and 85 vol% Cu substrate began to break when a proof mass of 0.4 g.

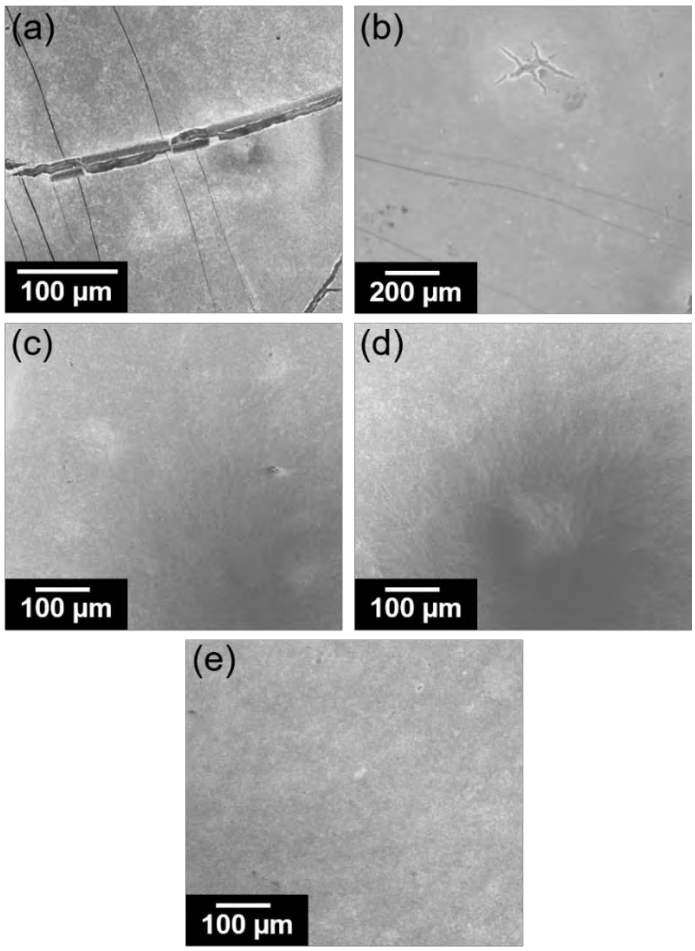

Figure 5-18: The top surface SEM of 800 °C post-sintered PZT on (a) pure Cu tape, (b) Cu/PZT with 2.5 vol% PZT inclusion, (c) Cu/PZT with 5 vol% PZT inclusion, (d) Cu/PZT with 10 vol% PZT inclusion, and (e) Cu/PZT with 15 vol% PZT inclusion.

5.2.8 Cold sintering textured PZT thick films on metal substrates for high FoM PEH

Currently, all cold sintered materials are randomly oriented. Randomly oriented PZT has reduced $e_{31,f}$ and large relative permittivity, giving low FoM for energy harvesting applications. Textured PZT fabricated by co-casting PZT powder and high aspect ratio $BaTiO_3$ as a seed for templated grain growth promises higher FoM but the grain growth rate is quite limited in PZT during sintering. [33] This produces a lower Lotgering factor in PZT compared to other lead-based

relaxors [34]. With CSP [35], grain growth in PZT pellets has been observed at 700 °C, providing a potential solution. However, studies on textured ceramic CSP rely on tape cold sintering, which needs additional development. For instance, Bordia *et al*. found that a high sample aspect ratio benefited the in-plane directional "necking" and reduced the driving force for out-of-plane directional pore shrinkage.[36] Sudre *et al* [37] indicated the removal of porosity in ceramics with high aspect ratio inclusions is influenced by a non-uniform transformation strain. Additionally, large uniaxial pressure may crush $BaTiO_3$ and disturb the alignment of the templates during CSP. [38] If the cold sintering process can be carried out at 300 °C, the required pressure of the CSP to reach the same density may decrease.

5.2.9 A design of multi-layered piezo MEMS structure for high power PEH

A stack of multi-layered PZT films, instead of one layer of piezoelectric ceramic on each side of the substrate, should improve the open circuit voltage of PEHs. However, multi-layer stacks have stress/strain distribution issues. Zhu *et al*. found the efficiency of multi-layered PEH drops as the number of layers increase; it is not worthwhile to stack more than 2 layers due to decreased power output. [39] This is likely due to the existence of strain gradients along thickness, as shown in Figure 5-19. A layer of material(s) placed between two stacks to pre-bias the piezoelectrics with compressive strain or simply a layer of elastomers to relieve the strain would allow further stacking before cracking occurs.

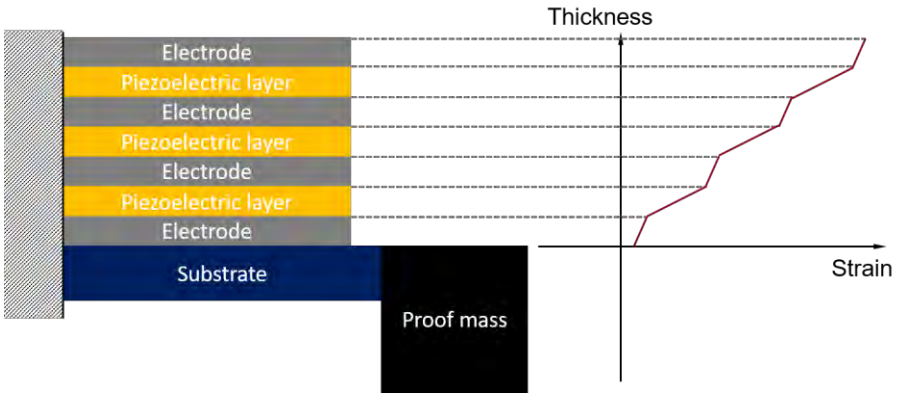

Figure 5-19: A schematic description of strain accumulation across a multi-layer PZT energy harvester. (The thicknesses of the piezoelectric layers are exaggerated)

5.2.10 Fabrication of high frequency ultrasound transducer array by cold sintered PZT tape

The CSP of PZT tape may benefit high-frequency ultrasound transducers as well. Piezoelectric ultrasonic transducers transmit and/or receive ultrasound via electro-mechanical coupling. In order to generate high resolution images for medical ultrasound, the center resonance frequency (f_c) of the transducer must be high. [40] In medical transducers, the maximum kerf width and ceramic width need to be smaller at higher f_c to avoid lateral resonances [41], complicating transducer fabrication.

Piezoelectric transducer arrays can be fabricated by the dice and fill method [42], lost mold method [43], injection molding [44], etc.; the dice and fill method is generally applied due to its simplicity. In this method, the kerf and ceramic widths are limited by the thickness of the blade and the grain size of the ceramics. [45]. As the kerf width and ceramic width get smaller, the structure of the transducer array becomes fragile. Stacking tape cast PZT to make the transducer array leads to structural collapse during sintering [46,47]. Kwon *et al*. reported a tape casting method producing a fine scale 2-2 composite transducer using 3-side supports to protect the

arrays from collapsing. When the supports were reduced to 2 sides, the structure began to deform. [48]

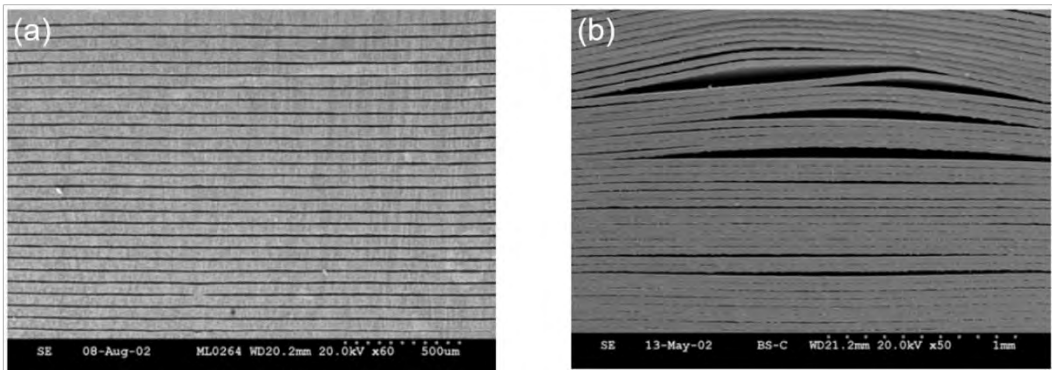

Figure 5-20: Structures of the PZT/ceramic 2-2 composite with (a) 3-side ceramic supports and (b) 2-side supports. (SEM images from Kwon *et al*. [48])

If the structure of the array can be densified and strengthened during CSP to hold its shape during the processing, fabricating transducer arrays with thinner kerf width and ceramic width may be possible. Here a hypothetical stacking strategy is proposed. The teeth-shaped (stack A) and rectangle-shaped (stack B) PZT and sacrificial material tapes can be laminated, burnt out, and cold sintered in a sequence of …ABABAB… Once the sacrificial layers are eliminated during post-sintering, the 1-3 transducer array can be formed.

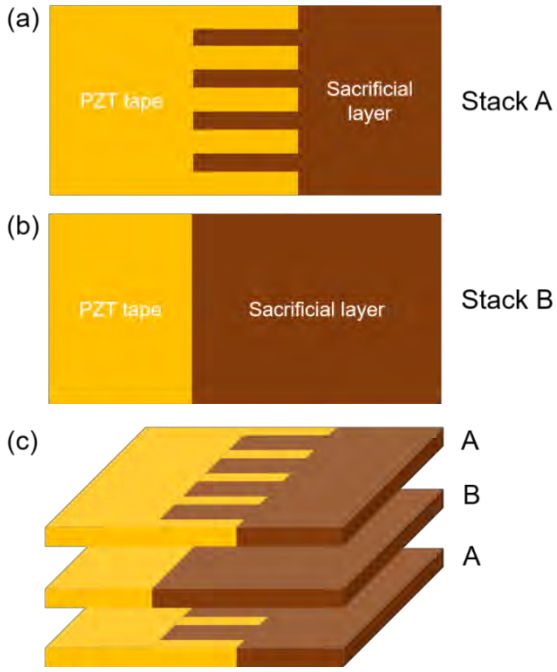

Figure 5-21: (a) The A-layer stacking with teeth-like structured PZT and sacrificial layer tapes. (b) The B-layer stacking with rectangle-shaped PZT and sacrificial layer tapes.

There are several processing challenges in this proposed method. First, it is suggested this the green tape could be cut to shape using a laser. It would then be critical to align these tapes precisely to avoid gaps. Finally, the sacrificial layer must survive burn out but must be removed during post-sintering. Some materials such as polyimide and graphite should be suitable for this process. One may even consider tape casting polyimide powder or carbon black powder so that the sacrificial layers can be co-sintered with PZT tapes and achieve low internal stress samples. This portion of the work is currently under investigation by Shruti Gupta in the Trolier-McKinstry group.

References

[1] Kolah, A. K.; Asthana, N. S.; Vu, D. T.; Lira, C. T.; Miller, D. J. Reaction Kinetics of the Catalytic Esterification of Citric Acid with Ethanol. Ind. Eng. Chem. Res. 2007, 46 (10), 3180–3187.

[2] Xu, H.; Zhu, T.; Yu, R. P. Study on the Absorption and Fluorescence Spectra of Ethylene Glycol and Glycerol. Guang Pu Xue Yu Guang Pu Fen Xi/Spectroscopy Spectr. Anal. 2007, 27 (7), 1381–1384.

[3] Michael-Sapia, E. K.; Li, H. U.; Jackson, T. N.; Trolier-McKinstry, S. Nanocomposite Bismuth Zinc Niobate Tantalate for Flexible Energy Storage Applications. J. Appl. Phys. 2015, 118 (23), 234102.

[4] Langton, N. H.; Matthews, D. The Dielectric Constant of Zinc Oxide over a Range of Frequencies. Br. J. Appl. Phys. 1958, 9 (11), 453–456.

[5] Valant, M.; Suvorov, D. Dielectric Characteristics of Bismuth Oxide Solid Solutions with a Fluorite-Like Crystal Structure. J. Am. Ceram. Soc. 2004, 87 (6), 1056–1061.

[6] Michael, E. K.; Trolier-McKinstry, S. Bismuth Pyrochlore-Based Thin Films for Dielectric Energy Storage, Pennsylvania State University, 2015.

[7] Li, Q.; Chen, L.; Gadinski, M. R.; Zhang, S.; Zhang, G.; Li, H.; Haque, A.; Chen, L.-Q.; Jackson, T.; Wang, Q. Flexible High-Temperature Dielectric Materials from Polymer Nanocomposites. Nature 2015, 523 (7562), 576–579.

[8] Shen, Z. H.; Wang, J. J.; Lin, Y.; Nan, C. W.; Chen, L. Q.; Shen, Y. High-Throughput Phase-Field Design of High-Energy-Density Polymer Nanocomposites. Adv. Mater. 2018, 30 (2), 1–6.

[9] Bridger, K.; Sutherland, A.; Fiore, E.; Bailey, A.; Christodoulou, J.; Winzer, S. Lead Magnesium Niobate Dielectrics for High-Field Applications. In Proceedings of the IEEE 35th International Power Sources Symposium; IEEE, 1992; pp 387–390.

[10] Yang, H.; Yan, F.; Lin, Y.; Wang, T.; Wang, F.; Wang, Y.; Guo, L.; Tai, W.; Wei, H. Lead-Free $BaTiO_3$-$Bi_{0.5}Na_{0.5}TiO_3$-$Na_{0.73}Bi_{0.09}NbO_3$ Relaxor Ferroelectric Ceramics for High Energy Storage. J. Eur. Ceram. Soc. 2017, 37 (10), 3303–3311.

[11] Zhou, M.; Liang, R.; Zhou, Z.; Dong, X. Achieving Ultrahigh Energy Storage Density and Energy Efficiency Simultaneously in Sodium Niobate-Based Lead-Free Dielectric Capacitors via Microstructure Modulation. Inorg. Chem. Front. 2019, 6 (8), 2148–2157.

[12] Zhao, X.; Guo, J.; Wang, K.; Herisson De Beauvoir, T.; Li, B.; Randall, C. A. Introducing a ZnO–PTFE (Polymer) Nanocomposite Varistor via the Cold Sintering Process. Adv. Eng. Mater. 2018, 20 (7), 1–8.

[13] Du, Y.; Inman, D. Precipitation of Finely Divided $A1_2O_3$ Powders by a Molten Salt Method. J. Mater. Chem. 1996, 6 (7), 1239–1240.

[14] Liu, H.; Hu, C.; Wang, Z. L. Composite-Hydroxide-Mediated Approach for the Synthesis of Nanostructures of Complex Functional-Oxides. Nano Lett. 2006, 6 (7), 1535–1540.

[15] Dash, A.; Vaßen, R.; Guillon, O.; Gonzalez-Julian, J. Molten Salt Shielded Synthesis of Oxidation Prone Materials in Air. Nat. Mater. 2019, 18 (5), 465–470.

[16] Liu, X.; Fechler, N.; Antonietti, M. Salt Melt Synthesis of Ceramics, Semiconductors and Carbon Nanostructures. Chem. Soc. Rev. 2013, 42 (21), 8237–8265.

[17] Pearson, R. G. Hard and Soft Acids and Bases, HSAB, Part I: Fundamental Principles. J. Chem. Educ. 1968, 45 (9), 581–587.

[18] Pearson, R. G. Hard and Soft Acids and Bases, HSAB, Part II: Underlying Theories. J. Chem. Educ. 1968, 45 (10), 643–648.

[19] Hawthorne, F. C. Toward Theoretical Mineralogy: A Bond-Topological Approach. Am. Mineral. 2015, 100 (4), 696–713.

[20] Centre for Research in Computational Thermochemistry. KOH-NaOH phase diagram http://www.crct.polymtl.ca/fact/phase_diagram.php?file=KOH-NaOH.jpg&dir=FTsalt%0A.

[21] Akedo, J. Room Temperature Impact Consolidation (RTIC) of Fine Ceramic Powder by Aerosol Deposition Method and Applications to Microdevices. J. Therm. Spray Technol. 2008, 17 (2), 181–198.

[22] Akedo, J.; Lebedev, M. Piezoelectric Properties and Poling Effect of Pb(Zr, Ti)O_3 Thick Films Prepared for Microactuators by Aerosol Deposition. Appl. Phys. Lett. 2000, 77 (11), 1710–1712.

[23] Suzuki, M.; Ushijima, H.; Tsuchiya, T.; Akedo, J. Polarization Properties of Aggregate PZT Films Produced at Room Temperature. In Proceedings of the 19th US-Japan Seminar on Dielectric & Piezoelectric Ceramics; Kato, K., Brennecka, G., Eds.; Tsukuba, Japan, 2019; pp 147–148.

[24] Shugaev, M. V.; Manzo, A. J.; Wu, C.; Zaitsev, V. Y.; Helvajian, H.; Zhigilei, L. V. Strong Enhancement of Surface Diffusion by Nonlinear Surface Acoustic Waves. Phys. Rev. B - Condens. Matter Mater. Phys. 2015, 91 (23), 1–11.

[25] Cha, H. R. Densification of the Nanopowder by Using Ultrasonic Vibration Compaction. Rev. Adv. Mater. Sci. 2011, 28 (1), 90–93.

[26] Karban, O.; Kanunnikova, O.; Khazanov, E.; Salamatov, E.; Khasanov, O.; Taranov, A. Structure and Composition of Ba-W-Ti-O Ceramics Interface Regions Formed at Ultrasonic Vibration. ISRN Nanomater. 2012, 2012, 1–7.

[27] Xu, M.; Lu, Y. N.; Liu, Y. F.; Shi, S. Z.; Qian, T. S.; Lu, D. Y. Sonochemical Synthesis of Monosized Spherical $BaTiO_3$ Particles. Powder Technol. 2006, 161 (3), 185–189.

[28] Wirunchit, S.; Charoonsuk, T.; Vittayakorn, N. Facile Sonochemical Synthesis of Near Spherical Barium Zirconate Titanate ($BaZr_{1-y}Ti_yO_3$; BZT); Perovskite Stability and Formation Mechanism. RSC Adv. 2015, 5 (48), 38061–38074.

[29] Xu, Z. J.; Chu, R. Q.; Li, G. R.; Shao, X.; Yin, Q. R. Preparation of PZT Powders and Ceramics via a Hybrid Method of Sol-Gel and Ultrasonic Atomization. Mater. Sci. Eng. B Solid-State Mater. Adv. Technol. 2005, 117 (2), 113–118.

[30] Khasanov, O.; Dvilis, E.; Sokolov, V.; Pokholkov, Y. Mechanisms of Dry Powder Net-Shaping Under Ultrasonic Vibration and By the Collector Method. In Proceedings of the 2nd International Congress on Ceramics; Institute of Science and Technology for Ceramics-National Research Council, 2008; pp 359–368.

[31] Sugimura, K.; Hirao, K. Effect of a $BaTiO_3$ Nanoparticle Additive on the Quality of Thin-Film Ni Electrodes in MLCC. J. Ceram. Soc. Japan 2009, 117 (1369), 1039–1043.

[32] Kang, J.-H.; Joo, D.; Cha, H.-M.; Jung, Y.-G.; Paik, U. Shrinkage Behavior and Interfacial Diffusion in Ni-Based Internal Electrodes with $BaTiO_3$ Additive. Ceram. Int. 2008, 34 (6), 1487–1494.

[33] Muramatsu, H.; Kimura, T. Preparation of Bulk $Pb(Zr, Ti)O_3$ with Crystallographic Texture by Templated Grain Growth Method. J. Electroceramics 2004, 13 (1–3), 531–535.

[34] Chang, Y.; Watson, B.; Fanton, M.; Meyer, R. J.; Messing, G. L. Enhanced Texture Evolution and Piezoelectric Properties in CuO-Doped $Pb(In_{1/2}Nb_{1/2})O_3$-$Pb(Mg_{1/3}Nb_{2/3})O_3$-$PbTiO_3$ Grain-Oriented Ceramics. Appl. Phys. Lett. 2017, 111 (23), 232901.

[35] Wang, D.; Guo, H.; Morandi, C. S.; Randall, C. A.; Trolier-McKinstry, S. Cold Sintering and Electrical Characterization of Lead Zirconate Titanate Piezoelectric Ceramics. APL Mater. 2018, 6 (1), 016101.

[36] Bordia, R. K.; Scherer, G. W. On Constrained Sintering—III. Rigid Inclusions. Acta Metall. 1988, 36 (9), 2411–2416.

[37] Sudre, O.; Bao, G.; Fan, B.; Lange, F. F.; Evans, A. G. Effect of Inclusions on Densification: II, Numerical Model. J. Am. Ceram. Soc. 1992, 75 (3), 525–531.

[38] Uskokovic, D. P.; Palmour III, H.; Spriggs, R. M. Science of Sintering; Uskoković, D. P., Palmour, H., Spriggs, R. M., Eds.; Springer US: Boston, MA, 1989.

[39] Zhu, D.; Almusallam, A.; Beeby, S. P.; Tudor, J.; Harris, N. R. A Bimorph Multi-Layer Piezoelectric Vibration Energy Harvester. In Proceedings of PowerMEMS; IOP Publishing, 2010; pp 335–338.

[40] Zhou, Q.; Lau, S.; Wu, D.; Kirk Shung, K. Piezoelectric Films for High Frequency Ultrasonic Transducers in Biomedical Applications. Prog. Mater. Sci. 2011, 56 (2), 139–174.

[41] Ritter, T. A.; Shrout, T. R.; Tutwiler, R.; Shung, K. K. A 30-MHz Piezo-Composite Ultrasound Array for Medical Imaging Applications. IEEE Trans. Ultrason. Ferroelectr. Freq. Control 2002, 49 (2), 217–230.

[42] Savakus, H. P.; Klicker, K. A.; Newnham, R. E. PZT-Epoxy Piezoelectric Transducers: A Simplified Fabrication Procedure. Mater. Res. Bull. 1981, 16 (6), 677–680.

[43] Becker, E. W.; Ehrfeld, W.; Hagmann, P.; Maner, A.; Münchmeyer, D. Fabrication of Microstructures with High Aspect Ratios and Great Structural Heights by Synchrotron Radiation Lithography, Galvanoforming, and Plastic Moulding (LIGA Process). Microelectron. Eng. 1986, 4 (1), 35–56.

[44] Bowen, L. J.; French, K. W. Fabrication of Piezoelectric Ceramic/Polymer Composites by Injection Molding. In ISAF ’92: Proceedings of the Eighth IEEE International Symposium on Applications of Ferroelectrics; IEEE, 1992; pp 160–163.

[45] Janas, V. F.; Safari, A. Overview of Fine-Scale Piezoelectric Ceramic/Polymer Composite Processing. J. Am. Ceram. Soc. 1995, 78 (11), 2945–2955.

[46] Hackenberger, W.; Ming-Jen Pan; Kuban, D.; Ritter, T.; Shrout, T. Novel Method for Producing High Frequency 2-2 Composites from PZT Ceramic. In Proceedings of the 2000 IEEE Ultrasonics Symposium. Proceedings. An International Symposium (Cat. No.00CH37121); IEEE, 2000; Vol. 2, pp 969–972.

[47] Zhang, Y.; Jiang, Y.; Lin, X.; Xie, R.; Zhou, K.; Button, T. W.; Zhang, D. Fine-Scaled Piezoelectric Ceramic/Polymer 2-2 Composites for High-Frequency Transducer. J. Am. Ceram. Soc. 2014, 97 (4), 1060–1064.

[48] Kwon, S.; Hackenberger, W.; Rehrig, P.; Snook, K.; Rhee, S.; Shrout, T. R.; Geng, X. Ceramic/Polymer 2-2 Composites for High Frequency Transducers by Tape Casting. In IEEE Symposium on Ultrasonics, 2003; IEEE, 2003; Vol. 1, pp 366–369.

Appendix A

Supplementary Materials for Chapter 2

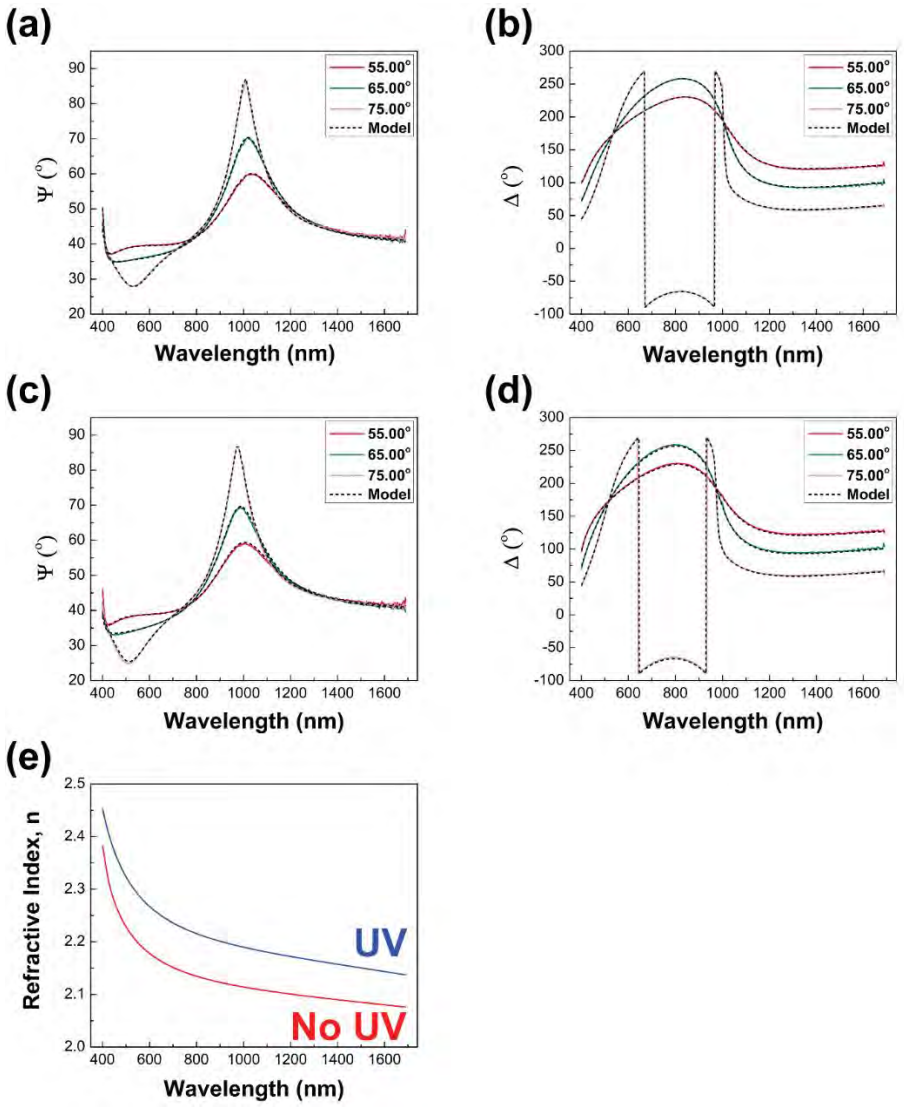

Figure **A-1**: (a)-(b) The spectroscopic ellipsometry data (Ψ and Δ vs. wavelength) of 450 °C-annealed BNO with DUV treatment. The mean square error (MSE) is 7.530. (c)-(d) The spectroscopic ellipsometry data (Ψ and Δ vs. wavelength) of 450 °C-annealed BNO with no DUV treatment. The MSE is 15.582. (e) The extracted refractive index vs. wavelength for 450 °C-annealed BNO thin films with and without UV exposure.

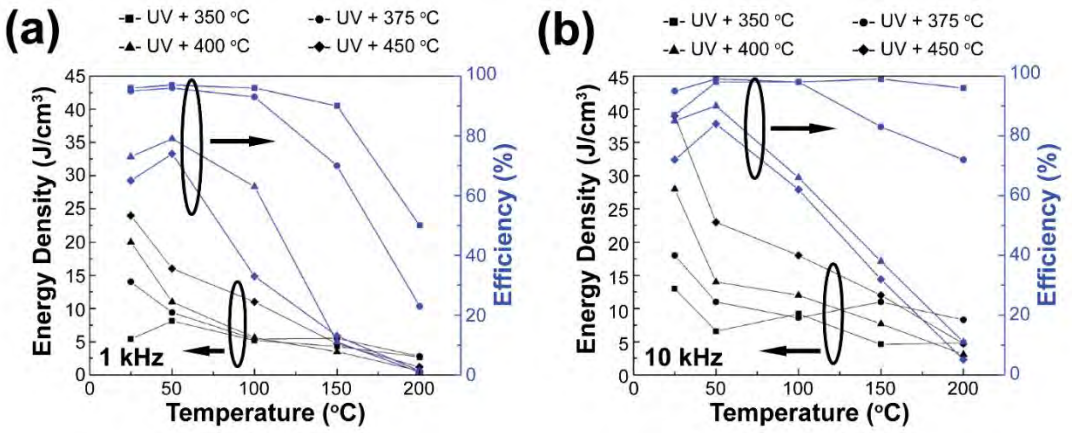

Figure **A-2**: (a) The 1 kHz energy densities and efficiencies of the UV treated BNO thin films measured under different temperatures at their maximum electric fields. (b) The 10 kHz energy densities and efficiencies of the UV treated BNO thin films measured at different temperatures at their maximum electric fields.

Table **A-1**: A summary of the additional information on the materials mentioned in Figure 2-25 including maximum processing temperatures, energy densities, maximum applied fields, efficiencies, frequencies, sample thicknesses, electrode materials and electrode diameters. The numbers in the table correspond to the numbers in Figure 2-25.

#	Material	Maximum processing temperature (°C)	Energy density (J/cm^3)	Maximum applied field (kV/cm)	Efficiency (%)	Frequency (Hz)	Sample thickness (μm)	Electrode	Electrode diameter
Polymers/polymer-based nanocomposites									
1	Poly(vinylidene fluoride-co-hexafluoropropylene)-graft-poly(dopamine methacrylamide)	140	33	8590	--	0.1	5.5	Au/Pt	3 mm
2	poly(vinylidene fluoride-hexafluoropropylene)	110	25	7000	--	10	3-11	Al	3.18 mm
3	$(Ba_{0.94}Ca_{0.06})(Zr_{0.16}Ti_{0.84})O_3$ + poly(methyl methacrylate)	100	23	3000	--	100	10-20	Cu/Ag	--
4	boron nitride nanosheets + poly(vinylidene fluoride-ter-trifluoroethylene-ter-chlorofluoro- ethylene)	110	20	6500	77	10	15	Au	3 mm
5	$Ba_{0.6}Sr_{0.4}TiO_3$ nanofibers + poly(vinylidene fluoride)	45	6.95	3800	50	10	10-20	Au	2 mm
6	$BaTiO_3$ + poly(vinylidene fluoride)	80	4.12	2050	67	100	30-40	Au	2 mm
7	poly(vinylidene fluoride-hexafluoropropylene)/poly(vinylidene fluoride)	190	30.1	8540	--	10	4	Pt	--
8	poly(vinylidene fluoride-chlorotrifluoroethylene)	230	25	6000	--	10	10	Al	--
9	$BaTiO_3$@TiO_2 nanofibers + poly(vinylidene fluoride)	200	20	6460	--	10	10	Cu	4 mm
10	Kaolinite + poly(vinylidene fluoride-hexafluoropropylene)	200	19	7800	64	10	10-12	Au	3.3 mm
11	$Ba_{0.2}Sr_{0.8}TiO_3$ nanowires + poly(vinylidene fluoride)	200	15	4500	65	1, 000	10	Au	--
12	γ-poly(vinylidene fluoride)	200	14	5000	--	10	20-30	Au	--
13	$BaTiO_3$ nanowires/mTiO_2 + poly(vinylidene fluoride-hexafluoropropylene)	200	9.53	4400	65	10	15	Cu	12 mm
14	$SrTiO_3$ + poly(vinylidene fluoride)	200	5.1	2700	65	100	10-15	--	--

	#	Material	Maximum processing temperature (°C)	Energy density (J/cm^3)	Maximum applied field (kV/cm)	Efficiency (%)	Frequency (Hz)	Sample thickness (µm)	Electrode	Electrode diameters
Thin film ceramics	15	$Bi_{1.5}Zn_{0.9}Nb_{1.35}Ta_{0.15}O_{6.9}$ nanocomposite	350	40	3800	93	10, 000	0.11	Pt	200 µm
	16	UV + 450 °C annealed Bi_3NbO_7	450	39	3600	72	10, 000	0.12	Pt	200 µm
	17	400 °C annealed Bi_3NbO_7	400	28	3000	85	10, 000	0.12	Pt	200 µm
	18	375 °C annealed Bi_3NbO_7	375	18	2500	95	10, 000	0.14	Pt	200 µm
	19	350 °C annealed Bi_3NbO_7	350	13	2300	87	10, 000	0.14	Pt	200 µm
	20	$SrTiO_3/La_{0.67}Sr_{0.33}MnO_3$	700	307	6800	89	2, 000	0.71	LSMO/Au	100 µm (LSMO)
	21	$(Ba_{0.5}Na_{0.5})_{0.9118}La_{0.02}Ba_{0.0582}(Ti_{0.97}Zr_{0.03})O_3$	700	154	3500	97	10, 000	0.35	Au	100 µm
	22	$Bi_{1.5}Zn_{0.9}Nb_{1.35}Ta_{0.15}O_{6.9}$	600	67	6100	80	10, 000	0.15	Pt	200 µm
	23	$Pb_{0.96}La_{0.04}Zr_{0.98}Ti_{0.02}O_3$	650	61	4300	33	10, 000	0.69	LNO/Pt	250 µm (Pt)
	24	$Pb_{0.97}Y_{0.02}[(Zr_{0.6}Sn_{0.4})_{0.925}Ti_{0.075}]O_3$	700	32.7	1800	93	1, 000	0.5	Pt	178 µm
	25	$0.94(Na_{0.5}Bi_{0.5}TiO_3)$-$0.06BaTiO_3/Pb_{0.8}La_{0.1}Ca_{0.1}Ti_{0.975}O_3$	650	17	3310	74	1, 000	0.29	Pt	200 µm
	26	HfO_2	700	21	4000	75	10, 000	0.063	LNO/Au	200 µm
	27	$Pb_{0.99}Nb_{0.02}(Zr_{0.55}Sn_{0.40}Ti_{0.05})_{0.98}O_3$	700	16	1600	71	1, 000	0.55	Au	200 µm

	#	Material	Maximum processing temperature (°C)	Energy density (J/cm^3)	Maximum applied field (kV/cm)	Efficiency (%)	Frequency (Hz)	Sample thickness (μm)	Electrode	Electrode diameters
Bulk ceramics	28	$AgNb_{0.85}Ta_{0.15}O_3$	1100	4.2	240	69	1	200	Ag	--
	29	$0.8BaTiO_3$-$0.2BiYO_3$	1100	0.316	66	82.7	100	--	Ag	--
	30	$Pb_{0.99}Nb_{0.02}(Zr_{0.95}Ti_{0.05})_{0.98}O_3$	1150	1.75	50	--	2	250	Ag	10 mm x 10 mm (square)
	31	$BaTiO_3$-$Bi(Zn_{0.5}Ti_{0.5})O_3$	1200	2.8	330	--	1	29	Pt-Au-Pd	--
	32	$0.63SiO_2 \cdot 0.12BaO \cdot 0.16B_2O_3 \cdot 0.09Al_2O_3$ (Schott AF-45)	1225	39	12000	--	DC	30	Pt	2.53 mm
	33	$0.65Bi_2O_3$-$0.20B_2O_3$-$0.15SiO_2$ + $BaTiO_3$	1225	10	1000	--	50	16	Ag	6 mm
	34	$0.9(K_{0.5}Na_{0.5})NbO_3$-$0.1Bi(Mg_{2/3}Nb_{1/3})O_3$	1220	4.1	300	63	5	200	Ag	6 mm x 6 mm (square)
	35	0.5 mol% Mn-doped $0.8CaTiO_3$-$0.2CaHfO_3$	1300	9.6	1300	--	1	9	Ag	2 mm
	36	$0.7BaTiO_3$-$0.3BiScO_3$	1250	6.1	730	--	10, 000	15	Ag	--
	37	$(Pb_{0.87}Ba_{0.1}La_{0.02})(Zr_{0.68}Sn_{0.24}Ti_{0.08})O_3$	1280	3.2	180	--	--	600	Ag	5 mm
	38	$Ba_{0.997}Sm_{0.002}Zr_{0.15}Ti_{0.85}O_3$	1270	1.15	10	92	10	--	Ag	--
	39	$SrTiO_3$-$Bi_{0.5}Na_{0.5}TiO_3$-$BaAl_{0.5}Nb_{0.5}O_3$	1350	1.89	190	77	10	200	--	--
	40	$0.85BaTiO_3$-$0.15Bi(Mg_{2/3}Nb_{1/3})O_3$	1350	1.13	143.5	95.8	10	--	Au	--

Appendix B

Supplementary Materials for Chapter 3

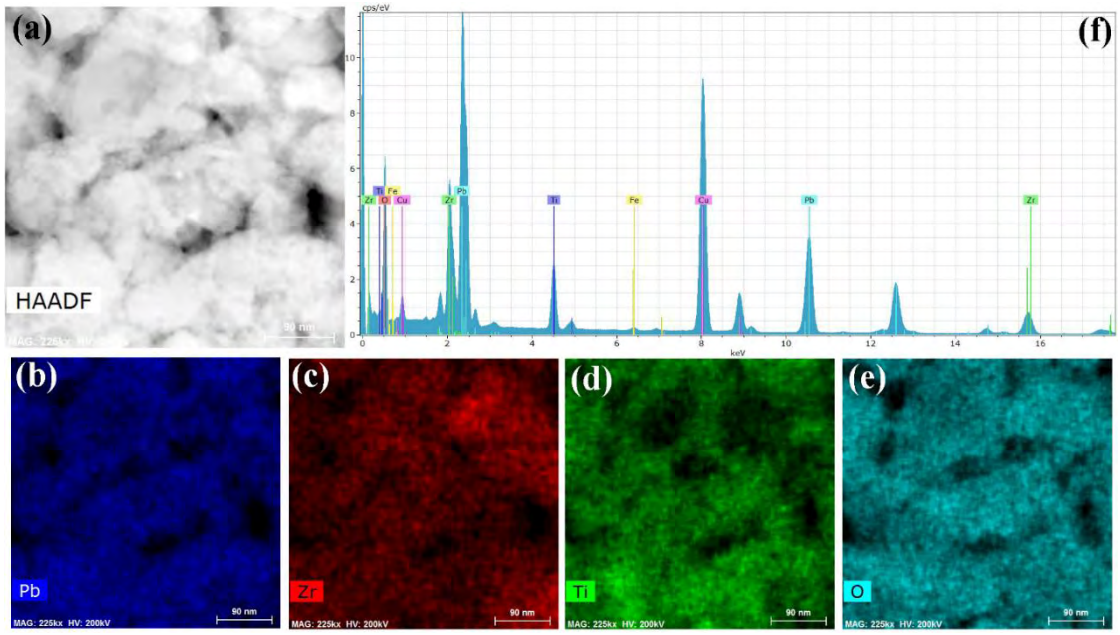

Figure **B-1**: (a) Representative HAADF micrograph, (b)-(e) corresponding EDS chemical mapping, and (f) EDS spectrum, of the PZT ceramics cold sintered at 300 ºC.

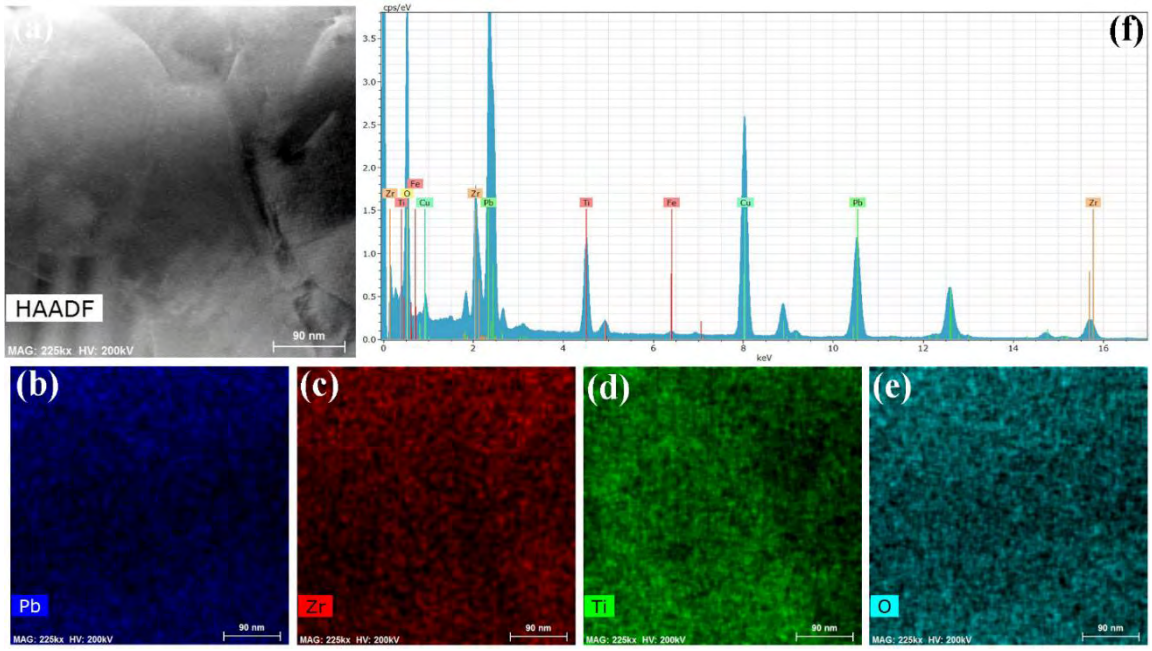

Figure **B-2**: (a) Representative HAADF micrograph, (b)-(e) corresponding EDS chemical mapping, and (f) EDS spectrum, of the cold sintered PZT ceramics after annealing at 700 ºC.

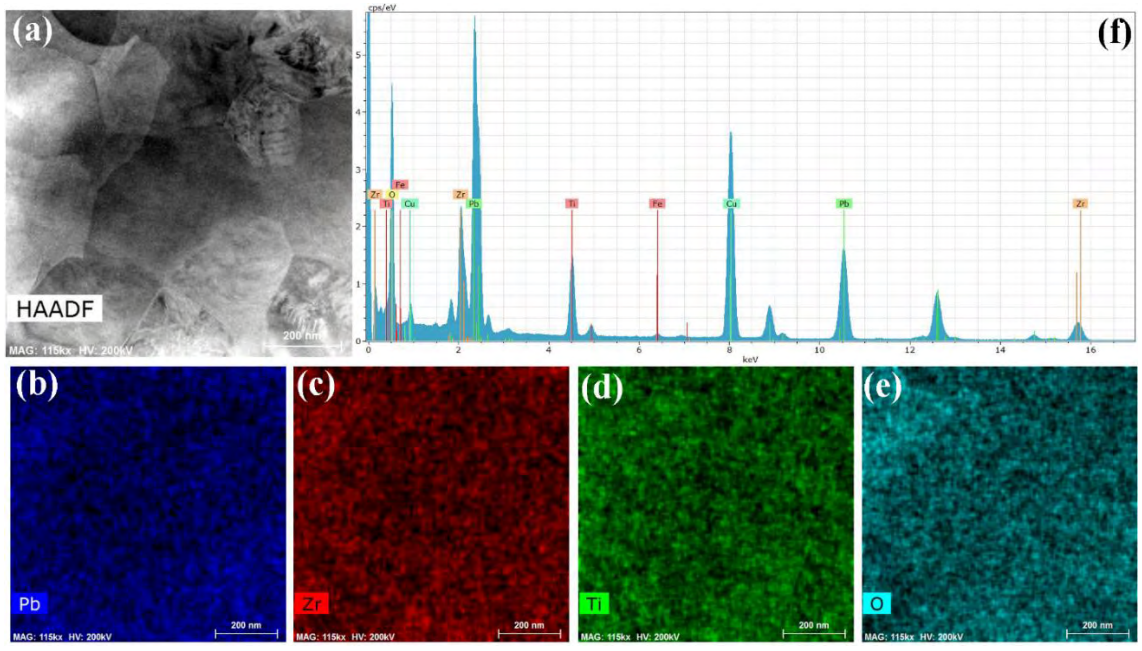

Figure **B-3**: (a) Representative HAADF micrograph, (b)-(e) corresponding EDS chemical mapping, and (f) EDS spectrum, of the cold sintered PZT ceramics after annealing at 900 ºC.

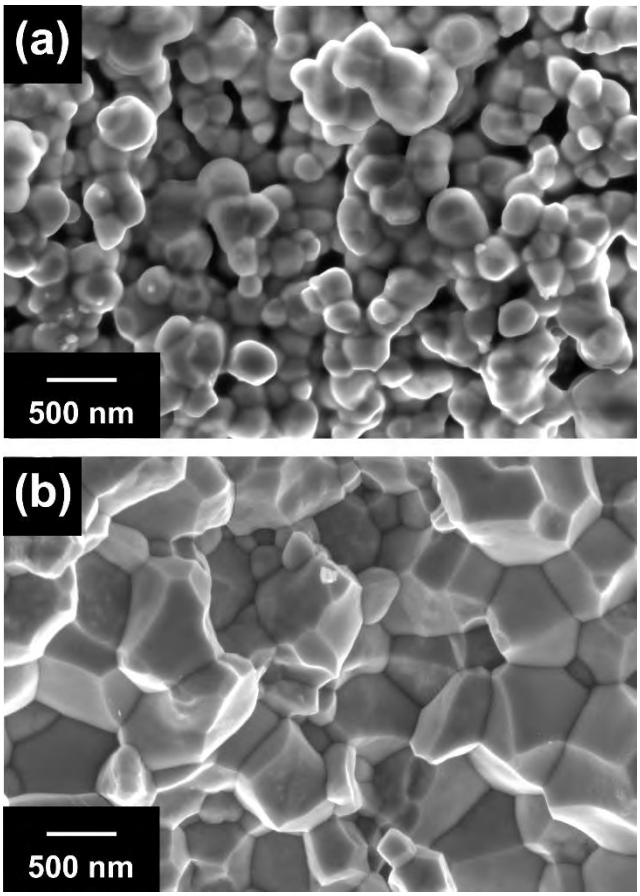

Figure **B-4**: (a) FESEM fracture surface image of a bimodal PZT pellet uniaxially pressed without cold sintering (e.g. no lead nitrate or liquid at 300 ºC for 3 hrs) under 500 MPa and post-annealed at 900 ºC for 3 hrs in air. (b) The bimodal PZT cold sintered with lead nitrate sintering aid at 300 ºC for 3 hrs under 500 MPa and post-annealed at 900 ºC for 3 hrs in air.

Appendix C

Supplementary Materials for Chapter 4

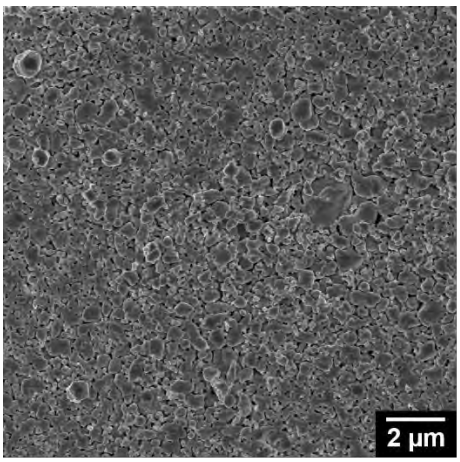

Figure **C-1**: The surface morphology of an 800 °C annealed PZT tape without lead nitrate as a sintering aid.

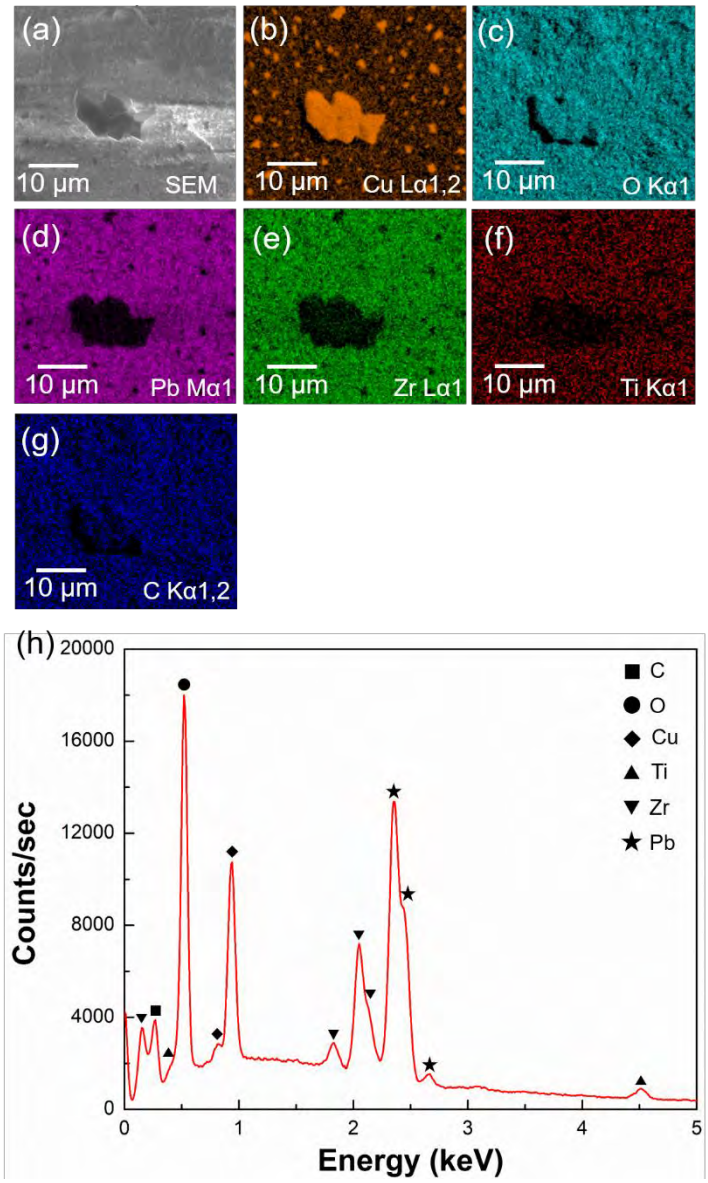

Figure C-2: (a) The top surface of 800 °C annealed PZT indicating a Cu_2O crystal. (b)-(g) EDS mapping of Cu, O, Pb, Zr, Ti, and C respectively. (h) The EDS spectrum of PZT surface.

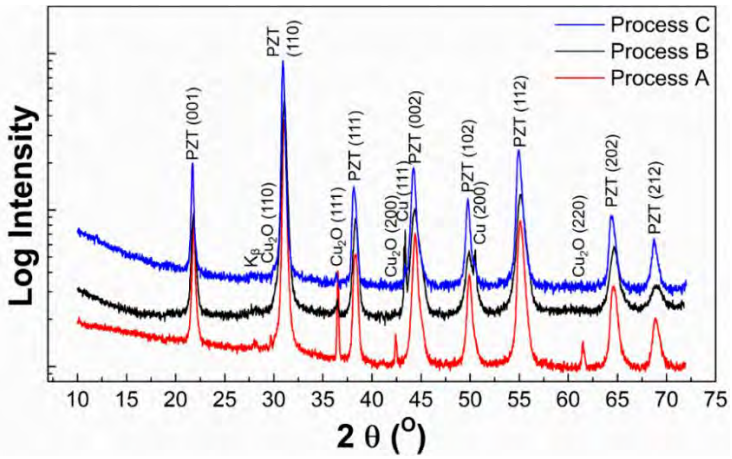

Figure **C-3**: The XRD spectra of 800 °C post-sintered PZT on Cu with Cu_2O contamination (Process A), the 800 °C post-sintered PZT on Cu from PZT tape without lead nitrate (Process B), and the sintered PZT/Cu composite using a cleaned (at 900 °C for 12 hours) alumina sample holder (Process C).

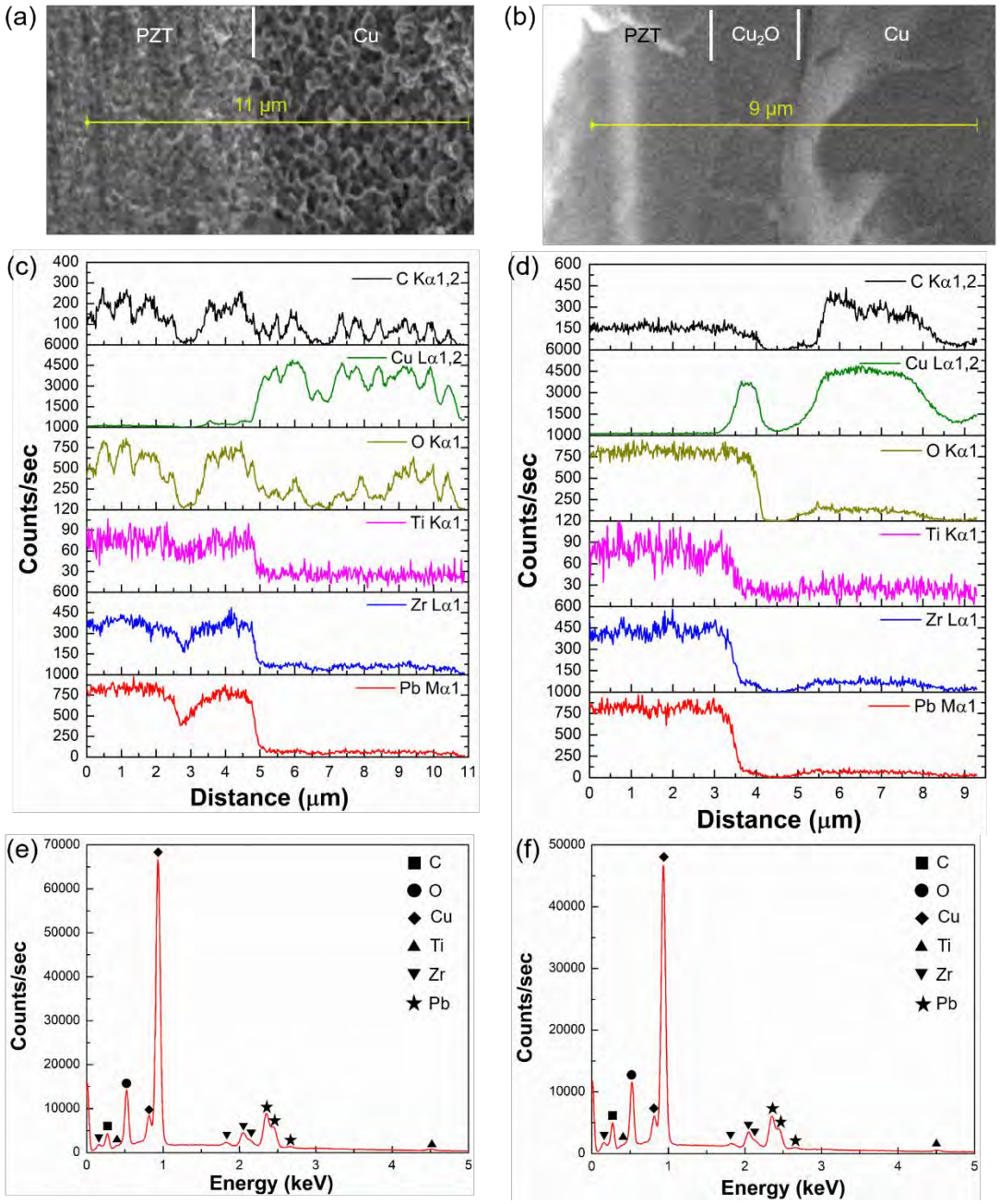

Figure **C-4**: (a) (b) Cross-sectional SEM of as cold-sintered PZT/Cu (left) and 800 °C annealed PZT/Cu (right) showing the EDS line scan positions. (c) (d) The EDS line scans of the two above regions. (e) (f) The EDS spectra from the line scans on as cold-sintered PZT/Cu (left) and 800 °C annealed PZT/Cu (right).

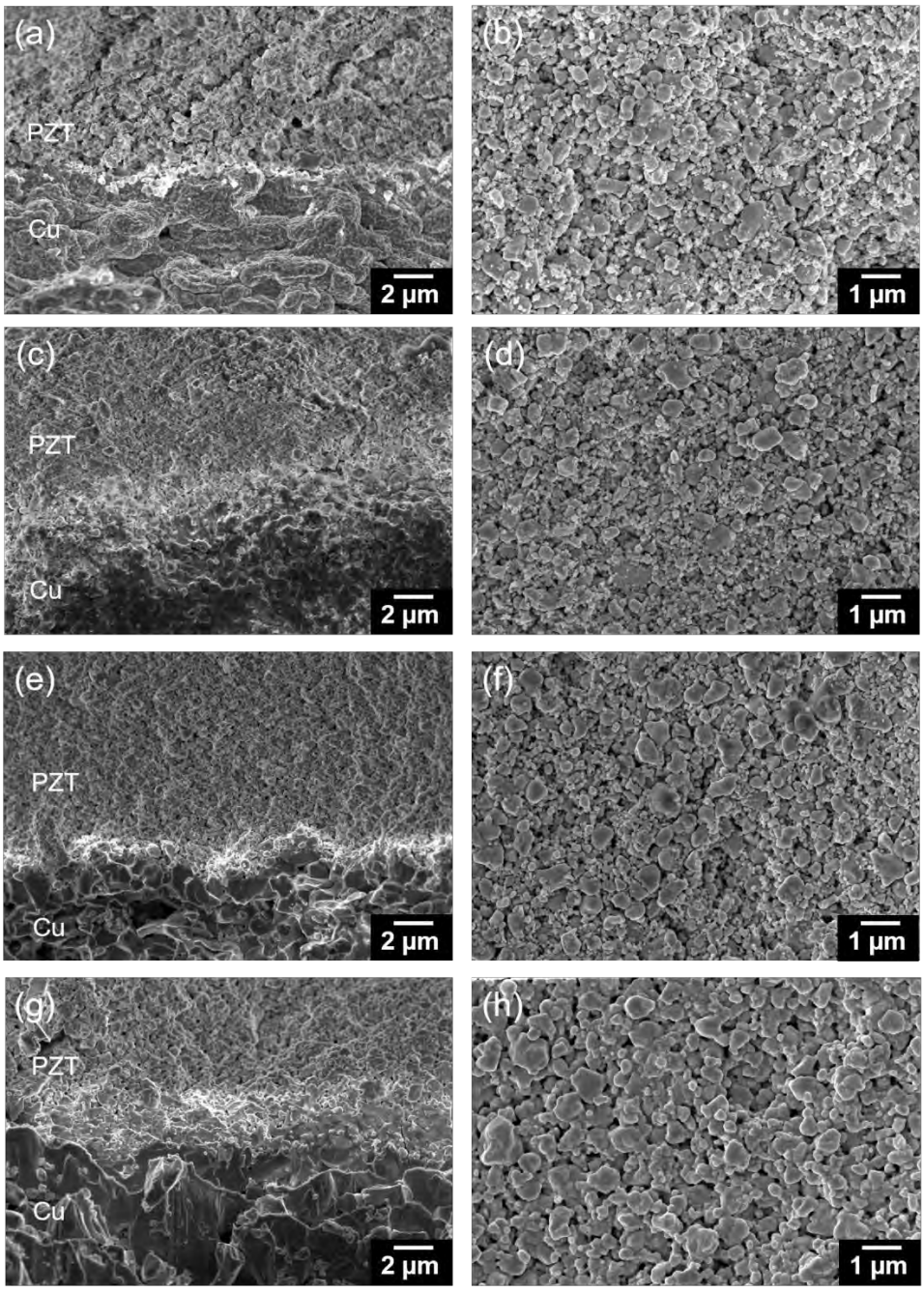

Figure C-5: (a) Cross-sectional and (b) top-down SEM of cold sintered and 400 °C 3hrs annealed PZT/Cu. (c) (d) Cross-sectional and top-down SEM of cold sintered and 500 °C 3hrs annealed PZT/Cu. (e) (f) SEM of cold sintered and 600 °C 3hrs annealed PZT/Cu. (g) (h) SEM of cold sintered and 700 °C 3hrs annealed PZT/Cu.

VITA

Dixiong Wang

Dixiong Wang was born in Harbin, China in May 1992. He entered high school in 2008 during which he started to show interests in physics and chemistry. In 2011, he was admitted by the Honor School of Harbin Institute of Technology (HIT) majoring in Materials Science and Engineering. One year later, he became an undergraduate research assistant in Dr. Yaming Wang's group working on nitrogen and boron doped graphene nanosheet supercapacitor. He then transferred to Pennsylvania State University (PSU) in 2013. In January 2014, he acquired his first chemical vapor deposited graphene in Dr. Joshua Robinson's lab. This study helped him complete his B.S. degree at PSU and B.Eng. degree at HIT in 2015. From August 2015, he continued to pursuit his doctorate degree in Dr. Susan Trolier-McKinstry's group till today. During this time, his research has focused on low temperature processing of dielectric/ piezoelectric thin films and ceramics.